The University Of Sheffield.

Modelling and scaling rules for high-shear wet granulation of pharmaceuticals

Stefan Bellinghausen

A thesis submitted in partial fulfillment
of the requirements for the degree of
Doctor of Philosophy

The University of Sheffield
Faculty of Engineering
Department of Chemical and Biological Engineering

May 2020

Industrial supervisors:

Dr. Emmanuela Gavi

Small Molecule Technical Development Formulation

F. Hoffmann-La Roche AG

Laura Jerke

Small Molecule Technical Development Formulation

F. Hoffmann-La Roche AG

Academic supervisors:

Prof. James D. Litster

Department of Chemical and Biological Engineering

The University of Sheffield

Prof. Agba D. Salman

Department of Chemical and Biological Engineering

The University of Sheffield

ABSTRACT

Wet granulation processes are difficult to scale up because conventional methods require ample experimental data at all scales to determine the most favourable operating conditions. A systematic model-driven design framework can facilitate this scale-up process by reducing the number of experiments required. To achieve this, a predictive model is required which should be developed based on a good understanding of all major wet granulation mechanisms. Such a model can give a better insight into the process and the effects of the operating conditions on the granulation endpoint which is needed for process design and scale-up studies.

In this study, a new nucleation model is developed to predict the nuclei size distribution. For the first time, model predictions are in good agreement with nucleation experiments over a wide range of operating conditions.

A novel predictive high-shear wet granulation model is developed using a one-dimensional population balance modelling framework. The wet granulation mechanisms are represented by rate expressions which are based on mechanistic understanding. Material characterisation tests and granulation experiments are designed to verify critical modelling assumptions and determine the modelling parameters. Based on a generic sensitivity analysis approach, the impactful parameters to estimate are identified: critical pore saturation, and coefficients for consolidation, collision and breakage. The model is validated based on predictions of experiments across four different scales from 2 L to 70 L, which is a novelty.

A novel model-driven design approach for process scale-up is proposed and applied to a high-shear wet granulation process in a case study. The model predictions are used for process design at pilot scale by visualising the predicted process behaviour in new operating performance maps for the key granule properties like size and porosity. The optimum operating range is identified by predicting the required conditions to fulfil product specifications. For the industrial implementation, detailed guidelines are given for all essential model-driven design tasks that are required for scale-up. Using model-driven design, industrial scale-up is improved to significantly reduce the experimental effort.

ACKNOWLEDGEMENTS

First of all, I would like to thank my supervisor Prof. Jim Litster for all the support throughout the years. Especially, the time invested in my personal development is very much appreciated, and the research experience gained and research methods learned are invaluable. I would also like to thank my industrial supervisor Dr. Emmanuela Gavi for always supporting and encouraging me, valuable contributions and prompt feedback. I also appreciate the good organisation the research stays in Basel and providing me with the chance to gain work experience.

To F. Hoffmann-La Roche AG for financially funding this research project and making the research facilities available for gathering data. To Laura Jerke for valuable discussions, feedback and useful insights to industrial R&D methods. To Dr. Pranay Ghosh for important support and feedback. To Dr. Dana Barrasso and Dr. Sean Bermingham for crucial technical support and sharing their modelling expertise. To Dr. Maitraye Sen for good scientific discussions. To Prof. Agba Salman for proficient research discussions and giving me the chance to use laboratory facilities. To Dr. Solomon Brown, Aaron Yeardley and Dr. Robert Milton for supporting parts of the modelling study and sharing their expertise on computational methods.

To everyone from F. Hoffmann-La Roche AG I have met and worked with for supporting the experimental work and making my stays as worthwhile as possible, especially Andreas Ewert, Alessia Schönemann, Georg Hummel and Vincent Spittler. To Dr. Rachel Smith for valuable academic support and discussions. To the entire Particle Technology Group for good support and enjoyable group events.

To my friends in and outside of Sheffield for all the joyful moments over the last years, it would not have been the same without you. To everyone I got to know on this journey for making it this unforgettable.

To my family for everything!

STATEMENT OF ORIGINALITY

Unless otherwise stated in the text, the work described in this thesis was carried out solely by the candidate. None of this work has already been accepted for any degree, nor is it concurrently submitted in candidature for any degree.

Candidate: _____

Stefan Bellinghausen

Supervisor: _____

Prof. James D. Litster

CONTENTS

LIST OF FIGURES

LIST OF TABLES

LIST OF ACRONYMS

ANN Artificial neural network

API Active pharmaceutical ingredient

CFD Computational fluid dynamics

CFN Constant Froude number

CM Compartmental modelling

comp Compartment

CPPs Critical process parameters

CQAs Critical quality attributes

CTS Constant tip speed

D Dimensional

DEM Discrete element method

DOE Design of experiments

EKE Equipartition of kinetic energy

Exp Experiment

FDM Finite difference method

FVM Finite volume method

GSA Global sensitivity analysis

LND Log-normal distribution

MCS Monte Carlo simulations

MDD Model-driven design

MPD Modified Poisson distribution

MRI Magnetic resonance imaging

OPMs Operating performance maps

PBM Population balance modelling

PD Poisson distribution

PEPT Positron emission particle tracking

PIV Particle image velocimetry

PSD Particle size distribution

Chapter 1

INTRODUCTION

Particle technology is the study of dispersed materials, in particular solid particles and powders. The isolated behaviour and the interactions between particles are investigated to make use of their effects in particulate processes. Particle technology has many applications in different industrial sectors, e.g. chemical, petrochemical, pharmaceutical, food, energy, and environmental industries. These industries combined are worth several 100 billion pounds sterling in the UK alone [HM Treasury, 2010; CIA, 2015], which makes particle technology a commercially attractive discipline. Within particle technology, wet granulation is an important process, which is widely applied to manufacture pharmaceuticals, among many other products. Wet granulation is a size enlargement process whereby granules are formed from a particulate feed using a liquid binder. The motivation to wet granulate for different industrial sectors is summarised in Table 1.1. The granules produced usually have a more uniform property distribution than the particulate feed [Agrawal and Naveen, 2011; Shanmugam, 2015]. This is crucial for the production of pharmaceutical tablets because tablet blends are composed of different materials, namely API and excipients. The goal of the process is to achieve specific granule properties which are suitable for pressing good quality tablets. Additionally, the advantages of granular materials over fine powders are essential for the further handling of the tablet blend. The most relevant advantages of granular materials are improved flowability, reduced dustiness, homogeneity, and tablettability.

Wet granulation equipment can be divided into low-shear and high-shear technologies (Figure 1.1). Low-shear wet granulation can be carried out in fluid bed granulators, drum granulators and low-shear mixers. For high-shear wet granulation, twin-screw granulators and high-shear mixers are most commonly used. In high-shear mixers, the impeller can have a vertical or horizontal axis. The right choice of equipment often depends on feed material properties or product specifications.

High-shear wet granulation is governed by the following rate processes (Figure 1.2): wetting and nucleation, consolidation, layering, coalescence, breakage, and attrition. In wetting and nucleation,

Table 1.1: Motivation for wet granulation of powder [Litster, 2016]

Reason to wet granulate	Typical application
Improve powder flowability	All applications
Reduce health and safety issues due to dust	All applications
Prevent caking during storage	Fertilizers, detergents
Increase bulk density for packaging	Detergents, food products
Control dispersion and dissolution	Food products
Prevent segregation of powder blends	Pharmaceuticals, agricultural chemicals, ore smelting
Control porosity and surface to volume ratio	Catalysts, absorbents
Improve permeability for future processing	Ore smelting
Provide useful structural forms	Powder metallurgy
Improve product appearance	Food products, consumer goods
Improve compressibility for tabletting	Pharmaceuticals

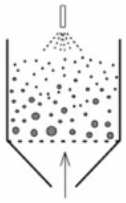

(a) Fluid bed granulator

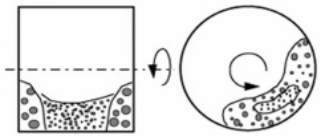

(b) Drum granulator

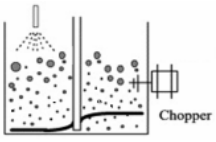

(c) High-shear mixer with a vertical axis

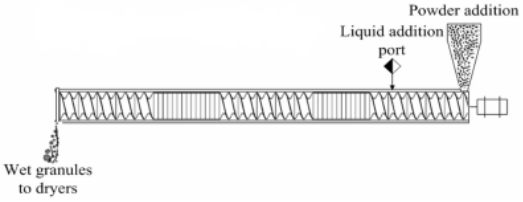

(d) Twin-screw granulator

Figure 1.1: Types of wet granulation equipment (Reprinted from [Kumar et al., 2013])

a liquid binder is sprayed onto the surface of the powder bed. The liquid binder drops penetrate the powder and form nuclei by combining with powder particles. As a result of collisions, the granules consolidate. During this process, liquid binder is squeezed out and forms a liquid layer on the surface of the granule. More powder particles adhere to the liquid layer (layering), or two granules might stick together during a collision (coalescence). The granule size can also decrease during the granulation process. Granules break into two or more daughter granules upon impacts (breakage), or fine particles abrade, especially when the granules are surface-dry (attrition).

(a) Wetting and nucleation

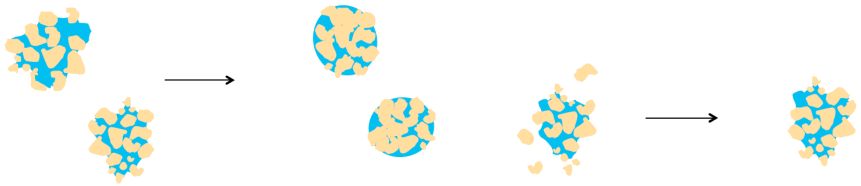

(b) Consolidation (c) Layering

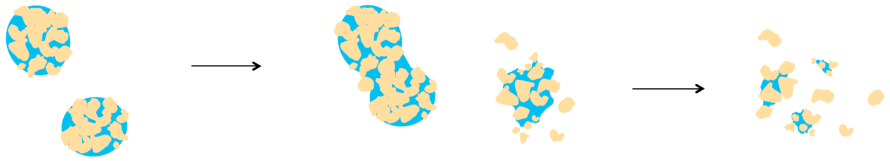

(d) Coalescence (e) Breakage

(f) Attrition

Figure 1.2: The most relevant rate processes in high-shear wet granulation [Ennis and Litster, 2008] (Reprinted from [Pohlman, 2015])

Processes are often designed and scaled up based on heuristics and experiments. This approach is

not very efficient, and optimising process conditions is often not investigated intensively. Employing process modelling helps to improve the process design and scale-up stages (model-driven design (MDD)). Firstly, less experimental data is required which makes this approach more economical and time-efficient [National Research Council, 2003]. Secondly, process conditions can be studied more systemically. Adequate models are key to this approach and essential to benefit from MDD. Having said this, modelling decisions are usually complex and not easy to make. On the one hand, a sufficient level of detail is important to provide accurate results for the quantities of interest, but on the other hand, the model should be concise and focus on the essentials to avoid a time-consuming development stage and lengthy simulations. Furthermore, process modelling is needed for other computational engineering disciplines, for instance: process control and optimisation.

Until recently, process modelling has not been applied widely to wet granulation processes due to the complexity of particulate processes and computational limitations. Nevertheless, the understanding of the phenomena in the wet granulation process has improved significantly, and advances in computing technology facilitate the use of computationally expensive simulations. Due to this progress in recent years, significant progress has also been made in process modelling of wet granulation processes, and various promising approaches have been proposed for wet granulation. However, every modelling approach focuses on capturing specific details of the process to generate the output of interest with the desired accuracy. For this reason, the objectives should be taken into account to choose a modelling approach because the most promising approach depends on the application.

In particle technology, process-scale and particle-scale modelling approaches are of particular interest. Particle-scale modelling is computationally expensive, and its complexity increases with the equipment scale, which makes it unfavourable for scale-up purposes. Process-scale modelling is a practical tool to track particle properties at process level, which can be applied at any equipment scale. Therefore, process-scale modelling is more promising for scale-up studies which focus on the particle or product properties. At process-scale, utilising mechanistic process understanding is crucial to generate a predictive model, and empirical correlations can be used additionally. A suitable process-scale tool is population balance modelling (PBM) because a combination of mechanistic and empirical elements can be incorporated. In PBM, capturing the rate processes with appropriate mathematical expressions is key. For this purpose, empirical and mechanistic expressions are available in the literature. Empirical expressions are purely based on statistical approaches. In

many cases, the effects of some physical properties are taken into account additionally; the resulting expressions are semi-empirical. Mechanistic expressions are based on first principles. A mechanistic expression that includes fitting parameters is classified as semi-mechanistic. Mechanistic expressions have several advantages over empirical expressions, e.g. more predictive and less experimental data required for parameter estimation. However, the wet granulation mechanisms are complex and difficult to capture, and that is why mechanistic expressions have been less investigated in the past.

In this study, the use of predictive modelling tools for scale-up of high-shear wet granulation is investigated.

1.1 *Research objectives*

1. Develop a predictive model for high-shear wet granulation employing the process-scale tool population balance modelling.
2. Validate the model developed at different process scales and varying process conditions for high-shear wet granulation using a model pharmaceutical formulation.
3. Develop a framework which gives guidance for the development, calibration and validation of a predictive model.
4. Develop a novel model-driven design workflow for scale-up of particulate processes based on predictive modelling.

1.2 *Thesis structure*

Relevant literature is critically reviewed in Chapter 2. All experimental methods used in this study are described in Chapter 3. Nuclei size distribution modelling approaches are proposed and experimentally validated in Chapter 4 to identify the most appropriate approach for further applications. In Chapter 5, population balance modelling (PBM) is employed to develop a high-shear wet granulation model which incorporates rate expressions based on mechanistic understanding. An Experimental investigation to determine the impact of equipment scale and critical process parameters (CPPs) on critical quality attributes (CQAs) is conducted in Chapter 6. The model developed is applied, and its predictive power is assessed in Chapter 7. In Chapter 8, a model-driven design framework is proposed and assessed for scale-up purposes. Conclusions and recommendations are in Chapter 9.

Chapter 2

LITERATURE REVIEW

2.1 *Wet granulation mechanisms*

Wet granulation is a particle enlargement process. By agglomeration of fine powder particles, larger particles (granules) are formed with the help of liquid binder. The desired size of granules depends heavily on the application and can range from 0.1 mm to 10 mm. Granular material is easier to handle and has less health and safety concerns due to better flowability, improved tablettability, and less dust formation.

The wet granulation process consists of several rate processes: wetting and nucleation, consolidation, layering and coalescence, and breakage and attrition. In the following, these rate processes will be described, and modelling approaches will be presented.

2.1.1 Wetting and nucleation

The wetting and nucleation rate process starts with the spraying of liquid binder onto a dry powder bed. In order to evenly wet the powder, the powder is moved through the spray zone where one or more nozzles spray liquid binder on the surface of the powder bed. The drops penetrate into the bed and form nuclei by combining with powder particles (primary particles). In high-shear wet granulation, the drops are typically larger than the powder particles which means each drop forms a nucleus out of many primary particles. This assumption has been confirmed by showing that the drop size is directly related to the size of the nuclei [Abberger et al., 2002; Ax et al., 2008]. Having said that, drops might overlap on top of the powder bed and coalesce before penetrating. Consequently, only one large nucleus will be formed. The probability of drop coalescence can be estimated using two dimensionless groups, the dimensionless drop penetration time and the dimensionless spray flux. The dimensionless drop penetration time τ_p is the ratio of the time the drop needs to fully penetrate the powder bed to the time interval between leaving and re-entering the spray zone [Hapgood et al., 2003]:

$$\tau_p = \frac{t_p}{t_c} \tag{2.1}$$

where t_p is the drop penetration time and t_c is the circulation time. The circulation time can be measured experimentally, determined using modelling tools like DEM or estimated based on the impeller rate. For high-shear mixers, 15 % of the impeller tip speed is a reasonable estimate for the surface velocity. The drop penetration time can be estimated using different approaches. Hapgood et al. [2002] proposed and validated a model for the drop penetration time assuming a constant drawing area:

$$t_p = 1.35 \frac{V_d^{2/3}}{\varepsilon_{eff}^2 R_{eff}} \frac{\mu}{\gamma^{lv} \cos\theta} \tag{2.2}$$

where V_d is the drop volume, ε_{eff} is the effective bed porosity, R_{eff} is the effective pore radius, μ is the binder viscosity, γ^{lv} is the liquid-vapour surface tension, and θ is the dynamic contact angle of the liquid within the solid capillary. The effective porosity takes macro-voids into account, which inhibit the liquid flow through the capillary. The effective bed porosity ε_{eff} can be estimated:

$$\varepsilon_{eff} = \varepsilon_{tap}(1 - \varepsilon_{bulk} + \varepsilon_{tap}) \tag{2.3}$$

where ε_{bulk} is the bulk porosity and ε_{tap} is the tap porosity. The effective pore radius can be estimated using the Kozeny approach:

$$R_{eff} = \frac{\varphi d_{32} \varepsilon_{eff}}{3(1 - \varepsilon_{eff})} \tag{2.4}$$

where φ is a shape factor and d_{32} is the Sauter mean diameter of the powder bed particles.

The effect of the process conditions on the nucleation process can be evaluated with a second dimensionless group the dimensionless spray flux [Litster et al., 2001]. The dimensionless spray flux is the ratio of the flux of the area wetted to the flux of the powder bed surface area as it passes through the spray zone:

$$\Psi_a = \frac{3\dot{V}}{2\dot{A}d_d} \tag{2.5}$$

where $\dot{V}$ is the volumetric spray rate, d_d is the drop diameter, and $\dot{A}$ is the flux of the powder bed surface area through the spray zone. By evaluating the two dimensionless groups the dimensionless drop penetration time and the dimensionless spray flux, the operating regimes of the nucleation

process can be determined. In experimental studies, Hapgood et al. [2003] identified three different regimes (Figure 2.1): drop-controlled regime, intermediate regime, and mechanical dispersion regime.

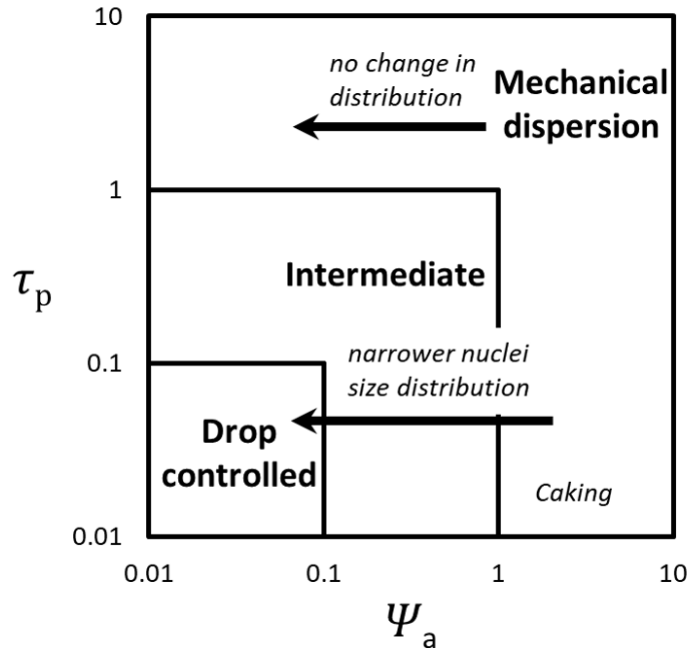

Figure 2.1: Nucleation regime map (Ψ_a dimensionless spray flux, τ_p dimensionless drop penetration time) [Hapgood et al., 2003]

In the drop-controlled regime, only few drops coalesce, hence the size distribution of nuclei formed is rather narrow. In the mechanical dispersion regime, formation of large lumps is very likely which is usually undesired. Nevertheless, these lumps can be broken up by the impeller or chopper in a high-shear mixer. It is favourable to operate in the drop-controlled regime because of a narrower nuclei size distribution. If a higher binder spray rate is required, an operation in the drop-controlled regime is often not feasible.

While a drop penetrates the powder bed, it forms a nuclei which is larger in size than the drop due to the addition of solid and gas. Consequently, this can lead to more coalescence due to overlapping of nuclei during their formation. The size increase can be quantified by the diameter ratio of nuclei to drop and can be measured experimentally [Abberger et al., 2002; Ax et al., 2008]. Wildeboer et al. [2005] incorporated this nuclei-to-drop diameter ratio K_d and introduced the dimensionless nucleation number Ψ_n as a new dimensionless group for nuclei coalescence:

$$\Psi_n = {K_d}^2 \frac{3\dot{V}}{2\dot{A}d_d} = {K_d}^2 \Psi_a \tag{2.6}$$

The assumption of a constant drawing area during the drop penetration might not be valid for all cases [Hapgood et al., 2002]. If the drop penetrates the bed very slowly, the drop might remain on the surface of the powder bed until it is covered up with powder. In this case, drop penetration with a decreasing drawing area can be assumed [Hapgood et al., 2002]. In any case, fine powder particles adhere to the drop surface and immerse into the drop until a nearly uniform solid content is reached. The volume of the resultant nucleus is larger than the volume of the drop due to the addition of solids. If the spray drops are smaller the primary particles, wetting and nucleation are governed by different mechanisms. A qualitative description of this scenario can be found in Litster [2016].

Wetting and nucleation rate expressions

Two types of models are required for the wetting and nucleation process. One model should determine the drop or nuclei size distribution based on the spray characteristics, and additionally, a second model which considers the kinetics of the nuclei formation process is needed to predict the increase in volume.

Ideally, every nucleus is formed by exactly one drop, and this assumption has been used in modelling leading to uniform nuclei size distribution [Poon et al., 2008; Barrasso and Ramachandran, 2016]. To achieve this experimentally, rapid penetration of drops and a low spray rate is required. However, this is usually not realisable in practice. That is why, this assumption does not lead to accurate results for the nuclei size distribution due to overlapping and coalescence of drops.

Hapgood et al. [2004] carried out Monte Carlo simulations (MCS) to determine the nuclei size distribution assuming a uniform distribution of drops, spatial randomness, and uniform drop size. Furthermore, they proposed an analytical solution based on the Poisson distribution (PD) function. This approach has been extended by Hapgood et al. [2009] to determine the probability of drop coalescence based on the dimensionless spray flux Ψ_a:

$$P_n = \exp\left(-4\Psi_a\right) \frac{(4\Psi_a)^n}{n!} \tag{2.7}$$

where P_n is the probability for a single drop to coalesce with n other drops. By comparing the results of the PD model to experimental data, it could be seen that this model is able to predict the nuclei size distribution in the drop-controlled regime [Hapgood et al., 2009]. However, the PD

model does not predict broad or multi-modal distributions outside the drop-controlled regime which were observed in the experiments.

Wildeboer et al. [2005] extended and assessed the MCS approach proposed by Hapgood et al. [2004]. A truncated normal distribution of drops has been assumed over the width of the spray zone; this approach is based on spray characteristics experiments [Wauters et al., 2002]. Furthermore, the model takes drop coalescence during the nuclei formation into account. A larger nuclei size distribution is predicted if it is assumed that coalescence can occur after nucleation. The reason for that is the addition of solid and gas during nucleation and the resultant increase in total volume. A log-normal distribution is considered for the drop diameter.

Liu et al. [2013a] developed a model which includes a nuclei size distribution model [Hapgood et al., 2009] and a breakage model [Liu et al., 2009] to capture the effects of nuclei breakage on the nuclei size distribution.

The kinetics of nuclei formation are often neglected in modelling studies because drop penetration can be assumed to be rapid, especially for non-viscous binders [Chaudhury et al., 2014b]. However, models which capture the nuclei formation are available in the literature. Poon et al. [2008] developed a model and applied it in 3-D population balance modelling (PBM). The model predicts the nuclei formation rate K_{nuc} based on a spreading coefficient λ:

$$K_{nuc} = k_{nuc}\dot{V}\exp\left(\frac{\lambda}{RT}\right) \tag{2.8}$$

where k_{nuc} is the nucleation rate constant, R is the ideal gas constant, and T is the temperature. The spreading coefficient is a measure of the ability of a liquid to spread over a solid. The drop penetration has been modelled by applying the Washburn equation [Denesuk et al., 1993]. The volume of unpenetrated liquid is:

$$V_{un} = V_d - \pi r_d^2 \varepsilon \left(\frac{R_p \gamma^{lv} \cos\theta}{2\mu} t\right)^{1/2} \tag{2.9}$$

where V_{un} is the liquid volume on the surface of the powder bed, V_d is the drop volume, r_d is the radius of the drawing area, and R_p is the pore radius. However, the model developed by Poon et al. [2008] assumes for long drop penetration times that liquid that did not penetrate at the time of bed turnover is added to the existing granules to avoid overlapping of drops in the spray zone.

Hounslow et al. [2009] has developed two mechanistic models which both capture the immersion mechanism but consider different driving forces to be dominant. The first model assumes that the

primary particles are drawn into the drop by the surface tension at the liquid-solid-air interface. This model predicts the change in solid volume inside the nucleus:

$$\frac{\mathrm{d}v_s}{\mathrm{d}t} = \frac{1}{2t_{max}} \frac{v_l^2}{v_s} \left(\frac{1-\phi_{cp}}{\phi_{cp}} \right)^2 \tag{2.10}$$

and the final volume of the nucleus:

$$v = v_l \left(1 + \frac{1-\phi_{cp}}{\phi_{cp}} \sqrt{\frac{\vartheta}{t_{max}}} \right) \tag{2.11}$$

with

$$t_{max} = \frac{18.75 \mu r_d^2}{\gamma d} \frac{1-\phi_{cp}^{1/3}}{\phi_{cp}^3} \tag{2.12}$$

where v_s is the solid volume, t_{max} is the time to complete the nucleation process for spherical drops, v_l is the liquid volume, ϕ_{cp} is liquid volume fraction at critical packing state, v is the nucleus volume, ϑ is the age of the granule, r_d is the initial radius of the drop, γ is the capillary force per unit length, and d is the primary particle diameter. The similar approach of both kinetic approaches becomes evident when Eqs. 2.2 and 2.12 are compared. This shows that the surface tension-driven immersion mechanism is closely related to the drop penetration mechanism investigated by Hapgood et al. [2002].

The second model assumes that liquid is squeezed out of a nucleus onto the solid surface by small deformations. In consequence, the primary particles diffuse further into the drop. This model assumes that the process is deformation-driven and the particle flow due to surface tension is negligible. The change in solid volume can be determined:

$$\frac{\mathrm{d}v_s}{\mathrm{d}t} = 12 D_{eff} \left(\frac{4\pi\phi_{cp}}{3v_l} \right)^{2/3} \left(\frac{1-\phi_{cp}}{\phi_{cp}} v_l - v_s \right) \tag{2.13}$$

as well as the final volume of the nucleus:

$$v \cong \frac{v_l}{\phi_{cp}} \left(1 - \left(1-\phi_{cp}\right) \exp\left(-\frac{12 D_{eff} \phi_{cp}^{2/3}}{r_d^2} \vartheta \right) \right) \tag{2.14}$$

where D_{eff} is the binary effective diffusivity for particles and liquid as a consequence of repeated deformations. The models developed by Hounslow et al. [2009] have not been validated experimentally so far.

Critical review of wetting and nucleation rate expressions

- The effect of spray characteristics on the nuclei size distribution is not well investigated quantitatively.
- Monte Carlo simulations are a promising tool to predict the nuclei size distribution, however, it is not feasible to include them in PBM.
- The analytical model developed can only give accurate predictions at low spray rates.
- Drop penetration time is often assumed to be negligible in modelling studies because penetration is often a relatively quick process.

2.1.2 Consolidation

During the consolidation rate process, the porosity of the granules reduces, which leads to an increase in (envelope) density. Consolidation results from plastic deformation which occurs due to collisions with other granules and equipment surfaces. It is important to investigate consolidation based on envelope density (or envelope porosity) because bulk and tap density are largely dependent on the particle packing fraction and therefore particle size distribution (PSD) [Hoffmann and Finkers, 1995].

The dynamic yield strength of the granules and the impact energy of the collision control the consolidation rate. A granule can be considered to behave like an elastic-perfectly plastic material. Under this assumption, plastic deformation will occur if the dynamic yield strength is exceeded during a collision. Hence, an important dimensionless group to evaluate consolidation is the Stokes deformation number, which is the ratio of the internal stress resulting from the collision to dynamic yield strength [Iveson and Litster, 1998b]:

$$St_{def} = \frac{\rho_g v_{coll}^2}{2Y_d} \tag{2.15}$$

where ρ_g is the envelope density of the granules, v_{coll} is the collision velocity, and Y_d is the dynamic yield strength, which depends on the strain rate. In order to calculate the Stokes deformation number, a value for the collision velocity is required which is difficult to determine. However, a good estimation for the collision velocity in high-shear mixers is 15 % of the impeller tip speed [Forrest et al., 2003; Tran, 2015]. The dynamic yield strength should be measured at low strain rates [Iveson et al., 2003; Iveson and Page, 2005]. Alternatively, the dynamic yield strength for non-spherical particles can be estimated using a relationship developed by Smith [2007]:

$$Str^* = \left(7 + 221Ca^{0.58}\right) AR^{-4.3} \tag{2.16}$$

with

$$Str^* = \frac{Y_d d_p}{\gamma^{lv} \cos\theta} \tag{2.17}$$

where Str^* is the dimensionless strength, Ca is the Capillary number, AR is the aspect ratio of primary particles, and d_p is the diameter of the primary particles. Experimental observations have also shown that the strength can be strongly dependent on pore saturation [Iveson et al., 2002; Kayrak-Talay and Litster, 2011; Pohlman and Litster, 2015]. The Capillary number is the ratio of viscous dissipation to capillary force in the granule:

$$Ca = \frac{\mu v_{coll}}{\gamma^{lv} \cos\theta} \frac{d_p}{d_g} \tag{2.18}$$

where μ is the liquid binder viscosity and d_g is the granule diameter.

Another relevant dimensionless group is the viscous Stokes number St_v, which is the ratio of the kinetic energy to the energy dissipated by viscous forces [Ennis et al., 1991]:

$$St_v = \frac{4\rho_g v_{coll} d_g}{9\mu} \tag{2.19}$$

Understanding consolidation is important due to its effects on the granule properties, which influence other rate processes. Especially, the increase in surface liquid enhances the granule growth process significantly. Liquid which is entrapped in the pores of the granule gets squeezed out during the consolidation process.

Consolidation rate expressions

Several consolidation models are available in the literature. Ouchiyama and Tanaka [1980] developed a consolidation model based on capillary pressure of the binder:

$$\frac{\mathrm{d}\varepsilon}{\mathrm{d}\tau_{cons}} = -\left[1 - \frac{(1-\varepsilon)^3}{\varepsilon K_\varepsilon}\right]^n \tag{2.20}$$

where τ_{cons} is the dimensionless consolidation time, K_ε is the dimensionless granule consolidation rate, and n is a parameter describing a distribution of granule impact energies.

Ennis et al. [1991] focused on the effect of binder viscosity on consolidation and developed a relationship between the inter-particle gap Δx and the viscous Stokes number St_v:

$$\Delta x = \delta_l \left[1 - \exp(-St_v)\right] \tag{2.21}$$

where δ_l is the thickness of the liquid layer. Alternatively, consolidation can be modelled using an exponential decay model. Iveson et al. [1996] and Iveson and Litster [1998a] have shown that the decrease in porosity ε is similar to exponential decay by applying the following model to a drum granulation process:

$$\frac{\varepsilon - \varepsilon_{min}}{\varepsilon_0 - \varepsilon_{min}} = e^{-k_{cons} n} \tag{2.22}$$

where k_{cons} is the consolidation rate constant, and n is the number of drum revolutions. This model is very easy to use, and it is most commonly used to describe consolidation. However, this model is empirical, that is why all parameters have to be estimated using experimental data. An approach to make this model more mechanistic has been proposed by [Litster and Ennis, 2004]. They suggested to employ the Stokes deformation number to determine the consolidation rate:

$$k_{cons} = k_{cons,0} \exp(a St_{def}) \tag{2.23}$$

where k_{c0} is a pre-exponential factor and a is an adjustable parameter. Even though including the Stokes deformation number makes the model more mechanistic and potentially more predictive, more fitting parameters (k_{c0} and a) are also introduced. Gantt et al. [2006] proposed to replace k_{c0} with a size-dependent impact rate which they determined using DEM.

An expression for the consolidation rate process, which is also based on the Stokes deformation number, has been proposed by Barrasso et al. [2015b]:

$$\frac{\mathrm{d}V_g}{\mathrm{d}t} = -k_{cons} V_p f_{coll} \left[1 - \exp(-St_{def})\right] \tag{2.24}$$

where V_g is the granule volume, V_p is the pore volume, and f_{coll} is the collision rate. This kernel only contains one fitting parameter k_{cons}. However, the impact rate can only be determined using DEM since there is no experimental technique available to measure it.

The two models developed by Hounslow et al. [2009] (see Section 2.1.1) can also be used to model consolidation. Employing these models would be a more mechanistic approach to represent

consolidation. However, further research is needed to validate the model experimentally before it can be used for this purpose.

The influence of liquid binder content and viscosity on consolidation has been observed experimentally [Kristensen et al., 1985a,b; Iveson et al., 1996]. On this basis, Maxim et al. [2004] proposed a correlation for the minimum porosity which depends on the presence of surface liquid. Nevertheless, these influences are often neglected in modelling studies for the sake of simplicity.

Critical review of consolidation rate expressions

- Consolidation is well understood but is usually modelled using empirical kernels.
- More mechanistic approaches have been proposed but not validated experimentally.

2.1.3 Layering and coalescence

A granule can grow by layering and coalescence. The layering rate process occurs when the surface of a granule is wet. In this case, layers of fine powder particles adhere to the wet surface of the granule. Additionally to granule growth by layering, granules can also grow by coalescence. During a particle-particle collision, the granules might stick together due to the formation of a liquid bridge [Iveson et al., 2001a]; this mechanism is called coalescence. The conditions under which two granules coalesce are determined by the impact energy and the granule properties, such as size, yield strength, surface liquid, and liquid viscosity.

Granules will initially be surface-dry due to capillary action. Since granules usually need surface liquid to grow the granules need to consolidate first. At this stage, granules can already grow by layering because it requires only a small amount of surface liquid. This initial phase is also called induction phase. When sufficient surface liquid is present, the growth phase starts. In this phase, the granules also grow by coalescence. However, weak granules can consolidate very quickly, that is why granule growth can occur without a significant induction time. This phenomenon is also called steady growth. A significant induction time can usually be observed for strong granules; this phenomenon is called induction growth.

The growth regime depends on the consolidation rate and hence also on the impact energy and strength of the granules. For this reason, the Stokes deformation number St_{def} has been used to propose a growth criterion:

$$St_{def} < 2 \times 10^{-3} \quad \text{for induction growth} \tag{2.25}$$

$$St_{def} > 2 \times 10^{-3} \quad \text{for steady growth.} \tag{2.26}$$

Furthermore, it is important that the liquid content of the granules is sufficient to generate surface liquid while consolidating [Iveson et al., 2001b]. Therefore, the granule liquid pore saturation S (Eq. 2.27) should be in between two critical values: 0.7 and 1. Only nucleation and layering will occur if the liquid pore saturation is below 0.7, and rapid growth might occur if the liquid pore saturation exceeds 1. All regimes including the critical values are shown in Figure 2.2.

$$S = \frac{L/S\rho_s\,(1-\varepsilon)}{\rho_l \varepsilon} \tag{2.27}$$

where L/S is the mass-based liquid-to-solid ratio, ρ_s and ρ_l are the solid and liquid density respectively, and ε is the granule porosity.

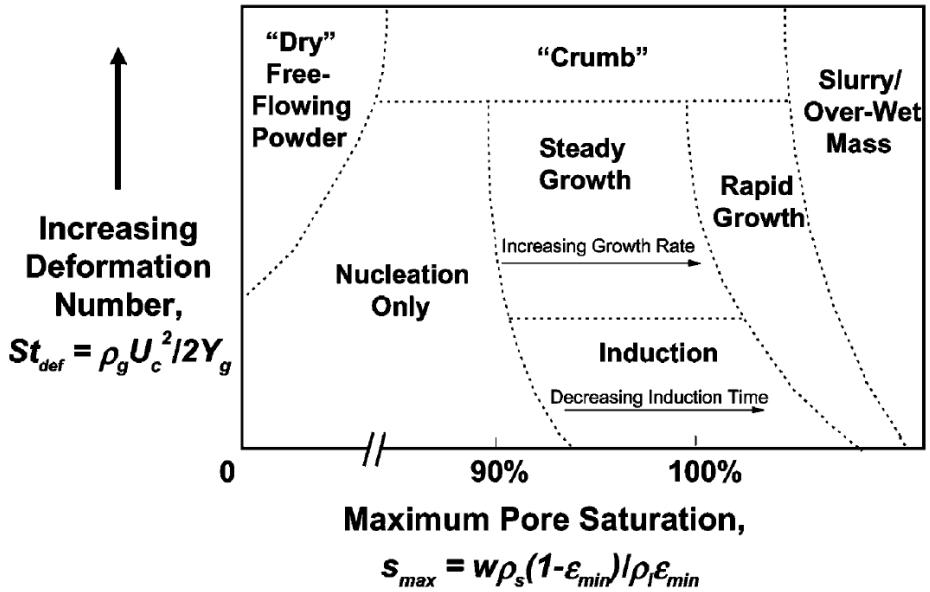

Figure 2.2: Growth regime map (Reprinted from [Iveson et al., 2001b])

Layering rate expressions

Coalescence is often the most dominant growth process if both rate processes occur simultaneously. For this reason, layering has not been investigated as much as coalescence and is, therefore, often not

considered in wet granulation modelling. However, layering models can be found in the literature. Barrasso and Ramachandran [2016] and Sayin [2016] proposed a rate expression which assumes that the increase in solid volume is proportional to the surface area of the wet granule and the volume of fine particles:

$$\frac{\mathrm{d}v_S}{\mathrm{d}t} = k_l \frac{\pi d^2 m_p}{\rho_s} \tag{2.28}$$

where v_S is the solid volume of the granule, k_l is the layering rate constant, d is the granule diameter, and m_p is the mass of primary particles. A mechanistic rate expression should take the availability of fine particles as well as the amount of surface liquid into account. This rate expression captures the effects of the availability of fine particles but ignores the effect of surface liquid. As a result, the surface liquid will consequently influence the parameter estimation, especially the layering rate constant.

Cameron et al. [2005] and Wang et al. [2006] proposed and applied a layering model based on the Monod model (kinetic model for microbial growth [Levenspiel, 1980]). This model predicts layering to occur as soon as a critical moisture content c^* is exceeded:

$$\frac{\mathrm{d}v_S}{\mathrm{d}t} = G_{max} \frac{m_p}{k \sum_i m_i + m_p} \exp\left[-a\,(c - c^*)^2\right] \tag{2.29}$$

where G_{max} is the maximum growth rate, m_i is the mass of particles in the i^{th} size class, c is the moisture content, and a and k are adjustable parameters.

The models developed by Hounslow et al. [2009] (see Section 2.1.1) are theoretically capable of modelling granule growth by layering, and few researchers have applied this approach [Oullion et al., 2009; Yu et al., 2017]. The usage of these models would be a more mechanistic way of modelling the layering rate process. However, these models have not been validated so far, that is why further research is required before this approach can be applied reliably.

Coalescence rate expressions

Modelling of coalescence has been well investigated in previous studies. An overview of relevant coalescence kernels are shown in Table 2.1. Empirical and mechanistic kernels have been proposed in the literature.

Table 2.1: Coalescence kernels (modified from Kumar et al. [2013]) (d granule diameter, v granule volume, β_0 rate constant, c moisture content, $*$ critical value, $1/2$ colliding granules, $\tilde{}$ reduced quantity)

Approach	Kernel
Size-independent [Kapur and Fuerstenau, 1969]	$\beta = \beta_0$
Based on granule size	
Size-dependent [Kapur, 1972a]	$\beta = \beta_0 \frac{(d_1+d_2)^a}{(d_1 d_2)^b}$
Time- and size-dependent [Sastry, 1975]	$\beta = \beta_0(t)(d_1^2 + d_2^2)\left(\frac{1}{d_1^3} + \frac{1}{d_2^3}\right)$
Cut-off [Adetayo and Ennis, 1997]	$\beta = \begin{cases} \beta_0, & W \le W^* \\ 0, & W > W^* \end{cases}$ where $W = \frac{(v_1 v_2)^b}{(v_1+v_2)^a}$
Based on collision theory	
Equipartition of translational momentum [Hounslow, 1998]	$\beta = \beta_0 (d_1 + d_2)^2 \sqrt{\frac{1}{d_1^6} + \frac{1}{d_2^6}}$
Equipartition of kinetic energy [Hounslow et al., 2001]	$\beta = \beta_0 (d_1 + d_2)^2 \sqrt{\frac{1}{d_1^3} + \frac{1}{d_2^3}}$
Based on Stokes criterion [Ennis et al., 1991]	
Stokes criterion [Cryer, 1999]	$\beta = \beta_0 \int_{-\infty}^{St_v^*} f(\phi, t)\, \mathrm{d}\phi$ where $f(\phi, t)$ is a discrete probability function for St_v
Stokes criterion, plastic deformation [Liu et al., 2000]	$\beta = \begin{cases} \beta_1, & \text{for coalescence without deformation} \\ \beta_2, & \text{for coalescence with deformation} \\ 0, & \text{for rebound} \end{cases}$

Continued on next page

Table 2.1 – continued from previous page

Approach	Kernel
Stokes criterion, plastic deformation [Immanuel and Doyle III, 2005]	$\beta = \beta_0 \frac{4\pi v_{coll}(d_1+d_2)^2}{W}$ where W is the Fuch stability ratio
Stokes criterion [Rajniak et al., 2009]	$\beta = \beta_0 \psi_{12} d_{43}^{\gamma} (d_1 + d_2)^2 \sqrt{\frac{1}{d_1^3} + \frac{1}{d_2^3}}$ where ψ_{12} is the success factor
Based on granule liquid content	
Sequential [Adetayo et al., 1995]	$\beta = \begin{cases} \beta_1(S), & t \le t^* \\ 0, & t > t^*; S \le S^* \\ \beta_2(d_1, d_2), & t > t^*; S > S^* \end{cases}$ where S is the pore saturation
Liquid fraction-dependent [Biggs et al., 2003]	$\beta = \beta_0 \frac{(\max(c_1,c_2)/c^*)^{48}}{1+(\max(c_1,c_2)/c^*)^{48}} f(v_1, v_2)$
Liquid fraction-dependent [Madec et al., 2003]	$\beta = \beta_0 \left(d_1^3 + d_2^3\right) \left((c_1 + c_2)^{\alpha} \left(1 - \frac{c_1+c_2}{2}\right)^{\delta}\right)^{\alpha}$
Surface liquid-dependent [Darelius et al., 2006]	$\beta = \beta_0 \frac{v_{1,l} - v_{1,lp}}{4\pi\left(\frac{d_1}{2}\right)^2 \frac{v_{1,s}+v_{1,l}}{v_1}} \frac{v_{2,l} - v_{2,lp}}{4\pi\left(\frac{d_2}{2}\right)^2 \frac{v_{2,s}+v_{2,l}}{v_2}}$ where v_{lp} is the liquid volume in pores
Wet surface area-dependent [Chaudhury et al., 2014b]	$\beta = \begin{cases} \beta_0 \frac{A_{1,wet} A_{2,wet}}{A_1 A_2}, & \tilde{St} \le \tilde{St}^* \\ 0, & \tilde{St} > \tilde{St}^* \end{cases}$ where $\tilde{St}_v = \frac{8\tilde{m} v_{coll}}{3\pi\mu\tilde{d}^2}$ and A is the surface area

Empirical coalescence kernels typically include a (time-dependent) coalescence rate parameter β_0 and a size-dependent term β^* [Sastry, 1975]:

$$\beta = \beta_0 \beta^* (d_1, d_2), \tag{2.30}$$

where d_1 and d_2 are the diameters of two granules. Kernels with a time-dependent function

[Sastry, 1975] or switching time [Adetayo et al., 1995] have been proposed. However, as Hounslow et al. [2001] pointed out, the need for a time-dependent function only indicates an unidentified physical property which changes over time and influences the rate process.

A more mechanistic approach to determine the coalescence rate is to assume that the coalescence rate is the product of collision frequency and coalescence probability [Gantt et al., 2006]. The collision frequency is usually estimated using experimental data. However, it can also been determined using DEM simulations [Tan et al., 2004a; Gantt et al., 2006; Barrasso and Ramachandran, 2016]. In order to predict the coalescence probability, researchers tried to identify physical properties which have significant effects on coalescence. In experimental studies, the effects of the liquid binder content have been observed [Scott et al., 2000]. For this reason, kernels have been proposed that capture the effect of liquid fraction [Biggs et al., 2003; Madec et al., 2003] and especially surface liquid [Liu et al., 2000; Darelius et al., 2006; Rajniak et al., 2009; Chaudhury et al., 2014b]. (Semi-)mechanistic kernels will be discussed in more detail in the following due to their higher predictive power (see Section 2.3.1).

Le et al. [2009] selected two kernels a size-independent kernel and the equipartition of kinetic energy (EKE) kernel. The size-independent kernel assumes that coalescence occurs when the liquid fraction of at least one colliding granule exceeds some critical value. As opposed to that, the EKE kernel neglects any effects of the liquid on coalescence. They compared both kernels to experimental data and concluded that the size-independent kernel is able to model the coalescence rate more accurately. This supports the hypothesis that the liquid layer has a significant effect on coalescence.

Apart from kernels that determine coalescence probability, coalescence kernels have been proposed that are based on collision theory. These kernels are also called collision frequency functions. Since coalescence rate is considered to be the product of collision frequency and coalescence probability, the combination of two coalescence kernels has been investigated. Lee et al. [2017] assessed several collision frequency functions by comparing them to DEM simulation results and concluded that the EKE kernel provides results which are in good agreement with the DEM data. The EKE kernel has been applied by several researchers to estimate the collision frequency [Tan et al., 2004a; Le et al., 2009; Oullion et al., 2009; Rajniak et al., 2009; Bouffard et al., 2012].

Ennis et al. [1991] proposed a criterion based on the viscous Stokes number to determine the outcome of a collision (coalescence or rebound). The criterion was developed using an energy

balance which determines whether or not the liquid layer is sufficient to dissipate the impact energy. In this case, granules are assumed to be perfectly elastic and non-deformable. This approach has been used to develop a number of coalescence kernels [Cryer, 1999; Liu et al., 2000; Rajniak et al., 2009]. Cryer [1999] and Rajniak et al. [2009] developed coalescence kernels for the fluid bed granulation process. Due to low collision velocities in this process, plastic deformation upon impact is negligible [Ennis and Litster, 2008]. Hence, the assumption of perfectly elastic and non-deformable granules applies. Rajniak et al. [2009] combined the approach of Ennis et al. [1991] with the EKE kernel developed by Hounslow et al. [2001].

Liu et al. [2000] extended the Stokes criterion developed by Ennis et al. [1991] to account for absorption of impact energy by deformation using contact mechanics principles for elastic-plastic solids [Johnson, 1985]. The coalescence kernel proposed also predicts the plastic deformation of the granules after the collision. Most recently, the coalescence kernel was extended by Pohlman and Litster [2015] for usage in a 3-D PBM framework. The coalescence kernel has been applied by Liu and Litster [2002], Liu et al. [2012] and Pohlman and Litster [2015], and it could be shown that the predictions are in good agreement with experimental data for different materials and process conditions. Figure 2.3 shows the predictions of this coalescence kernel. Coalescence without deformation (Type I) is only predicted for small granules with a low porosity - low impact energy and surface liquid available. Coalescence with deformation is predicted for larger granules - surface liquid layer not sufficient to absorb impact energy. Granules with a high porosity do not have a surface liquid which is sufficiently thick to absorb the impact energy, that is why rebound is predicted. The coalescence kernel by Liu et al. [2000] has been further developed by Immanuel and Doyle III [2005] to account for dynamic changes in the process.

Critical review of layering and coalescence rate expressions

- Layering is a relevant wet granulation rate process but often neglected in modelling studies.
- Only simplistic models have been proposed but not validated.
- Coalescence has been well investigated in the past, and a series of models has been proposed and validated experimentally.
- While coalescence is often modelled using empirical approaches, more mechanistic approaches have only been investigated more extensively in recent years.
- A mechanistic coalescence model should include the effect of the liquid layer which dissipates

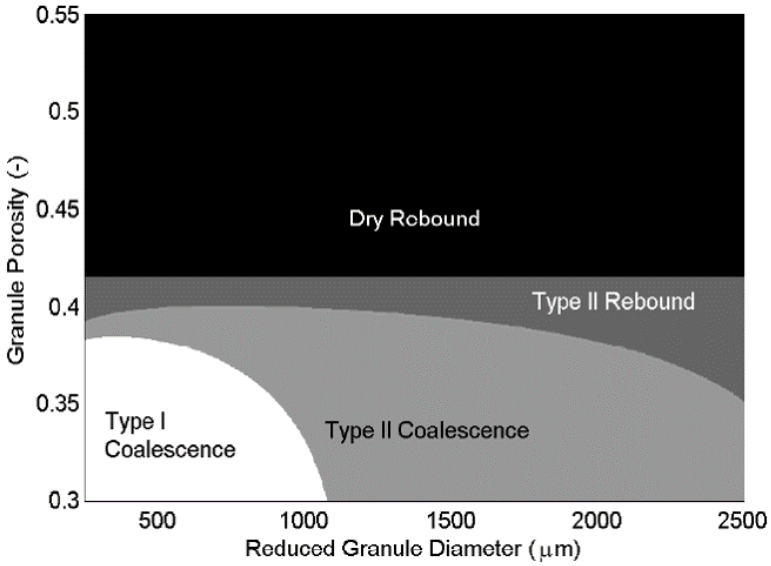

Figure 2.3: Simulation results of the coalescence kernel as a function of granule diameter and porosity (Reprinted from [Pohlman and Litster, 2015])

impact energy. In high-shear wet granulation, plastic deformation should also be considered.

2.1.4 Breakage and attrition

The breakage and attrition rate processes lead to a reduction in granule size. Granules can break into several smaller granules due to collisions with other granules or equipment surfaces. Additionally, attrition of dry granules can occur which results in the generation of very fine particles. Since fine particles are unwanted in the granulation product, attrition of granules should be avoided. However, breakage of particles is often desired to be able to control the (maximum) granule size and to achieve the desired size distribution. In high-shear wet granulation, the granules are most likely to break close to the impeller or chopper due to the high energy input. Having said this, the effect of chopper rate and design has been determined to be negligible in vertical axis high-shear mixers [Michaels, 2003; Holm, 1987].

A breakage criterion has been developed by Tardos et al. [1997]:

$$St_{def,max} > St^*_{def} \tag{2.31}$$

where $St_{def,max}$ is the maximum Stokes deformation number. To capture collisions with the impeller or chopper, the collision velocity can be assumed to be equal to the tip speed. Very high breakage rates were observed when the Stokes deformation number exceeded a critical value of 0.2, which agrees with the crumb regime in Fig. 2.2 [Tardos et al., 1997; Liu et al., 2009].

An alternative breakage criterion based on the maximum strain ϵ_{max} was developed by Keningley et al. [1997]:

$$\epsilon_{max} > \epsilon^* \tag{2.32}$$

with

$$\epsilon_{max}^2 = \frac{1}{540} \frac{\varepsilon^2}{1-\varepsilon^2} \frac{\rho_g v_{coll} d_{3,2}}{\mu} \tag{2.33}$$

where ϵ^* is the critical value for the maximum strain. In experiments, it has been found out that breakage can occur if the maximum strain exceeds a critical value of 0.1.

Attrition is a rate process that has been observed for dry granules in fluid bed granulators at high gas velocity [Litster, 2016]. Since the evaporation rate in high-shear mixers is negligible, attrition can generally be neglected.

Breakage and attrition rate expressions

Sanders et al. [2003] attempted to model breakage with a coalescence model by adjusting the rate constant. However, the model failed to predict experimental results, since coalescence is a second-order process while breakage is a first-order process [Tan et al., 2005a]. In the following years, breakage models have been developed and applied to wet granulation. Furthermore, it has been observed that particle breakage in impact mills behaves similarly to granule breakage in granulators. That is why, milling models are often applied to model breakage in high-shear wet granulation processes [Kumar et al., 2016].

In order to describe particle breakage quantitatively, mathematical expressions that determine the breakage probability and size distribution of daughter particles are required. Therefore, Table 2.2 gives an overview of breakage probability functions, and fragment size distribution functions are listed in Table 2.3.

Table 2.2: Breakage probability functions (d granule diameter, k_{br} rate constant, G shear rate)

Approach	Kernel
	Based on granule size
Power law [Kapur, 1972b]	$K_{br} = k_{br} d^{k_1}$
Power law [Klimpel and Austin, 1984]	$K_{br} = k_{br} \left(\frac{d}{d^*}\right)^{k_1} \frac{1}{1+\left(d/\bar{d}\right)^{k_2}}$
	Based on shear rate
Power law [Pandya and Spielman, 1983]	$K_{br} = k_{br} G d^{k_1}$
Semi-empirical [Soos et al., 2006]	$K_{br} = \sqrt{\frac{4}{15\pi}} G \exp\left(-\frac{k_{br}}{G^2 d}\right)$
	Based on fracture mechanics
Crack propagation [Vogel and Peukert, 2003]	$K_{br} = k_{br}\left[1 - \exp\left(-f_{Mat} n d \left(E_{m,kin} - E_{m,min}\right)\right)\right]$ where n is the number of impacts, f_{Mat} is the material strength parameter, and $E_{m,kin}$ and $E_{m,min}$ is the kinetic and minimum breakage energy respectively
Crack propagation [Capece et al., 2014b]	$K_{br} = k_{br}\left[1 - \exp\left(f_{Mat} d \sum_{i=1}^{n} f_{coll,i}\left(E_{m,kin} - E_{m,min,i}\right)\right)\right]$ where f_{coll} is the collision frequency
Stress-strength ratio [Ramachandran et al., 2009]	$K_{br} = \sum_{\vec{x}_2} \frac{\sigma^p_{ext}(\vec{x}_1,\vec{x}_2)}{\sigma_{int}(\vec{x}_1)} n(\vec{x}_2) N_A \frac{A_p}{A_p+A_w+A_i}$ $+\frac{\sigma^w_{ext}(\vec{x}_1)}{\sigma_{int}(\vec{x}_1)} \frac{A_w}{A_p+A_w+A_i} + \frac{\sigma^i_{ext}(\vec{x}_1)}{\sigma_{int}(\vec{x}_1)} \frac{A_p}{A_p+A_w+A_i} + \frac{\sigma^{fl}_{ext}(\vec{x}_1)}{\sigma_{int}(\vec{x}_1)}$ where p, w, i, and fl stand for particle, wall, impeller, and fluid, $\vec{x}$ are the properties of colliding particles, σ_{ext} is the external stress, σ_{int} is the intrinsic strength, σ_{ext} is the external stress, n is the particle density, N_A is the Avogadro constant, A is the surface area

The first approaches to determine were purely empirical and were often based on the power law

[Kapur, 1972b; Pandya and Spielman, 1983]. However, breakage models based on more mechanistic approaches have several advantages (see Section 2.3.1), that is why they will be discussed in more detail in the following.

Vogel and Peukert [2003] developed a semi-mechanistic breakage model, which is based on a fracture mechanics approach developed by [Rumpf, 1973]. This model has been extended for determining particle breakage in impact mills [Vogel and Peukert, 2004, 2005], and successfully applied to predict breakage of pharmaceutical powders [Meier et al., 2008]. Further modifications to adapt the breakage model to batch or continuous processes were proposed by Capece et al. [2014b,a].

Dhanarajan and Bandyopadhyay [2007] proposed an energy-based model, which determined the breakage rate with the ratio of impact energy to granule strength. This approach was applied by Ramachandran et al. [2009] to develop a mechanistic breakage model. For the experimental validation of the model, binary breakage has been assumed.

The size distribution of daughter particles can be determined using a discrete fragment size distribution function b, which can be expressed as a function of the cumulative function B [Austin et al., 1981]:

$$b(i,j) = B(i,j) - B(i,j+1) \tag{2.34}$$

Additionally, the conservation of mass leads to the following equation:

$$B(i,j) = \sum_{j=1}^{i-1} b(i,j) \tag{2.35}$$

Accurate predictions and reliable experimental validation of the number and size of daughter particles are challenging, that is why binary breakage is often assumed in modelling of breakage. A further simplification can be made by assuming that a granule can only break into two equi-sized particles. However, fragment size distribution functions have been proposed in the literature (Table 2.3). Many fragment size distribution functions are based on the power law.

Attrition has not been well investigated since its effect is often dominated by breakage. An approach to model attrition has been proposed by [Kostoglou et al., 1997] by assuming that one very small particle breaks off a granule.

Tan et al. [2004b] proposed a model for attrition. This approach has been extended by Tan et al. [2005b] to model both breakage and attrition assuming one collision can lead to breakage of granules as well as abrasion of fine particles.

Table 2.3: Fragment size distribution function (B cumulative function, d granule diameter, i parent particle, j daughter particle, d_{max} maximum fragment diameter, and $d_{j,min}$ minimum fragment diameter)

Name	Kernel
Exponential [Broadbent and Callcott, 1956]	$B(i,j) = \frac{1-\exp\left(-d_j/d_i\right)}{1-\exp(-1)}$
Power law [Kapur, 1972b]	$B(i,j) = \left(\frac{d_i}{d_j}\right)^q$
Sum-type [Austin et al., 1976]	$B(i,j) = \phi\left(\frac{d_i}{d_j}\right)^{q_1} + (1-\phi)\left(\frac{d_i}{d_j}\right)^{q_2}$ with $\phi_j = \phi_1\left(\frac{d_j}{d_{max}}\right)^{-q_3}$
Power law [Berthiaux et al., 1996]	$B(i,j) = K(d_j)/K(d_i)$
Sum of powers [Kostoglou and Karabelas, 1998]	$B(i,j) = \sum_{k=1}^{n} c_k\left(\frac{d_i}{d_j}\right)^{q_k}$ with $\sum_{k=1}^{n} \frac{c_k}{q_k+2} = 1$
Power law [Hounslow et al., 2001]	$B(i,j) = \left(\frac{d_i}{d_j}\right)^3$
Velocity-dependent [Vogel and Peukert, 2005]	$B(i,j) = \left(\frac{d_i}{d_j}\right)^q \frac{1}{2}\left[1 + \tanh\left(\frac{d_j - d_{j,min}}{d_{j,min}}\right)\right]$ with $q = c_1 v + c_2$, where v is the impact velocity

Critical review of breakage and attrition rate expressions

- Granule breakage is similar to particle breakage in milling processes.
- More mechanistic approaches to determine the breakage probability have been proposed in recent years.
- Fragment size distribution of granule breakage is poorly understood and models have not been fully validated.
- Attrition can be neglected in high-shear wet granulation.

2.1.5 Understanding wet granulation mechanisms

Understanding the wet granulation process means understanding the mechanisms in wet granulation. Based on this understanding, the process can be controlled effectively to produce the product desired. Furthermore, a qualitative and quantitative understanding of all occurring mechanisms is key to a mechanistic modelling approach.

In order to understand all rate processes, every rate process should be investigated separately in experiments and simulations. Therefore, process conditions should be identified that favour one specific rate process. At these conditions, the other rate processes should be suppressed. Some processes do not occur in the absence of specific compounds: nucleation (penetrating drops), layering (fine particles), or coalescence (surface liquid). Others are negligible at specific conditions: coalescence (very high impact energy) breakage (low impact energy). Consolidation cannot be suppressed completely since surface tension is sufficient to initiate this rate process.

Critical review of wet granulation mechanisms

- Wet granulation can be divided into rate processes which can be investigated separately.
- While some rate processes can be isolated more easily (e.g. nucleation), others are difficult to separate (e.g. consolidation/coalescence or consolidation/breakage).
- Mechanistic modelling of some rate processes (coalescence and breakage) has been well investigated, while other rate processes are often neglected in modelling studies or modelled simplistically (nucleation, consolidation, and layering).

2.2 *Operation and scale-up*

Experimental studies on high-shear wet granulation have been conducted to identify operating regimes and their impact on the granulation process. Operating regimes that are closely linked to rate processes are discussed in the respective section.

Tran [2015] identified different powder flow patterns in a high-shear mixer. The two major patterns are bumping flow, which occurs at lower impeller rates and roping flow, which can be observed at higher impeller rates. In the bumping flow regime, limited axial mixing has been identified, which can lead to inhomogeneous product properties. In order to achieve good axial mixing, roping flow is required. The powder flow regime can be determined using the Froude number Fr:

$$Fr = \frac{D_{imp}\omega^2}{2g} \tag{2.36}$$

where D_{imp} is the impeller diameter, ω is the angular velocity, and g is the gravitational acceleration. To ensure roping flow, the Froude number at the operating point should be at least 20 [Litster, 2016].

Conventionally, high-shear wet granulation is scaled up by using simplistic scaling rules, which advise to keep certain input parameters or dimensionless groups constant. Most importantly, the equipment should be geometrically similar, which means that essential size ratios should be kept constant across scales [Litster et al., 2002; Michaels, 2003]. The following parameters are typically considered to be very relevant: mixer height H, mixer diameter D, impeller diameter D_{imp}, and bed height H_b. The following size ratios, which should be kept constant, can be derived: $\frac{H}{D}$, $\frac{D_{imp}}{D}$, and $\frac{H_b}{H}$ [Ameye et al., 2002]. For equipment that is not geometrically similar across scales, the bed height can also be determined by keeping the ratio to the impeller diameter constant: $\frac{H_b}{D}$ [Mort, 2005].

Table 2.4: Scaling rules for equipment and operational parameters proposed in the literature (D_{imp} impeller diameter, n_{imp} impeller rate, m_l liquid binder mass, m_s solid powder mass, $\dot{V}$ volumetric spray rate, $\dot{A}$ area powder flux through the spray zone, d_d drop diameter, L/S liquid-to-solid ratio, ρ_l liquid density, t_{kn} kneading time, t total granulation time, A_w wall surface area, V granulator volume, V_{imp} impeller volume, P impeller power consumption)

Name	Scaling rule
Determine impeller rate	
Constant tip speed [Ameye et al., 2002; He et al., 2008; Aikawa et al., 2008]	$n_{imp} D_{imp} = const$
Constant Froude number [Horsthuis et al., 1993; Tao et al., 2015; Smrčka et al., 2015]	$n_{imp} D_{imp}^{0.5} = const$
Constant shear stress [Tardos et al., 2004; Rahmanian et al., 2008a; Michaels et al., 2009]	$n_{imp} D_{imp}^{0.8} = const$
Constant relative swept volume [Kristensen and Schaefer, 1987; Schæfer et al., 1993]	$\frac{n_{imp} V_{imp}}{V} = const$
Determine binder liquid amount	
Constant liquid-to-solid ratio [Sato et al., 2005; Michaels et al., 2009; Kayrak-Talay et al., 2013]	$L/S = \frac{m_l}{m_s} = const$
Constant pore saturation [Iveson and Litster, 1998b]	$\frac{L/S \rho_s (1-\varepsilon_{min})}{\rho_l \varepsilon_{min}} = const$
Determine spray rate	
Constant dimensionless spray flux [Litster et al., 2001; Hapgood et al., 2010; Luo et al., 2017]	$\frac{3\dot{V}}{2\dot{A} d_d} = const$
Constant spray time [Campbell et al., 2011; Kayrak-Talay et al., 2013]	$\frac{m_s L/S}{\dot{V} \rho_l} = const$
Determine granulation time	
Constant kneading time [Kayrak-Talay et al., 2013; Rohrer, 2017]	$t_{kn} = const$

Continued on next page

Table 2.4 – continued from previous page

Name	Scaling rule
Constant granulation time [Sato et al., 2005]	$t = const$
Extended kneading time [Tao et al., 2015]	$\frac{t_{kn}}{D_{imp}} = const$
Constant granulation rate [Rahmanian et al., 2008a,b]	$\frac{tA_w}{V} = const$
Constant specific energy input [Landin et al., 1999; Sirois and Craig, 2000; Clancy, 2017]	$\int \frac{P}{m_s} \mathrm{d}t = const$

Apart from geometrical parameters, operational parameters have a significant impact, and it is typically recommended to keep the most crucial operational parameters constant to achieve similar conditions and product properties. Common scaling rules suggested previously can be found in Table 2.4.

Many researchers have studied and compared different scale-up approaches by keeping either the Froude number, impeller tip speed, shear stress, or relative swept volume constant [Horsthuis et al., 1993; Rahmanian et al., 2008a; Tao et al., 2015; Rohrer, 2017]. While a constant Froude number preserve the powder flow regime [Tran, 2015], a constant tip speed implies a constant Stokes deformation number, which leads to the same growth regime [Iveson and Litster, 1998b]. Unfortunately, the performance of each scaling rule seems to depend on other factors, since different scale-up studies concluded that different rules are most suitable for high-shear wet granulation. Other influencing factors could be the granulator design or formulation properties. Even though it is not possible to keep all crucial operational parameters constant, all crucial parameters should still be monitored to ensure the operation in the desired operating regime [Litster, 2003].

The amount of liquid required at large scale is usually determined by initially keeping the liquid-to-solid ratio L/S constant. However, the liquid-to-solid ratio is often altered at large scale if the product does not meet the specification. Iveson and Litster [1998b] identified the effect of granule porosity on granule growth, hence proposed to keep the pore saturation constant (see Section 2.1.3). Having said that, product characterisation is required to determine the pore saturation because

porosity strongly depends on process conditions [Iveson et al., 1996; Mackaplow et al., 2000; Oulahna et al., 2003].

The spray rate is often chosen arbitrarily for various reasons. Nevertheless, approaches have been suggested to keep the spray time [Kayrak-Talay et al., 2013] or dimensionless spray flux [Litster et al., 2001] constant. A constant spray time ensures that the time provided for rate processes is maintained. This concept relies on the assumption that the kinetics do not change drastically across scales. Keeping the dimensionless spray flux constant produces similar nucleation conditions (see Section 2.1.1).

Kneading time is another crucial operational parameter, that has a significant effect on the granulation endpoint. Michaels et al. [2009] suggest that the process should reach steady state so that the endpoint is fairly independent of kneading time. The advantage of this approach would be less variability between experiments. Others suggested short kneading times if higher granule porosity is desired [Shi et al., 2011; Pandey and Badawy, 2016] or avoid rapid growth [Shi et al., 2010]. In these cases, the kneading time is often kept constant [Kayrak-Talay et al., 2013] or estimated using empirical correlations [Rahmanian et al., 2008a]. Alternatively, the kneading time can be used as an operational parameter, which means the experiment is ideally stopped when the product has the desired properties [Faure et al., 2001]. Process control strategies are applicable to the latter approach, and the power consumption of the impeller is usually selected as the controlled variable with a feedback control system [Faure et al., 1999; Holm et al., 2001; Levin, 2007; Campbell et al., 2011; Clancy, 2017].

Overall, conventional scaling rules are based on keeping critical equipment and operational parameters constant. Many successful scale-up studies have been conducted using various approaches. However, comparative studies often result in contradicting conclusions which indicates the presence of unidentified factors. As a consequence, manual adjustment is often required at large scale, which should be avoided due to the high associated costs. Additionally, it is very challenging to predict all product properties at larger scale. That is why, the most critical property is usually identified, and other properties are only monitored.

In order to reduce experimental effort especially at larger scale, computational modelling has been explored to predict favourable conditions. However, an efficient workflow is needed to benefit from computational modelling. Wang et al. [2019] developed a suitable workflow (Figure 2.4) by applying model-driven design (MDD). For MDD approaches, the usage of a model that is predictive

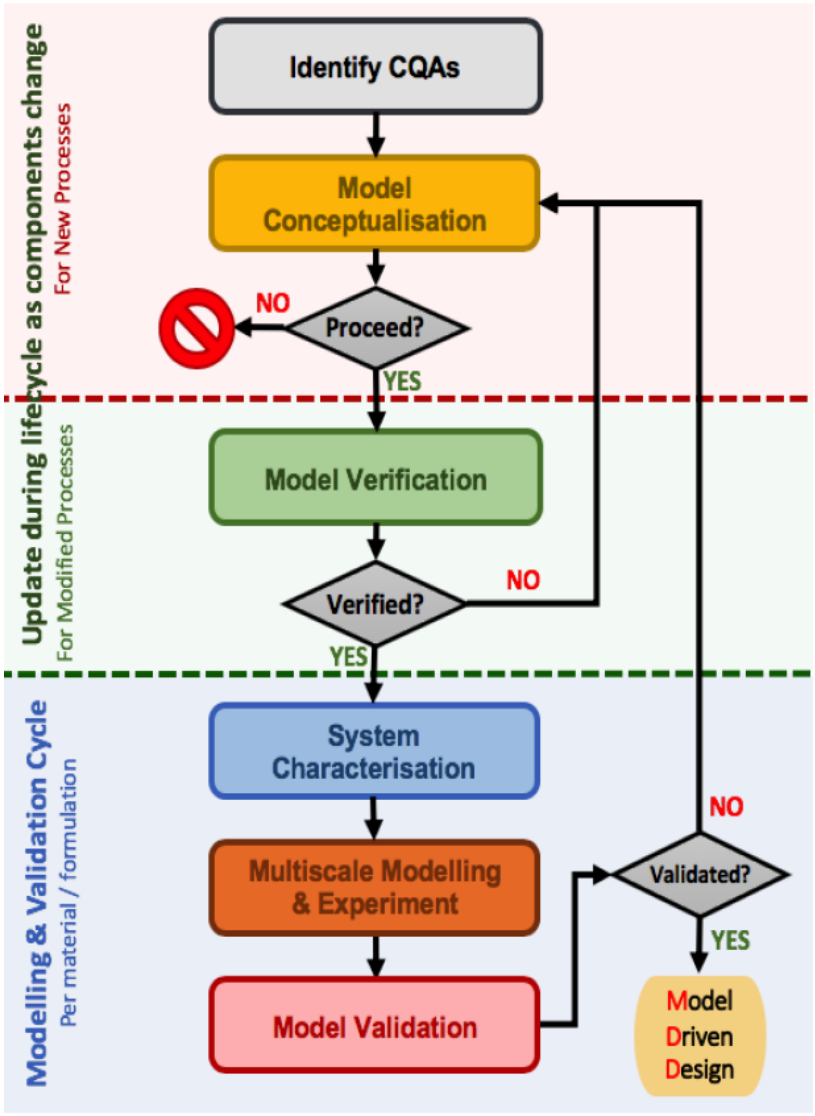

Figure 2.4: Model-driven design workflow (Reprinted from [Wang et al., 2019])

across scales is essential. Since the process is known to be scale-dependent, capturing the scale-dependent aspects should be emphasised [Gavi, 2019]. Several suitable modelling techniques have been explored: population balance modelling (PBM) [Pohlman and Litster, 2015; Yu et al., 2017], discrete element method (DEM) [Nakamura et al., 2013; Chan et al., 2015], and empirical approaches [Wehrlé et al., 1993; Miyamoto et al., 1997; Landin, 2017]. PBM is based on the assumption that particles with the same characteristics behave similarly. In this way, particle properties can be tracked more easily, especially at large scale. Applying PBM approaches has good potential because the computational time for simulations of large-scale equipment is low, and the experimental effort required to develop a predictive model is reasonable [Kumar et al., 2013]. Although PBM is widely used to model wet granulation, it has only been used in few scale-up studies. The alternatives (DEM and empirical approaches) do not fulfil both requirements. Additionally to identifying favourable conditions, good predictions of product properties are valuable for process design and scale-up [Litster, 2003]. For this reason, PBM is the most promising modelling approach for these applications [Niklasson Björn et al., 2005].

2.2.1 Critical review of operation and scale-up

- Usage of geometrically similar equipment is essential for process scale-up.
- Useful scaling rules have been derived from mechanistic understanding of wet granulation.
- Conventional scaling rules alone do not work reliably due to unidentified influences.
- The population balance modelling approach is promising for scale-up purposes.

2.3 *Modelling techniques*

Various modelling techniques have been employed to model particulate processes like wet granulation. The most frequently used method is population balance modelling (PBM). PBM is a process-scale approach which keeps track of particle properties over time. However, it is challenging to capture particle-scale behaviour in process-scale modelling because particle-scale behaviour cannot be observed easily and is, therefore, not well understood. For this reason, the use of the particle-scale modelling tool discrete element method (DEM) has been investigated in addition to PBM. Compared to PBM, DEM is a first-principles modelling approach. Other first-principles modelling tools like computational fluid dynamics (CFD) have also been employed, especially in modelling of fluid bed granulation processes [Fries et al., 2011; Sen et al., 2014]. Since both modelling approaches have

their benefits, combined approaches have also been investigated. This combination is also called multi-scale modelling (Figure 2.5). Alternative approaches include purely empirical modelling tools like artificial neural network (ANN) [Landin and Rowe, 2013]. PBM and DEM will be reviewed in more detailed in the following because they are the most promising tools to model high-shear wet granulation mechanistically.

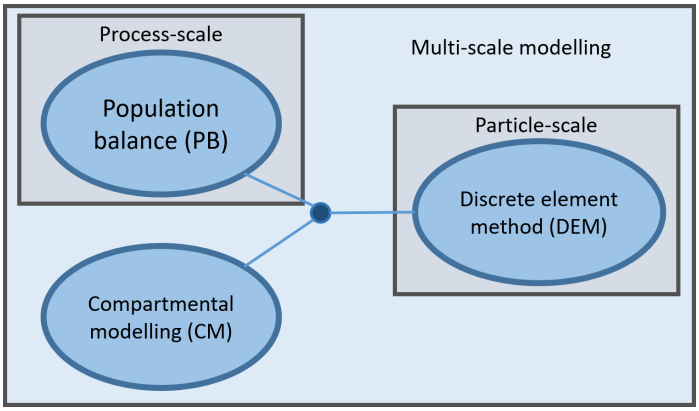

Figure 2.5: Multi-scale modelling approach

2.3.1 Population balance modelling

Population balance modelling (PBM) is a widely used tool which is typically employed to model particulate processes like crystallisation [Costa et al., 2007; Sulttan and Rohani, 2019], polymerisation [Sood et al., 2016; Brunier et al., 2017], granulation [Meyer et al., 2015; Shirazian et al., 2018], milling [Kumar Akkisetty et al., 2010; Capece et al., 2011], and mixing [Sen et al., 2012; Boukouvala et al., 2012]. Population balance equations are partial integro-differential equations which include conservation laws of integral fluxes.

In PBM, one or more properties are selected to group the particles into bins; all remaining particle properties are averaged. Consequently, this approach is based on the assumption that all particles in one bin have similar properties. It is evident that the selection of properties of interest and bin size can have a significant effect on the accuracy of the method. Due to this simplification, only the number of particles in each bin and their properties are tracked over time rather than tracking every particle individually. The changes in particle properties is determined by evaluating rate processes. A population balance equation can be written as [Ramkrishna and Mahoney, 2002]:

$$\frac{\partial V n(\vec{x},t)}{\partial t} + \frac{\partial}{\partial \vec{x}}\left[V n(\vec{x},t)\frac{\mathrm{d}\vec{x}}{\mathrm{d}t}\right] = \dot{V}_{in} n_{in}(\vec{x},t) - \dot{V}_{out} n_{out}(\vec{x},t) + V\left[\dot{b}(\vec{x},t) - \dot{d}(\vec{x},t)\right] \tag{2.37}$$

where V is the control volume, n is the volume-specific number density of particles, $\vec{x}$ is the set of granule properties of interest, t is time, $\dot{V}_{in}$ and $\dot{V}_{out}$ are the volumetric flowrates which are entering and leaving the control volume, and $\dot{b}$ and $\dot{d}$ are the volume-specific birth and death rates resulting from rate processes which result in a discrete change of properties: nucleation, coalescence, and breakage. The term $\frac{\partial}{\partial \vec{x}}\left[V n(\vec{x},t)\frac{\mathrm{d}\vec{x}}{\mathrm{d}t}\right]$ accounts for a continuous change of properties, which occurs due to the rate processes consolidation, layering, and attrition. However, the effects of attrition are usually negligible in high-shear wet granulation, that is why it does not need to be considered. Hence, the population balance equation becomes:

$$\begin{aligned}\frac{\partial V n(\vec{x},t)}{\partial t} + \frac{\partial}{\partial \vec{x}}\left[V n(\vec{x},t)\left(\dot{G}_{lay} + \dot{G}_{cons}\right)\right] &= \dot{V}_{in} n_{in}(\vec{x}) - \dot{V}_{out} n_{out}(\vec{x}) \\ &+ V\left[\dot{b}_{nuc}(\vec{x}) + \dot{b}_{coal}(\vec{x}) + \dot{b}_{br}(\vec{x}) - \dot{d}_{coal}(\vec{x}) - \dot{d}_{br}(\vec{x})\right]\end{aligned} \tag{2.38}$$

where $\dot{G}_{lay}$ and $\dot{G}_{cons}$ are the rate of change due to layering and consolidation respectively, $\dot{b}_{nuc}$, $\dot{b}_{coal}$ and $\dot{b}_{br}$ are the birth rates due to nucleation, coalescence and breakage, and $\dot{d}_{coal}$ and $\dot{d}_{br}$ are the death rates due to coalescence and breakage. This population balance equation can be either 1-D or multi-D. The dimensionality is defined by the number of properties of interest, which are represented by $\vec{x}$.

Compartmental modelling

In PBM, the remaining granule properties are averaged over the entire control volume, that is why this modelling approach should only be applied to ideally mixed systems. Having said that, it has been shown that most granulators cannot be assumed to be ideally mixed because of equipment design, segregation, flow regime, etc. [Scott et al., 2000]. Furthermore, different rate processes might be dominant in different regions of the granulator due to the sprayer, impeller or chopper [Bouffard et al., 2012] and affect the granule properties. Therefore, zones (or compartments) need to be identified which have homogeneous process conditions throughout and an even distribution of remaining granule properties. Primarily, the process conditions and granule properties which influence the rate processes should be considered at this point, e.g. flow kinematics and presence of

liquid or fine particles. PBM can be applied to these identified compartments [Bouffard et al., 2012; Li et al., 2013b]. This approach is called compartmental modelling (CM).

CM is applicable to represent twin-screw granulators [Barrasso et al., 2015a,b; McGuire et al., 2018a,b; Shirazian et al., 2019], fluid bed systems [Maronga and Wnukowski, 1997; Börner et al., 2013], rotating drums [Ramachandran and Chaudhury, 2012; Kumar et al., 2015], and high-shear mixers with vertical axis [Bouffard et al., 2012; Chaudhury et al., 2015; Tran, 2015; Chaturbedi et al., 2017; Yu et al., 2017; Abrahamsson et al., 2018] and horizontal axis [Portillo et al., 2007; Li et al., 2013b; Sen et al., 2013a; Pohlman, 2015; Davis, 2016; Lee et al., 2017].

In high-shear mixers, the following compartments are most commonly identified: spray, bulk, and breakage compartment. Only the dominant rate processes need to be represented in each compartment [Davis, 2016; Yu et al., 2017]. The dimensions and location of compartments are often derived from generic process understanding and heuristics. The spray compartment can be constructed around the spray area [Bouffard et al., 2012; Chaturbedi et al., 2017], and the impeller or chopper depicts the breakage compartment [Davis, 2016]. Approaches to identify compartments based on experimental techniques [Tran, 2015] and CFD simulations [Yu et al., 2017] have been studied as well. A method to estimate the spray zone depth based on a collision kernel is proposed by Yu et al. [2016].

The powder flow between compartments can be estimated by evaluating the flow regime and powder velocity. Experimental techniques, like PEPT [Tran, 2015], and DEM simulations [Bouffard et al., 2012] have been used for this purpose. Empirical correlations to determine the flow regime (see Section 2.2) and powder velocity (see Section 2.1.2) have also been proposed.

This approach is of particular interest for design and scale-up purposes because the CM decisions are based on the equipment design. Hence, slight design variations (e.g. for geometrically different equipment) can be accounted for without modifying the remaining model.

Model formulation

Empirical and mechanistic expressions have been developed to quantify the wet granulation rate processes (see Section 2.1). Empirical expressions, which are more commonly used, require a lot of experimental data since many parameters need to be estimated. Furthermore, empirical approaches might only be applicable to the equipment or formulation investigated and typically result in poor predictions outside their experimental design space.

While an empirical approach is based on experimental observation, a mechanistic approach is derived from first principles. Empirical approaches that include the effects of physical properties are also classified as semi-empirical, and mechanistic expressions that require fitting parameters can be called semi-mechanistic. Mechanistic expressions try to account for the physical phenomena and are, therefore, based on process parameters and material properties. Process parameters and material properties can often be measured. However, conventional parameter estimation techniques might be required to determine process parameters or material properties which cannot be determined otherwise. Mechanistic approaches have been developed to make the prediction of experimental results more reliable. The development of mechanistic expressions is more challenging because the mechanisms of the rate processes have to be identified correctly. For this reason, only few mechanistic kernels have been proposed in the literature, and only a small fraction of those kernels have been applied in modelling studies which also included adequate validation of the model.

Many models in the literature are one-dimensional (1-D) and can consequently only track one property of interest, typically granule size. However, it might not possible to represent all rate processes accurately if only 1-D PBM is employed [Iveson, 2002]. An uneven distribution of granule properties (e.g. liquid content and porosity) can have a significant effect on the rate processes [Scott et al., 2000; Reynolds et al., 2005; Štěpánek et al., 2009]. Therefore, multi-D PBM has been proposed to be able to track more than one property of interest. In addition to granule size, liquid content and porosity are often chosen as properties of interest [Braumann et al., 2007; Poon et al., 2008; Ramachandran and Barton, 2010; Barrasso et al., 2013; Pohlman, 2015]. Alternatively or additionally, the granule composition can be defined as a property of interest to investigate multi-component wet granulation [Lee et al., 2008; Matsoukas et al., 2009; Barrasso and Ramachandran, 2012]. However, validating the distribution of these additional properties is challenging. While the granule size distribution can be easily determined by mechanical screening (e.g. sieve analysis), the other property distributions cannot be determined accurately without screening a very large number of granules individually. Furthermore, multi-D PBM is very computationally expensive compared to 1-D PBM.

By applying reduced order modelling techniques, the computational time can be drastically reduced without completely neglecting the effects of the uneven property distribution. The most commonly used technique is the lumped parameter approach proposed by Hounslow et al. [2001]. The lumped parameter approach assumes that one or more granule properties (e.g. liquid content

and porosity) depend on the property of interest (e.g. size). Therefore, the multi-D PBM approach is lumped into the property of interest. As a consequence, a uniform distribution of granule properties is assumed for every interval of the property of interest. For example, all granules in one size bin have the same liquid content and porosity. For this approach, it is presumed that the granule properties mainly depend on the granule size. The difference to a conventional 1-D PBM approach is that a conventional 1-D PBM approach assumes uniform distribution of all other properties across the control volume, which is been shown to be inaccurate [Wauters et al., 2003]. That is why, the lumped parameter approach is advantageous. Reducing the population balance equation by one dimension results in a decrease in the computational time of around 95 % [Barrasso and Ramachandran, 2012]. This approach has been applied in various modelling studies [Biggs et al., 2003; Barrasso and Ramachandran, 2012, 2016].

Solution techniques

The population balance equation is typically solved using a numerical solution technique since only simplified population balance equations can be solved analytically [Ramkrishna, 1985]. Therefore, several different approaches have been developed in the past. The method of moments solves the population balance equation by solving for moments [Hulburt and Katz, 1964]. The types of this method which are most commonly used are the quadrature method of moments [Marchisio et al., 2003; Su et al., 2007], the direct quadrature method of moments [Marchisio and Fox, 2005; Selma et al., 2010] and the extended quadrature method of moments [Yuan et al., 2012; Passalacqua et al., 2018; Pigou et al., 2018]. Alternatives to the method of moments are discretised and stochastic methods which solve the population balance equation for the granule property distributions. The following discretised methods have been proposed: fixed pivot technique [Kumar and Ramkrishna, 1996a; Vale and McKenna, 2005], moving pivot technique [Kumar and Ramkrishna, 1996b], finite element method [Nicmanis and Hounslow, 1996; Mantzaris et al., 2001c; Mahoney and Ramkrishna, 2002; John et al., 2009], finite difference method (FDM) [Mantzaris et al., 2001a; Sheshadri and Fritzson, 2011], finite volume method (FVM) [Verkoeijen et al., 2002; Filbet and Laurençot, 2004; Gunawan et al., 2004], cell average technique [Kumar et al., 2006, 2008b,a; Kostoglou, 2007; Chaudhury et al., 2013], and other methods [Hounslow et al., 1988; Mantzaris et al., 2001b]. Alternatively, the stochastic Monte Carlo method has been used, which can be time-driven [Liffman, 1992] and event-driven [Smith and Matsoukas, 1998; Lin et al., 2002; Haibo et al., 2005]. The most

relevant solution techniques are discussed in more detail in the following.

Hounslow et al. [1988] developed a discretised method for the population balance equation. This discretised method was extended by Litster et al. [1995] and Wynn [1996] to an adjustable geometric discretisation.

The fixed pivot technique developed by Kumar and Ramkrishna [1996a] is a simplistic method which is similar to the discretised method developed by Hounslow et al. [1988]. The technique focuses on predicting selected moments accurately. As a result, the granule property distributions in the large granule size range are consistently over-predicted, which leads to a diverging behaviour of the higher moments [Kumar, 2006]. To avoid over-predicting the granule property distribution, the more complex moving pivot technique has been proposed by [Kumar and Ramkrishna, 1996b].

FVM solves the population balance by transforming the problem to mass conservation laws [Filbet and Laurençot, 2004]. Good predictions of the granule property distributions can be obtained using this method. However, the 0^{th} moment cannot be predicted accurately. In FVM, the properties of interest are tracked at the midpoint of each bin. For this reason, discrete changes of properties can be incorporated well using FVM. FDM is based on an approximation of the differential form of the partial differential equation [Mantzaris et al., 2001a]. In FDM, the properties of interest are evaluated at the boundaries of each bin. Therefore, FDM is appropriate to include continuous change rates. FVM and FDM are used to solve the PBM equation in the process modelling software package gPROMS (Process Systems Enterprise Ltd).

The cell average technique was developed to overcome the issues encountered with other discretised methods [Kumar et al., 2006]. Kumar et al. [2006] compared the cell average technique with the fixed pivot method and concluded that the granule property distributions and higher moments can be calculated more accurately using the cell average technique. Furthermore, the computational time required by the cell average technique to determine the final solution is comparable to the time required by the fixed pivot method. In a comparison study by Kumar et al. [2009], it was shown that the cell average technique is able to predict the moments more accurately, while the finite volume method (FVM) gives better predictions of the granule property distributions. Additionally, it was observed that the type of grid has an influence on the accuracy of the predictions, especially for the FVM. While good predictions can be achieved using the cell average technique on fine as well as a coarse grid, the FVM requires a fine grid to predict results accurately.

The Monte Carlo method determines the solution based on a probability function which results

in a certain degree of uncertainty. Zhao et al. [2007] analysed four different Monte Carlo methods and recommended event-driven methods since they are generally faster and more accurate than time-driven methods. Marshall et al. [2011] assessed an event-driven Monte Carlo method and the direct quadrature method of moments by comparing the results to a direct discrete solution. They concluded that the Monte Carlo method provides a good level of accuracy, while the accuracy of the method of moments highly depends on the complexity of the kernel applied.

To solve a multi-D population balance equation, the Monte Carlo method is a good option, since other solution techniques can become computationally expensive [Braumann et al., 2010b; Kumar et al., 2013]. As an alternative, Kumar [2006] and Chaudhury et al. [2016] proposed to employ reduced order modelling techniques to overcome this issue (see Section 2.3.1). In conclusion, the choice of solution technique is a trade-off between the accuracy of results and computational efficiency.

Parameters can be estimated using a set of experimental data. Apart from an effective parameter estimation technique, experimental data that shows the sensitivity to the parameters is crucial to determine accurate values for the parameters.

Ideally, the effects of parameters should be isolated to estimate each parameter separately. Effects of parameters can be isolated by examining the process mechanisms individually. The predictive power of a mechanistic model can be increased significantly with this technique because the parameter values estimated are more likely to be applicable outside the experimental design space. However, parameters are often interdependent. That is why, it is often necessary to estimate several parameters simultaneously. Parameters can be estimated using mathematical optimisation techniques.

Effects of parameters can be isolated by creating conditions that highly favour one mechanism and suppresses others. This approach has been applied to isolate various wet granulation mechanisms [Hapgood et al., 2004; Ramachandran et al., 2009; de Koster, 2018]. They carried out a parameter estimation study using a breakage-only granulator, in order to estimate the parameters of the consolidation and breakage kernels.

A common alternative approach is the factorial design of experiments. This approach has the advantage that combined effects of operational parameters can be identified and quantified which is valuable for wet granulation due to the high number of important parameters [Braumann et al., 2010a; Chaudhury et al., 2014a].

In order to estimate parameters, an optimisation problem has to be solved which minimises the

discrepancy between the experimental data and the simulation results by varying the parameters (least squares method):

$$\min_{\vec{x}} \quad f(\vec{x}) = \sum_{i=1}^{n} \left(O_i - E_i(\vec{x})\right)^2, \tag{2.39}$$

where $\vec{x}$ is the set of parameters, n is number of experiments, O_i is the set of experimental results, and E_i is the set of simulation results. Different optimisation techniques are available for this purpose [Rao, 2009]: derivative-free methods [Nelder and Mead, 1965], gradient-based methods [Levenberg, 1944; Broyden, 1970; Goldfarb, 1970; Shanno, 1970], and stochastic methods [Braumann et al., 2011].

Parameter estimation is often a multi-objective optimisation problem because the goal is to predict more than one granule property. A solution to a multi-objective optimisation problem is a trade-off between several objectives, while none of the objectives might be optimal. Since the problem can have more than one solution, identifying the best trade-off can be challenging. For this reason, methods to solve this problem have been proposed: weighted sum method and ε-constraint method.

The weighted sum method converts a multi-objective optimisation into a single-objective optimisation problem by summing the products of objective functions $F_i(x)$ and the assigned weighting factors w_i:

$$\min_{\vec{x}} \quad f(\vec{x}) = \sum_{i=1}^{m} w_i F_i(\vec{x}), \tag{2.40}$$

where m is the number of objective functions. More important objectives can be weighted higher.

In order to apply ε-constraint method, a primary objective function has to be selected. This primary objective function $F_j(x)$ is then minimised while constraints ε_i are introduced for the other objectives:

$$\begin{aligned} &\min_{\vec{x}} \quad f(\vec{x}) = F_j(\vec{x}) \\ &\text{s.t.} \quad F_i(\vec{x}) \leq \varepsilon_i, \quad i = 1, \ldots, m, \quad i \neq j. \end{aligned} \tag{2.41}$$

Model validation

In order to assess the accuracy of the simulation results, the model developed must be validated. Therefore, experimental data is commonly employed. A series of models which have been validated

using experimental data can be found in Table 2.5. In the following, the more recent model validation studies are discussed in more detail.

In most modelling studies, the wet granulation rate processes are not clearly separated and studied individually. This means that the results of the parameter estimation depend on the experimental range chosen, and the parameter values estimated might not be applicable outside the experimental range. As a consequence, less accurate model predictions can be obtained with these parameter values.

Models are usually validated by comparing the simulation results to experimental results using parameter values estimated. Therefore, only the experimental data which was used for the parameter estimation study is commonly used. Typically, models are not assessed further by comparing predictions to additional experimental results. Critical assessment of model predictions is valuable for models that are subsequently used for process design and scale-up purposes [Chaudhury et al., 2014a]. The aim of this approach is to use a limited amount of experimental data. As a consequence, the approach relies heavily on the accuracy of the predictions. That is why assessing the model predictions is inevitable.

Table 2.5: Model validation studies for wet granulation in high-shear mixers (MC Monte Carlo)

Source	Mixer type	Modelling approach	Solution technique	Mechanisms
Ramachandran et al. [2009]	Vertical axis (4.7 L Kenwood)	3-D PBM	Finite volume method	Consolidation, breakage
Pohlman [2015]	Ploughshare (10 L, 20 L, 50 L Lödige)	3-D PBM, CM	Finite volume method	Nucleation, consolidation, coalescence, breakage
Kastner et al. [2013]	Ploughshare (5 L Kenwood)	5-D PBM	Direct simulation MC method	Nucleation, penetration, solidification, consolidation, coalescence, breakage

Continued on next page

Table 2.5 – continued from previous page

Source	Mixer type	Modelling approach	Solution technique	Mechanisms
Biggs et al. [2003]	Vertical axis (10 L Roto Junior, 7.9 L Gral)	2-D PBM	Hounslow's method	Coalescence
Darelius et al. [2006]	Vertical axis (4 L DIOSNA)	3-D PBM	Volume-based approach	Consolidation, coalescence
Lee et al. [2017]	Ploughshare (5 L Kenwood)	5-D PBM, CM, DEM	Direct simulation MC method	Nucleation, penetration, solidification, consolidation, coalescence, breakage
Bouffard et al. [2012]	Vertical axis (4 L Caleva Spheronizer)	2-D PBM, CM, DEM	Event-driven MC method	Wetting, coalescence, breakage
Yu et al. [2017]	Vertical axis (1.9 L MiPro, 4 L DIOSNA)	2-D PBM, CM, CFD	Constant volume MC method	Nucleation, layering, coalescence, breakage
Le et al. [2009]	Vertical axis (10 L Roto Junior)	2-D PBM	Hounslow's method	Coalescence
Oullion et al. [2009]	Vertical axis (10 L Roto Junior)	2-D PBM	Constant number MC method	Nucleation, layering, coalescence
Sanders et al. [2003]	Vertical axis (10 L Roto Junior)	1-D PBM	Hounslow's method	Coalescence
Wauters et al. [2003]	Ploughshare (50 L Lödige)	1-D PBM	Hounslow's method	Consolidation, coalescence
Chaudhury et al. [2014a]	Vertical axis (1 L DIOSNA)	3-D PBM	Cell-average technique	Coalescence, breakage
Žižek et al. [2013, 2014]	Vertical axis (4 L DIOSNA)	1-D PBM	Hounslow's method	Coalescence
Dhanarajan and Bandyopadhyay [2007]	Vertical axis (0.25 L MiPro)	1-D PBM	Discretised method	Breakage

Continued on next page

Table 2.5 – continued from previous page

Source	Mixer type	Modelling approach	Solution technique	Mechanisms
Chaturbedi et al. [2018]	Vertical axis (10 L DIOSNA)	1-D PBM, CM	Cell-average technique	Dissolution, consolidation, coalescence breakage

Critical review of population balance modelling

- PBM is an efficient tool to model high-shear wet granulation.
- A compartmental modelling approach is required for non-ideally mixed systems.
- A multi-D PBM framework is required to capture the effects of an uneven granule properties distribution.
- Mechanistic kernels are preferable in predictive modelling.
- Parameters in mechanistic kernels should be measured directly or estimated using efficient techniques.
- The number of parameters which are estimated simultaneously should be limited by isolating rate processes in order to understand the effects of the individual parameters better.
- In model validation studies, predictions are usually not compared to experimental results which would be required to benefit from modelling for process design and scale-up purposes.

2.3.2 Discrete element method

The discrete element method (DEM) has been applied to a large variety of particulate processes, like wet granulation [Kuo et al., 2004; Hassanpour et al., 2013; Kulju et al., 2016], coating [Freireich et al., 2011a, 2015; Li et al., 2013b], milling [Cleary et al., 2003; Capece et al., 2014b], and powder mixing [Liu et al., 2013b; Sen et al., 2013b]. The use of this method has increased extensively in recent years, since computational limitations have been overcome [Ketterhagen et al., 2009].

DEM is a modelling approach which is able to track the motion of individual particles in a system by applying Newton's laws of motion, while accounting for the effects of external force fields, like gravity, and capturing collisions with equipment surfaces and other particles:

$$m_i \frac{\mathrm{d}v_i}{\mathrm{d}t} = F_{i,ext} + F_{i,coll} \tag{2.42}$$

where m_i and v_i are the mass and velocity of particle i, and $F_{i,ext}$ and $F_{i,coll}$ is the force exerted by external force fields and collisions respectively.

In order to represent interactions between particles, contact models are required. The use of two contact models has been extensively investigated: hard-particle models and soft-particle models. Hard-particle models assume that all particles are rigid, and collisions are instantaneous and ideal without the loss of energy [Liss and Glasser, 2001; Lasinski et al., 2004]. The use of hard-particle models is limited because of their fundamental assumptions. However, these assumptions are a reasonable approximation in dilute systems [Ketterhagen et al., 2009]. Soft-particle models are typically based on a more sophisticated approach. Several soft-particle models have been proposed to be able to capture different collision mechanisms. Which soft-particle model is most appropriate should be decided based on the material properties, such as particle stiffness and coefficient of restitution. Soft-particle models are usually preferred to model particle interactions in dense systems, such as high-shear wet granulation [Ketterhagen et al., 2009]. Soft-particle models simulate an overlapping of particles to account for particle deformation. The most relevant soft-particle models are described in more detail in the following.

The linear spring, dashpot model assumes that the particles behave like a spring-damping system during the collision [Cundall and Strack, 1979; Haff and Werner, 1986; Cleary and Sawley, 2002]. Johnson [1985], Lee [1994], Ristow and Herrmann [1994], and Zhang et al. [2004] proposed to extend this model by including a non-linear spring force based on the theory of elastic contact by Hertz [1881]. However, the simulation results do not agree with experimental data [Taguchi, 1992] (as cited in Ketterhagen et al. [2009]). For this reason, a non-linear spring, non-linear dashpot model was proposed [Kuwabara and Kono, 1987; Brilliantov et al., 1996]. This model assumes viscoelastic behaviour and is based on experimental data. Walton and Braun [1986] proposed a partially latching, hysteretic spring model to take the effect of plastic deformation on the repulsive force into account. Fewer particles can be tracked with the soft-particle model compared to a hard-particle model due to higher computational cost.

DEM is limited to simulating experiments at laboratory scale due to the very large number of particles at larger scales [Kumar et al., 2013]. For this reason, wet granulation processes are often modelled using fewer larger particles [Hassanpour et al., 2009]. Freireich et al. [2009] analysed the

sensitivity of DEM results to particle size and concluded that flow-scale behaviour is represented well at a larger particle size. However, particle-scale information like collision frequency and impact velocity is sensitive to particle size and cannot be determined accurately using this approach.

An alternative approach to reduce the complexity of a model is periodic sectioning, which takes advantage of the effect of symmetry [Gao et al., 2012a,b]. Therefore, only a part of the system needs to be modelled and simulated which can reduce the computational time significantly. However, granulators are usually not symmetric, since choppers, spray nozzles and other components are commonly installed eccentrically.

Validation studies have shown that the particle velocity and mixing behaviour predicted by DEM simulations is in good agreement with experimental data using measuring techniques: positron emission particle tracking (PEPT) [Stewart et al., 2001; Yang et al., 2003; Hassanpour et al., 2011; Marigo et al., 2013], magnetic resonance imaging (MRI) [Yamane et al., 1998], video imaging [Pandey et al., 2006], and particle image velocimetry (PIV) [Muguruma et al., 2000; Jain et al., 2002]. However, Freireich et al. [2009] showed that validating particle velocity is not sufficient to validate collision frequency since a change in material properties can have opposite effects on the particle velocity and collision frequency. Experimental data to fully validate DEM simulation results is difficult to obtain. While flow patterns and particle velocity in high-shear mixers can be determined experimentally, an experimental method to obtain the collision frequency is currently not available. Determining an accurate estimate for the collision frequency would be of great interest in predictive modelling of granulation processes.

Critical review of the discrete element method

- DEM can be used to determine specific particle-scale information preferably at small scale.
- Soft-particle contact models are recommended for high-shear wet granulation processes.
- DEM has not been experimentally validated, especially particle-scale information like collision frequencies, which are of great interest in wet granulation modelling.

2.3.3 Coupling of PBM and DEM

While PBM has been developed to determine process-level information, DEM can obtain particle-scale information and the flow regime. In PBM, particle-scale information is usually estimated using expressions which are often based on experimental data. Employing DEM simulations is a more

mechanistic and predictive way of determining particle-scale information. Despite the advantageous of DEM, the method also has limitations. The computational time for DEM simulations is extremely high compared to PBM, which makes DEM unsuitable for modelling a large-scale wet granulation process accurately [Chaudhury et al., 2017]. However, in order to take full advantage of both modelling tools, PBM and DEM can be coupled [Ingram and Cameron, 2004, 2005]. In order to benefit from coupling the two modelling tools, the usage of both tools should be limited to a specific scope. Options for coupling are discussed in the following.

A practicable way of coupling of PBM and DEM is one-way coupling [Freireich et al., 2011b; Sen et al., 2013b; Li et al., 2013a]. In one-way coupling, a DEM simulation is carried out, and the results obtained will be used as PBM inputs. The advantage of this method lies in its simplicity. However, finding a set of appropriate input parameters for the DEM simulation is challenging because many parameters are changing over time in wet granulation processes, especially the granule size distribution. For this reason, one-way coupling (one DEM simulation) is not sufficient to provide particle-scale information which is size-dependent.

An alternative to one-way coupling is two-way coupling. In two-way coupling, results are exchanged by both PBM and DEM and subsequently used as inputs by the other method [Barrasso et al., 2015b; Barrasso and Ramachandran, 2015, 2016] (Figure 2.6). Therefore, it is necessary to run the two models alternately, and the scheduling of the simulations can be determined by evaluating the change in granule properties (e.g. size distribution). This option is very computationally expensive since several DEM simulations are required to provide inputs. Additionally, automated communication between the PBM and DEM environment can be challenging.

Due to the high computational cost, reduced order modelling techniques have been investigated to include the results from DEM simulation in PBM [Boukouvala et al., 2013]. The following reduced order modelling techniques are feasible: artificial neural network (ANN) [Kumar Akkisetty et al., 2010; Barrasso et al., 2014, 2015c], Kriging method and response surface methodology [Jia et al., 2009; Boukouvala et al., 2010]. In reduced order modelling, a simplistic model is developed which can represent the DEM simulation results. The model development usually requires a very large amount of DEM results to ensure accurate results from the simplistic model. In contrast to the DEM model, the simplistic model is not predictive, that is why it can only be applied within the design space.

Data tables can also be employed to include DEM data in PBM. Therefore, DEM simulation

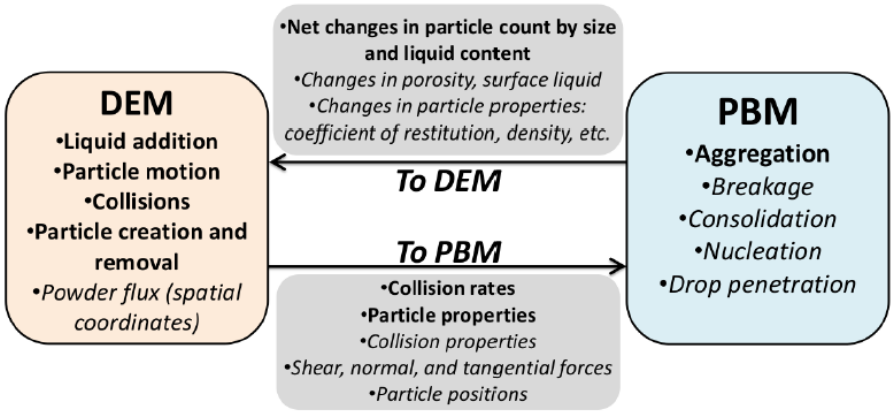

Figure 2.6: Two-way coupling of PBM and DEM (Reprinted from [Barrasso, 2015])

results need to be generated for the whole range of expectable granule properties. These results are then saved in data tables and used as an input for PBM. Since granule properties are changing over time, it is not possible to generate DEM data with the exact granule property distribution. That is why, a method needs to be developed to generate data for the granule properties from the data tables, e.g. by interpolation.

Critical review of coupling of PBM and DEM

- One-way coupling is not suitable to model wet granulation processes because of changes in granule properties.
- Two-way coupling is complex and computationally expensive.
- Reduced order modelling is not predictive and requires a lot of input data.
- Data tables are a good and simple option. However, an appropriate interpolation method is required to employ data tables.

2.4 *Critical summary*

Table 2.6 shows an overview of the critical review of the literature given after every subsection.

Table 2.6: Critical review summary

Critical review of subsection
Wetting and nucleation rate expressions
• The effect of spray characteristics on the nuclei size distribution is not well investigated quantitatively.
• Monte Carlo simulations are a promising tool to predict the nuclei size distribution, however, it is not feasible to include them in PBM.
• The only analytical nuclei size distribution model fails to predict experimental results at higher spray rates.
• Drop penetration time is often assumed to be negligible in modelling studies because drop penetration is usually a relatively quick process.
Consolidation rate expressions
• Consolidation is well understood but is usually modelled using empirical kernels.
• More mechanistic approaches have been proposed but not validated experimentally.
Layering and coalescence rate expressions
• Layering is a relevant wet granulation rate process but often neglected in modelling studies.
• Only simplistic models have been proposed but not validated.
• Coalescence has been well investigated in the past, and a series of models has been proposed and validated experimentally.
• While coalescence is often modelled using empirical approaches, more mechanistic approaches have only been investigated more extensively in recent years.
• A mechanistic coalescence model should include the effect of the liquid layer which dissipates impact energy. In high-shear wet granulation, plastic deformation should also be considered.
Breakage and attrition rate expressions
• Granule breakage is similar to particle breakage in milling processes.
• More mechanistic approaches to determine the breakage probability have been proposed in recent years.
• Fragment size distribution of granule breakage is poorly understood and models have not been fully validated.
• Attrition can be neglected in high-shear wet granulation.

Continued on next page

Table 2.6 – continued from previous page

Critical review of subsection
Wet granulation mechanisms • Wet granulation can be divided into rate processes which can be investigated separately. • While some rate processes can be isolated more easily (e.g. nucleation), others are difficult to separate (e.g. consolidation/coalescence or consolidation/breakage). • Mechanistic modelling of some rate processes (coalescence and breakage) has been well investigated, while other rate processes are often neglected in modelling studies or modelled simplistically (nucleation, consolidation, and layering).
Operation and scale-up • Usage of geometrically similar equipment is essential for process scale-up. • Useful scaling rules have been derived from mechanistic understanding of wet granulation. • Conventional scaling rules alone do not work reliably due to unidentified influences. • A population balance modelling approach is promising for scale-up purposes.
Population balance modelling • PBM is an efficient tool to model high-shear wet granulation. • A compartmental modelling approach is required for non-ideally mixed systems. • A multi-D PBM framework is required to capture the effects of an uneven granule properties distribution. • Mechanistic kernels are preferable in predictive modelling. • Parameters in mechanistic kernels should be measured directly or estimated using efficient techniques. • The number of parameters which are estimated simultaneously should be limited by isolating rate processes in order to understand the effects of the individual parameters better. • In model validation studies, predictions are usually not compared to experimental results which would be required to benefit from modelling for process design and scale-up purposes.
Discrete element method • DEM can be used to determine specific particle-scale information preferably at small scale. • Soft-particle contact models are recommended for high-shear wet granulation processes. • DEM has not been experimentally validated, especially particle-scale information like collision frequencies, which are of great interest in wet granulation modelling.

Continued on next page

Table 2.6 – continued from previous page

Critical review of subsection
Coupling of PBM and DEM
• One-way coupling is not suitable to model wet granulation processes because of changes in granule properties.
• Two-way coupling is complex and computationally expensive.
• Reduced order modelling is not predictive and requires a lot of input data.
• Data tables are a good and simple option. However, an appropriate interpolation method is required to employ data tables.

PBM is suitable to develop a predictive model for the high-shear wet granulation process, which can be applied at different scales. (Semi-)mechanistic expressions should be employed to model wet granulation rate processes in PBM. In order to obtain meaningful parameter values, parameters should be measured or determined using first-principles modelling tools if possible. Fitting parameters can be estimated, but having said that, an effective parameter estimation method should be applied with a limited number of parameters estimated simultaneously. By coupling PBM and DEM, particle-scale information can be included; however, the DEM simulations should be carefully designed, and an efficient coupling method is recommended to reduce the computational effort.

Several (semi-)mechanistic rate expressions are available in the literature for most wet granulation rate processes. Nevertheless, nuclei size distribution modelling is underdeveloped in the literature. The consequence is that inappropriate assumptions are often used in modelling studies.

High-shear wet granulation models are often not validated adequately in order to be able to make use of them for process design and scale-up purposes because comparison of model predictions to experimental data is usually not included, which is essential to assess the model's predictive power.

Chapter 3

EXPERIMENTAL MATERIALS AND METHODS

The experiments were performed at F. Hoffmann-La Roche AG in Basel, Switzerland. Therefore, the equipment and standard experimental methods are provided by Formulation and Process Sciences, F. Hoffmann-La Roche AG. A team of technicians helped to run experiments: Andreas Ewert, Alessia Schönemann, Georg Hummel and Vincent Spittler.

3.1 *Formulation*

For the granulation experiments, a model formulation from F. Hoffmann-La Roche AG is selected. The formulation contains the API naproxen sodium, and the excipients lactose monohydrate and microcrystalline cellulose [Rohrer, 2017]. Polyvinylpyrrolidone is used as a binder and added as a powder to the mixture. The composition of the powder mixture can be found in Table 3.1, and the bulk density of the powder mixture is 416.7 $\frac{\text{kg}}{\text{m}^3}$ [Rohrer, 2017]. The skeletal density ρ_s and nuclei-to-drop diameter ratio K_d are determined to be 1.412 ± 0.006 $\frac{\text{kg}}{\text{L}}$ and 1.26 ± 0.07 respectively. During the experiments, purified water is sprayed onto the powder bed to liquefy the binder.

Table 3.1: Composition of powder mixture used for granulation experiments

Component	Mass fraction $\left[\frac{\text{kg}}{\text{kg}}\right]$
Naproxen sodium	0.518
Lactose monohydrate	0.171
Microcrystalline cellulose	0.207
Polyvinylpyrrolidone	0.104

The feedstock materials are sieved (1.2 mm) to break up lumps before the experiments.

3.2 *Equipment*

The following equipment is used for the granulation experiments: 2 L, 10 L, 25 L and 70 L DIOSNA granulators (Dierks & Söhne GmbH). Figure 3.1 shows the granulator design. The dimensions of all four granulators are compared in Table 3.2. To spray liquid, a Pharmabehälter JC 1 pressure pot (Wilhelm Schmidt GmbH) is used for all granulators up to 25 L, and for the 70 L granulator, a 520 U peristaltic pump (Watson-Marlow Ltd) is used. Nozzles (Düsen-Schlick GmbH) with the following orifice diameters and spray cone angles are used: 0.4 mm, 30°; 0.8 mm, 30°; 0.8 mm, 45°; 1.1 mm, 45°.

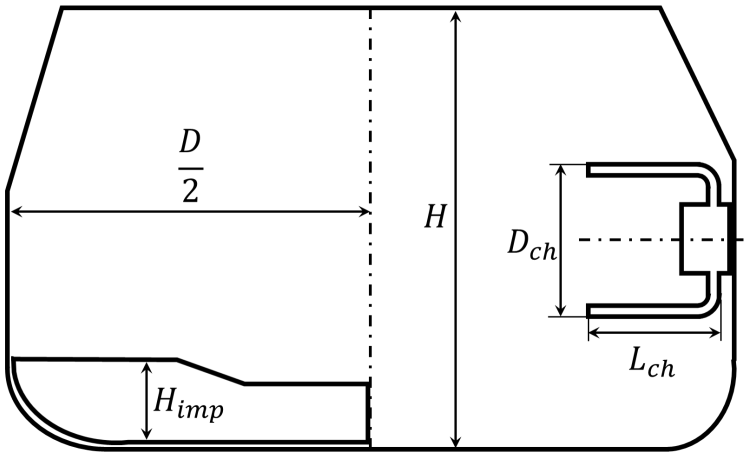

Figure 3.1: Granulator design

Table 3.2: Comparison of granulator dimensions at different scales (V granulator volume, H height, D diameter, H_{imp} impeller height, D_{ch} chopper diameter, L_{ch} chopper length)

V [L]	H/D [−]	H_{imp}/H [−]	D_{ch}/H [−]	L_{ch}/D [−]
2	0.56	0.15	0.20	0.11
10	0.54	0.15	0.38	0.21
25	0.50	0.19	0.45	0.18
70	0.69	0.12	0.27	0.19

3.3 *Experimental methodology*

3.3.1 Granulation experiments

In order to achieve an equivalent fill level of 48 %, 2 L experiments are carried out with 0.4 kg of dry powder mixture, 10 L with 2 kg, 25 L with 5 kg, and 70 L with 14 kg of dry powder mixture. The process steps are listed in Table 3.3.

Table 3.3: Process steps of the granulation experiments

Phase	Time [min]	Spray rate $\left[\frac{\text{mL}}{\text{min}}\right]$	Impeller rate $\left[\frac{1}{\text{min}}\right]$	Chopper rate $\left[\frac{1}{\text{min}}\right]$
Loading	–	0	0	0
Mixing	5	0	100	1200
Wetting	1 – 15	57 – 240	250 – 760	0 – 1200
Kneading	0 – 5	0	250 – 760	0 – 1200
Discharging	–	0	100	0

After the experiments, representative samples (60 g each) are dried in a tray oven (Vinci Technologies) for 6 h (moisture content below 0.04 $\frac{\text{kg}}{\text{kg}}$). An additional sample of 2 kg (if available) is dried separately in a 12 L fluid bed dryer GPCG 2 LabSystem (Glatt GmbH). The fluid bed dryer is operated at 60 °C and a gas supply of 50 $\frac{\text{m}^3}{\text{h}}$ (moisture content 0.1 $\frac{\text{g}}{\text{kg}}$). The sample is dried until the granules reach a moisture content of 0.04 $\frac{\text{kg}}{\text{kg}}$ (approximately 45 min).

3.3.2 Nucleation-only experiments

In order to isolate nucleation, the granulation experiment needs to be stopped after a very short period of time. Hence, the spray time is limited to 20 s, and no kneading step is included. Furthermore, the chopper is not used. The 10 L granulator is used for these experiments, and the spray rate ranges between 60 $\frac{\text{g}}{\text{min}}$ and 200 $\frac{\text{g}}{\text{min}}$. This methodology is adapted from Hapgood et al. [2004]. A sieve analysis is carried out to identify any nuclei formed. It is assumed that the size distributions of the dry powder mixture and nuclei are not overlapping. Additionally, nuclei breakage is neglected. Therefore, the nuclei size distribution is determined by subtracting the particle size distribution (PSD) of the dry powder mixture.

3.3.3 Sieve analysis

The granule size distribution is determined by sieve analysis of a dry sample of approximately 100 g. Two sieve towers (Fritsch GmbH/Retsch GmbH) are used for the size analysis: for coarse product (with sieve trays of 5000, 4000, 3150, 2240, 1800, 1400, 1250 and 1000 µm) and for fine product (1000, 710, 500, 355, 250, 180, 125 and 90 µm). The sample is poured onto the top sieve of the sieve tower used, and the tower is placed on a shaker for 5 min with amplitude of 2 mm. The sieve analysis for coarse product is only applied for samples that contain a significant amount ($> 0.02\,\frac{\mathrm{kg}}{\mathrm{kg}}$) of larger particles ($> 1000\,\mu\mathrm{m}$). Every sieve is weighed with and without material to determine the particle masses Δm_i. From the results, the mass frequency $f_{m,i}$ and log mass frequency $f_i(\ln x)$ are determined [Allen, 1968]:

$$f_{m,i} = \frac{\Delta m_i}{\sum_{j=1}^{n} \Delta m_j} \frac{1}{x_i - x_{i-1}} \tag{3.1}$$

$$f_i(\ln x) = \frac{\Delta m_i}{\sum_{j=1}^{n} \Delta m_j} \frac{1}{\log_{10}(x_i/x_{i-1})} \tag{3.2}$$

where x_i is the maximum particle diameter of size range i. For determining the mass frequencies, all particles are assumed to be between 45 µm and 7 mm. The cumulative mass fraction $W\,(< x_i)$ is:

$$W\,(< x_i) = \frac{\sum_{j=1}^{i} \Delta m_j}{\sum_{j=1}^{n} \Delta m_j} \tag{3.3}$$

and the cumulative residue mass fraction $W\,(> x_i)$ is:

$$W\,(> x_i) = 1 - W\,(< x_i) \tag{3.4}$$

To plot the PSD results, the geometric mean diameter $\bar{x}_i$ is used:

$$\bar{x}_i = \sqrt{x_{i-1} x_i} \tag{3.5}$$

To calculate the granulated mass fraction W_{gran}, the dry powder mass fraction m_p is subtracted:

$$W_{gran} = \frac{\sum_{j=1}^{n} \Delta m_j - \Delta m_{p,j}}{\sum_{j=1}^{n} \Delta m_j} \tag{3.6}$$

An example analysis calculation is provided in Appendix A.1.

3.3.4 Density

The skeletal density is measured using an AccuPyc II 1340 (Micromeritics Instrument Corporation). Therefore, the sample is weighed, and placed in the chamber. Gas is drawn out of the chamber, and helium is injected until a gauge pressure of 19.5 psig is reached. An equilibrium rate of 0.005 psig/min is chosen. Helium penetrates the pores of the particles; in this way, the skeletal volume is measured. 20 cycles of low and high-pressure steps are applied, and the average skeletal density ρ_s is determined:

$$\rho_s = \frac{m_s}{V_s} \tag{3.7}$$

where m_s and V_s are the solid skeletal mass and volume respectively.

The envelope density is determined using a GeoPyc 1365 Envelope Density Analyzer (Micromeritics Instrument Corporation). Before the measurement, the product is sieved to control the granule size between 1 mm and 1.4 mm. A sample is taken and weighed (0.2 g – 0.25 g). A bed of small, rigid powder particles (Dry Flo), which have a high flowability, is placed in the cylinder. The volume of the powder bed is between 1.3 cm^3 and 1.7 cm^3. The bed is compressed 10 times with piston, applying a force of 28 N, and the volume is measured and averaged. The sample is added to the powder bed, and both are well-mixed. The volume of the powder bed with the sample is measured in the same manner, and the volume displaced by the sample is calculated. During the volume measurement, the powder bed is slightly agitated to fill the void spaces around the granules. The small powder particles are assumed to surround the granules without penetrating into the intra-granule pores. This measurement is carried out 3 times per experiment, and the average envelope density ρ_{env} is determined:

$$\rho_{env} = \frac{m_s}{V_s + V_p} \tag{3.8}$$

where V_p is pore volume. (Envelope) porosity ε is the ratio of pore volume to total volume, and for a dry sample, it can be determined using Eqs. 3.7 and 3.8:

$$\varepsilon = \frac{V_p}{V_s + V_p} = \frac{(V_p + V_s) - V_s}{V_s + V_p} = 1 - \frac{V_s}{V_s + V_p} = 1 - \frac{m_s \rho_{env}}{\rho_s m_s} = 1 - \frac{\rho_{env}}{\rho_s} \tag{3.9}$$

The bulk density and tap density of dry samples are measured using glass cylinders. A tap density tester JEL Stampfvolumeter STAV 2003 (J. Engelsmann AG) is used for bulk samples with a 250 m^3 glass cylinder, and manual taps are used for all other measurements. The material is weighed and poured into a glass cylinder. The cylinder is handled carefully, and the bulk volume is recorded. Then, the tap volume is determined after 10, 500, 1250 and 2500 taps, or 10 s, 1 min, 2 min and 3 min for manual taps. The following glass cylinders are used, depending on the sample size: 10 m^3, 25 m^3, 50 m^3 and 250 m^3. The bulk or tap density $\rho_{bulk/tap}$ is determined as follows:

$$\rho_{bulk} = \frac{m_s}{V_{bulk}} \tag{3.10}$$

$$\rho_{tap} = \frac{m_s}{V_{tap}} \tag{3.11}$$

where V_{bulk} and V_{tap} are the bulk and tap volume respectively.

Additionally to bulk samples, samples with a narrow size range are analysed (500 µm – 710 µm). To avoid dry powder particles in the sample, the narrow size range should not overlap with the dry powder PSD. It is ensured that the diameter of the glass cylinder is at least 15 times larger than the maximum particle diameter. The tap density of a sample with a narrow size range is a measure for envelope density because a similar packing fraction (or inter-particle void volume fraction) can be assumed for every measurement. The bed porosity (or inter-particle void fraction) of a settled bed is typically between 0.36 and 0.38 [Dullien, 1979; Hoffmann and Finkers, 1995], and 0.38 is assumed in this study. The bed porosity ε_{bed} is here defined as:

$$1 - \varepsilon_{bed} = \frac{V_s + V_p}{V_{tap}} \tag{3.12}$$

The envelope density ρ_{env} is therefore determined from Eqs. 3.8, 3.11 and 3.12:

$$\rho_{env} = \frac{m_s}{V_s + V_p} = \frac{m_s}{V_{tap}\,(1 - \varepsilon_{bed})} = \frac{\rho_{tap}}{1 - \varepsilon_{bed}} \tag{3.13}$$

An example analysis calculation is shown in Appendix A.2.

3.3.5 Spray characteristics

The spray characteristics of the nozzles used are determined; especially, the drop size and spatial drop distribution are of interest. A SprayTec laser diffraction system (Malvern Panalytical) is used to measure the drop size distribution. The different nozzles are tested at the distance of 9 cm, the average distance between nozzle and powder bed (not in motion) in the 10 L granulator. Apart from the centre of the spray cone, the drop size distribution on the sides are measured for comparison (+30 mm and −30 mm). It is assumed that the spray cone is symmetrical.

In order to measure the spatial drop distribution, a grid of cuvettes (10×10 containers with size 1 cm $\times$ 1 cm) is placed 9 cm below the spray nozzle (Figure 3.2). The cuvettes are supported with a frame to prevent spillage during the measurement. It is ensured that the grid is large enough to capture the entire spray cone. After spraying for a short period of time, the cuvettes are weighed to determine the amount of liquid. The cumulative mass in each row or column is determined to obtain the spatial drop distribution and standard deviation.

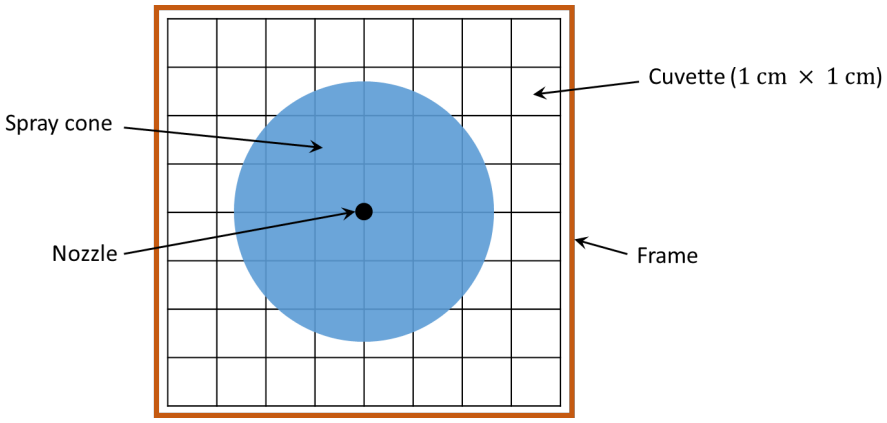

Figure 3.2: Experimental setup to measure the spatial drop distribution

The range of operating conditions of the nozzles used are listed in Table 3.4. The pressure is measured in the headspace of the pressure pot.

3.3.6 Drop nucleation experiments

The powder mixture is poured into a Petri dish. Any additional powder is carefully removed to produce a powder bed with a flat surface. A syringe with a small needle is placed 9 cm above the static powder bed. Through gentle taps, single water drops are formed, which fall onto the bed

Table 3.4: Overview of nozzles and operating conditions tested

Orifice [mm]	Spray angle [°]	Spray rate $\left[\frac{\text{mL}}{\text{min}}\right]$	Pressure [bar]
0.4	30	60 – 85	1.5 – 5
0.8	30	200 – 300	2 – 5
0.8	45	285	4
1.1	45	410 – 445	2.5 – 4

and form granules. To ensure reproducible conditions, the powder bed is roughly 4 times deeper than the granule diameter, and the distance to the walls is at least 5 times larger than the granule diameter. In total, 15 granules are formed and analysed. The experimental method has previously been demonstrated by Pitt et al. [2018] and de Koster et al. [2019].

The mass of the water drops is measured using a microbalance. Overall, 4 drops are weighed, and the results are averaged. The granule volume is measured using the GeoPyc 1365 Envelope Density Analyzer (see Section 3.3.4). Therefore, 5 granules are measured simultaneously. The nuclei-to-drop diameter ratio K_d can be calculated from the results as follows:

$$K_d = \frac{d_1}{d_d} = \left(\frac{V_1}{V_d}\right)^{\frac{1}{3}} = \left(\frac{V_1 \rho_l}{m_d}\right)^{\frac{1}{3}} \tag{3.14}$$

where d_1 and V_1 are the (single-drop) nuclei diameter and volume respectively, d_d, V_d, m_d are the drop diameter, volume and mass respectively, and ρ_l is the liquid water density.

With the method applied, the drop diameter ($2680 \pm 15\,\mu\text{m}$) significantly larger than the typical spray drop diameter ($60\,\mu\text{m} - 300\,\mu\text{m}$). Hence, the underlying assumptions are that the nuclei-to-drop size ratio is not size-dependent, and drops with a consistent size can be produced manually with a syringe. Both assumptions have been confirmed experimentally [Ax et al., 2008; de Koster, 2018].

Chapter 4

NUCLEI SIZE DISTRIBUTION MODELLING IN WET GRANULATION

This work was originally published in:

Bellinghausen, S., Gavi, E., Jerke, L., Ghosh, P. K., Salman, A. D., and Litster, J. D. (2019). Nuclei size distribution modelling in wet granulation. *Chemical Engineering Science: X*, 4:100038.

4.1 *Introduction*

In this chapter, two new nuclei size distribution models are proposed and assessed. The emphasis of this work is to address the weaknesses of the previously published modelling approaches since a reliable nuclei size distribution model is needed for any mechanistically-based wet granulation model but not available (see Section 2.1.1). For the development of the models, two different approaches are considered, one empirical and one semi-mechanistic. The empirical approach applies the log-normal distribution (LND) function, and the semi-mechanistic approach is based on the Poisson distribution (PD) function. Both models can be included in a population balance modelling (PBM) framework without increasing the computational cost significantly. Monte Carlo simulations (MCS) data is used to estimate modelling parameters of both models. The model assessment includes a comparison to experimental data from the literature. A sensitivity analysis is conducted to assess the MCS modelling assumptions and the applicability of the LND model.

4.2 *Model development*

4.2.1 Log-normal distribution model

An empirical model is proposed that can determine the nuclei size distribution. First, we define the a dimensionless mass frequency and dimensionless nuclei diameter. The dimensionless mass frequency f'_m can be derived from the mass frequency f_m and the diameter of a nucleus formed by a single drop d_1:

$$f'_m = f_m d_1 \tag{4.1}$$

and the dimensionless nuclei diameter d'_n is defined as the ratio of the nuclei diameter d_n to the diameter of a nucleus formed by a single drop d_1:

$$d'_n = \frac{d_n}{d_1} \tag{4.2}$$

The model assumes that the dimensionless nuclei mass frequency follows a log-normal distribution (LND):

$$f'_m(d'_n, \mu_n, \sigma_n) = \frac{1}{d'_n \sigma_n \sqrt{2\pi}} \exp\left(-\frac{\left(\ln d'_n - \mu_n\right)^2}{2\sigma_n^2}\right) \tag{4.3}$$

where μ_n and σ_n are the logarithmic mean and logarithmic standard deviation of the dimensionless nuclei diameter.

It is assumed that the two parameters μ_n and σ_n depend on the dimensionless nucleation number Ψ_n as well as the standard deviation of the spatial drop distribution in the spray σ_x. Based on this assumption, the following two functions are proposed:

$$\mu_n = (m_1 \sigma_x + m_2)\, \Psi_n + m_3 \tag{4.4}$$

and

$$\sigma_n = (s_1 \sigma_x + s_2)\, \Psi_n + s_3 \tag{4.5}$$

where m_1, m_2, m_3, s_1, s_2, and s_3 are fitting parameters. Combining Eqs. 4.3, 4.4, and 4.5:

$$f'_m = \frac{1}{d'_n \left((s_1 \sigma_x + s_2)\, \Psi_n + s_3\right) \sqrt{2\pi}} \exp\left(-\frac{\left(\ln d'_n - \left((m_1 \sigma_x + m_2)\, \Psi_n + m_3\right)\right)^2}{2\left((s_1 \sigma_x + s_2)\, \Psi_n + s_3\right)^2}\right) \tag{4.6}$$

In order to predict the nuclei size distribution, the diameter of a nucleus formed by a single (average) drop needs to be known. By transformation, the dimensionless results can be converted:

$$f_m = \frac{1}{d_n \left(\left(s_1\sigma_x + s_2\right)\Psi_n + s_3\right)\sqrt{2\pi}} \exp\left(-\frac{\left(\ln\frac{d_n}{d_1} - \left(\left(m_1\sigma_x + m_2\right)\Psi_n + m_3\right)\right)^2}{2\left(\left(s_1\sigma_x + s_2\right)\Psi_n + s_3\right)^2}\right) \tag{4.7}$$

with

$$d_1 = K_d d_d \tag{4.8}$$

The six fitting parameters m_1, m_2, m_3, s_1, s_2, and s_3 need to be estimated; in this study, the average nuclei mass frequency $\bar{f}'_m$ derived from MCS data is used for this purpose. Therefore, a weighted optimisation is chosen with the dimensionless diameter values d'_n as weights. The weights are chosen to improve the match at larger nuclei sizes. The final objective function is solved using the least squares method:

$$\min_{\vec{x}} \quad \sum_{i=1}^{6}\sum_{j=1}^{10}\sum_{k} d'_n(k)\left(\bar{f}'_m\left(i,j,k\right) - f'_m\left(\sigma_x(i), \Psi_n(j), d'_n(k), \vec{x}\right)\right) \tag{4.9}$$

with

$$\vec{x} = [m_1, m_2, m_3, s_1, s_2, s_3] \tag{4.10}$$

where i and j are the levels tested for spatial standard deviation and dimensionless nucleation number respectively and k are the nuclei size levels.

4.2.2 Modified Poisson distribution model

The semi-mechanistic Poisson distribution (PD) model approach was proposed by Hapgood et al. [2004, 2009]. This approach has been used to predict drop coalescence on powder beds. However, it is also suitable to predict nuclei coalescence by accounting for substituting the smaller drop size with the larger nuclei size. For the development of Hapgood's model, the PD function is applied to determine the probability of a (new) drop/nucleus to coalesce with n other drops/nuclei:

$$P_n = \exp\left(-\lambda B\right)\frac{\left(\lambda B\right)^n}{n!} \tag{4.11}$$

where λ is the intensity of distribution, and B is a subregion. Hapgood et al. [2009] assumed that the intensity λ is a function of the dimensionless spray flux only since drop coalescence was considered. Furthermore, it was assumed that the area that leads to coalescence is 4 times larger than the area of a single drop and is independent of the number of drops already coalesced (see Figure 4.1):

$$\lambda B = 4\Psi_a \tag{4.12}$$

In this study, nuclei coalescence rather than drop coalescence is assumed. Therefore, the dimensionless nucleation number Ψ_n and the cross-sectional area of a single drop nuclei a_1 are used to determine the intensity of distribution:

$$\lambda = \frac{\Psi_n}{a_1} \tag{4.13}$$

In this case, subregion B is the area that leads to nuclei coalescence (nuclei exclusion area). If the centre point of a new drop lands inside this nuclei exclusion area, the drop will coalesce with the nucleus. The nuclei exclusion area is effectively assumed to be one radius larger than the nuclei in every direction. The nuclei exclusion area increases with the number of drops as illustrated in Figure 4.1. For the development of the MPD model, the constant nuclei exclusion area is replaced with a function for the nuclei exclusion area a_n which depends on the number of drops:

$$B = a_n(n) \tag{4.14}$$

From Eqs. 4.13 and 4.14, the term λB of the MPD model can be derived:

$$\lambda B = \frac{a_n(n)}{a_1}\Psi_n = k(n)\Psi_n \tag{4.15}$$

where $k(n)$ is the ratio of nuclei exclusion area to single nucleus area. Combining Eqs. 4.11 and 4.15:

$$P_n = \exp\left(-k(n)\Psi_n\right)\frac{\left(k(n)\Psi_n\right)^n}{n!} \tag{4.16}$$

To represent the spatial distribution of drops, a uniform distribution is assumed in the direction of the powder flow, and a normal distribution is applied perpendicular to the powder flow. Therefore, the spray zone is divided into 10 equal-size sections to model the normal distribution of drops. The

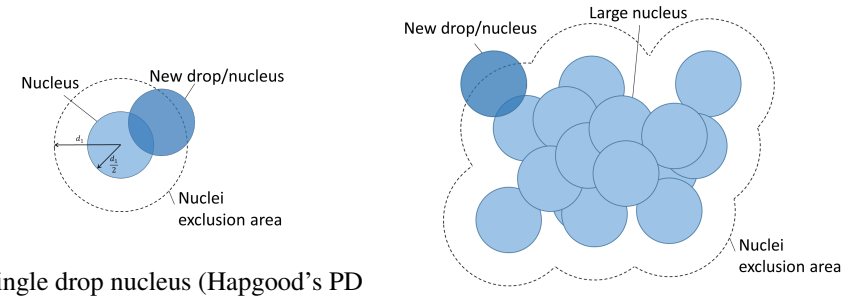

(a) Single drop nucleus (Hapgood's PD model)

(b) Large nucleus (MPD model)

Figure 4.1: Illustration of nuclei exclusion area and criterion for nuclei coalescence (d_1 single drop nucleus diameter)

nuclei size distribution is determined based on the average dimensionless nucleation number of each section:

$$\Psi_n(x, \mu_x, \sigma_x) = \frac{\bar{\Psi}_n}{P\sigma_x\sqrt{2\pi}} \exp\left(-\frac{(x-\mu_x)^2}{2\sigma_x^2}\right) \tag{4.17}$$

where x is a dimensionless coordinate, $\bar{\Psi}_n$ is the dimensionless nucleation number averaged over the spray zone, P is the percentage of drops within the spray zone, and μ_x and σ_x are the mean and the standard deviation of the distribution function respectively. The following power function is applied to determine the nuclei exclusion area ratio:

$$k(n) = 4 + bn^c \tag{4.18}$$

where b and c are fitting parameters. Here, $k(0)$ equals 4 which is the nuclei exclusion area ratio for a single drop nucleus. This power function is the essential contrast to Hapgood's PD model, which assumes: $k(n) = 4$. The average nuclei exclusion area for up to 1000 drops is determined using a MCS approach. The non-linear least squares method 'fit' from MATLAB is used to fit the power function to the simulation results.

In order to calculate the factorial of the MPD, Ramanujan's approximation is used [Andrews and Berndt, 2005]:

$$n! \approx \sqrt{\pi}\left(\frac{n}{e}\right)^n \sqrt[6]{8n^3 + 4n^2 + n + \frac{1}{88}}. \tag{4.19}$$

This approximation is also used to scale the equation. Scaling is needed since terms of the PD function can exceed numerical limits of mathematical solvers especially at higher coalescence rates. From Eqs. 4.16 and 4.19, the scaled equation can be derived:

$$P_n = \frac{\left(\sqrt[n]{\exp\left(-k(n)\Psi_n\right)}\frac{e}{n}k(n)\Psi_n\right)^n}{\sqrt{\pi}\sqrt[6]{8n^3+4n^2+n+\frac{1}{88}}}. \tag{4.20}$$

While the PD function is normalised, the modifications made lead to a model, which results in a sum of probability greater than 1. The reason for that is the intensity function λB which increases with the number of drops n; the PD function was developed for a constant intensity function. As a consequence, the probability distribution results from Eq. 4.20 need to be normalised.

After determining the probability distribution using Eq. 4.20, the nuclei size distribution is determined by discretising the normalised results applying a linear grid with the bin boundaries $d'_{n,k}$:

$$d'_{n,k} = 0.5k \tag{4.21}$$

4.2.3 Monte Carlo simulations for parameter estimation

Two sets of Monte Carlo simulations (MCS) are conducted to determine the model parameters for both models. In the first set of MCS, the entire spray zone is simulated to generate data to fit the empirical LND model (Eq. 4.7). The second set of MCS determines the nuclei exclusion area, which is needed for the MPD model (Eq. 4.18). In both approaches, the spray zone is assumed to be a flat surface, and nuclei are represented as circles. A flowchart of the simulations is shown in Figure 4.2.

In the first set of MCS, circular nuclei are randomly placed on a quadratic area which represents the liquid addition onto a powder bed surface using a nozzle. This approach is adapted from Wildeboer et al. [2005]. The simulations are based on only one input parameter - the dimensionless nucleation number. The circles represent nuclei because the approach is based on nuclei coalescence rather than drop coalescence. Instead of representing the spray as drops which vary in size [Wildeboer et al., 2005], a uniform drop diameter is assumed in this case. In the direction of the powder flow, the spatial distribution of drops is assumed to be uniform over the spray zone because the surface of the powder bed is moving steadily through the spray zone. A truncated normal distribution is applied perpendicular to the direction of the powder flow:

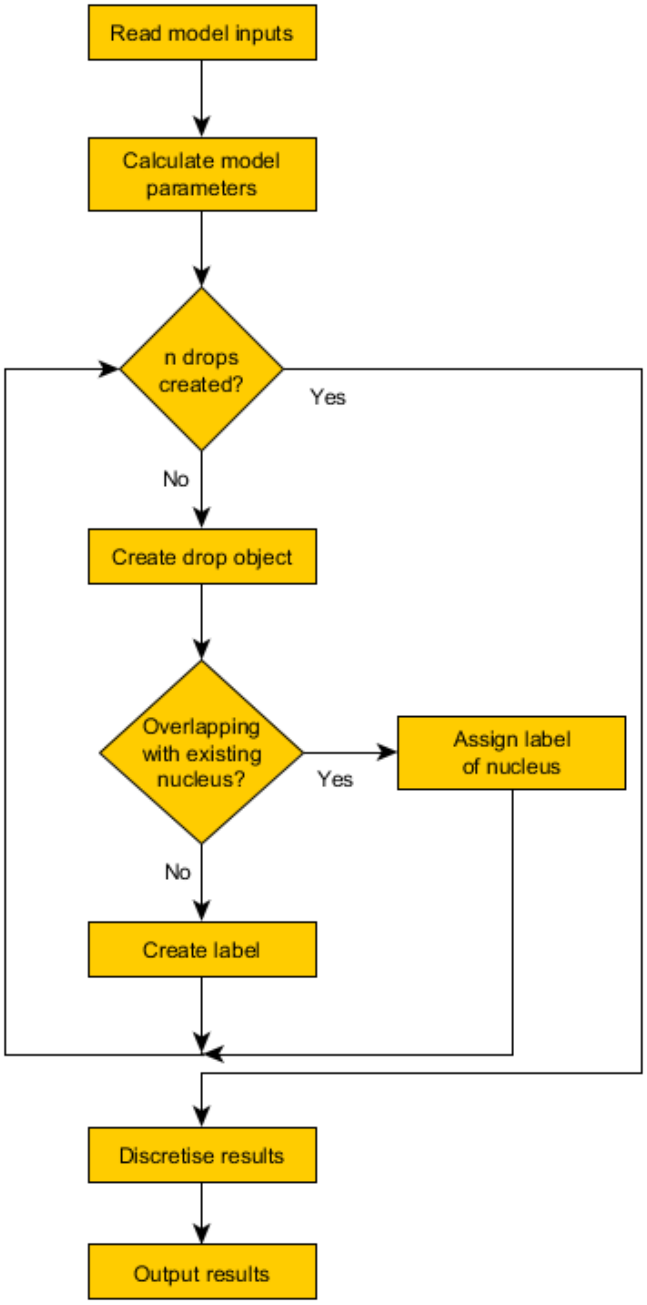

Figure 4.2: Flowchart of the MCS [Wildeboer et al., 2005]

$$N(x, \mu_x, \sigma_x) = \frac{1}{P\sigma_x\sqrt{2\pi}} \exp\left(-\frac{(x-\mu_x)^2}{2\sigma_x^2}\right) \tag{4.22}$$

where x is a dimensionless coordinate, P is the percentage of drops within the spray zone, and μ_x and σ_x are the mean and the standard deviation of the distribution function respectively. The mean location is set to the centre of the spray zone, and the standard deviation is varied between 0.15 and 0.25 of the width of the spray zone, which is a typical range for spray systems [Wauters et al., 2002; Sehmbi, 2019]. The normal distribution is truncated at the boundaries of the spray zone. In order to determine whether or not nuclei coalesce, an overlapping criterion is applied:

$$\left(x_i - x_j\right)^2 + \left(y_i - y_j\right)^2 \leq \frac{\left(d_{1,i} + d_{1,j}\right)^2}{4} \tag{4.23}$$

where x and y are the centre coordinates of the drops i and j. Based on this criterion, nuclei are identified, and their sizes are determined. The results are discretised to generate a nuclei size distribution using a linear grid. The bin boundaries $d'_{n,k}$ are given by:

$$d'_{n,k} = 0.5k \tag{4.24}$$

The size of the spray zone is 2000×2000 pixels, and the single drop nuclei diameter d_1 is 10 pixels. The number of drops per simulation varies between 5100 and 51 000 which correlates to a dimensionless nucleation number between 0.1 and 1.0. The MCS results are averaged over 10 simulations. The model to carry out the MCS is implemented in Python; one simulation can take between several minutes and several hours depending on the dimensionless nucleation number used.

Additional MCS are carried out based on the same approach. In these simulations, the following inputs are varied: the standard deviation of the spatial drop distribution in the direction perpendicular to the powder flow ($\frac{1}{16} - \frac{1}{2}$ of the spray zone width) and the nuclei diameter ($10 - 20$ pixels). Furthermore, a log-normal drop size distribution is introduced with a logarithmic standard deviation between 0.1 and 0.6 of the logarithmic mean diameter.

In the second set of MCS, nuclei with up to a 1000 drops are simulated. The objective is to determine the average nuclei exclusion area (Figure 4.1). Therefore, every drop is added individually; and after every drop, the nuclei exclusion area is determined. Every drop (except for the first drop) is placed randomly applying a uniform distribution with a minor constraint: the new drop has to overlap with the existing nucleus (Overlapping criterion: Eq. 4.23). The final results are averaged over 100 simulations.

4.2.4 Model assessment

For the model validation and assessment, the deviation of the model results from the reference data at every grid point is determined, and the sum of squared errors is calculated. To be able to utilise different sets of reference data, the relative sum of squared errors is reported, while all results are relative to the results of Hapgood's PD model.

4.3 *Literature experiments for model validation*

In order to assess the model predictions, experimental data is used, as well as MCS data. The deviation of the model predictions is quantified with the sum of squared errors at every grid point. The results reported are relative to Hapgood's PD model results.

Two sets of experiments are selected which were published by Litster et al. [2001, 2002]. An overview of all experiments can be found in Table 4.1.

Table 4.1: Overview of experiments

Source	Equipment	Dimensionless nucleation number Ψ_n [−]
Litster et al. [2001]	Ex-granulator	0.5; 0.6; 0.7; 1.2; 2.7
Litster et al. [2002]	High-shear mixer	0.5; 0.7; 1.2

Litster et al. [2001] conducted ex-granulator nucleation experiments using a powder bed on a rotating table with different rotational velocities. A nozzle was placed above the powder bed to spray liquid onto the powder bed. Litster et al. [2002] conducted nucleation-only experiments in a Fielder PharmaMATRIX 25 L high-shear mixer with a spray time of 5 s. Experiments at different impeller frequencies are conducted to test the impact of the dimensionless nucleation number on the nuclei size distribution.

In all experiments, the powder bed consisted of lactose monohydrate which was screened before to facilitate the separation of nuclei during the characterisation. Water was used as binder liquid which was delivered by a single flat spray nozzle. The spray pressure applied was 3.1 bar, which lead to an average drop diameter of 96 µm, a spray rate of 58 $\frac{\text{mL}}{\text{min}}$, and a spray zone width of 8 cm. A

relative standard deviation of the spatial drop distribution of 0.25 of the width of the spray zone can be derived from characterisation measurements for the spray nozzle and pressure applied [Wauters et al., 2002], and a nuclei-to-drop diameter ratio of 1.5 has been determined. The experiments are described in more detail by Litster et al. [2001, 2002] and Hapgood et al. [2004, 2009].

4.4 *Results and discussion*

The nuclei size distribution in the spray zone is simulated using MCS, and a selection of the results are illustrated in Figure 4.3. The MCS results show clearly the uniform distribution in the vertical direction and the normal distribution horizontally.

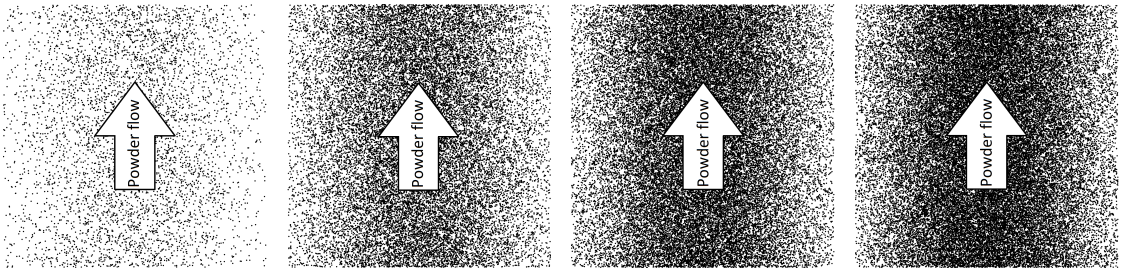

(a) $\Psi_n = 0.1$ (b) $\Psi_n = 0.5$ (c) $\Psi_n = 0.8$ (d) $\Psi_n = 1.0$

Figure 4.3: Surface area coverage in spray zone at different dimensionless nucleation number values from MCS data ($\sigma_x = 0.25$)

4.4.1 Log-normal distribution model

First, two parameter estimation studies are carried out to estimate parameter values for the log-normal distribution (LND) model (Eq. 4.6). Therefore, the model is fitted to the MCS results for each dimensionless nucleation number individually (1st parameter estimation; Eq. 4.3) and for all results simultaneously (2nd parameter estimation; Eq. 4.6). A comparison of the parameter values of both studies is shown in Figure 4.4. The results of the 1st parameter estimation show that the values estimated increase almost linearly with increasing dimensionless nucleation number. Furthermore, both parameter estimation studies result in very similar parameters for the dimensionless nucleation number range chosen. This confirms that both model parameters can be represented with linear

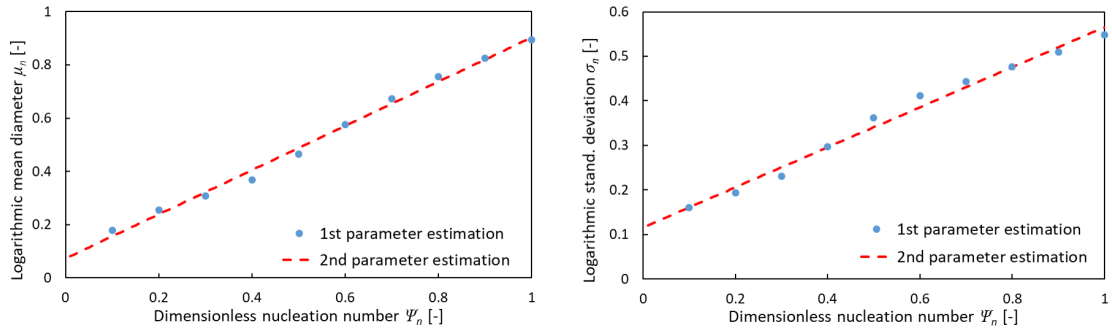

(a) Logarithmic mean diameter

(b) Logarithmic standard deviation of the diameter

Figure 4.4: Parameter values estimated in the 1st and 2nd parameter estimation using Eqs. 4.3 and 4.6 respectively, of the LND model ($\sigma_x = 0.25$)

functions of the dimensionless nucleation number only (Eqs. 4.4 and 4.5). The results of the parameter estimation are given including a 95 % confidence interval (using Eq. 4.6):

$$m_1 = -3.0 \pm 0.88 \tag{4.25}$$

$$m_2 = 1.9 \pm 0.18 \tag{4.26}$$

$$m_3 = -0.046 \pm 0.050 \tag{4.27}$$

$$s_1 = -3.4 \pm 0.87 \tag{4.28}$$

$$s_2 = 0.98 \pm 0.18 \tag{4.29}$$

$$s_3 = 0.32 \pm 0.024 \tag{4.30}$$

The Monte Carlo simulations (MCS) and the fitted LND model results are compared in Figure 4.5. The MCS data shows that most nuclei do not coalesce at a low dimensionless nucleation number, giving a very narrow size distribution. With increasing dimensionless nucleation number, more large nuclei are predicted. Due to the formation of more larger nuclei, a distribution with a long tail is predicted. However, the peak of the mass frequency remains at a very small nuclei diameter. The fitted LND model results agree very well with the MCS at low as well as high dimensionless nucleation number values. The narrow size distribution at a low dimensionless nucleation number is correctly represented as well as the long tail at a higher dimensionless nucleation number. This shows that the LND model is suitable for representing the MCS data for the dimensionless nucleation

number range chosen. The LND model can be applied to predict the nuclei size distribution for a wide range of conditions using the parameter values reported (Eqs. 4.25 to 4.30).

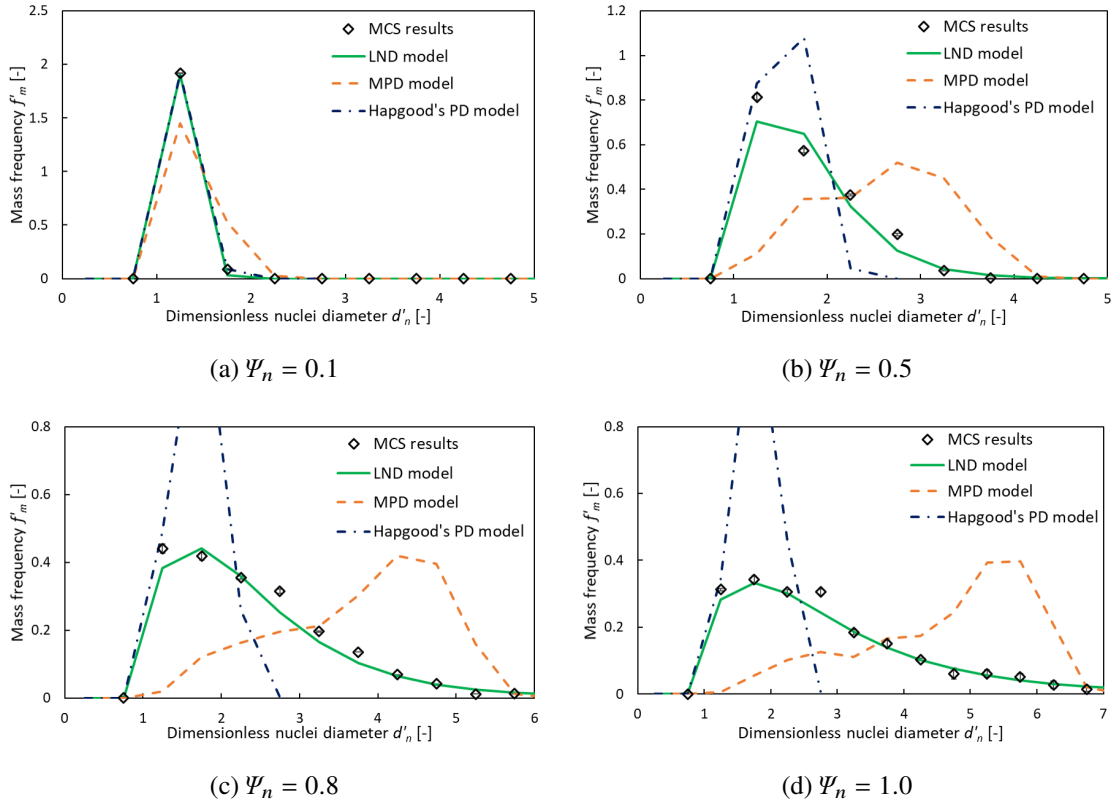

(a) $\Psi_n = 0.1$ (b) $\Psi_n = 0.5$

(c) $\Psi_n = 0.8$ (d) $\Psi_n = 1.0$

Figure 4.5: Comparison of the LND, MPD, and Hapgood's PD model results with MCS data ($\sigma_x = 0.25$)

4.4.2 Poisson distribution model

The nuclei exclusion area results determined using MCS are shown in Figure 4.6. The 95 % confidence interval of the MCS shows that the uncertainty of the results is an acceptable range. The results show that the power function fitted is in very good agreement with the simulation results. The parameters b and c of Eq. 4.18 are estimated, and the respective 95 % confidence intervals are determined:

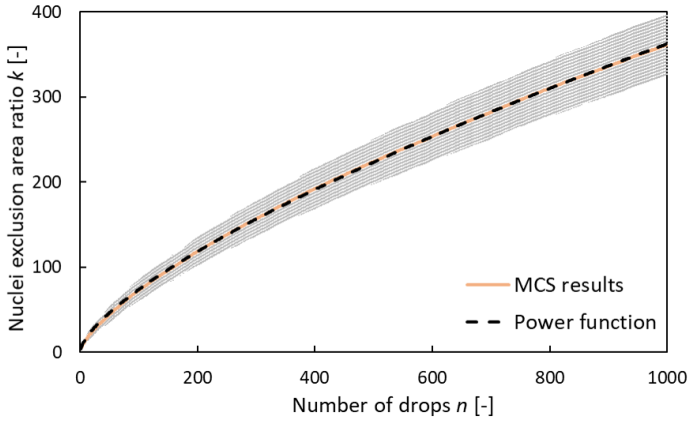

Figure 4.6: Average exclusion area ratio with a 95 % confidence interval from MCS data and the power function fitted

$$b = 2.70 \pm 0.01 \tag{4.31}$$

$$c = 0.708 \pm 0.001 \tag{4.32}$$

In Figure 4.5, the MPD model and Hapgood's PD model are compared to MCS data. The MCS data used for this comparison is not used to estimate model parameters of the MPD model, and Hapgood's PD model does not require any parameter estimation. Therefore, all model results compared to MCS data in this section are predictions. Hapgood's PD model predicts the nuclei size distribution for $\Psi_n = 0.1$ very accurately. Also, the mass frequency of small nuclei ($d'_n < 1.5$) is in very good agreement with the MCS data which corresponds with previous model assessment results [Hapgood et al., 2004]. As described in Section 4.2.2, only the area of larger nuclei is underpredicted but the area of very small nuclei is determined accurately. The fact that this model is capable of predicting specific MCS results shows the strength of this model; the MCS approach is very computationally expensive compared to Hapgood's PD model. However, the nuclei size distribution is clearly underpredicted outside the drop-nucleation regime because the formation of larger nuclei is not predicted (Figure 4.5b,c,d).

While the predictions of the MPD model agree reasonably well at lower dimensionless nucleation numbers, the discrepancy of the predictions becomes apparent at higher dimensionless nucleation numbers. Both the MCS and the MPD model predict the average nuclei size to increase; however, the

resulting distributions do not match. The MCS results show a much broader distribution at higher dimensionless nucleation numbers with a long tail of large nuclei while the peak of the distribution remains always at $d'_n \approx 1-2$. This is in contrast to the MPD model predictions which show a narrower nuclei size distribution and a large increase of the peak at higher dimensionless nucleation numbers. The MPD model does not contain an overlapping criterion like the MCS. It solely determines the likelihood of n nuclei/drops to land within the area $a_n(n)$ (average nuclei exclusion area formed by n drops). This can lead to an overprediction of larger nuclei since the drops that land in a_n do not necessarily overlap.

A quantitative comparison of the accuracy of the model predictions can be found in Figure 4.8. Hapgood's PD model underpredicts the nuclei size distribution outside the drop-controlled regime while the MPD model overpredicts the nuclei size distribution. Neither model captures the breadth of the nuclei size distributions at $\Psi_n \geq 0.5$.

4.4.3 Comparison of model predictions with experimental results

Both the semi-mechanistic MPD model and the empirical LND model are compared to experimental data from Litster et al. [2001, 2002] in order to assess the accuracy of the model results. Although these two models require parameter fitting, only MCS results are used for this purpose. The experimental data shown is only used to assess model predictions. The experiments selected are ex-granulator experiments as well as nucleation-only experiments in a high-shear mixer. The dimensionless nucleation number in these experiments ranges between 0.5 and 2.7.

The model predictions are compared to the experimental data in Figure 4.7. The experimental data shows a narrow distribution with a small average size at lower dimensionless nucleation numbers, which indicates that only few drops coalesced to agglomerates. However, a significantly broader bi-modal distribution is obtained at higher dimensionless nucleation numbers ($\Psi_n = 1.2, 2.7$), which confirms the speculation that drop coalescence on the powder bed surface can have a significant effect on the nuclei size distribution. Nevertheless, the (first) peak of the distribution remains at a low nuclei diameter, even at the highest nucleation number tested ($\Psi_n = 2.7$). A comparison between the two experimental techniques shows that the high-shear mixer experiments (Figure 4.7b,e,g) result in a slightly larger nuclei size distribution than the ex-granulator experiments (Figure 4.7a,d,f) even at the same dimensionless nucleation number Ψ_n. This potentially indicates nuclei growth during the high-shear mixer experiments, which is not considered by any of the models assessed.

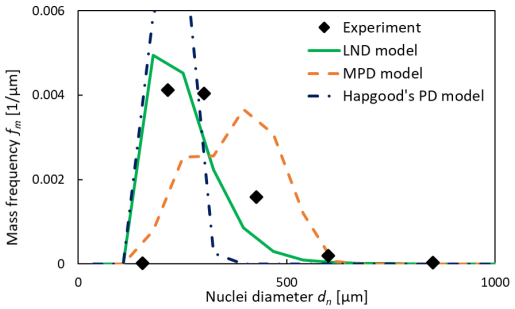

(a) Ex-granulator, $\Psi_n = 0.5$

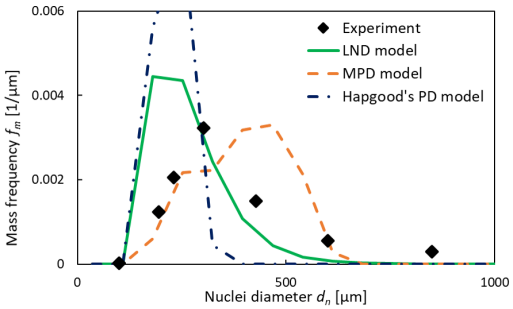

(b) High-shear mixer, $\Psi_n = 0.5$

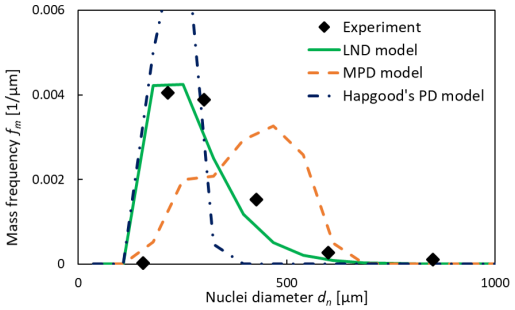

(c) Ex-granulator, $\Psi_n = 0.6$

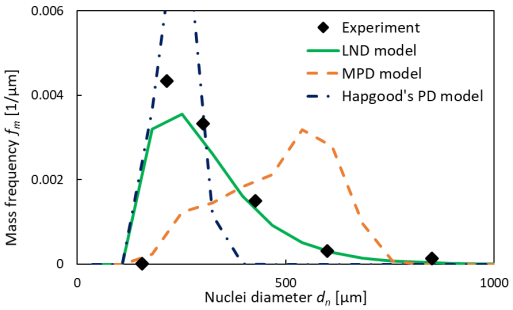

(d) Ex-granulator, $\Psi_n = 0.7$

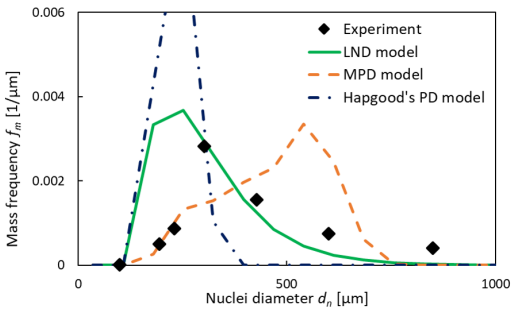

(e) High-shear mixer, $\Psi_n = 0.7$

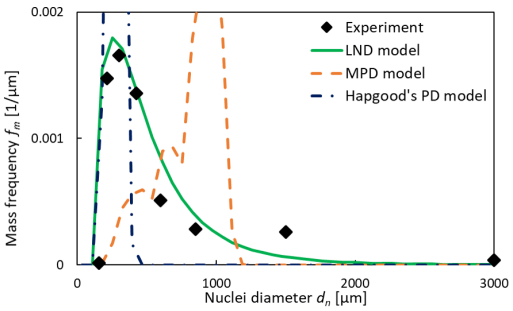

(f) Ex-granulator, $\Psi_n = 1.2$

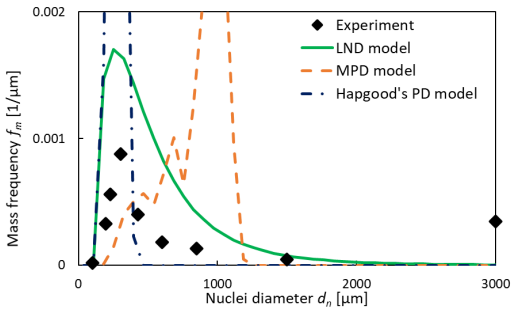

(g) High-shear mixer, $\Psi_n = 1.2$

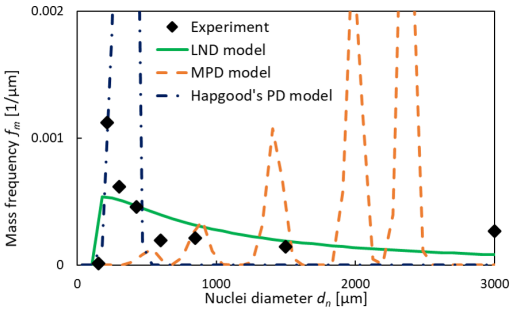

(h) Ex-granulator, $\Psi_n = 2.7$

Figure 4.7: Comparison of model results with experimental data

The MPD model predictions diverge from the experimental results. At lower dimensionless nucleation numbers, the experimental nuclei size distributions are slightly overpredicted; and with increasing dimensionless nucleation number, the MPD model predicts a shift of the peak to larger nuclei diameters rather than a significantly broader distribution. The LND model results are in good agreement with the experimental data at lower dimensionless nucleation numbers, which are within the empirical design space of this model ($\Psi_n \leq 1.0$). A comparison with experimental data outside the empirical design space shows a qualitative mismatch because bi-modal distributions are not predicted. Nevertheless, broad distributions are predicted which capture the experimental data reasonably well.

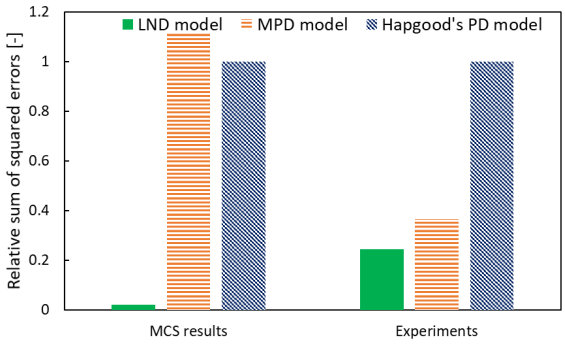

Figure 4.8: Sum of squared errors of the model results to MCS and experimental data (relative to Hapgood's PD model results)

The performance is also assessed quantitatively based on the sum of squared errors. This assessment is based on lumped results, Figures 4.5 and 4.7 provide the detailed results. The results show that the LND model provides the most accurate predictions out of all the models evaluated (Figure 4.8). Overall, the LND model agrees well with the experimental data, even though the experimental conditions were not fully characterised and reported. Therefore, the LND model can be applied to a wide range of wet granulation processes that operate under similar conditions. The fact that the LND model does not only agree with ex-granulator results but also with nucleation-only experiments in a high-shear mixer shows that this model can be applied to predict the nuclei size distribution in different wet granulation processes.

4.4.4 *Sensitivity analysis for the LND model*

A sensitivity analysis is conducted to gain more insight into the LND model results. The sensitivity analysis is based on Monte Carlo simulations (MCS) data which have been used to estimate the parameter values for the LND model. These MCS are based on assumptions about the spray characteristics which should capture experimental conditions well. In this sensitivity analysis, the effects of the spray characteristics on the results are studied, and the critical assumptions, which have to be validated experimentally, are identified. All MCS results shown are obtained applying the default settings with $\Psi_n = 1.0$ as described in Section 4.2.3 unless reported otherwise.

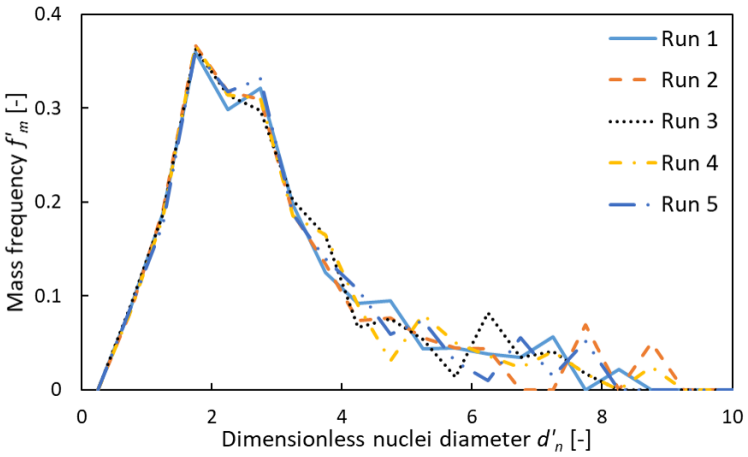

Figure 4.9: Assessment of repeatability based on 5 MCS with default settings

First, the repeatability of MCS is assessed. For this purpose, the results from 5 simulations are compared in Figure 4.9. A slight quantitative difference between the results can be noticed at large nuclei diameter. However, the uncertainty is rather low and the resulting distributions are qualitatively equivalent. Consequently, a qualitative assessment can be based on a sensitivity analysis without averaging MCS results.

A normal spatial drop distribution with a standard deviation σ_x of $\frac{1}{4}$ is applied in the MCS. In order to understand the impact of the spatial drop distribution on the nuclei size distribution, the standard deviation of the normal distribution is varied as shown in Figure 4.10. The results show that although the location of the (first) peak of the nuclei size distribution remains unchanged, a much broader or narrower nuclei size distribution can be observed when the spatial distribution varied. While a broader spatial distribution ($\sigma_x = \frac{1}{2}$) results in a very narrow nuclei size distribution with no

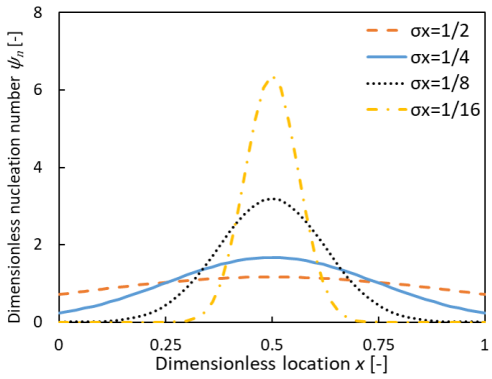

(a) Spatial drop distribution

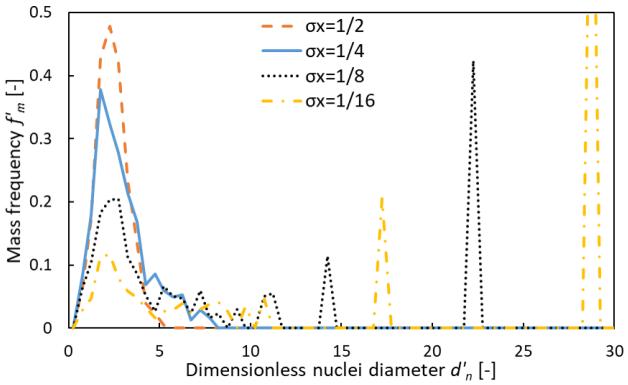

(b) Nuclei size distribution

Figure 4.10: Assessment of the impact of the spatial drop distribution on the nuclei size distribution (σ_x standard deviation of the normal distribution)

large nuclei, a very narrow spatial distribution ($\sigma_x = \frac{1}{8}; \frac{1}{16}$) generates a very broad spatial distribution with few very large nuclei. With $\sigma_x = \frac{1}{2}$, the distribution is almost uniform and the dimensionless nucleation number is similar across the whole spray zone. At $\sigma_x = \frac{1}{16}$, the dimensionless nucleation number is very high at the centre and very low at the edges, leading to a very broad nuclei size distribution. This shows that the spatial drop distribution has a significant impact and should, therefore, be well characterised for the nozzle system of interest.

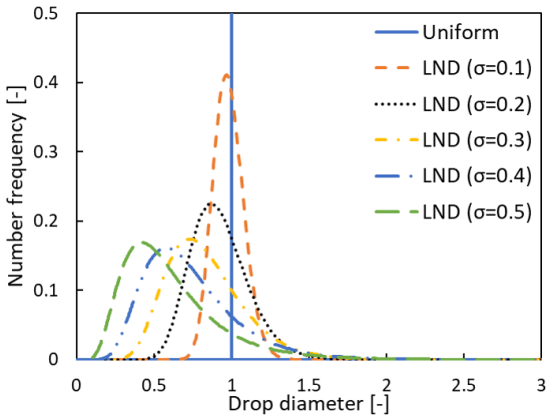

(a) Spray drop size distribution

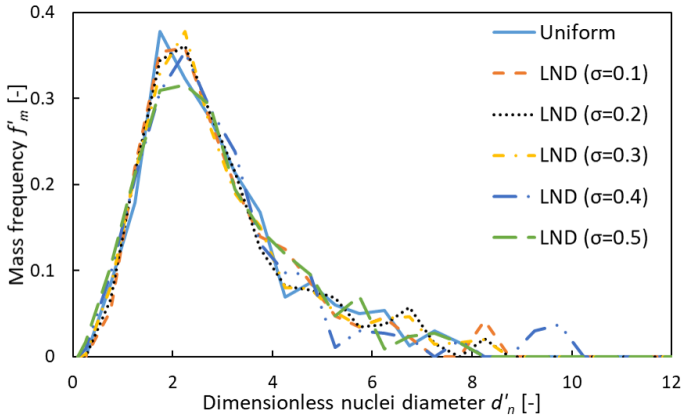

(b) Nuclei size distribution

Figure 4.11: Impact of the spray drop size distribution on the nuclei size distribution with a constant Sauter mean drop diameter (σ logarithmic standard deviation of drop size distribution)

The uniform drop size assumption is assessed by introducing a log-normal drop size distribution while maintaining a constant Sauter mean diameter (Figure 4.11). As the results show, the spray

drop size distribution has a very small impact on the nuclei size distribution, which is of the same of magnitude as the uncertainty (see Figure 4.9). Overall, it is concluded that a mono-modal drop size distribution can be assumed to be uniform for this purpose. However, only log-normal drop size distributions with a maximum logarithmic standard deviation σ of 0.5 have been tested in this sensitivity analysis. Even broader or multi-modal drop size distributions could have a significant impact on the nuclei size distribution.

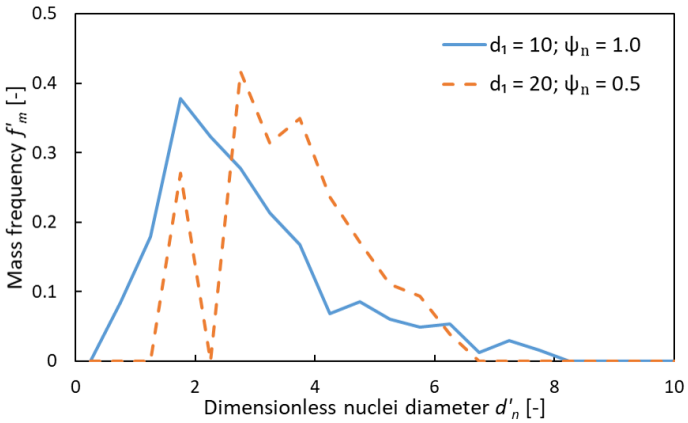

Figure 4.12: Assessment of mean drop size with a constant volumetric flowrate (d_1 single-drop nuclei diameter; Ψ_n dimensionless nucleation number)

The effect of increasing the mean drop diameter while keeping the volumetric flowrate constant is also tested (Figure 4.12). According to Eq. 2.6, the dimensionless nucleation number decreases as a result. As expected, the results show that an increase in drop diameter results in an increase of minimum nuclei size. However, due to the constant volumetric flowrate, the total cross-sectional area of drops (and consequently the dimensionless nucleation number) decreases which leads to less coalescence. The resulting nuclei size distribution is significantly narrower with less large lumps due to the drop diameter increase. This result shows that measuring the mean drop diameter is essential to predict the breadth of the nuclei size distribution.

The LND model with the parameter values reported (see Section 4.4.1) can be applied to any process if the MCS assumptions capture the spray characteristics well. In practice, deviations of the spatial drop distribution and the spray drop size distribution are expected. Considerable deviations from the MCS assumptions might require additional MCS data to re-estimate the parameters before the LND model can be applied.

4.4.5 Recommendations for nuclei models to use in PBM

Based on the results presented in this chapter, we recommend the LND model (Eqs. 4.4 to 4.6) for systems with any dimensionless spray flux from 0 to 5. The model parameters m_1, m_2, m_3, s_1, s_2, and s_3 are sensitive to spatial drop distribution and will need to be recalibrated with MCS from the values given in Eqs. 4.25 to 4.30 if the standard deviation of this distribution is distinctively outside the range used in this study (0.15 to 0.25). That aside, this is a simple, general and very robust model for incorporation in process level population balance models for high-shear, drum and fluid bed granulators that meet the criteria for immersion nucleation. The spray characteristics required as input for the model (spray geometry, spray drop size, and spatial drop distribution) are relatively easy to measure using standard techniques.

There is an implicit assumption in this model that drop immersion into the powder bed is fast ($\tau_p < 0.1$), and it can be assumed that the nuclei form instantaneously. This is common in practice where a low viscosity binder is used that wets the powder bed well. Where the binder liquid is more viscous or the powder is very fine, we may have a case where $\tau_p > 0.1$. The kinetics of the immersion process cannot be neglected, and powder will take a finite time to imbibe into the drop. This process can be modelled using the model of Hounslow et al. [2009] where the LND model can still be used to describe the drop size distribution that is the starting point for the immersion process. Additionally, a developed spray or drop atomisation is required for this approach, which can be challenging for very viscous liquids.

In some specialist applications such as detergent manufacture, where extremely viscous or semi-solid binders are used, binders cannot be atomised in a nozzle. For these cases, the LND model is not applicable. Instead, a breakage model for nuclei formation is needed to determine the initial binder "drop" distribution [Davis, 2016], and Hounslow's immersion model can still be used to account for the kinetics by which solid is embedded into the binder particle. Thus, we now have a suite of models that can be used to cover the full range of behaviours on Hapgood's regime map (Figure 4.13).

4.5 *Conclusions*

The LND model is able to represent MCS data very accurately at low and high dimensionless nucleation numbers. The model results are also in good agreement with experimental results, even at dimensionless nucleation numbers well above 1. While the MPD model gives acceptable predictions

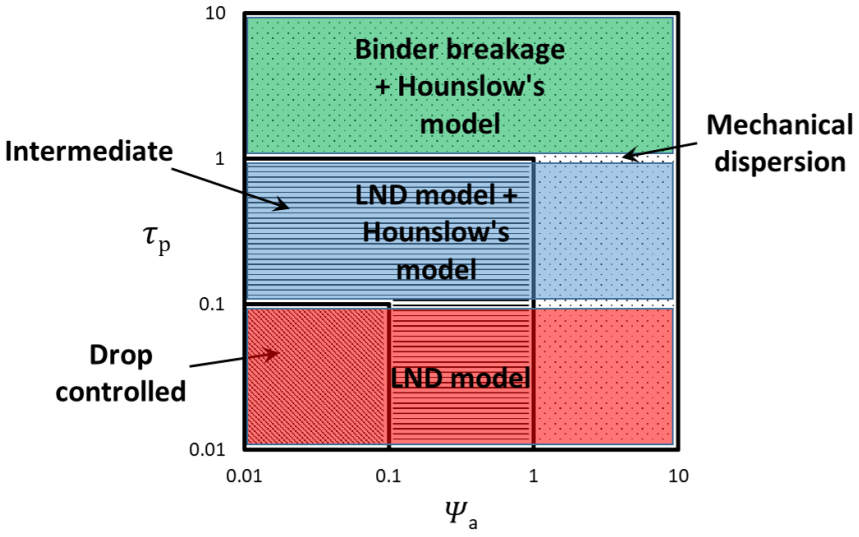

Figure 4.13: Choice of model for granule nucleation for the full nucleation regime map

at low dimensionless nucleation numbers, it fails to predict MCS and experimental data at high dimensionless nucleation numbers. Especially, the LND model is a significant improvement of the state of the art (Hapgood's PD model [Hapgood et al., 2009]), which underpredicts the nuclei size distribution significantly outside the drop-nucleation regime.

The LND model is suitable for determining the nuclei size distribution and can be easily applied for process modelling studies. A sensitivity analysis has shown that spray characteristics have a major impact on the nuclei size distribution. Especially, the spatial drop distribution in the spray needs to determined because the LND model requires it as an input parameter, and the MCS assumption about the drop size distribution needs to be validated experimentally before applying the LND model. A PD model could reduce the high computational effort that is required for MCS. Moreover, selected results are in very good agreement with MCS data. Nevertheless, a coalescence criterion that captures this mechanism well is required before the PD function can be applied for this purpose.

Chapter 5

HIGH-SHEAR WET GRANULATION MODELLING

5.1 *Introduction*

In this chapter, a high-shear wet granulation model is proposed, and all relevant modelling decisions and assumptions are explained. Experiments are designed to assess the most critical decisions and assumptions. The aim is to develop a predictive model that can be used within a model-driven design (MDD) framework.

5.2 *Model development*

The model is based on the population balance modelling (PBM) approach (see Section 2.3.1). In the following, the essential model components are described in detail including the kernels which have been chosen to mechanistically represent the major wet granulation rate processes. A review of wet granulation kernels that are available in the literature can be found in Section 2.1.

Table 5.1: Overview of model including key modelling equations and assumptions*

Rate process	Details
Population balance	1-D PBM: • Granule size as property of interest • Lumped parameter approach
Pore saturation	Liquid layer thickness: $\delta_l = \begin{cases} d\frac{\varepsilon(S-S_{crit})}{6} & \text{for } S \geq S_{crit} \\ 0 & \text{for } S < S_{crit} \end{cases}$ • Critical value needs to be reached to form surface liquid

Continued on next page

Table 5.1 – continued from previous page

Rate process	Details
Nucleation and wetting	Nuclei size distribution: $f_m = \frac{1}{d_n((s_1\sigma_x+s_2)\Psi_n+s_3)\sqrt{2\pi}} \exp\left(-\frac{\left(\ln\frac{d_n}{K_d d_d}-((m_1\sigma_x+m_2)\Psi_n+m_3)\right)^2}{2((s_1\sigma_x+s_2)\Psi_n+s_3)^2}\right)$ • LND model can predict the nuclei size distribution • Pore penetration is rapid
Consolidation	Consolidation rate: $\frac{\mathrm{d}\varepsilon}{\mathrm{d}t} = -k_{cons}(\varepsilon-\varepsilon_{min})n_{imp}\left[1-\exp(-St_{def})\right]$ • Endpoint porosity depends on L/S and tip speed
Layering	Layering rate: $\frac{\mathrm{d}v}{\mathrm{d}t} = \begin{cases} \frac{\delta_l}{\varepsilon S}\pi d^2 & \text{for } m_p > m_{p,crit} \text{ and } S > S_{crit} \\ \frac{\delta_l}{\varepsilon S}\pi d^2 \frac{m_p}{m_{p,crit}} & \text{for } m_{p,crit} > m_p > 0 \text{ and } S > S_{crit} \\ 0 & \text{for } m_p = 0 \text{ or } S \le S_{crit} \end{cases}$ • Layering is rapid • Occurs as long as powder particles and liquid layering are present
Coalescence	Coalescence rate: $\beta = v_{coll}\,(d_1+d_2)^2\sqrt{\frac{1}{d_1^3}+\frac{1}{d_2^3}}\left[10^{-k_I}\xi_I + 10^{-k_{II}}\,(1-\xi_I)\,\xi_{II}\right]$ • Collisions result in coalescence if kinetic energy is absorbed
Breakage	Breakage rate: $K_{br}\,(d) = k'_{br}\left[1-\exp\left(-f_{Mat}\,d\,\left(E_{m,kin}-E_{m,min}\right)\right)\right]$ • Only granules near the impeller tip can break • Effect of chopper is negligible (see Section 2.1.4)
Mixing	1-comp PBM: • Granulator is well-mixed 2-comp PBM: • Every compartment is well-mixed • Powder flow follows roping flow regime

*Definition of symbols is given in the nomenclature and in Section 5.2

5.2.1 Population balance modelling framework

A one-dimensional (1-D) PBM approach is used to track product properties. The most crucial property, granule diameter, is selected to be the property of interest and hence discretised into bins. All other properties are averaged. By applying the lumped parameter approach [Hounslow et al., 2001], the following properties are tracked and averaged over only one size bin to capture the size dependency: liquid volume and void volume. Other important properties are calculated from the properties that are tracked. An implied assumption of PBM is that the equipment is ideally mixed and conditions are homogeneous. To overcome this issue, compartmental modelling (CM) is applied.

In 1-D PBM for any well-mixed compartment, the particle size distribution (PSD) is determined by tracking the volume-specific number density of particles n for every size bin i over time t [Ramkrishna and Mahoney, 2002]:

$$\begin{aligned}\frac{\partial Vn(v,t)}{\partial t} + \frac{\partial}{\partial v}\left[Vn(v,t)\left(\dot{G}_{lay} + \dot{G}_{cons}\right)\right] &= \dot{V}_{in}n_{in}(v) - \dot{V}_{out}n(v) \\ &+V\left[\dot{b}_{nuc}(v) + \dot{b}_{coal}(v) + \dot{b}_{br}(v) - \dot{d}_{coal}(v) - \dot{d}_{br}(v)\right]\end{aligned} \tag{5.1}$$

where n is the volume-specific number density of particles, v is the particle volume, V is the control volume, $\dot{V}_{in}n_{in}$ and $\dot{V}_{out}n_{out}$ are the particle flowrates which are entering and leaving the control volume, $\dot{G}_{lay}$ and $\dot{G}_{cons}$ are the rate of change due to layering and consolidation respectively, $\dot{b}_{nuc}$, $\dot{b}_{coal}$ and $\dot{b}_{br}$ are the birth rates due to nucleation, coalescence and breakage, and $\dot{d}_{coal}$ and $\dot{d}_{br}$ are the death rates due to coalescence and breakage. Even though a batch system is modelled, the terms $\dot{V}_{in}n_{in}$ and $\dot{V}_{out}n_{out}$ are required for compartmental modelling (CM) because specific parts of the granulator are modelled as one control volume. The rates of change $\dot{G}$ are defined as:

$$\dot{G}_{cons} = v\left(\frac{\mathrm{d}\varepsilon}{\mathrm{d}t}\right)_{cons} \tag{5.2}$$

$$\dot{G}_{lay} = \left(\frac{\mathrm{d}v}{\mathrm{d}t}\right)_{lay} \tag{5.3}$$

where ε is the porosity. The birth $\dot{b}$ and death $\dot{d}$ rates are defined as:

$$\dot{b}_{nuc}\left(v_i\right) = \frac{\dot{V}_{nuc}}{K_d^3 V} f_n\left(v_i\right) \tag{5.4}$$

$$\dot{b}_{coal}\left(v_i\right) = \frac{1}{2}\int_0^v \beta\left(v_i, v_2\right) n\left(v\right) n\left(v_2\right)\ \mathrm{d}v_2 \tag{5.5}$$

$$\dot{b}_{br}\left(v_j\right) = \int_{v_j}^{\infty} b\left(v_i, v_j\right) K_{br}\left(v_i\right) n\left(v_i\right)\ \mathrm{d}v_i \tag{5.6}$$

$$\dot{d}_{coal}\left(v_1\right) = \int_0^{\infty} \beta\left(v_1, v_2\right) n\left(v_1\right) n\left(v_2\right)\ \mathrm{d}v_2 \tag{5.7}$$

$$\dot{d}_{br}\left(v_i\right) = K_{br}\left(v_i\right) n\left(v_i\right) \tag{5.8}$$

where $\dot{V}_{nuc}$ is the rate of liquid volume that forms nuclei, K_d is the nuclei-to-drop diameter ratio, i is the nucleated/coalesced/parent particle, 1 and 2 are colliding particles, j indicates daughter particles, and b is the discrete fragment size distribution. The volume of coalesced/mother particles v is equal to the sum of colliding/daughter particle volumes:

$$v_i = v_1 + v_2 \tag{5.9}$$

$$v_i = \sum_{j=1}^{n} v_j \tag{5.10}$$

where n is the number of daughter particles. All particles are assumed to be spherical:

$$v = \pi\frac{d^3}{6} \tag{5.11}$$

The discrete fragment size distribution b is defined as:

$$b\left(d_i, d_j\right) = \frac{\mathrm{d}B\left(d_i, d_j\right)}{\mathrm{d}d_j} \tag{5.12}$$

where B is the cumulative fragment size distribution.

The mass balance to determine the fine powder mass m_p is:

$$\frac{\mathrm{d}m_p}{\mathrm{d}t} = \rho_{bulk}\left(\dot{V}_{nuc}K_d^3 + \int_0^{\infty} Vn(v)\dot{G}_{lay}(v)\,\mathrm{d}v\right) \tag{5.13}$$

where ρ_{bulk} is the bulk density. An overall mass balance determines the total mass in each compartment M_{tot}:

$$\frac{\mathrm{d}M_{tot}}{\mathrm{d}t} = \int_0^\infty \frac{\mathrm{d}\left(m(v)\dot{V}n(v)\right)}{\mathrm{d}t}\,\mathrm{d}v = \int_0^\infty m(v)\left(\dot{V}_{in}n_{in}(v) - \dot{V}_{out}n(v)\right)\,\mathrm{d}v \tag{5.14}$$

5.2.2 *Pore saturation*

In wet granulation, it is important to understand the distribution of the liquid phase. Only liquid at the surface of the granule is available for granule growth. Pore saturation S is defined as the ratio of liquid to pore volume:

$$S = \frac{v_l}{v_p} \tag{5.15}$$

where v_l is the liquid volume and v_p is the pore volume. It is assumed that the liquid volume in the pores is limited, and above the critical pore saturation S_{crit}, any additional liquid will remain on the granule surface (Figure 5.1). Consequently, the pore volume v_p is calculated:

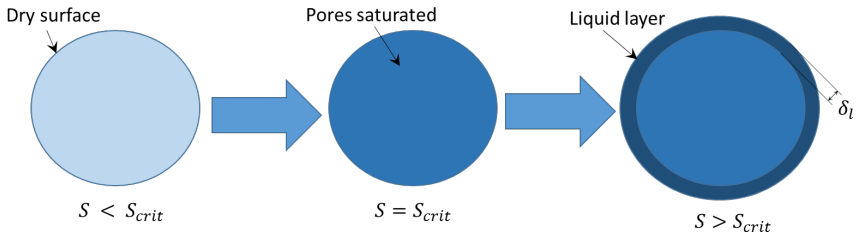

Figure 5.1: Formation of liquid layer

$$v_p = \varepsilon\left(v - v_{l,ext}\right) = \varepsilon\left(v_s + v_l + v_v - v_{l,ext}\right) \tag{5.16}$$

where v, v_s, v_l and v_v are the granule, solid, liquid and void volume respectively. The liquid volume on the granule surface $v_{l,ext}$ is calculated under the assumption that granules are spherical and much larger than the liquid layer ($d \gg \delta_l$):

$$v_{l,ext} = \pi d^2 \delta_l \tag{5.17}$$

The liquid layer thickness δ_l is determined [Liu et al., 2000]:

$$\delta_l = \begin{cases} d\frac{\varepsilon(S-S_{crit})}{6} & \text{for } S \geq S_{crit} \\ 0 & \text{for } S < S_{crit} \end{cases} \tag{5.18}$$

where d is the granule diameter and ε is the granule porosity.

5.2.3 Nucleation and wetting

When spray drops come in contact with fine powder that passes through the spray zone, nuclei are formed. For formulations with rapid drop penetration, nucleation kinetics can be neglected. However, overlapping and coalescence of drops in the spray zone can lead to a significant size increase [Hapgood et al., 2004]. This effect is included by applying the log-normal distribution (LND) model (see Chapter 4). Therefore, the dimensionless nucleation number Ψ_n is used to characterise the spray pattern and formation of nuclei [Wildeboer et al., 2005]:

$$\Psi_n = {K_d}^2 \frac{3\dot{V}}{2\dot{A}d_d} \tag{5.19}$$

where K_d is the nuclei-to-drop diameter ratio, $\dot{V}$ is the volumetric spray rate, $\dot{A}$ is the flux of the powder bed surface area through the spray zone, and d_d is the Sauter mean drop diameter. It is assumed that the powder velocity at the surface is similar to the average powder velocity to estimate the powder bed surface area flux $\dot{A}$ [Tran, 2015]:

$$\dot{A} = wv_{bed} = 2H_n \tan\left(\frac{\alpha}{2}\right) 0.15 v_t \tag{5.20}$$

where w is the width of the spray zone and v_{bed} is the bed velocity, α is the spray cone angle, H_n is the nozzle height, and v_t is the impeller tip speed.

The mass frequency f_m of the nuclei size distribution is predicted using:

$$f_m(d_n) = \frac{1}{d_n\left(\left(s_1\sigma_x + s_2\right)\Psi_n + s_3\right)\sqrt{2\pi}} \exp\left(-\frac{\left(\ln\frac{d_n}{K_d d_d} - \left(\left(m_1\sigma_x + m_2\right)\Psi_n + m_3\right)\right)^2}{2\left(\left(s_1\sigma_x + s_2\right)\Psi_n + s_3\right)^2}\right) \tag{5.21}$$

where d_n is the nuclei diameter, σ_x is the standard deviation of the spatial drop distribution in the spray, and $m_{1..3}$ and $s_{1..3}$ are empirical parameters. The conversion from number frequency f_n to mass frequency f_m, under the assumption of uniform nuclei mass density ρ_n:

$$f_m(d_n) = \frac{f_n(d_n)\, v(d_n)\, \rho_n}{\int f_n(d_n)\, v(d_n)\, \rho_n \, \mathrm{d}d_n} = \frac{f_n(d_n)\, v(d_n)}{\int f_n(d_n)\, v(d_n)\, \mathrm{d}d_n} \tag{5.22}$$

The liquid sprayed is distributed over all particles that pass through the spray zone. While drops that land on dry fine powder form nuclei, drops that land on granules are picked up by the granules. The additional liquid penetrates into the granule pores or remains on the surface, depending on pore saturation. Consequently, the liquid volume v_l increases, while the porosity is not affected. However, the granule void volume v_v is tracked rather than the porosity. Thus, an additional rate expression is required. If the pore saturation S is below its critical value S_{crit}, any liquid added penetrates into the pores and replaces void. As a result, the void volume decreases. If the critical pore saturation is reached, the additional liquid is assumed to remain on the granule surface, and the void volume remains constant. The effect of wetting at different pore saturations is illustrated in Figure 5.2. To represent this mathematically, a decision variable ξ_w is introduced:

$$\xi_w = \begin{cases} 1 & \text{for } S \geq S_{crit} \\ 0 & \text{for } S < S_{crit} \end{cases} \tag{5.23}$$

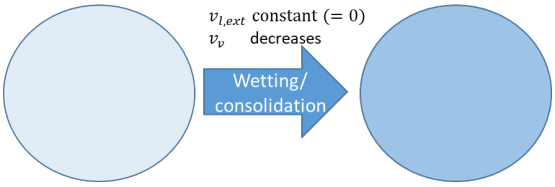

(a) Pore saturation $S < S_{crit}$

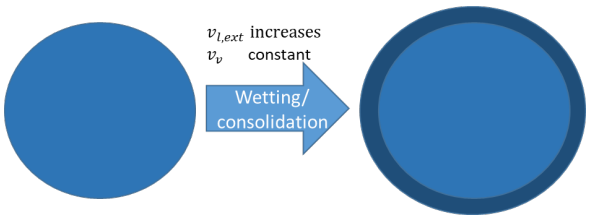

(b) Pore saturation $S \geq S_{crit}$

Figure 5.2: Effect of wetting (increase in v_l) or consolidation (decrease in ε) on granule properties (v_l liquid volume, ε porosity, $v_{l,ext}$ external liquid volume, v_v void volume)

Based on ξ_w, the void volume change rate $\frac{\mathrm{d}v_v}{\mathrm{d}t}$ is determined:

$$\left(\frac{\mathrm{d}v_v}{\mathrm{d}t}\right)_{wet} = -\left(1-\xi_w\right)\left(\frac{\mathrm{d}v_l}{\mathrm{d}t}\right)_{wet} \tag{5.24}$$

The rate of total liquid volume added to granules $\dot{V}_{wet}$ is:

$$\dot{V}_{wet} = \int_0^\infty Vn(v)\left(\frac{\mathrm{d}v_l}{\mathrm{d}t}\right)_{wet}\mathrm{d}v \tag{5.25}$$

where $n(v)$ is the volume-specific number density of particles. The fraction of drops that land on granules is estimated based on the fine powder mass fraction. Therefore, it is assumed that the particle distribution is uniform throughout the compartment. Consequently, the liquid balance is:

$$\dot{V}_{wet} = \dot{V} - \dot{V}_{nuc} = \dot{V}\left(1-\frac{m_p}{m_{p,0}}\right) \tag{5.26}$$

where $\dot{V}$ is the volumetric spray rate, $\dot{V}_{nuc}$ is the rate of liquid volume that forms nuclei, m_p is the fine powder mass present, and $m_{p,0}$ is the initial fine powder mass.

5.2.4 Consolidation

The consolidation rate is expressed as the rate at which the granule pore volume decreases. A decrease in pore volume v_p can have two different effects depending on the pore saturation (Eq. 5.27). If the critical pore saturation is not reached, void volume v_v is being removed during consolidation. However, when the pore saturation is above its critical value, v_v remains constant. In this case, a decrease in pore volume only leads to internal pore liquid being squeezed out of the pores and becoming external liquid. The effect of consolidation on the granule properties is illustrated in Figure 5.2. The decision variable ξ_w is used to determine if the critical pore saturation is reached.

$$\left(\frac{\mathrm{d}v_v}{\mathrm{d}t}\right)_{cons} = \left(1-\xi_w\right)v\left(\frac{\mathrm{d}\varepsilon}{\mathrm{d}t}\right)_{cons} \tag{5.27}$$

The decrease in granule porosity ε is determined by the consolidation kernel [Barrasso and Ramachandran, 2016]:

$$\left(\frac{\mathrm{d}\varepsilon}{\mathrm{d}t}\right)_{cons} = -k_{cons}(\varepsilon-\varepsilon_{min})n_{imp}\left[1-\exp(-St_{def})\right] \tag{5.28}$$

where k_{cons} is the (kinetic) consolidation coefficient, ε_{min} is the endpoint porosity for specific experimental conditions, n_{imp} is the impeller rate and St_{def} is the Stokes deformation number. ε_{min}

is difficult to predict a priori but is expected to be a function of L/S and impeller tip speed (see Section 2.1.2). Here, we use an empirical correlation which must be fitted to porosity data from lab-scale granulation experiments for the formulation of interest:

$$\varepsilon_{min} = \begin{cases} 0.6 & \text{for } \varepsilon'_{min} > 0.6 \\ \varepsilon'_{min} & \text{for } 0.6 > \varepsilon'_{min} > 0.3 \\ 0.3 & \text{for } 0.3 > \varepsilon'_{min} \end{cases} \tag{5.29}$$

and

$$\varepsilon'_{min} = e_1 v_t \frac{\mathrm{s}}{\mathrm{m}} (e_2 - L/S) + e_3 \tag{5.30}$$

where ε'_{min} is an auxiliary variable, v_t is the impeller tip speed, L/S is the liquid-to-solid ratio, and $e_{1..3}$ are empirical parameters. In the empirical correlation, the units $\frac{\mathrm{s}}{\mathrm{m}}$ are needed for dimensional consistency because a dimensional parameter v_t is used to characterise impact forces instead of the dimensionless group St_{def}. In contrast to Barrasso and Ramachandran [2016], an endpoint porosity ε_{min} that depends on the operating conditions is considered (Eq. 5.30). The Stokes deformation number St_{def} and dimensionless strength Str^* are defined as:

$$St_{def} = \frac{\rho_{env} v_{coll}^2}{2Y_d} \tag{5.31}$$

and

$$Str^* = \frac{Y_d d_p}{\gamma^{lv} \cos\theta} \tag{5.32}$$

where ρ_{env} is the envelope density, Y_d is the dynamic tensile strength, d_p is the primary particle diameter, γ^{lv} is the surface tension, and θ is the dynamic contact angle. The collision velocity v_{coll} and dimensionless strength Str^* are estimates using correlations from the literature [Tran, 2015; Smith, 2007]:

$$v_{coll} = 0.15 v_t = 0.15 \pi n_{imp} D_{imp} \tag{5.33}$$

$$Str^* = A + BCa^n \tag{5.34}$$

where A, B and n are empirical parameters. The capillary number Ca is defined as:

$$Ca = \frac{\mu v_{coll}}{\gamma^{lv} \cos\theta} \frac{d_p}{d} \tag{5.35}$$

where μ is the binder viscosity and d is the mean granule diameter.

5.2.5 *Layering*

It is assumed that as long as fine powder is present, surface-wet granules grow by layering [Sayin, 2016; Barrasso and Ramachandran, 2016]. The mechanism is illustrated in Figure 5.3. Furthermore, layering is assumed to be a rapid rate process for hydrophilic powders. The layering rate is consequently considered to be proportional to the liquid layer thickness δ_l. The new layer is assumed to have the same pore saturation S and porosity ε as the granule. The increase in granule volume v is determined accordingly:

$$\left(\frac{\mathrm{d}v}{\mathrm{d}t}\right)_{lay} = \begin{cases} \frac{\delta_l}{\varepsilon S}\pi d^2 & \text{for } m_p > m_{p,crit} \text{ and } S > S_{crit} \\ \frac{\delta_l}{\varepsilon S}\pi d^2 \frac{m_p}{m_{p,crit}} & \text{for } m_{p,crit} > m_p > 0 \text{ and } S > S_{crit} \\ 0 & \text{for } m_p = 0 \text{ or } S \leq S_{crit} \end{cases} \tag{5.36}$$

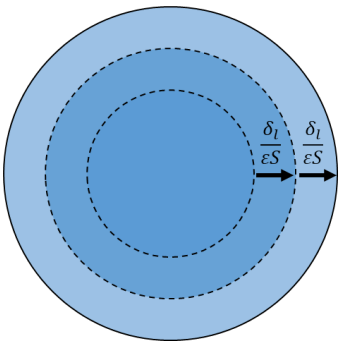

Figure 5.3: Layering ($\frac{\delta_l}{\varepsilon S}$ is the diameter increase through layering per unit time)

where δ_l is the liquid layer thickness, S is the pore saturation, d is the granule diameter, m_p is the mass of fine powder, $m_{p,crit}$ is the critical mass of fine powder, and S_{crit} is the critical pore saturation. In contrast to Sayin [2016] and Barrasso and Ramachandran [2016], it is assumed that the mass of fine powder does not affect the layering rate if it is above a critical value. Below this critical value, a linear function represents the dependency on the remaining mass of fine powder. The critical value $m_{p,crit}$ is assumed to be 10 % of the initial fine powder mass $m_{p,0}$.

5.2.6 Coalescence

The coalescence kernel proposed and extended by Liu et al. [2000]; Liu and Litster [2002]; Pohlman and Litster [2015] is used. The concept of this kernel is that a collision between two granules needs to have exactly one of the three following outcomes: coalescence without deformation (Type I), coalescence with deformation (Type II), or rebound. As a consequence, the rate of coalescence β is:

$$\beta = \begin{cases} \beta_I & \text{for coalescence without deformation} \\ \beta_{II} & \text{for coalescence with deformation} \\ 0 & \text{for rebound} \end{cases} \tag{5.37}$$

In order to characterise the granule collision, the reduced mass $\tilde{m}$ and diameter $\tilde{d}$, average liquid layer thickness $\bar{\delta}_l$, reduced viscous Stokes number $\tilde{St}_v$, reduced Stokes deformation number $\tilde{St}_{def}$, reduced Young's modulus $\tilde{E}$, and reduced dynamic yield strength $\tilde{Y}_d$ are defined for the two colliding granules 1 and 2:

$$\tilde{m} = \frac{m_1 m_2}{m_1 + m_2} \tag{5.38}$$

$$\tilde{d} = \frac{d_1 d_2}{d_1 + d_2} \tag{5.39}$$

$$\bar{\delta}_l = \frac{\delta_{l,1} + \delta_{l,2}}{2} \tag{5.40}$$

$$\tilde{St}_v = \frac{8\tilde{m} v_{coll}}{3\pi\mu\tilde{d}^2} \tag{5.41}$$

$$\tilde{St}_{def} = \frac{\tilde{m} v_{coll}^2}{2\tilde{d}^3 \tilde{Y}_d} \tag{5.42}$$

$$\tilde{E} = \frac{1}{\frac{(1-\nu^2)}{E_1} + \frac{(1-\nu^2)}{E_2}} = \frac{E_1 E_2}{(1-\nu^2)(E_1 + E_2)} \tag{5.43}$$

$$\tilde{Y}_d = \frac{Y_{d,1} Y_{d,2}}{Y_{d,1} + Y_{d,2}} \tag{5.44}$$

where ν is Poisson's ratio. The dimensionless Young's modulus E^* is defined as:

$$E^* = \frac{E d_p}{\gamma^{lv} \cos\theta} \tag{5.45}$$

and an empirical correlation is applied [Pohlman and Litster, 2015]:

$$E^* = k_E Ca^{p_E} \varepsilon^{q_E} S^{r_E} \tag{5.46}$$

where k_E, p_E, q_E and r_E are empirical parameters.

The Stokes criterion [Ennis et al., 1991] is applied to predict coalescence without deformation (Type I):

$$\tilde{St}_v < \ln\left(\frac{\bar{\delta}_l}{h_a}\right) \tag{5.47}$$

where h_a is the height of asperities. Additionally, contact mechanics principles for elastic-plastic solids are considered to account for the absorption of impact energy by deformation [Johnson, 1985]. Coalescence with deformation (Type II) is predicted if:

$$T_A < T_B \tag{5.48}$$

with

$$T_A = \left(\frac{\tilde{Y}_d}{\tilde{E}}\right)^{\frac{1}{2}} \left(\tilde{St}_{def}\right)^{-\frac{9}{8}} \tag{5.49}$$

$$\begin{aligned} T_B = \frac{0.172}{\tilde{St}_v} \left(\frac{\tilde{d}}{\bar{\delta}_l}\right)^2 \left[1 - \frac{1}{\tilde{St}_v} \ln\left(\frac{\bar{\delta}_l}{h_a}\right)\right]^{\frac{5}{4}} \left[\left(\frac{\bar{\delta}_l^2}{h_a^2} - 1\right) + \frac{2\bar{\delta}_l}{\delta''}\left(\frac{\bar{\delta}_l}{h_a} - 1\right)\right. \\ \left. + \frac{2\bar{\delta}_l^2}{(\delta'')^2} \ln\left(\frac{\bar{\delta}_l}{h_a}\right)\right] \left[1 - 7.36\frac{\tilde{Y}_d}{\tilde{E}} \left(\tilde{St}_{def}\right)^{-\frac{1}{4}} \left(1 - \frac{1}{\tilde{St}_v} \ln\left(\frac{\bar{\delta}_l}{h_a}\right)\right)^{-\frac{1}{2}}\right]^2 \end{aligned} \tag{5.50}$$

where T_A and T_B are auxiliary terms. The plastic deformation δ'' is determined:

$$\delta'' = \left(\frac{8}{3\pi}\right)^{\frac{1}{2}} \tilde{d} \left(\tilde{St}_{def}\right)^{\frac{1}{2}} \left[1 - \frac{1}{\tilde{St}_v} \ln\left(\frac{\bar{\delta}_l}{h_a}\right)\right] \left[1 - 7.36\frac{\tilde{Y}_d}{\tilde{E}} \left(\tilde{St}_{def}\right)^{-\frac{1}{4}} \left(1 - \frac{1}{\tilde{St}_v} \ln\left(\frac{\bar{\delta}_l}{h_a}\right)\right)^{-\frac{1}{2}}\right] \tag{5.51}$$

Two decision variables are introduced to determine the collision scenario:

$$\xi_I = \begin{cases} 1 & \text{for coalescence Type I} \\ 0 & \text{for Coalescence Type II or rebound} \end{cases} \tag{5.52}$$

$$\xi_{II} = \begin{cases} 1 & \text{for coalescence Type II} \\ 0 & \text{for rebound} \end{cases} \tag{5.53}$$

A function for the coalescence rate is derived from Eqs. 5.37, 5.52 and 5.53:

$$\beta = \left[\beta_I \xi_I + \beta_{II} \left(1 - \xi_I\right) \xi_{II}\right] \tag{5.54}$$

The equipartition of kinetic energy (EKE) kernel [Hounslow et al., 2001] is applied to provide estimates for the collision rates β_I and β_{II}:

$$\beta_{I/II} = 10^{-k_{I/II}} v_{coll} \left(d_1 + d_2\right)^2 \sqrt{\frac{1}{d_1^3} + \frac{1}{d_2^3}} \tag{5.55}$$

where k_I and k_{II} are collision coefficients. Combining Eqs. 5.54 and 5.55:

$$\beta\left(d_1, d_2\right) = v_{coll} \left(d_1 + d_2\right)^2 \sqrt{\frac{1}{d_1^3} + \frac{1}{d_2^3}} \left[10^{-k_I} \xi_I + 10^{-k_{II}} \left(1 - \xi_I\right) \xi_{II}\right] \tag{5.56}$$

It is assumed that the collision rate is independent of the type of coalescence:

$$k_{I/II} = k_I = k_{II} \tag{5.57}$$

5.2.7 Breakage

The kernel selected to determine the breakage rate K_{break} is proposed by Vogel and Peukert [2005] and Capece et al. [2014b]:

$$K_{br} = k'_{br} \left[1 - \exp\left(-f_{Mat} d \left(E_{m,kin} - E_{m,min}\right)\right)\right] \tag{5.58}$$

with

$$E_{m,min} d = 0.3 \, \frac{\mathrm{J\,m}}{\mathrm{kg}} \tag{5.59}$$

where k'_{br} is a breakage rate variable, f_{Mat} is the mass-based material strength parameter, d is the granule diameter, $E_{m,kin}$ is the mass-specific impact energy, and $E_{m,min}$ is the mass-specific threshold energy. For 1-comp PBM, it is assumed that the circulation time is proportional to the impeller rate n_{imp}. In 2-comp PBM, breakage is assumed to occur in the entire breakage compartment. k'_{br} is consequently defined as:

$$k'_{br} = \begin{cases} k_{br} n_{imp} & \text{for 1-comp PBM} \\ \frac{k_{br}}{\mathrm{s}} & \text{for 2-comp PBM} \end{cases} \tag{5.60}$$

where k_{br} is the breakage coefficient.

The cumulative fragment size distribution $B(i, j)$ with parent particle i and daughter particles j described in the following Vogel and Peukert [2005]:

$$B(d_i, d_j) = \left(\frac{d_i}{d_j}\right)^q \frac{1}{2}\left[1 + \tanh\left(\frac{d_j - d_{j,min}}{d_{j,min}}\right)\right] \tag{5.61}$$

where d_i is the parent particle diameter, d_j is the daughter particle diameter, q is the power law exponent, $d_{j,min}$ is the minimum fragment diameter.

5.2.8 Compartmental modelling

Breakage commonly just occurs in a small zone of the granulator. In one-compartment (1-comp) PBM, this phenomenon is captured by using the circulation time as a measure for the residence time outside the breakage zone, and this circulation time is assumed to be proportional to the impeller rate n_{imp}. Alternatively, a 2-comp model is developed based on compartmental modelling (CM). The 2-comp model consists of a bulk compartment and a breakage compartment (Figure 5.4). To predict the powder flow between compartments, an operation in the roping flow regime is assumed because this regime is favourable for the operation of high-shear mixers [Tran, 2015]. It is assumed that breakage mainly occurs in the area of the impeller tip, and all other mechanisms only occur in the bulk compartment. The length of the impeller tip L_t is assumed to be 5 % of the impeller diameter D_{imp}. The breakage compartment volume V_{br} is determined:

$$V_{br} = \pi D_{imp} H_{imp} L_t = 0.05 \pi D_{imp}^2 H_{imp} \tag{5.62}$$

where H_{imp} is the impeller height. In order to determine the residence time τ_{br}, all particles are assumed to pass the entire length of the impeller tip L_t to represent roping flow [Tran, 2015]:

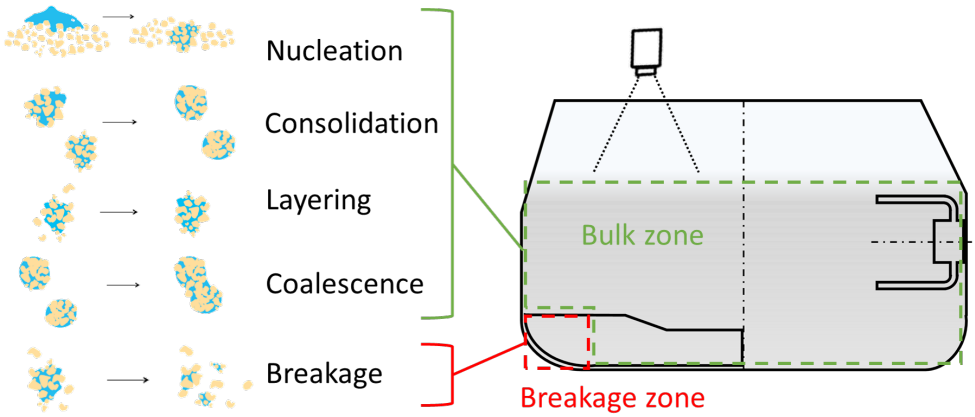

Figure 5.4: 2-comp PBM approach

$$\tau_{br} = \frac{L_t}{v_b} = \frac{L_t}{0.15 v_t} \tag{5.63}$$

The remaining powder is in the bulk compartment. Its volume V_{bulk} can be determined:

$$V_{bulk} = V_{bed} - V_{br} = \phi_f V - V_{br} \tag{5.64}$$

where V_{bed} is the bed volume, ϕ_f is the fill level, and V is the granulator volume. The residence time in the bulk compartment τ_{bulk} is determined assuming constant powder flow rates:

$$\tau_{bulk} = \tau_{br} \frac{V_{bulk}}{V_{br}} \tag{5.65}$$

The outlet flowrate $\dot{V}_{out} n$ of a well-mixed compartment is:

$$\dot{V}_{out} = \frac{V}{\tau} \tag{5.66}$$

5.3 *Solution method*

All simulations are run in gPROMS FormulatedProducts v1.5 (Process Systems Enterprise Ltd). The model is based on the gPROMS FormulatedProducts high-shear granulation library model, that is commercially available. The standard gPROMS solver for differential-algebraic equations DAEBDF is used to numerically solve the equation system. The finite volume method (FVM) is used to include the production rate processes (nucleation, coalescence and breakage). The transport rate

processes (consolidation and layering) are included by applying the finite difference method (FDM). Both solution techniques are described in more in detail in Section 2.3.1.

For the implementation of the model, certain submodels are readily available in gPROMS, others needed to be included, partially by modifying existing code. An overview of all submodels is given in Table 5.2. Since the library model can be operated in a continuous mode, the 2-comp PBM approach is implemented by creating a flowsheet with interconnected models (see Appendix C.1).

Table 5.2: Overview of submodels

Submodel	Origin	Implementation
Population balance	Ramkrishna and Mahoney [2002]; Hounslow et al. [2001]	Available in gPROMS
Pore Saturation	Liu et al. [2000]	Modification
Nucleation and wetting	Barrasso and Ramachandran [2016]	Available in gPROMS
Nuclei size distribution	See Chapter 4	Own implementation
Consolidation	Barrasso and Ramachandran [2016]	Own implementation
Layering	Sayin [2016]; Barrasso and Ramachandran [2016]	Own implementation
Coalescence	Liu et al. [2000]; Liu and Litster [2002]; Pohlman and Litster [2015]; Hounslow et al. [2001]	Own implementation
Breakage	Vogel and Peukert [2005]; Capece et al. [2014b]	Available in gPROMS
Compartmental modelling	Tran [2015]	Own implementation

A logarithmic grid is chosen with 10 bins for the granule size distribution (45 µm-7000 µm) and 5 bins for the primary powder size distribution (45 µm-355 µm). The PSD is determined using the gPROMS FormulatedProducts sieve analysis library model, and the discretisation is identical to that used for sieve analysis (see Section 3.3.3). This explained in more detail in Appendix C.1. Flowsheets for the 1-comp and 2-comp PBM approach are displayed in Figure 5.5.

A numerically robust model is required to reliably run the simulation. In order to improve the robustness of the model, discontinuities during the simulation should be avoided. Piecewise functions are known to cause discontinuities, which can lead to long computational times and failures. That

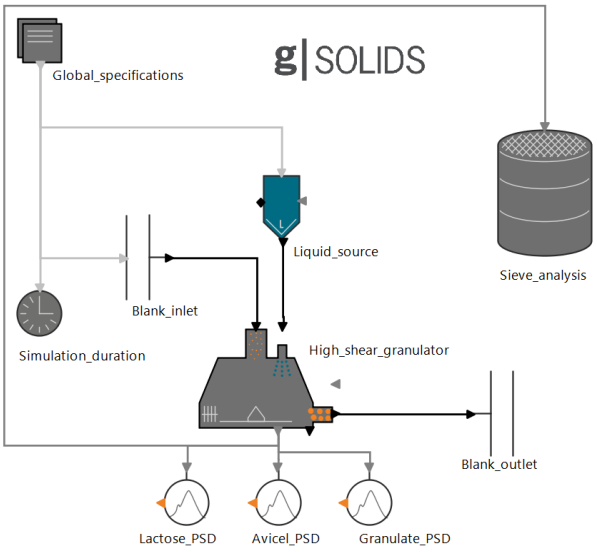

(a) 1-comp PBM approach

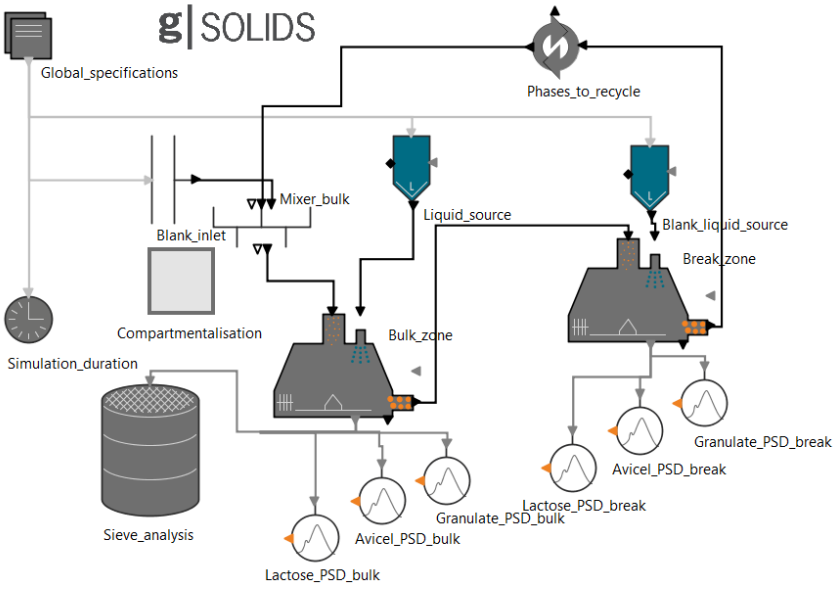

(b) 2-comp PBM approach

Figure 5.5: gPROMS flowsheets

is why, piecewise functions are implemented using a continuous trigonometric approximation. To determine the presence of surface liquid, a decision variable ξ_w is introduced (Eqs 5.23, 5.24 and 5.27). ξ_w should be ≈ 0 for $S < S_{crit}$ and ≈ 1 for $S > S_{crit}$. This is achieved using a trigonometric approximation:

$$\xi_w = \frac{1}{2} + \frac{1}{2} \tanh\left[c\left(S - S_{crit}\right)\right] \tag{5.67}$$

where c is a constant.

A comparison between approximation and target is displayed in Figure 5.6. The approximation represents the piecewise function well and is sufficient for this purpose, as the approximation only deviates slightly from the piecewise function for $S \approx S_{crit}$.

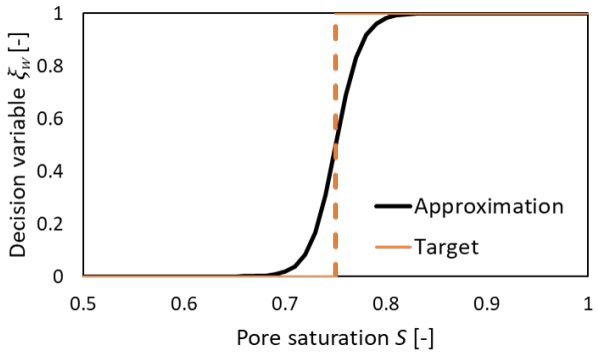

Figure 5.6: A hyperbolic tangent approximation for $S_{crit} = 0.75$ and $c = 40$

In order to determine δ_l (Eq 5.18) with continuous functions, an auxiliary variable δ_l' is introduced:

$$\delta_l' = d\frac{\varepsilon\left(S - S_{crit}\right)}{6} \tag{5.68}$$

An approximation is used to convert δ_l' values ≤ 0 into negligibly small positive values while representing positive values with very high precision (see Appendix D.5):

$$\frac{\delta_l}{\mu\text{m}} = \frac{10^{-5} + 10^6 \frac{\delta_l'}{\mu\text{m}} + \sqrt{\left(10^{-5} - 10^6 \frac{\delta_l'}{\mu\text{m}}\right)^2 + \left(10^{-5}\right)^2}}{2 \times 10^6} \tag{5.69}$$

By introducing two decision variables ξ_m and $\xi_{m,crit}$, a continuous function for layering rate (Eq. 5.36) is derived:

$$\left(\frac{\mathrm{d}v}{\mathrm{d}t}\right)_{lay} = \frac{\delta_l}{\varepsilon S}\pi d^2 \xi_w \xi_m \left(1 - \xi_{m,crit} + \xi_{m,crit}\frac{m_p}{m_{p,crit}}\right) \tag{5.70}$$

with

$$\xi_m = \frac{1}{2} + \frac{1}{2}\tanh\left[c\left(\frac{m_p}{m_{p,0}} - 10^{-3}\right)\right] \tag{5.71}$$

and

$$\xi_{m,crit} = \frac{1}{2} + \frac{1}{2}\tanh\left[c\left(\frac{m_{p,crit} - m_p}{m_{p,0}}\right)\right] \tag{5.72}$$

Trigonometric approximations are also applied to generate continuous function for the decision variables ξ_I and ξ_{II} (Eqs. 5.52 and 5.53):

$$\xi_I = \frac{1}{2} + \frac{1}{2}\tanh\left[c\left(\ln\left(\frac{\bar{\delta}_l}{h_a}\right) - \tilde{S}t_v\right)\right] \tag{5.73}$$

$$\xi_{II} = \frac{1}{2} + \frac{1}{2}\tanh\left[c\left(T_B - T_A\right)\right] \tag{5.74}$$

Additionally, divisions are avoided by rearranging equations, as very small values in the denominator can lead to large errors (e.g. in Eqs 5.38 to 5.43). This is shown with the aid of a generic example, with the minimum of $|A_3|$ being ≈ 0:

$$A_1 = \frac{A_2}{A_3} \tag{5.75}$$

where $A_{1..3}$ are terms. Eq 5.75 is transformed to:

$$A_1 A_3 = A_2 \tag{5.76}$$

5.4 *Methodology for model verification*

To verify the model, critical model assumptions are assessed using a range of experimental methods, as well as mechanistic understanding and model sensitivity analyses. An overview of the model verification methods is given in Table 5.3.

Table 5.3: Methodology to assess critical model assumptions

Model assumption	Method
Rapid drop penetration	Estimation of drop penetration time (see Appendix B.2)
LND model predictions	Nucleation-only experiments (see Section 6.3.4)
Breakage	Breakage-only experiments (see Section 6.3.7)
Role of chopper	Experiments with and without chopper (see Section 6.3.7)
Number of grid points	Sensitivity analysis 5.5
Mixing	Assessment of 1-comp and 2-comp PBM (see Section 7.3.3)

To evaluate the number of grid points, the grid is refined and coarsened by varying the number of grid points between 5-20. Computational time and model precision of the 1-comp PBM approach are used for this assessment, and the precision p_j is based on the relative deviation of the PSD to the simulation results generated using 40 grid points:

$$p_j = 1 - \left(\frac{w_{i,j} - w_{i,40}}{w_{i,40}} \right)^2 \tag{5.77}$$

where $w_{i,j}$ is the mass fraction on sieve i with j PBM grid points.

5.5 *Model verification*

The effect of the number of grid points on the computational time and model precision is shown in Figure 5.7. On one hand, the computational time increases significantly with an increasing number of grid points, but on the other hand, the model precision improves. Especially the coarse grid with 5 grid points resulted in an intolerable precision of roughly 50 % without speeding up the simulation greatly and refining the grid from 10 to 15 grid points nearly triples the computational time without improving the precision considerably. For comparison, a simulation with 40 grid points takes almost 5 h. In conclusion, a trade-off has to be made to determine the optimum number of grid points, and with 10 grid points, an acceptable computational time is achieved and the precision is with 99 % sufficient for the purpose.

Figure 5.8 shows important model outputs of a 1-comp PBM simulation (input parameters are listed in Appendix C.2). The dry powder mass fraction $m_p/m_{p,0}$ starts at 1 and then decreases

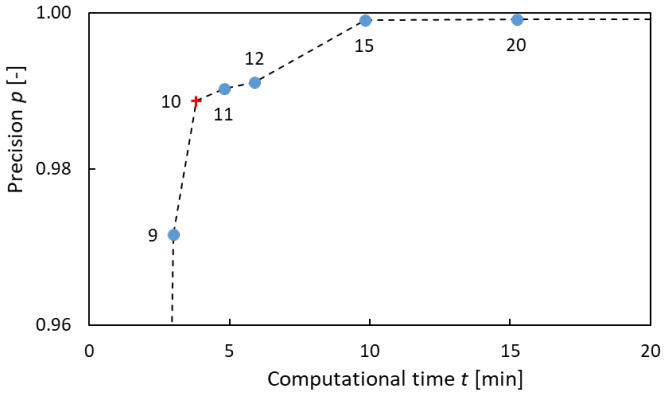

Figure 5.7: Computational time and model precision with different grid points (data labels)

continuously until it reaches 0. This result is consistent with the model assumptions because the granulator only contains dry powder initially, which is consumed by nucleation and layering as long as it is present during the experiment. The granule porosity ε starts at high value of above 0.6 because only a few porous nuclei have formed after the spraying phase started. Subsequently, the porosity decreases to 0.6, which is the lowest possible porosity ε_{min} at low liquid-to-solid ratio L/S ($< e_2$). Towards the end of the spraying phase, another decrease in porosity is observed. The continuous liquid addition leads to an increase in L/S and eventually ε_{min} below 0.6. In the kneading phase, no liquid is added, and ε_{min} remains constant. When the porosity approaches ε_{min}, consolidation slows down. This porosity trajectory qualitatively agrees with a postulate by Maxim et al. [2004]. Initially, the mass-median diameter D_{50} is equal to the D_{50} of dry powder ($\approx 100\,\mu m$). Due to the formation of granules, the D_{50} slowly increases. Due to consolidation, granules reach the critical pore saturation S_{crit}, and liquid cumulates on the granule surface. This phenomenon enhances size increase because it leads to granule growth by layering. Coalescence does not occur while large amounts of dry powder are still present because coalescence requires more surface liquid than layering and layering is assumed to be rapid. As soon as the dry powder is consumed, layering stops. Due to consolidation and further liquid addition, the amount of surface liquid increases rapidly. This increases eventually leads to coalescence, which results in the rapid size increase. The D_{50} levels off towards the end of the experiment. An increase in granule size leads to a significant increase in breakage. A constant size represents an equilibrium between coalescence and breakage.

This behaviour corresponds to the induction growth regime, which has been identified experi-

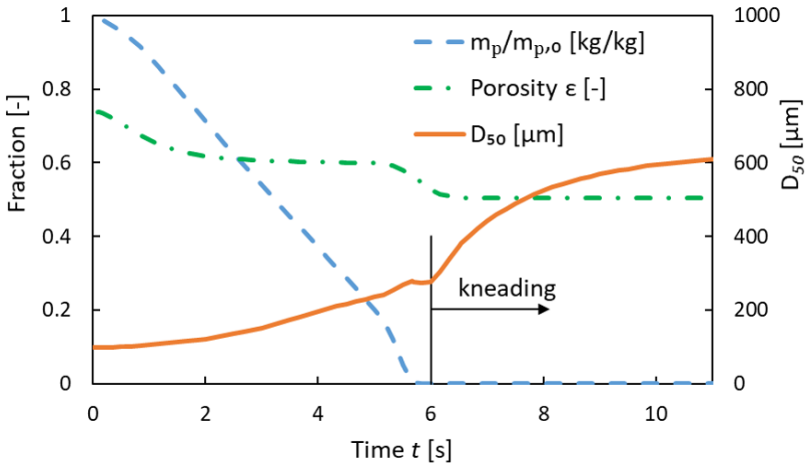

Figure 5.8: Predicted trajectories for porosity ε, dry powder mass fraction $m_p/m_{p,0}$ and mass-median diameter D_{50}

mentally [Iveson et al., 2001b]. The characteristics of this regime are only marginal size change during the induction time and rapid size increase after the end of the induction. In this example, the induction time is around 6 min, which is incidentally equal to the spray time.

5.6 *Model benefits and limitations*

The models developed have many benefits because of the modelling approach and submodels chosen. First of all, the process-scale PBM approach provides the opportunity to efficiently capture complex particle-scale phenomena. Consequently, the models are suitable for rigorous analysis techniques like sensitivity analysis, parameter estimation and optimisation due to their short simulation time. Mechanistic understanding is used to develop and select approaches to model the particle-scale phenomena, especially the wet granulation mechanisms and powder flow regime. Overall, the models contain a limited number of essential model parameters which cannot be measured in isolated experiments. For this reason, a limited number of experiments is required for parameter estimation, and promising model predictions can be made. This process is described in Section 7.2. All in all, the models proposed are suitable to be used for model-driven design (MDD).

Despite the benefits, the models are also limited due to critical assumptions made in the development. 1-D PBM is employed with granule size as the property of interest, and liquid content is

averaged over each size bin (see Section 5.2.1). As the liquid content plays an important role in wet granulation, an accurate representation for this property is required. As the lumped parameter approach can only capture narrow distributions well, the models are less capable to accurately predict experiments with broad distributions of liquid content. In this case, a multi-D PBM approach with liquid content as an additional property of interest is more promising [Iveson, 2002]. Apart from that, an implicit assumption in this PBM framework is a well-mixed control volume or compartment. To overcome this, compartmental modelling (CM) is applied, and the powder flow between compartments is determined by assuming roping flow conditions. For this reason, predictions outside this regime might less accurate. Even though CM is a suitable approach to capture the effect of powder flow, it is limited to predict the effect on breakage in 1-D PBM. In multi-D PBM, CM is more beneficial than in 1-D PBM because the mechanisms in the spray zone can be captured more appropriately. In the spray zone, wetting of granules can lead to a broad distribution of liquid content. The drawback of CM is the increased computational effort which makes the model less suitable for methods that are based on a large number of simulations like sensitivity analysis and parameter estimation. In the model developed, CM increases the required computational time by a factor of almost 3.

5.7 *Conclusions*

A high-shear wet granulation model is developed applying 1-D PBM. This model is customised for high-shear mixer with a vertical axis. Inhomogeneous conditions inside the granulator are taken into account through CM. Mechanistic understanding is applied to generate or select kernels for all wet granulation rate processes, and all modelling parameters are assumed to be scale-independent. All critical model assumptions can be assessed and confirmed based on experimental results. In conclusion, this is a promising predictive modelling approach for the high-shear wet granulation process, which can be applied and tested in a model-driven design (MDD) case study.

In chapter 6, model assumptions are assessed experimentally and empirical porosity parameters are estimated. In chapter 7, the model is calibrated and validated based on a sensitivity analysis, parameter estimation and predictions. In chapter 8, the model is applied in MDD case study.

Chapter 6

EXPERIMENTAL INVESTIGATION OF HIGH-SHEAR WET GRANULATION MECHANISMS

6.1 *Introduction*

In this chapter, experiments are designed and analysed for a model-driven scale-up case study. This experimental design focusses on the following objectives:

- determine appropriate processing and measurement techniques
- assess the reproducibility of experiments
- study the effects of operating parameters on high-shear wet granulation mechanisms
- verify critical model assumptions
- estimate modelling parameters
- validate the models developed in Chapter 5

To achieve these objectives, experiments are designed at different process scales. The experimental findings are compared to literature findings to assess and extend the established mechanistic process understanding.

6.2 *Experimental design*

In experimental design (especially scale-up), all relevant dimensionless groups have to be evaluated individually. For high-shear wet granulation, the dimensionless groups are: dimensionless spray flux Ψ_a (Eq. 2.5), Froude number Fr (Eq. 2.36), Stokes deformation number St_{def} (Eq. 2.15) and pore saturation S (Eq. 2.27). As Fr and St_{def} cannot be kept simultaneously constant across scales due to equipment limitations, the Fr is prioritised because operating in the roping flow regime is considered more important. To evaluate S, porosity measurements or estimates are required. The conceptual experimental design framework to achieve the objectives is shown in Table 6.1.

Table 6.1: Constraints for operating parameters

Objective	Method
Determine drying technique	Compare fluid bed drying to tray drying (see Section 3.3.1)
Determine porosity measurement technique	Assess GeoPyc and tap density measurements (see Section 3.3.4)
Assess reproducibility	Repeat experiments at critical conditions
Study wet granulation mechanisms	Isolate mechanisms and vary critical parameters
Verify modelling assumptions	See Table 5.3
Estimate modelling parameters	Focus on critical operating range
Validate models	Cover operating space

Generic engineering principles (see Sections 2.1 and 2.2) impose constraints for the operating parameters as shown in Table 6.2. Additionally, equipment-specific safety measures limit the operation. For this equipment, safety measures for spray pressure ($P < 5\,\text{bar}$) and impeller tip speed ($v_t < 7\,\frac{\text{m}}{\text{s}}$) are followed. When more than one constraint is imposed, desired operating conditions might not be achievable due to conflicting constraints. Spray conditions are limited due to the limited spray pressure range available. As the spray pressure affects the spray rate and drop diameter, the achievable dimensionless spray flux range is limited, and an operation in the drop-controlled nucleation regime is not feasible at 2 L. The impeller rotational speed is under similar conflicting constraints because the tip speed safety limit is scale-independent but the tip speed needs to be increased with increasing scale to ensure roping flow conditions. For these reasons, an operation in the drop-controlled and roping flow regime is not feasible at every scale as shown in Table 6.3.

The critical process parameters (CPPs) of high-shear wet granulation are liquid-to-solid ratio L/S, volumetric spray rate $\dot{V}$, impeller tip speed v_t and kneading time t_{kn}. The critical quality attributes (CQAs) are mass median diameter D_{50}, fines mass fraction W ($< 90\,\mu\text{m}$), coarse mass fraction W (> 1 mm) and granule porosity ε. An overview of the phenomena investigated is given in Table 6.4. The reproducibility is assessed based on the CQAs of replicate experiments. Nucleation-only experiments ($\Psi_a = 0.3 - 0.5$) are conducted to isolate nucleation and wetting (see Section

Table 6.2: Engineering principles for operation of high-shear wet granulation

Operating condition	Constraint	Reason
Spray conditions	Dimensionless spray flux $\Psi_a < 0.5$	Drop-controlled nucleation
	Spray pressure $P > P_{min}$	Well-developed spray[1]
Impeller speed	Froude number $Fr > 20$	Roping flow

[1]Drop diameter $D_{d,90} < D_{50}$ of desired granular product and standard deviation of spatial drop distribution $\sigma_x > 0.15$

Table 6.3: Equipment-specific operating range chosen (Ψ_a dimensionless spray flux, Fr Froude number)

Scale	Ψ_a [−]	Fr [−]
2 L	0.9 – 1.2	23 – 41
10 L	0.3 – 0.5	20 – 26
25 L	0.4	22
70 L	0.2 – 0.3	12

3.3.2). The nucleation-only experimental results are used to validate the LND model (Eq. 5.21) for this system and determine the Sauter mean nuclei diameter d_n. Additionally, the spray conditions ($d_n = 230\,\mu m - 570\,\mu m$) are varied in granulation experiments (see Section 3.3.1) to determine the effect on the granulation endpoint. Consolidation and growth are investigated at range of liquid-to-solid ratios ($L/S = 0.13\,\frac{kg}{kg} - 0.3\,\frac{kg}{kg}$) and impeller tip speeds ($v_t = 2\,\frac{m}{s} - 7\,\frac{m}{s}$) by measuring the porosity and particle size distribution (PSD). Based on the PSD results, the transition between layering and coalescence is investigated, and the critical L/S and critical pore saturation S_{crit} are determined. Experiments in the rapid growth ($S \gg S_{crit}$) and nucleation-only (breakage-only) regime ($S \ll S_{crit}$) are conducted to strongly favour and investigate coalescence and breakage respectively. The role of the chopper is assessed by varying the chopper rate ($n_{ch} = 0\,\frac{1}{min} - 1200\,\frac{1}{min}$). The kneading time ($t_{kn} = 0\,min - 5\,min$) is varied to study all kinetic mechanisms (consolidation, layering, coalescence and breakage) over time.

Table 6.4: Phenomena investigated and experimental design approach

Phenomenon	Type of experiment	Experimental conditions varied
Reproducibility	Granulation	Replicates of critical conditions
Nucleation & Wetting	Nucleation-only Granulation	Spray conditions $\Psi_a = 0.3 - 0.5$
Consolidation & Growth	Granulation Granulation	Liquid-to-solid ratio $L/S = 0.13\,\frac{kg}{kg} - 0.3\,\frac{kg}{kg}$ Impeller tip speed $v_t = 2\,\frac{m}{s} - 7\,\frac{m}{s}$
Coalescence	Granulation	Favour coalescence $S \gg S_{crit}$
Breakage	Granulation Granulation	Favour breakage $S \ll S_{crit}$ Chopper rate $n_{ch} = 0\,\frac{1}{min} - 1200\,\frac{1}{min}$

In the model-driven design (MDD) study, determining the critical conditions ($S \approx S_{crit}$) is of particular importance. For this reason, the experimental design for parameter estimation includes experiments at these critical conditions at 10 L lab scale with varying kneading time. Furthermore, the porosity parameters (Eq. 5.30) are estimated using experiments over a wide range of L/S and v_t. It is assumed that the minimum porosity is reached after 5 min of kneading, and tap density measurements are chosen to determine porosity. Overall, appropriate experimental results from a

range of scales (2 L, 10 L, 25 L and 70 L) are used to estimate the set of porosity parameters $\vec{x}$. The experimental design is not ideal for scale-up studies because of the requirement of large-scale experimental data. An experimental design with L/S and v_t varied over a wide range at lab scale (2 L and 10 L) is to be preferred. For the parameter estimation, the following objective function is applied:

$$\min_{\vec{x}} \quad \sum_{i=1}^{25} \left(\varepsilon_{min}^{exp}(i) - \varepsilon_{min}^{sim}(v_t(i), L/S(i), \vec{x}) \right) \tag{6.1}$$

with

$$\vec{x} = [e_1, e_2, e_3] \tag{6.2}$$

where ε_{min}^{exp} is the granule porosity measured at the endpoint, ε_{min}^{sim} is the simulated endpoint porosity and i is the experiment number.

Based on the logic above, the full experimental design at all scales is listed in Table 6.5. A total of 42 experiments are performed. The full datasets of experimental results are given in Appendix B.

Table 6.5: Plan of granulation experiments including conditions and relevant dimensionless groups (V granulator volume, n_{imp} impeller speed, $\dot{V}$ spray rate, t_{sp} spray time, L/S mass-based liquid to solid ratio, v_t impeller tip speed, Fr Froude number, St_{def} Stokes deformation number, Ψ_a dimensionless spray flux, n_{ch} chopper rate, t_{kn} kneading time)

Exp	V [L]	n_{imp} $\left[\frac{1}{\text{min}}\right]$	$\dot{V}$ $\left[\frac{\text{mL}}{\text{min}}\right]$	t_{sp} [s]	L/S $\left[\frac{\text{kg}}{\text{kg}}\right]$	v_t $\left[\frac{\text{m}}{\text{s}}\right]$	Fr [−]	St_{def} [−]	Ψ_a [−]	n_{ch} $\left[\frac{1}{\text{min}}\right]$	t_{kn} [min]
1	2	485	60	60	0.15	4.4	23	2.5×10^{-3}	0.9	1200	5
2	2	550	68	53	0.15	5.0	30	3.2×10^{-3}	1.0	1200	5
3	2	650	80	45	0.15	5.9	41	4.4×10^{-3}	1.2	1200	5
4	2	485	60	52	0.13	4.4	23	2.5×10^{-3}	0.9	1200	5
5	2	485	60	68	0.17	4.4	23	2.5×10^{-3}	0.9	1200	5
6	2	485	60	84	0.21	4.4	23	2.5×10^{-3}	0.9	1200	5
7	2	485	60	100	0.25	4.4	23	2.5×10^{-3}	0.9	1200	5
8	2	485	60	60	0.15	4.4	23	2.5×10^{-3}	0.9	1200	0
9	2	485	60	60	0.15	4.4	23	2.5×10^{-3}	0.9	1200	1
10	2	485	60	60	0.15	4.4	23	2.5×10^{-3}	0.9	1200	2
11	2	485	60	60	0.15	4.4	23	2.5×10^{-3}	0.9	1200	3
12	10	350	60	300	0.15	6.2	23	4.7×10^{-3}	0.3	1200	5
13	10	375	64	281	0.15	6.6	26	5.3×10^{-3}	0.3	1200	5
14	10	325	74	243	0.15	5.7	20	4.5×10^{-3}	0.5	1200	5

Continued on next page

Table 6.5 – continued from previous page

Exp	V [L]	n_{imp} $\left[\frac{1}{\text{min}}\right]$	$\dot{V}$ $\left[\frac{\text{mL}}{\text{min}}\right]$	t_{sp} [s]	L/S $\left[\frac{\text{kg}}{\text{kg}}\right]$	v_t $\left[\frac{\text{m}}{\text{s}}\right]$	Fr [−]	St_{def} [−]	Ψ_a [−]	n_{ch} $\left[\frac{1}{\text{min}}\right]$	t_{kn} [min]
15	10	350	60	260	0.13	6.2	23	4.7×10^{-3}	0.3	1200	5
16	10	350	60	340	0.17	6.2	23	4.7×10^{-3}	0.3	1200	5
16-1	10	350	300	68	0.17	6.2	23	4.7×10^{-3}	0.7	1200	5
17	10	350	60	420	0.21	6.2	23	4.7×10^{-3}	0.3	1200	5
18	10	350	60	500	0.25	6.2	23	4.7×10^{-3}	0.3	1200	5
19	10	250	57	316	0.15	4.4	12	2.5×10^{-3}	0.4	1200	5
20	10	350	80	225	0.15	6.2	23	4.7×10^{-3}	0.5	1200	5
21	10	350	200	90	0.15	6.2	23	4.7×10^{-3}	0.4	1200	5
22	10	350	60	300	0.15	6.2	23	4.7×10^{-3}	0.3	1200	5
23	10	350	60	300	0.15	6.2	23	4.7×10^{-3}	0.3	1200	5
24	10	350	60	20	0.01	6.2	23	4.7×10^{-3}	0.3	0	0
27	2	485	60	100	0.25	4.4	23	2.5×10^{-3}	0.9	1200	5
28	2	485	60	120	0.30	4.4	23	2.5×10^{-3}	0.9	1200	5
29	2	485	60	116	0.29	4.4	23	2.5×10^{-3}	0.9	1200	5
30	10	350	60	300	0.15	6.2	23	4.7×10^{-3}	0.3	1200	0
31	10	350	60	340	0.17	6.2	23	4.7×10^{-3}	0.3	1200	0
32	10	350	60	340	0.15	6.2	23	4.7×10^{-3}	0.3	1200	1
34	10	350	60	340	0.17	6.2	23	4.7×10^{-3}	0.3	1200	3

Continued on next page

Table 6.5 – continued from previous page

Exp	V [L]	n_{imp} $\left[\frac{1}{\text{min}}\right]$	$\dot{V}$ $\left[\frac{\text{mL}}{\text{min}}\right]$	t_{sp} [s]	L/S $\left[\frac{\text{kg}}{\text{kg}}\right]$	v_t $\left[\frac{\text{m}}{\text{s}}\right]$	Fr [−]	St_{def} [−]	Ψ_a [−]	n_{ch} $\left[\frac{1}{\text{min}}\right]$	t_{kn} [min]
36	10	350	60	340	0.17	6.2	23	4.7×10^{-3}	0.3	1200	5
37	10	350	60	340	0.17	6.2	23	4.7×10^{-3}	0.3	0	5
38	25	300	78	731	0.19	6.9	22	5.7×10^{-3}	0.4	1200	5
39	25	300	78	654	0.17	6.9	22	5.7×10^{-3}	0.4	1200	5
40	25	300	78	808	0.21	6.9	22	5.7×10^{-3}	0.4	1200	5
41	25	100	78	731	0.19	2.3	2	6.8×10^{-4}	1.2	600	5
42	70	200	196	814	0.19	5.6	12	3.9×10^{-3}	0.2	840	0
43	70	200	226	706	0.19	5.6	12	3.9×10^{-3}	0.3	840	2.5
44	70	200	240	595	0.17	5.6	12	3.9×10^{-3}	0.3	840	5
45	70	200	200	798	0.19	5.6	12	3.9×10^{-3}	0.2	840	5
46	70	200	207	730	0.18	5.6	12	3.9×10^{-3}	0.2	840	5

6.3 *Results and discussion*

6.3.1 Drying techniques

The effect of drying techniques on the particle size distribution (PSD) is assessed by comparing fluid bed dried and tray dried samples from a range of granulation experiments (Figure 6.2). The drying technique has an effect on the PSD, as the D_{50} of fluid bed dried samples is consistently smaller compared to tray dried samples. In addition, significantly more fine powder ($< 90\,\mu m$) is present after fluid bed drying (Figure 6.2b); however, the mass fraction of coarse particles (> 1 mm) decreases only to a small extent (Figure 6.2c). These results clearly confirm the size reduction during fluid bed drying. Attrition appears to be the dominant rate process as $W(< 90\,\mu m)$ is increasing drastically. The attrition rate for larger particles seems to be much lower, possibly due to smaller specific surface area or higher resistance. In conclusion, the assumption that tray drying has a smaller impact on the PSD is confirmed. The PSD should be determined using tray dried samples for this reason.

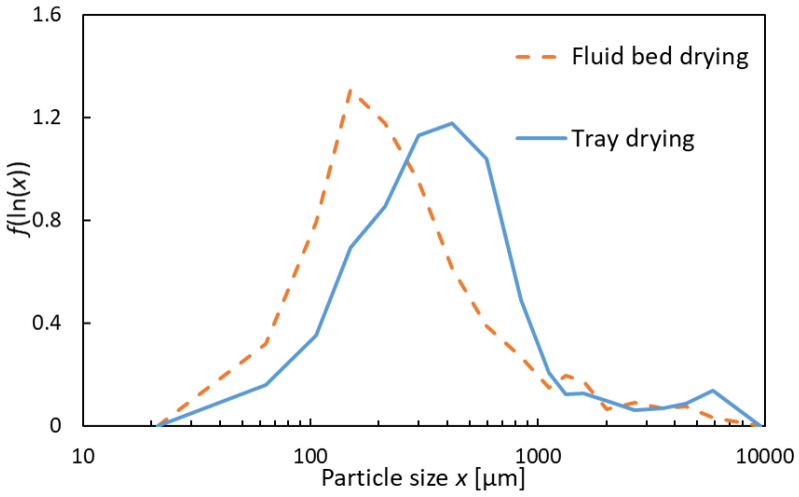

Figure 6.1: PSD of a fluid bed dried and a tray dried sample (Exp 36: $V = 10\,L$; $L/S = 0.17$; $t_{kn} = 5$ min)

6.3.2 Porosity measurement techniques

GeoPyc and tap density porosity measurements are compared in Figure 6.3a. The results of both techniques are quantitatively similar; nevertheless, small differences are apparent. While tap density

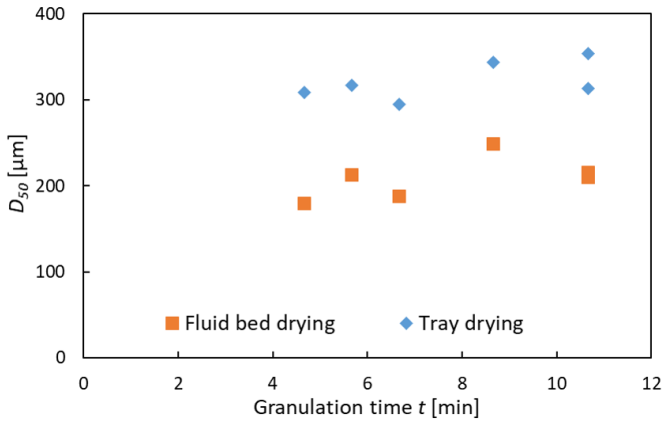

(a) Mass-median diameter D_{50}

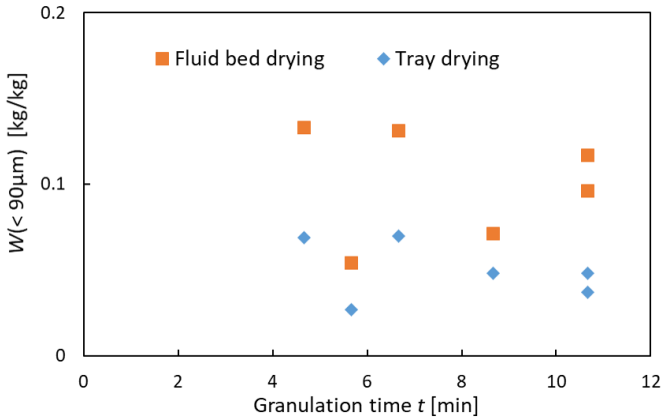

(b) Fines mass fraction $W(< 90\,\mu m)$

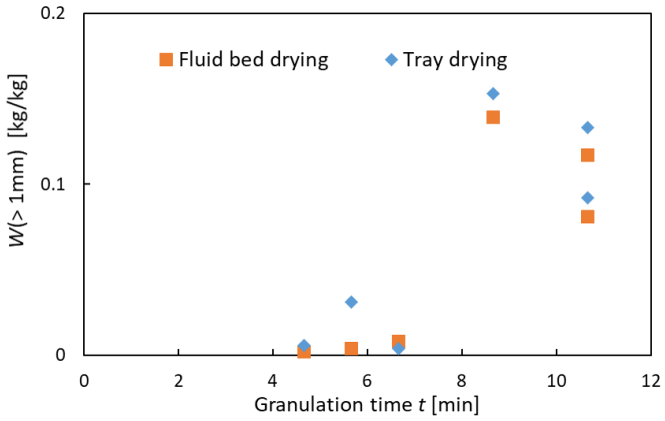

(c) Coarse mass fraction $W(> 1\,mm)$

Figure 6.2: PSD results of fluid bed dried and tray dried samples (Exp 30-37: $V = 10\,L$; $t_{sp} = 6\,min$; $L/S = 0.17$; $Fr = 23$; $v_t = 6.2\,\frac{m}{s}$)

porosity is reproducible in replicate experiments at $L/S = 0.17$, GeoPyc measurements vary significantly. This potentially is a result of the limited availability of material for the GeoPyc measurements (> 1 mm), as only very few granules of that size are formed in most experiments (Figure 6.3a). For this reason, the GeoPyc porosity results are not representative and remain questionable. All in all, the tap density porosity results are more representative because of the applicability at a more representative particle size range (Figure 6.3b).

6.3.3 Reproducibility

Overall, the qualitative reproducibility is very high, and only minor quantitative discrepancies are determined for experiments with significant growth (Figure 6.4). Figure 6.5 shows the moderate scattering of the replicate results which confirms the high reproducibility. Significant growth occurred at high liquid-to-solid ratio ($L/S > 0.17$), s, and the lower reproducibility is depicted by wider scattering. Poor liquid distribution inside the granulator is assumed to be primarily responsible for this lower reproducibility. At high L/S, the impeller and chopper might not be sufficient to distribute the liquid evenly assuming that the liquid is initially poorly distributed.

6.3.4 Wetting and nucleation

Results from a nucleation-only experiment using the method described in Section 3.3.2 are compared to LND model predictions in Figure 6.6. The experiment results in a very narrow PSD with a peak at around 300 µm and a short tail. The LND model predicts this result fairly accurately. The peak is predicted to be slightly broader, and the short tail is in good agreement. The accuracy of the model prediction verifies that the LND model is capable of predicting the nuclei size distribution (see Section 5.5).

The effect of spray conditions on the process is investigated at 10 L by varying the dimensionless spray flux and drop diameter (Table 6.6). As described by Hapgood et al. [2004] and Ax et al. [2008], increasing each of the parameters individually leads to a larger nuclei diameter. However, the combined effect is not easy to predict, as illustrated in Table 6.6. In this case, the dimensionless spray flux Ψ_a decreases but the drop diameter increases d_d which overall leads to an increase in nuclei diameter d_n. For this reason, the nuclei diameter d_n is used to quantify the spray conditions because the strong impact of both parameters Ψ_a and d_d on d_n. The Sauter mean nuclei diameter d_n is predicted qualitatively by evaluating the logarithmic mean of the nuclei size distribution

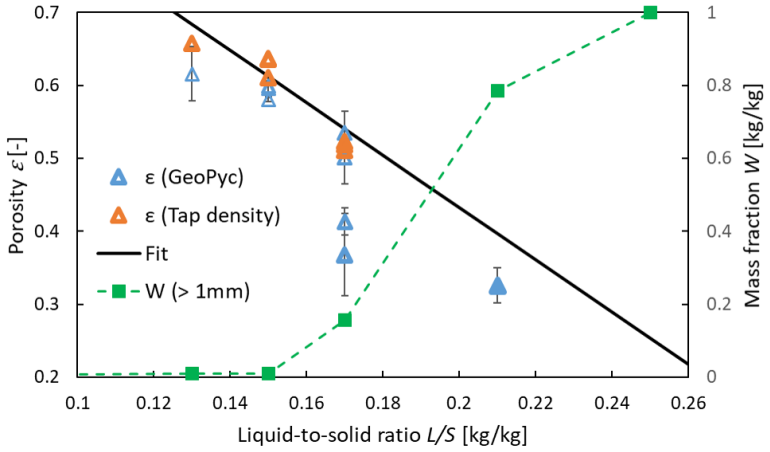

(a) Porosity ε and coarse mass fraction W (> 1 mm)

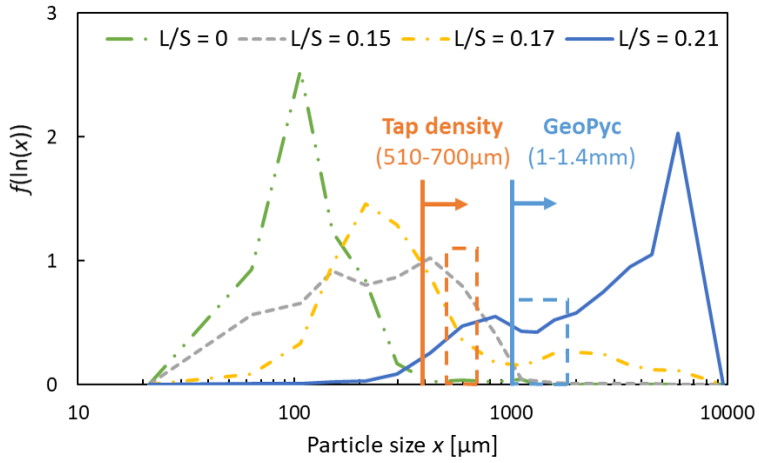

(b) Applicability of technique and size range chosen for measurements (illustrated by the dashed area ⬚)

Figure 6.3: Comparison of GeoPyc and tap density porosity measurement techniques (Exp 12, 15-17, 22, 23, 36 and 37: $V = 10\,\mathrm{L}$; $Fr = 23$; $v_t = 6.2\,\frac{\mathrm{m}}{\mathrm{s}}$; $\Psi_a = 0.3$)

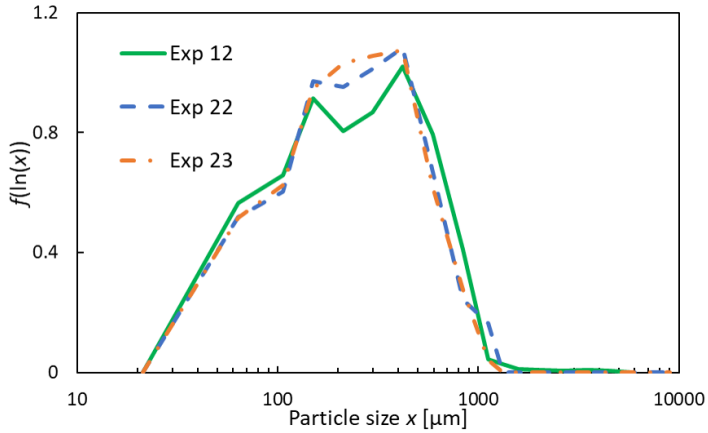

(a) Exp 12, 22 and 23: $V = 10\,\mathrm{L}$; $t_{sp} = 5\,\mathrm{min}$; $L/S = 0.15$; $Fr = 23$; $\Psi_a = 0.3$; $t_{kn} = 5\,\mathrm{min}$

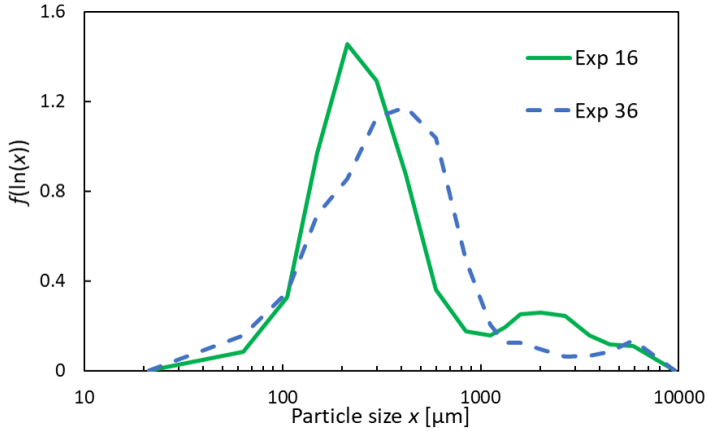

(b) Exp 16 and 36: $V = 10\,\mathrm{L}$; $t_{sp} = 5.7\,\mathrm{min}$; $L/S = 0.17$; $Fr = 23$; $\Psi_a = 0.3$; $t_{kn} = 5\,\mathrm{min}$

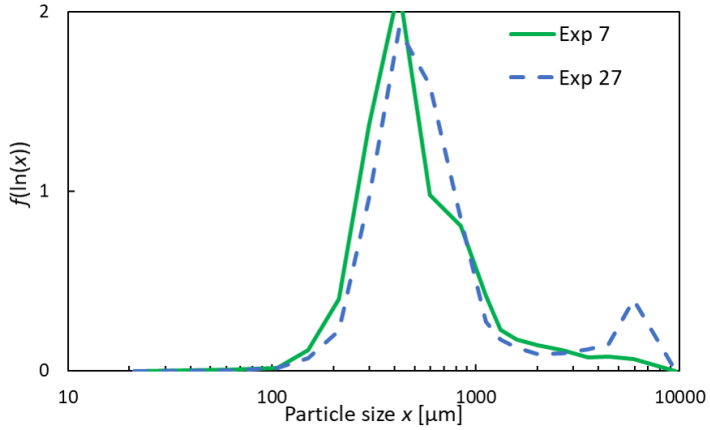

(c) Exp 7 and 27: $V = 2\,\mathrm{L}$; $t_{sp} = 5.7\,\mathrm{min}$; $L/S = 0.17$; $Fr = 23$; $\Psi_a = 0.9$; $t_{kn} = 5\,\mathrm{min}$

Figure 6.4: PSD of replicate experiments at various conditions

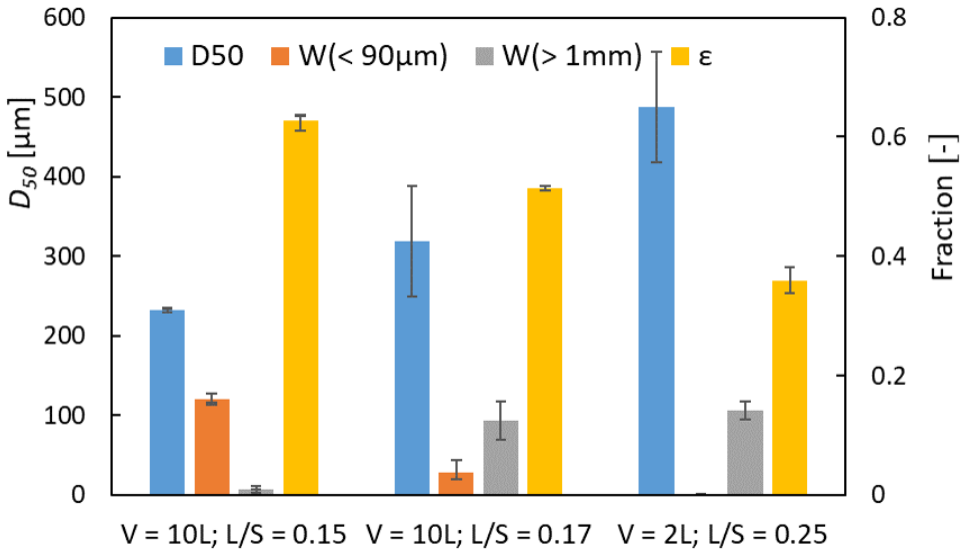

Figure 6.5: Individual and average CQA results of replicate experiments

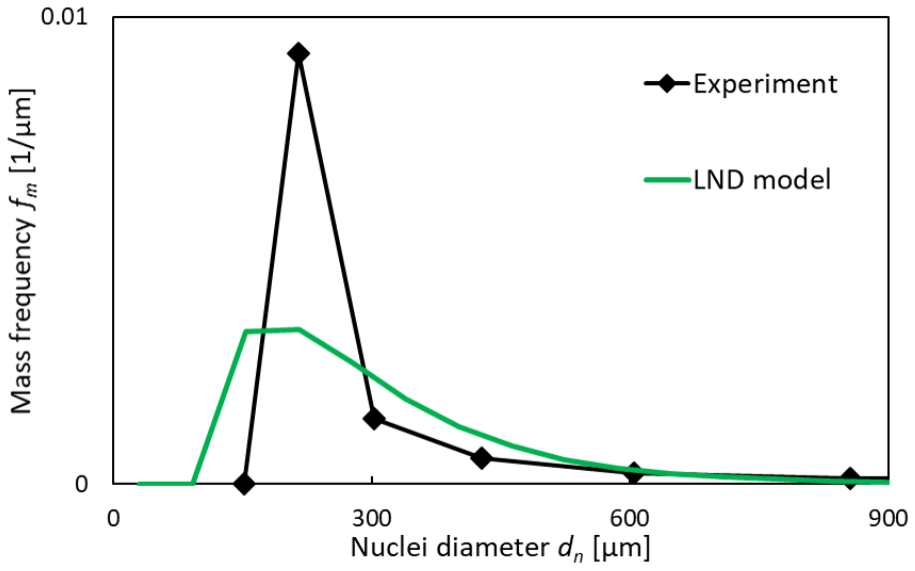

Figure 6.6: Experimental validation of nuclei size distribution prediction (Exp 24: $V = 10\,\mathrm{L}$; $t_{sp} = 20\,\mathrm{s}$; $v_t = 6.2\,\frac{\mathrm{m}}{\mathrm{s}}$; $Fr = 23$; $\Psi_a = 0.3$; $\Psi_n = 0.5$; $d_d = 98\,\mu\mathrm{m}$; $\sigma_x = 0.17$)

($\mu_n d_1$) using the LND model (Eqs. 4.4 and 4.8). However, a quantitative comparison between the experimental Sauter mean and predicted logarithmic mean is not possible.

Table 6.6: Overview of spray conditions (see Appendices B.1 and B.3)

Exp	Ψ_a [−]	d_d [µm]	d_n [µm]	$\mu_n d_1$ [µm]
20	0.5	69	230	340
22	0.4	98	230	250
21	0.3	232	570	830

Figure 6.7 shows that the granulation experiment with varying spray conditions do not result in any very large particles, most likely due to the low L/S of 0.15. Nevertheless, an effect of spray conditions on the PSD is observed. At $d_n = 230\,\mu m$, the PSD shows a single, narrow peak, while a much larger nuclei diameter d_n of 570 µm results in relatively broad PSD. Apart from that, the maximum granule diameter increases with increasing d_n. This shows that the spray conditions have a considerable influence on the PSD which is directly related to d_n. In conclusion, spray conditions have an impact on the width of the PSD, and it is necessary to monitor the nuclei diameter d_n to control the granulation process.

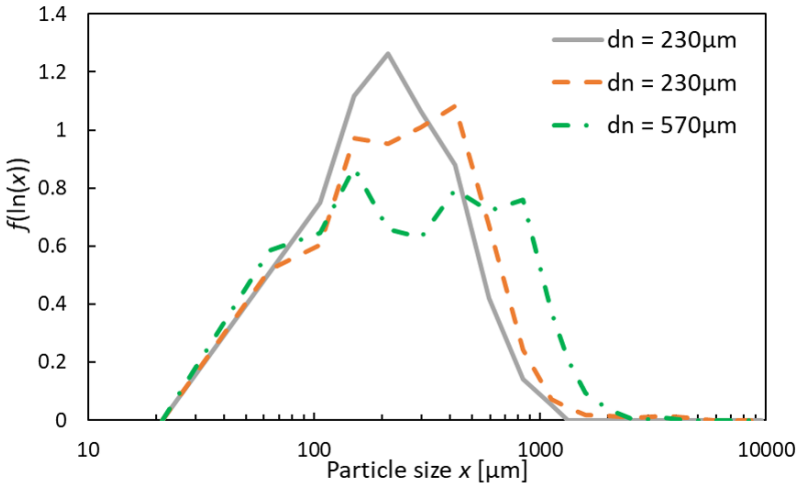

Figure 6.7: Effect of spray conditions (Exp 20-22: $V = 10\,L$; $L/S = 0.15$; $Fr = 23$; $t_{kn} = 5\,min$)

6.3.5 Consolidation

In Figures 6.3a and 6.8, the effect of liquid-to-solid ratio L/S on porosity is illustrated at different scales (2 L, 10 L, 25 L and 70 L). Porosity decreases significantly with increasing L/S at all scales. The porosity is rather high (> 0.6) at low L/S (< 0.15). With increasing L/S, the porosity decreases significantly until it reaches a minimum value of below 0.4. The decrease in porosity is almost linear; however, a drastic drop is observed at some critical L/S value. At this critical L/S, the coarse mass fraction W (> 1 mm) starts to increase considerably (Figure 6.3a). Very low porosities (< 0.4) are primarily observed at very high W (> 1 mm) of above 0.3 $\frac{\text{kg}}{\text{kg}}$ (illustrated by the solid fill ■ in Figure 6.8; see Appendix B.4).

Figure 6.9 shows the effect of the impeller tip speed v_t on the porosity at different liquid-to-solid ratios L/S (0.15 and 0.19) and different scales (2 L, 10 L and 25 L). Increasing v_t is expected to result in a decreasing porosity, as the Stokes deformation number St_{def} (Eq. 2.15) is determined to have an increasing effect on consolidation (see Section 2.1.2). At 2 L and 10 L, v_t is varied at low L/S of 0.15. Porosity decreases with v_t at 2 L but a significant effect of v_t on porosity is not determined at 10 L (Figure 6.9a,b). The results at 25 L are obtained at $L/S = 0.19$, and a decrease in porosity with increasing v_t is observed (Figure 6.9c). It is concluded that the effect of v_t is more pronounced at high L/S.

An approach to correlate the endpoint porosity ε_{min} with the liquid-to-solid ratio L/S and impeller tip speed v_t is tested. To sum up the findings, the L/S dependency appears linear for the range investigated, and the effect of v_t is increasing with increasing L/S. The empirical correlation for the endpoint porosity (Eq. 5.30) represents both observations, and the empirical parameters $e_{1..3}$ are determined including the 95 % confidence intervals:

$$\varepsilon_{min} = e_1 v_t \frac{\text{s}}{\text{m}} (e_2 - L/S) + e_3 \tag{6.3}$$

$$e_1 = 0.58 \pm 0.13 \tag{6.4}$$

$$e_2 = 0.13 \pm 0.03 \tag{6.5}$$

$$e_3 = 0.67 \pm 0.10 \tag{6.6}$$

By assessing the effect of operating parameters (Figures 6.3a, 6.8 and 6.9), a reasonable qualitative agreement between the empirical correlation and experimental results is determined. At low L/S,

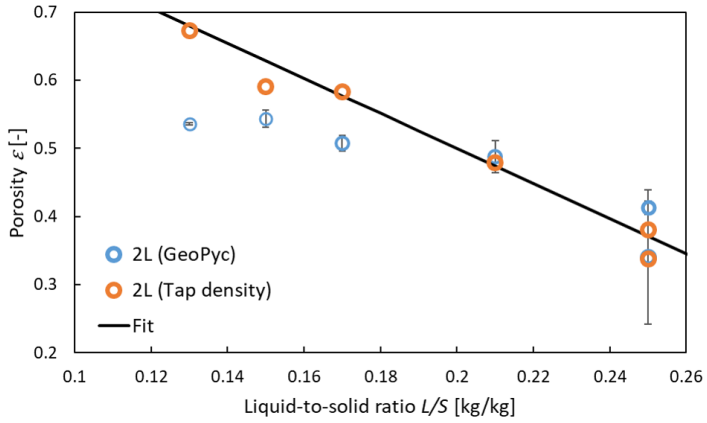

(a) Exp 1, 4-7, 27 and 28: $V = 2\,\mathrm{L}$; $Fr = 23$; $v_t = 4.4\,\frac{\mathrm{m}}{\mathrm{s}}$; $\Psi_a = 0.9$

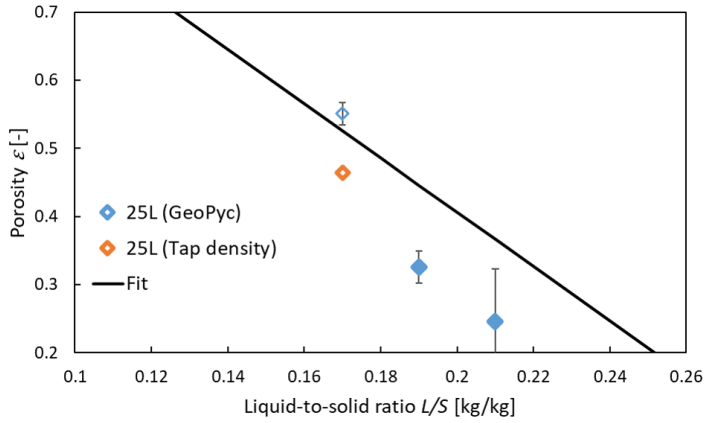

(b) Exp 38-40: $V = 25\,\mathrm{L}$; $Fr = 22$; $v_t = 6.9\,\frac{\mathrm{m}}{\mathrm{s}}$; $\Psi_a = 0.4$

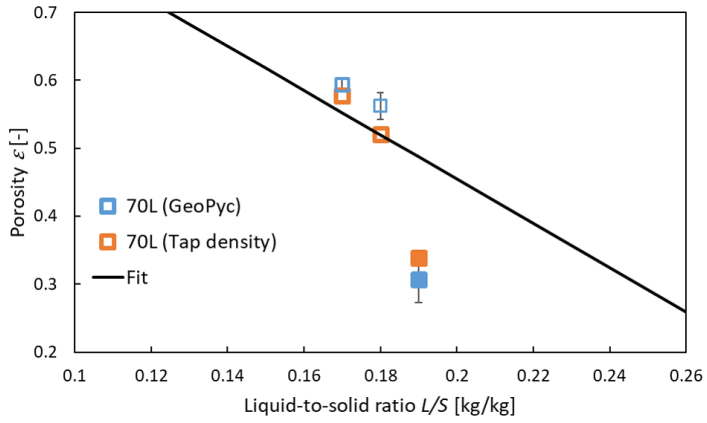

(c) Exp 44-46: $V = 70\,\mathrm{L}$; $Fr = 12$; $v_t = 5.6\,\frac{\mathrm{m}}{\mathrm{s}}$; $\Psi_a = 0.3$

Figure 6.8: Effect of liquid-to-solid ratio L/S on porosity and PSD at different scales V

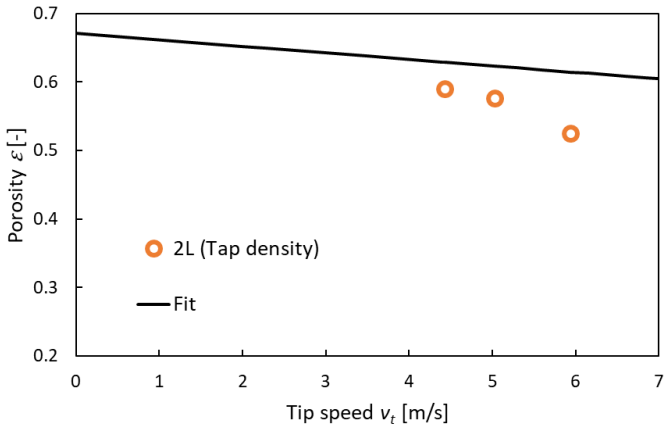

(a) Exp 1-3: $V = 2\,\mathrm{L}$; $t_{kn} = 5\,\mathrm{min}$; $L/S = 0.15$

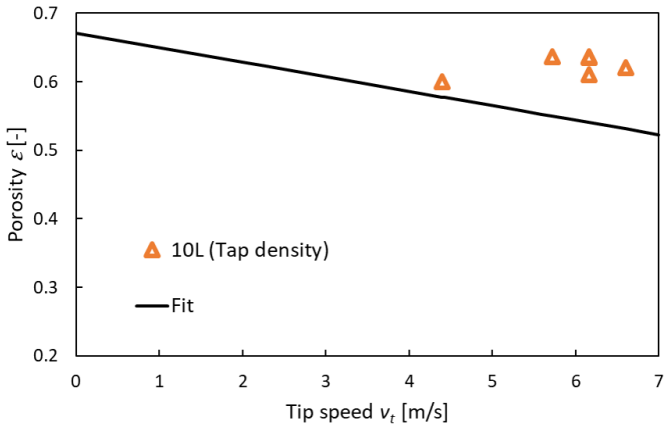

(b) Exp 12-14 and 19: $V = 10\,\mathrm{L}$; $t_{kn} = 5\,\mathrm{min}$; $L/S = 0.15$

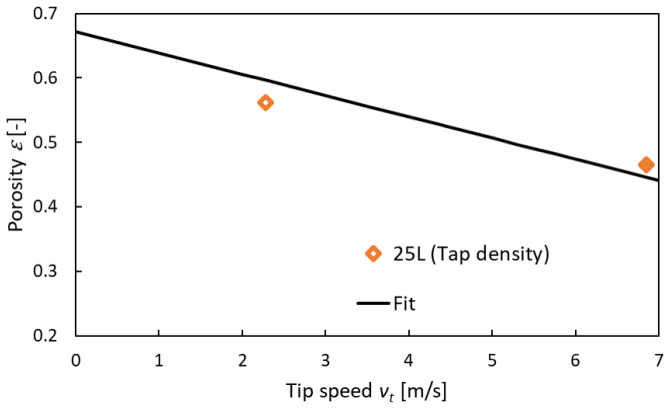

(c) Exp 38 and 41: $V = 25\,\mathrm{L}$; $t_{kn} = 5\,\mathrm{min}$; $L/S = 0.19$

Figure 6.9: Effect of tip speed v_t on porosity at different liquid-to-solid ratios L/S and scales V

minor deviations are observed but the correlations captures the effect of the two input parameters very well. Having said that, a significant mismatch is observed above the critical L/S. Under these conditions, the measured porosity drops non-linearly (see Figures 6.3a and 6.8). This is not captured well by the empirical correlation because a linear relationship is assumed. Maxim et al. [2004] postulated a significant decrease in porosity above the critical L/S due to the presence of surface liquid. Their prediction is qualitatively consistent with the experimental observation. To include the effect of surface liquid, pore saturation S and S_{crit} need to be considered. Since S depends on porosity (Eq. 2.27), an implicit correlation with more empirical parameters is required for the endpoint porosity to overcome this mismatch at high L/S. As more empirical parameters are undesired, this interrelation between porosity and pore saturation (shown in Figure 6.10) is not considered.

The empirical correlation proposed is in good agreement with lab-scale experimental data at 2 L and 10 L (Figures 6.3a and 6.8a). This indicates that an experimental design based exclusively on lab-scale experiments is very promising to achieve a similar accuracy. This makes the inclusion of large-scale experimental data unnecessary.

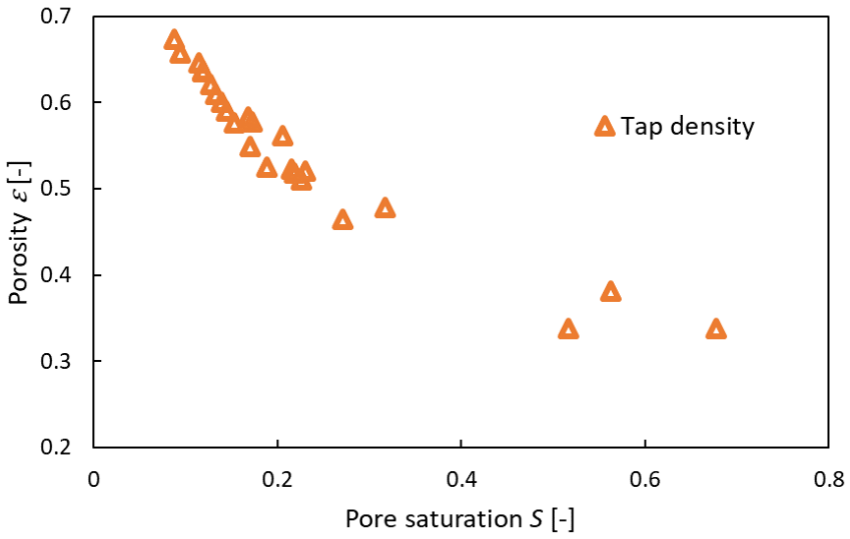

Figure 6.10: Interrelation between pore saturation S and porosity ε

Overall, the empirical correlation is in acceptable quantitative agreement with the experimental results (Figure 6.11). Having said this, the empirical correlation tends to overpredict low porosities.

While porosities below 0.4 are observed experimentally, the empirical correlation does not predict that within the operating range. Very low porosities are especially observed in experiments with a high coarse mass fraction (W ($> 1\,\mathrm{mm}$) $> 0.3\,\frac{\mathrm{kg}}{\mathrm{kg}}$; indicated by the solid fill ■ in Figure 6.11).

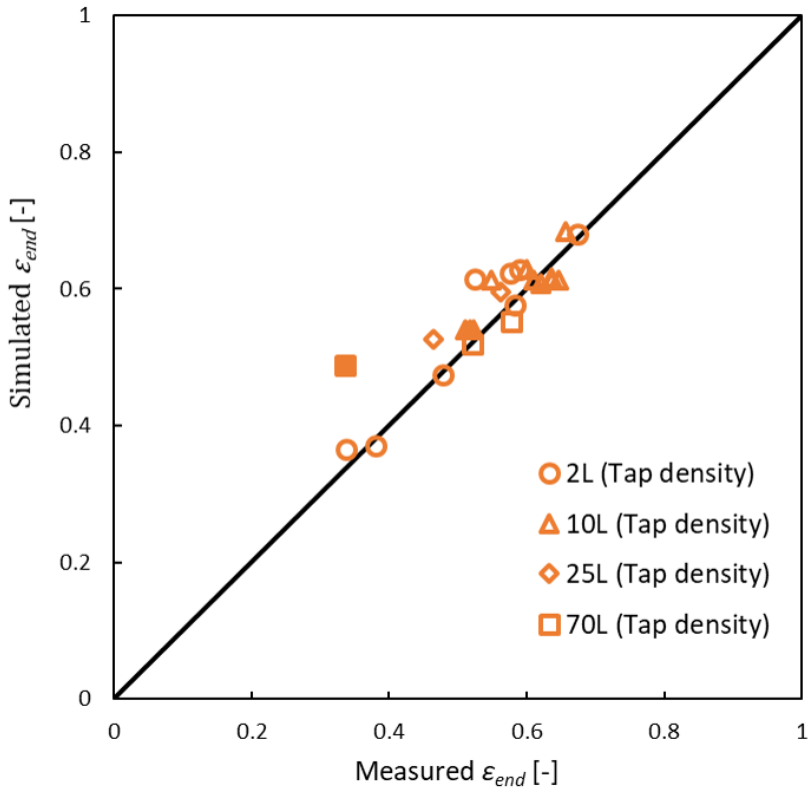

Figure 6.11: Comparison of simulated and measured endpoint porosity ε_{min}

Figure 6.12 shows the effect of kneading time on porosity ε at three different liquid-to-solid L/S (pore saturations S) and scales (2 L, 10 L and 70 L). The porosity remains almost constant at a low L/S of 0.15 and $S < S_{crit}$ (Figure 6.12a), which depicts a a high endpoint porosity and fast consolidation kinetics. At $S \approx S_{crit}$, a small drop in porosity is observed at the beginning of the kneading phase (Tap density, Figure 6.12b). Only at $S \gg S_{crit}$, a significant effect of kneading time is observed (Figure 6.12c). The porosity appears to decrease continuously at this condition, and the porosity at the endpoint is distinctly lower than at the start of kneading. In conclusion, a porosity decrease due to consolidation occurs especially at a higher pore saturation S. This investigation includes at different scales; however, it is assumed that the effect of pore saturation on consolidation

is dominant compared to the effect of scale.

6.3.6 Layering and coalescence

Figure 6.13 shows the effect of L/S on the PSD at various scales V. At $L/S = 0.15$ and below, the PSD is mono-modal and rather narrow with a relatively high mass fraction of fines W ($< 90\,\mu m$) and practically no particles above 1 mm. With increasing L/S, W ($< 90\,\mu m$) continuously decreases until it finally reaches 0. Experiments with W ($< 90\,\mu m$) ≈ 0 show the formation of particles above 1 mm, and a bi-modal PSD is observed. The transition from mono-modal to bi-modal PSD is detected at the critical L/S (non-linear drop in porosity). It is concluded that the critical L/S marks the transition between the nucleation-only and induction growth regime. In the nucleation-only regime, particles grow mainly by layering (see Section 2.1.3). When the amount of liquid suffices to consume all surrounding fine particles (through nucleation and layering), liquid is assumed to accumulate on the granule surface, which leads to the formation of large particles due to coalescence (see Section 2.1.3). At the critical L/S, the drastic drop in porosity leads to an increase in pore saturation S, so that $S > S_{crit}$, which is assumed to increase the surface liquid layer and enhance growth further. Beyond the critical L/S, W (> 1 mm) reaches 1 which depicts the rapid growth regime. Even though the transition between these regimes is observed at all scales, the critical value for L/S varies from scale to scale. The difference in porosity (due to different v_t) is assumed to be a reason for this scale-dependent critical L/S. Liquid typically penetrates into granule pores, and only liquid on the granule surface promotes growth. Overall, these findings show that liquid-to-solid ratio L/S and porosity need to be considered to understand granule growth, and the combined effect is characterised in pore saturation S:

$$S = \frac{L/S\rho_s\,(1-\varepsilon)}{\rho_l \varepsilon} \tag{6.7}$$

where ρ_s is the skeletal solid density and ρ_l is the liquid density.

At a low pore saturation ($S < 0.2$), S only has a small effect on particle size (Figure 6.14). The direct effect of S on both the D_{50} and $W(> 1$ mm) becomes apparent when a critical value is exceeded, as a significant particle size increase is observed. S_{crit} appears to decrease with increasing scale. At 2 L, S_{crit} is determined to ≈ 0.7, and a much lower value of $0.2 - 0.3$ is determined at 25 L and 70 L. At small scales, better mixing conditions are usually observed, which can lead to more controlled growth due to improved liquid distribution and reduced circulation time. Improved

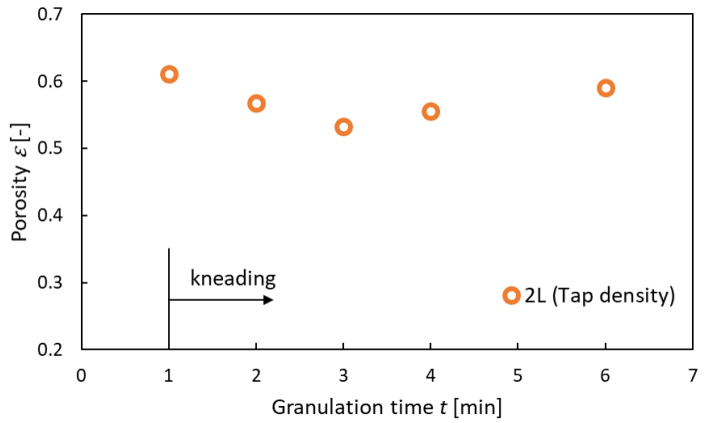

(a) $S = 0.14 < S_{crit}$ (Exp 1 and 8-11: $V = 2\,\mathrm{L}$; $t_{sp} = 1\,\mathrm{min}$; $L/S = 0.15$; $Fr = 23$; $v_t = 4.4\,\frac{\mathrm{m}}{\mathrm{s}}$)

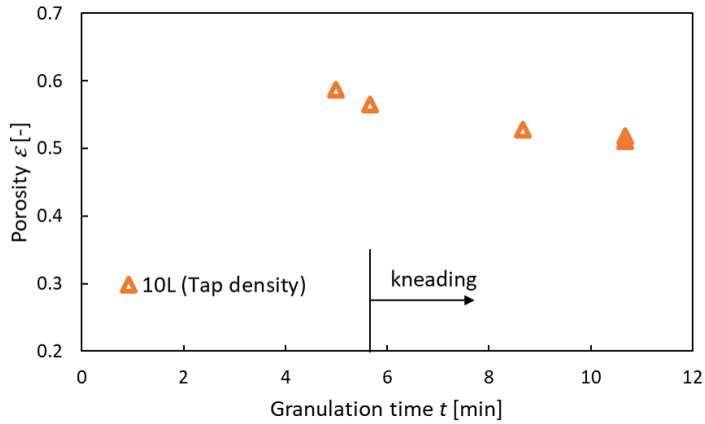

(b) $S = 0.2 \approx S_{crit}$ (Exp 16 and 30-37: $V = 10\,\mathrm{L}$; $t_{sp} = 6\,\mathrm{min}$; $L/S = 0.17$; $Fr = 23$; $v_t = 6.2\,\frac{\mathrm{m}}{\mathrm{s}}$)

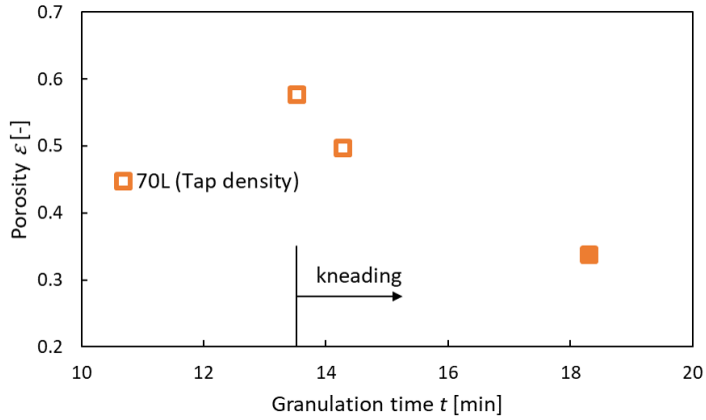

(c) $S = 0.52 \gg S_{crit}$ (Exp 42, 43 and 45: $V = 70\,\mathrm{L}$; $t_{sp} = 13\,\mathrm{min}$; $L/S = 0.19$; $Fr = 12$; $v_t = 5.6\,\frac{\mathrm{m}}{\mathrm{s}}$)

Figure 6.12: Consolidation at different pore saturations S and scales V

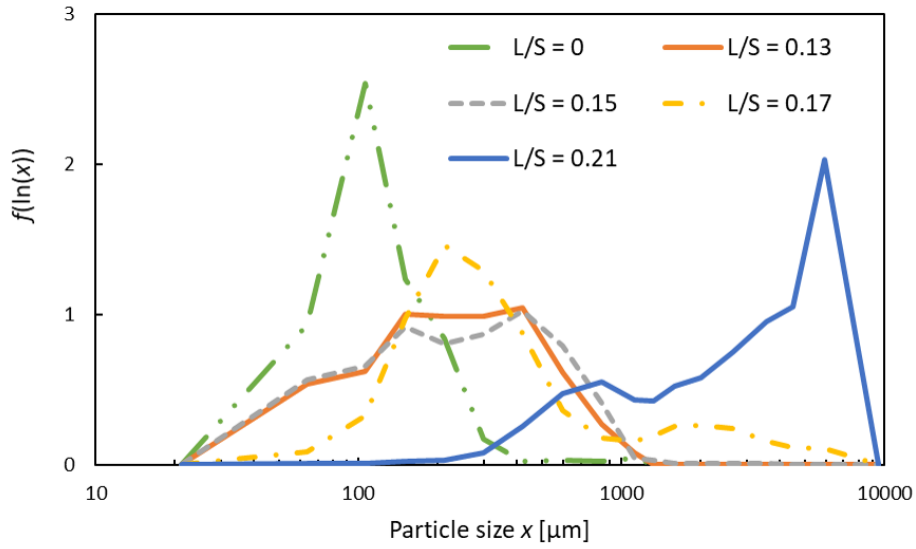

(a) PSD

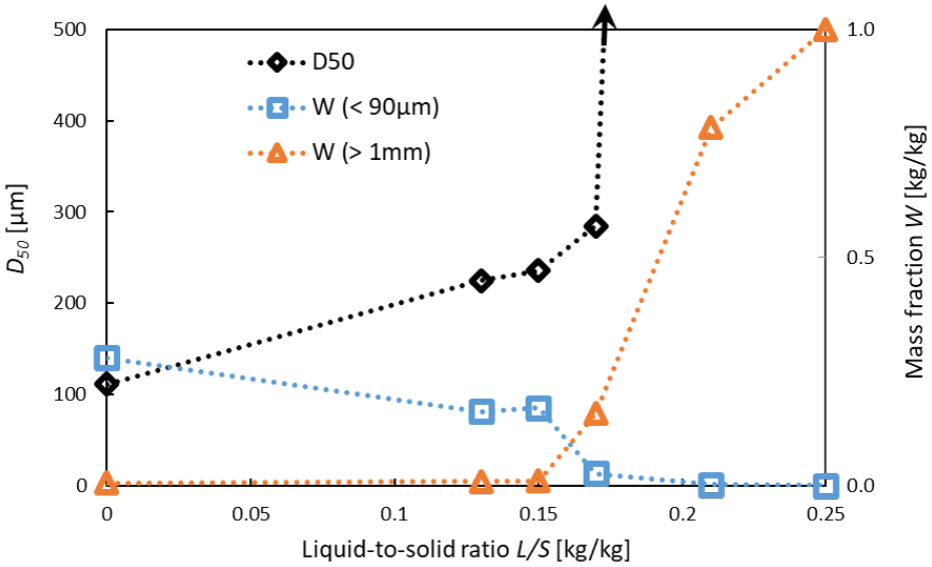

(b) Mass-median diameter D_{50}, fines mass fraction W ($< 90\,\mu m$) and coarse mass fraction W ($> 1\,mm$)

Figure 6.13: Effect of liquid-to-solid ratio L/S on PSD (Exp 12, 15-17, 22, 23, 36 and 37: $V = 10\,L$; $Fr = 23$; $v_t = 6.2\,\frac{m}{s}$; $\Psi_a = 0.3$)

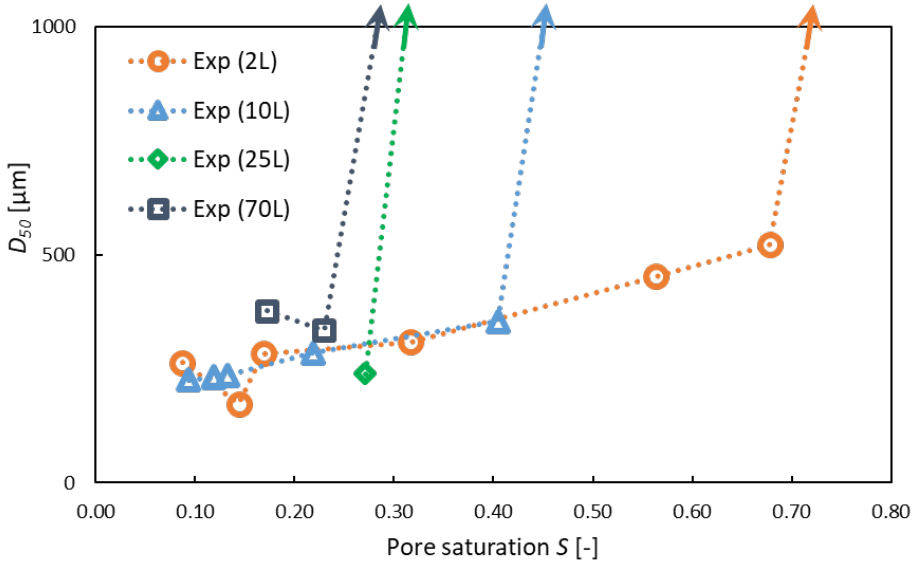

(a) Mass-median diameter D_{50}

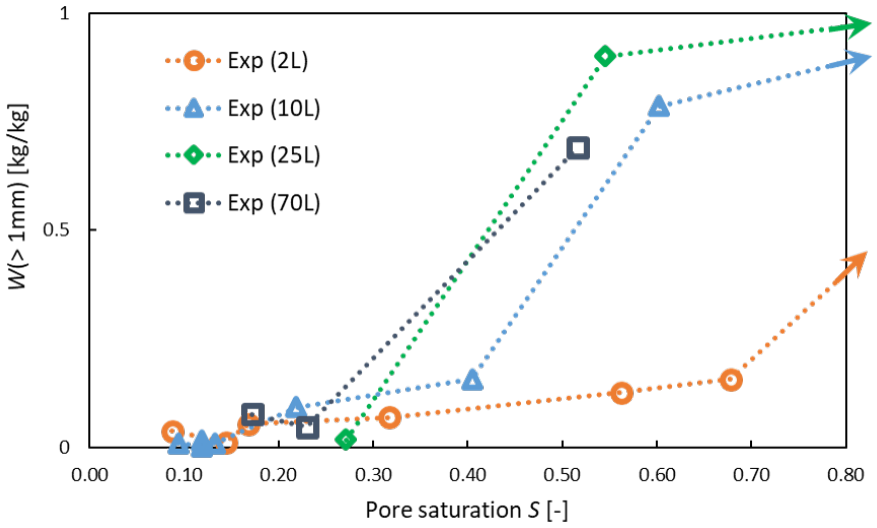

(b) Coarse mass fraction $W(> 1\,\text{mm})$

Figure 6.14: Effect of pore saturation on particle size at different scales

liquid distribution leads to less wet lumps that grow rapidly, and a reduced circulation time is likely to increase breakage because particles are exposed to high shear forces near the impeller more frequently. For these reasons, the measured S_{crit} is the effective critical pore saturation.

To characterise liquid distribution, the granulated mass fraction W_{gran} is determined as it is assumed that powder particles do not contain any liquid. W_{gran} heavily depends on pore saturation S (Figure 6.15a). While only around 50 % powder is granulated at $S < 0.2$, W_{gran} increases continuously with S until nearly all powder is granulated at $S > 0.6$. Under these conditions, liquid is assumed sufficiently distributed over all granules. To take the effect of liquid distribution on granule growth into account, D_{50} is evaluated as a function of granule-specific pore saturation S_{gran} (Figure 6.15b). By transforming S to S_{gran} all results are shifted for experiments with $W_{gran} < 1$. The critical range for S_{gran} is with 0.35-0.75 consequently higher than S_{crit}. The critical S_{gran} value appears to be scalable because the scales $V \geq 10\,\mathrm{L}$ show similar results for the critical S_{gran}. Having said this, a considerably higher critical S_{gran} shows that the 2 L scale does not show similar process behaviour. It is concluded that growth should not be studied at 2 L for scale-up purposes.

Figure 6.16 shows effect of granulation time t on PSD at 10 L and $L/S = 0.17$. At these conditions, only marginal changes PSD are observed during the first 7 min. Having said this, the PSD starts to increase considerably after that, and a broad PSD with a long tail is the result (7 min − 11 min). This significant size increase is an indication for coalescence. The phenomenon is identified as induction growth, as growth only started after an induction time of about 7 min. During the induction time, it is assumed that granules mainly grow by layering, as it is assumed that little surface liquid is sufficient for this mechanism (see Section 2.1.3). At this time, an overall size reduction can occur due to breakage. As soon as all fine particles are depleted, a drop is porosity is assumed to result in a formation of a surface liquid layer and granule growth by coalescence.

Figure 6.17 shows effect of granulation time t on PSD at 70 L and $L/S = 0.19$. The initial growth behaviour observed is similar to induction growth (Figure 6.16) with practically no change in PSD during the first 14 min. However, after 18 min, a large amount of coarse particles (> 1 mm) are present, and a significant drop in porosity is observed (Figure 6.12c). It is concluded that a drop in porosity leads to an increase in pore saturation S and growth. This behaviour indicates rapid growth (see Section 2.1.3). The experimental findings agree well with the qualitative granulation understanding captured in the growth regime map [Iveson and Litster, 1998b], as the main growth regimes are identified for the formulation chosen.

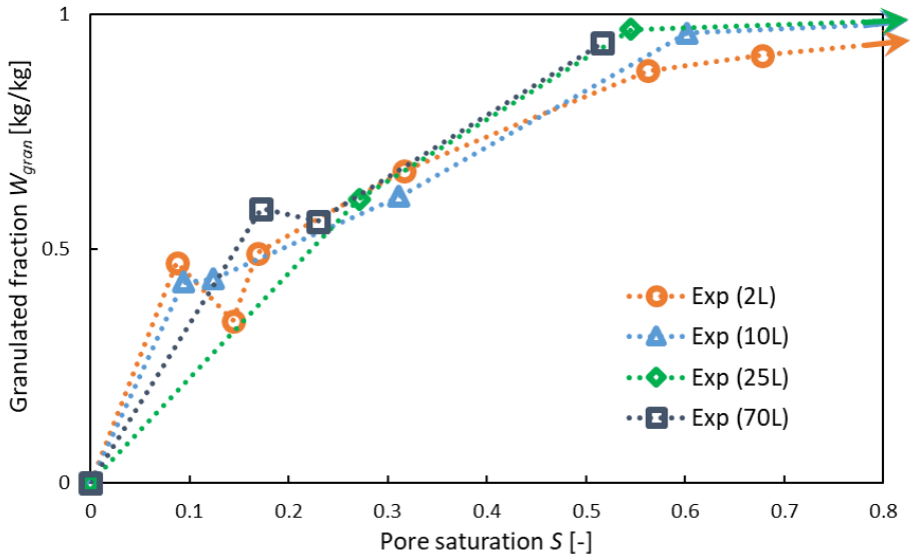

(a) Granulated mass fraction W_{gran} as a function of pore saturation S

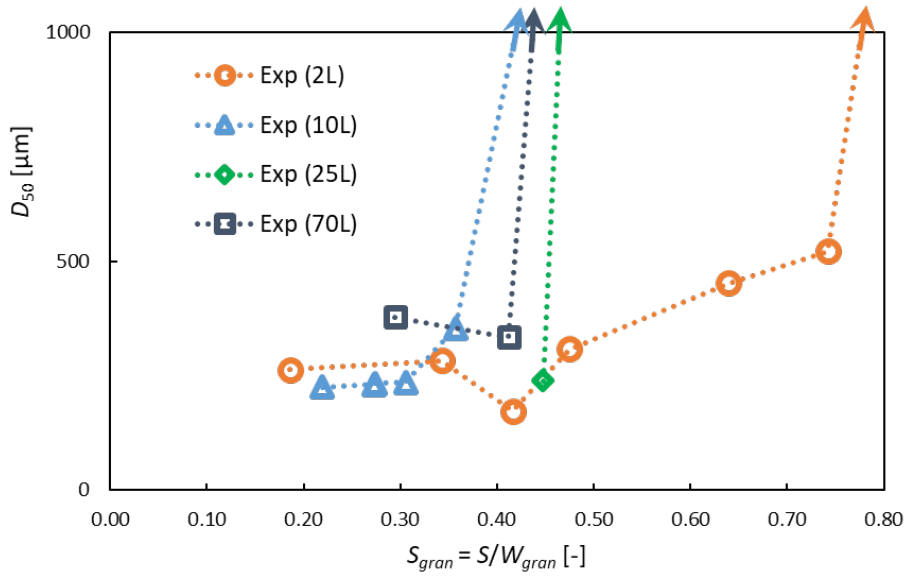

(b) Mass-median diameter D_{50} as a function of granule-specific pore saturation S_{gran}

Figure 6.15: Relationship between pore saturation S and granulated mass fraction W_{gran}

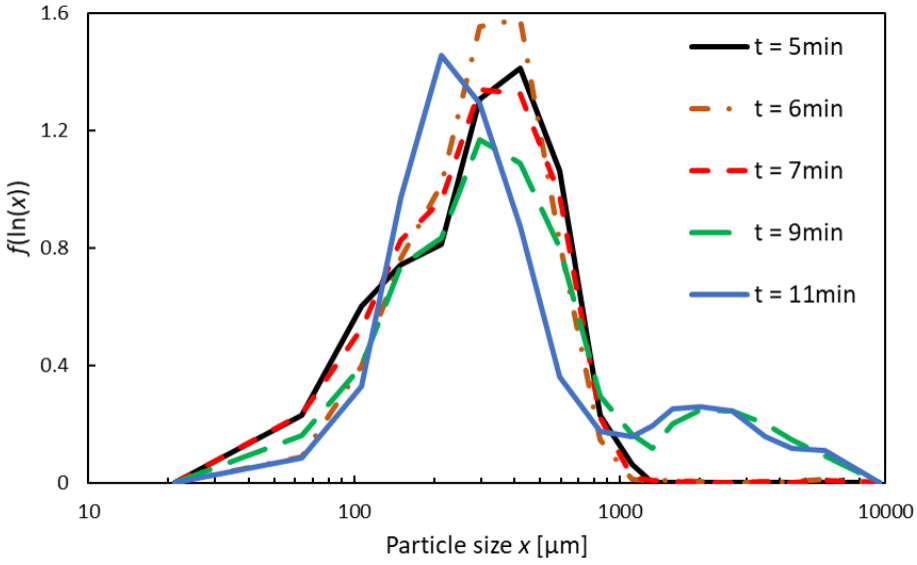

(a) PSD

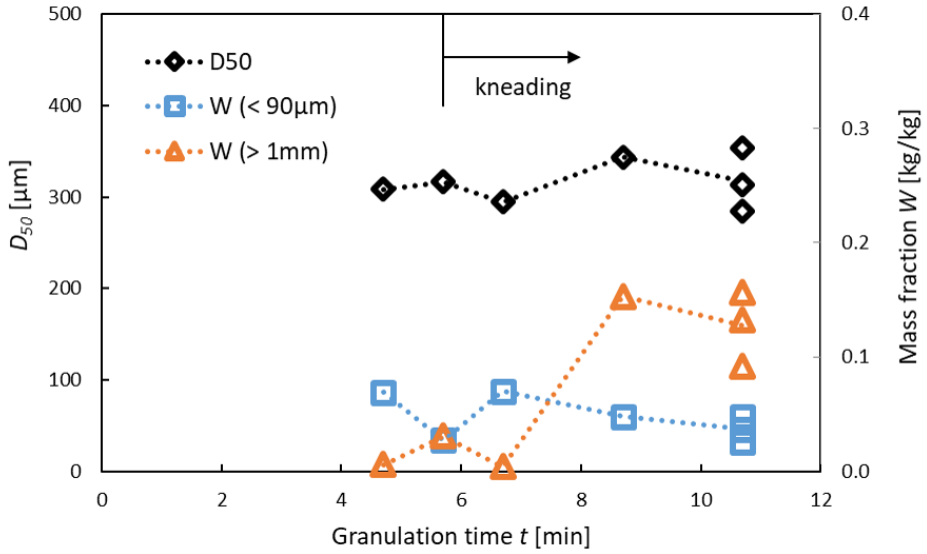

(b) Mass-median diameter D_{50}, fines mass fraction W ($< 90\,\mu m$) and coarse mass fraction W ($> 1\,mm$)

Figure 6.16: Induction growth conditions $S \approx S_{crit}$ (Exp 16 and 30-36: $V = 10\,L$; $t_{sp} = 5.7\,min$; $L/S = 0.17$; $Fr = 23$; $\Psi_a = 0.3$)

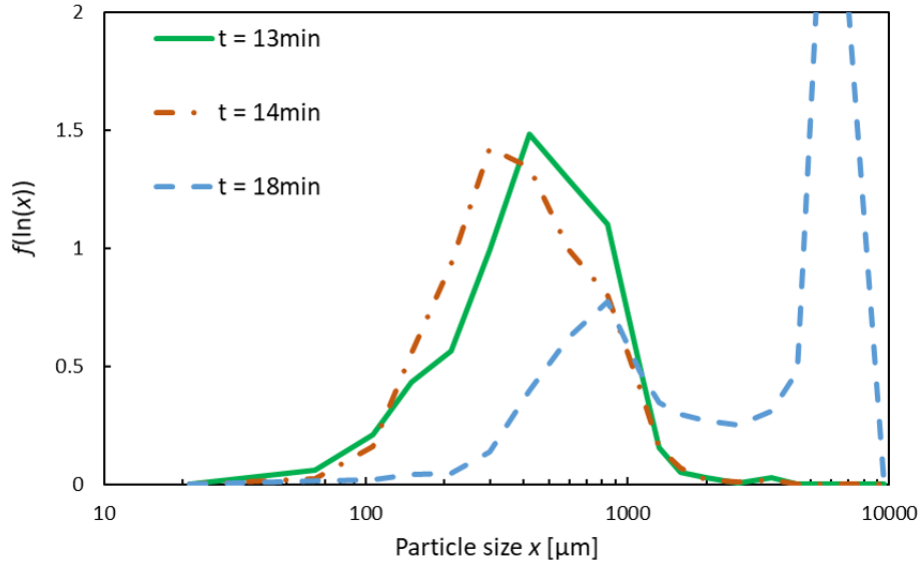

(a) PSD

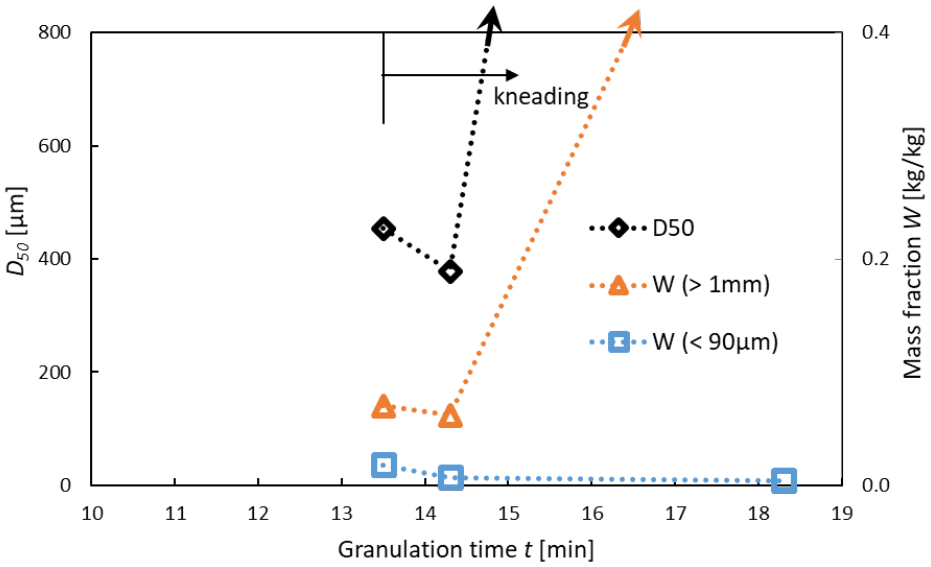

(b) Mass-median diameter D_{50}, fines mass fraction W (< 90 µm) and coarse mass fraction W (> 1 mm)

Figure 6.17: Rapid growth conditions $S \gg S_{crit}$ (Exp 42, 43 and 45: $V = 70$ L; $t_{sp} = 13$ min; $L/S = 0.19$; $Fr = 12$; $\Psi_a = 0.3$)

6.3.7 Breakage

Figure 6.18 shows PSD results of experiments at low L/S of 0.15. At these conditions, significant growth is not expected due to $S < S_{crit}$, and breakage is assumed to be the dominant mechanism. A continuous reduction in size is observed, as D_{50} and W (> 1 mm) continuously decrease with time. Additionally, W (< 90 µm) continuously increases with time. These findings indicate that granules break potentially due to high shear forces near the impeller tip. This confirms one of the critical model assumptions (see Section 5.4) because breakage consequently needs to be incorporated in modelling studies.

Experiments with and without chopper are compared in Figure 6.19. The PSD of the experiment without chopper is quantitatively very close to the other results. Moreover, the deviation from the original experiments appears smaller than the experimental error, and a size reduction is not observed at any particle size. Based on these results, it is concluded that the chopper does not have any effect on the mechanisms. This finding verifies the model assumption that the chopper does not have a significant effect (see Section 5.5).

6.4 *Conclusions*

In this chapter, a systematic experimental design approach for model-driven design (MDD) is demonstrated, in which experiments are designed at a wide range of operating conditions and four different process scales. The experimental design complies with process-specific engineering principles and safety guidelines. An assessment of drying methods shows that the conventional fluid bed drying method leads to a significant size reduction compared to tray oven drying. Since an accurate PSD measurement is essential for experimental investigations and downstream processing, tray dried samples should be used for product characterisation. Granule porosity is determined reliably from tap density measurements. The method produces representative results because it is applicable to any sample with a narrow size range.

It is demonstrated that all relevant wet granulation mechanisms can be isolated for systematic investigation. The findings of this investigation are in good agreement with mechanistic wet granulation understanding. By varying spray conditions in nucleation-only and granulation experiments, nucleation is investigated. The LND model is experimentally validated by assessing the nuclei size distribution predictions. To understand the effect spray conditions on nucleation, the drop diameter has to be taken into account as well as the dimensionless spray flux. Overall, spray conditions are

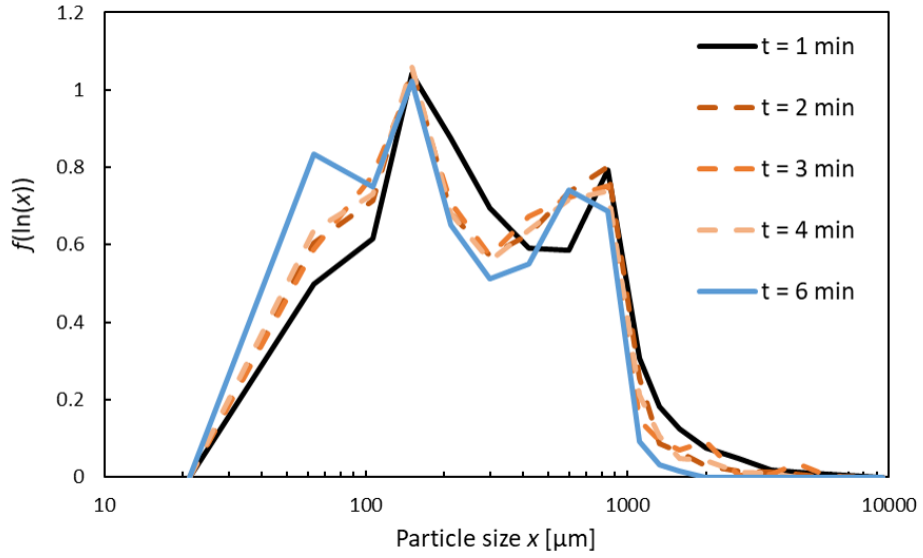

(a) PSD

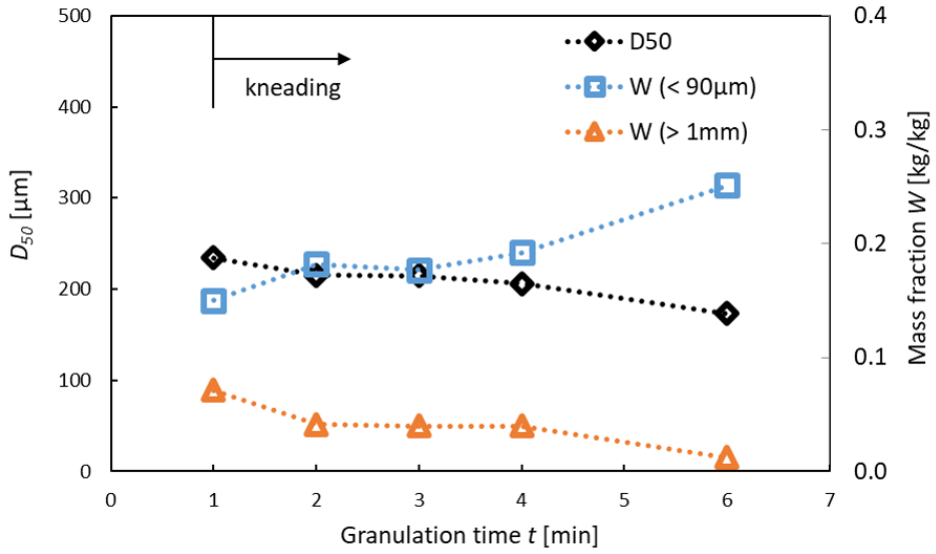

(b) Mass-median diameter D_{50}, fines mass fraction W ($< 90\,\mu m$) and coarse mass fraction W ($> 1\,mm$)

Figure 6.18: Breakage-only conditions (Exp 1 and 8-11: $V = 2\,L$; $t_{sp} = 1\,min$; $L/S = 0.15$; $Fr = 23$; $\Psi_a = 0.9$)

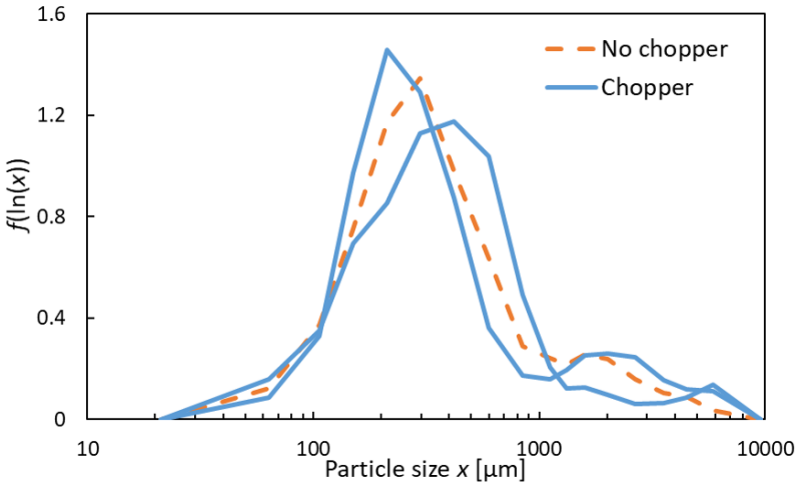

Figure 6.19: PSD of experiments with and without chopper (Exp 16, 36 and 37: $V = 10\,\mathrm{L}$; $t_{sp} = 5.7\,\mathrm{min}$; $L/S = 0.17$; $v_t = 6.2\,\frac{\mathrm{m}}{\mathrm{s}}$; $Fr = 23$; $\Psi_a = 0.3$; $n_{ch} = 1200\,\frac{1}{\mathrm{min}}$; $t_{kn} = 5\,\mathrm{min}$)

found to have a small impact on the granulation endpoint.

The porosity is measured at a wide range of operating conditions to study consolidation. Consolidation and the endpoint porosity heavily depends on liquid-to-solid ratio and impeller tip speed, and an empirical correlation for the endpoint porosity is assessed that is in acceptable agreement with the experimental data. Nevertheless, the empirical correlation overpredicts the porosity when rapid growth is observed. An accurate correlation for the endpoint porosity is beneficial for modelling and scale-up studies due to the impact of porosity on the granulation endpoint. Apart from denser granules, a lower porosity leads to significantly more growth. This finding shows the importance of evaluating the pore saturation to determine the growth regime. By evaluating pore saturation and PSD results, the growth regimes (nucleation-only, induction growth and rapid growth) are identified, and the critical range of the pore saturation is determined that marks the transition between these three regimes. In this study, the critical pore saturation is found to decrease with increasing scale. A range of phenomena are identified as reasons for the difference in behaviour at different scales: different mixing conditions which affect the distribution of liquid and different circulation time which affect granule breakage.

In breakage-only experiments, granule breakage is observed. It is concluded that breakage occurs mainly near the impeller tip because a significant effect of the chopper is not determined. These findings verify critical model assumptions. Overall, liquid-to-solid ratio is confirmed to be the most

crucial operating parameter. A significant impact of kneading time and impeller tip speed is only observed at high liquid-to-solid ratio.

Chapter 7

PREDICTIVE POPULATION BALANCE MODELLING OF HIGH-SHEAR WET GRANULATION

The parameter sensitivity study is supported by Aaron Yeardley, who trained a Gaussian Process metamodel with PBM simulation results to determine Sobol' indices under the supervision of Dr. Solomon Brown and Dr. Robert Milton.

7.1 *Introduction*

In this chapter, a case study is carried out applying the population balance modelling (PBM) framework developed in Chapter 5. The goal is to critically assess this model based on predictions of product properties (particle size distribution (PSD) and porosity) in the conventional operating space at different scales. A model assessment workflow is proposed that is suitable within a model-driven design (MDD) framework. In MDD, accurate predictions are important to derive key outputs such as the optimum operating range. The workflow is customised for scale-up purposes, as the experimental effort is reduced by minimising the requirement of small- and large-scale experimental data. Based on a systematic parameter sensitivity analysis approach, input parameters are determined from a combination of measurements, parameter estimation, literature data and assumptions with the goal to minimise the experimental effort and improve the model's predictive power. Compartmental modelling is assessed by comparing performance of the 1-comp and 2-comp PBM approaches. The model performance is assessed based on the accuracy of predictions at different scales. This is of particular importance because predicting the effect of scale on product properties and the critical L/S is crucial in scale-up and often fails with conventional scale-up approaches.

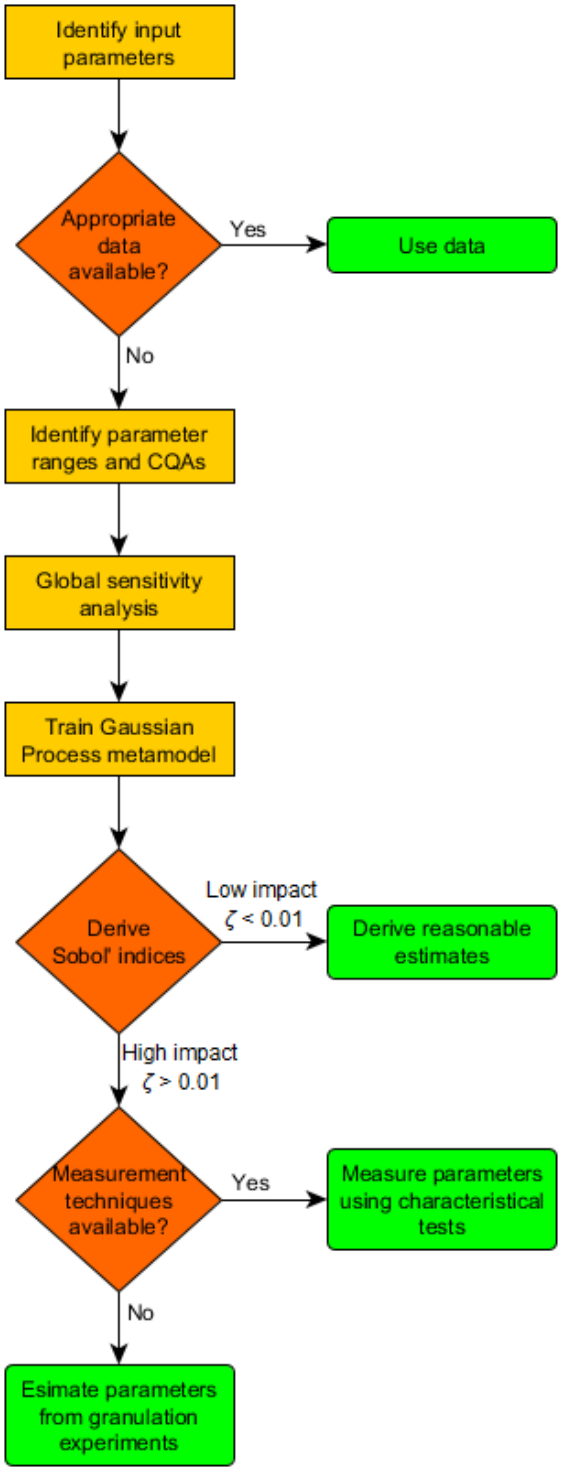

Figure 7.1: Workflow to determine model parameters

7.2 *Methodology*

A workflow is proposed which gives guidance on all critical decisions to determine the modelling parameters (Figure 7.1). The aim of this workflow is to limit the number of parameters to estimate. Reduced usage of parameter estimation improves the predictive power of models (see Section 2.3.1). The model requires input data for 34 physical properties and modelling parameters (Table 7.1).

Table 7.1: Overview of parameters

Parameter	Value	Source
$\rho_s \left[\frac{\mathrm{kg}}{\mathrm{m}^3}\right]$	1412 ± 6	Measurement
d_p [µm] (Eq. 5.32)	102	Section 3.1 and
K_d [−] (Eq. 5.19)	1.26 ± 0.07	Appendix B.2
$\rho_l \left[\frac{\mathrm{kg}}{\mathrm{m}^3}\right]$	1000	Tilton and Taylor [1922]
$\rho_{bulk} \left[\frac{\mathrm{kg}}{\mathrm{m}^3}\right]$ (Eq. 5.13)	416.7	Rohrer [2017]
μ [mPa s] (Eq. 5.35)	1	Korson et al. [1969]
$\gamma^{lv} \left[\frac{\mathrm{mN}}{\mathrm{m}}\right]$ (Eq. 5.32)	72.9	Pallas and Harrison [1990]
θ [°] (Eq. 5.32)	0	Assumption
h_a [µm] (Eq. 5.47)	1	Assumption
$f_{Mat} \left[\frac{\mathrm{kg\,m}}{\mathrm{J}}\right]$ (Eq. 5.58)	1	Assumption
$E_{m,kin} \left[\frac{\mathrm{J}}{\mathrm{kg}}\right]$ (Eq. 5.58)	1000	Assumption
q [−] (Eq. 5.61)	1	Assumption
$d_{j,min}$ [µm] (Eq. 5.61)	10	Assumption
ν [−] (Eq. 5.43)	0.03	Pohlman and Litster [2015]
k_E [−] (Eq. 5.46)	24.2	Pohlman and Litster [2015]
p_E [−] (Eq. 5.46)	0.17	Pohlman and Litster [2015]
q_E [−] (Eq. 5.46)	−6.9	Pohlman and Litster [2015]
r_E [−] (Eq. 5.46)	−1.5	Pohlman and Litster [2015]
A [−] (Eq. 5.35)	7	Smith [2007]
B [−] (Eq. 5.35)	221	Smith [2007]

Continued on next page

Table 7.1 – continued from previous page

Parameter	Value	Source
n [−] (Eq. 5.35)	0.58	Smith [2007]
m_1 [−] (Eq. 5.22)	-3.0 ± 0.9	Parameter estimation (PSD, 600 MCS) Section 4.4.1
m_2 [−] (Eq. 5.22)	1.9 ± 0.2	
m_3 [−] (Eq. 5.22)	-0.05 ± 0.05	
s_1 [−] (Eq. 5.22)	-3.4 ± 0.9	
s_2 [−] (Eq. 5.22)	1.0 ± 0.2	
s_3 [−] (Eq. 5.22)	0.32 ± 0.02	
e_1 [−] (Eq. 5.30)	0.58 ± 0.13	Parameter estimation (Porosity, 25 experiments) Section 6.3.5
e_2 [−] (Eq. 5.30)	0.13 ± 0.03	
e_3 [−] (Eq. 5.30)	0.67 ± 0.10	

Measurement data is already available for the physical properties ρ_s, ρ_l, ρ_{bulk} and d_p (see Section 3.1). Furthermore, the empirical parameters $m_{1..3}$, $s_{1..3}$ and $e_{1..3}$ are determined previously (see Sections 4.4.1 and 6.3.5). $m_{1..3}$ and $s_{1..3}$ are estimated based on data from 600 Monte Carlo simulations (MCS) which predict the nuclei size distribution. $e_{1..3}$ are estimated using endpoint porosity data from 25 experiments at different scales. Experimental data that includes the effect of L/S and impeller tip speed v_t is selected for this parameter estimation. The selection of experiments is not ideal for scale-up purposes because large-scale experimental data (25 L and 70 L) is used as input.

All remaining parameters are unknown. For these parameters, reasonable parameter ranges are identified, and four critical quality attributes (CQAs) are selected to represent the results: volume moment mean diameter d_{43}, fines mass fraction W ($< 90\,\mu m$), coarse mass fraction W (> 1 mm) and granule porosity ε.

A parameter sensitivity analysis is required to determine the impact of all unknown parameters on the CQAs. This parameter sensitivity analysis is carried out by applying a global sensitivity analysis (GSA) approach. In GSA, parameters are varied simultaneously to determine both the individual and combined effects of parameters [Iooss and Lemaître, 2015]. A new set of parameter

values is generated for each sampling point of the GSA. All parameter values are generated using a pseudo-random sampling method [Matsumoto and Nishimura, 1998] applying a normal distribution within the parameter ranges. 740 sampling points are generated, and the 1-comp PBM approach is used to determine the predicted values of the CQAs applying the experimental conditions of Exp 17 ($V = 10\,\mathrm{L}$, $L/S = 0.21$). The GSA tool of gPROMS is used to generate the sampling points and determine the predicted values of the CQAs.

A Gaussian Process metamodel is fitted to the GSA results with the goal to determine Sobol' indices for each parameter-CQA combination [Sobol', 2001; Marrel et al., 2009]. First-order Sobol' indices $\zeta_{i,j}$ quantify the relative impact of parameters on specific model outputs by determining the ratio of the variance Var of output y_j due to input x_i to the total variance Var of output y_j (Eq. 7.1). On this basis, the most important parameters are identified. First-order Sobol' indices only characterise the main effect of individual input parameters. Total parameter interactions are determined based on the sum of indices, which is 1 for each output (Eq. 7.2). This method is described in detail by Milton and Brown [2020].

$$\zeta_{i,j} = \frac{Var\left(x_i | y_j\right)}{Var\left(y_j\right)} \tag{7.1}$$

$$\Sigma_i \zeta_{i,j} = 1 \tag{7.2}$$

All parameters with low impact ($\zeta_{i,j} < 0.01$) are determined by applying reasonable assumptions. Physical parameters with high impact ($\zeta_{i,j} > 0.01$) are measured, and only empirical parameters with high impact are estimated using results from designed experiments (see Table 6.5). The parameter estimation workflow shown in Figure 7.2 is applied to separately determine the parameters of both models (1-comp and 2-comp PBM). Overall, the goal of this parameter estimation is to obtain estimates that provide accurate predictions across scales V to accurately determine the optimum operating range and the CQAs in this operating range. To estimate the set of parameters $\vec{x}$, the discrepancy between experimental (ε^{exp}, $f^{exp}\left(\ln(x)\right)$) and simulation ($\varepsilon^{sim}$, $f^{sim}\left(\ln(x)\right)$) results is optimised using the maximum likelihood objective function:

$$\min_{\vec{x}} \quad \sum_{i=1}^{n} \left[\frac{\varepsilon^{exp}\left(i\right) - \varepsilon^{sim}\left(\vec{p}(i), \vec{x}\right)}{\sigma_{\varepsilon}^2} + \frac{f^{exp}\left(\ln(x)\right)\left(i\right) - f^{sim}\left(\ln(x)\right)\left(\vec{p}(i), \vec{x}\right)}{\sigma_f^2} \right] \tag{7.3}$$

with

$$\vec{x} = \left[S_{crit}, k_{cons}, k_{br}, k_{I/II}\right] \tag{7.4}$$

where i is the experiment number, σ^2 is the measurement variance and $\vec{p}$ is the set of operating parameters.

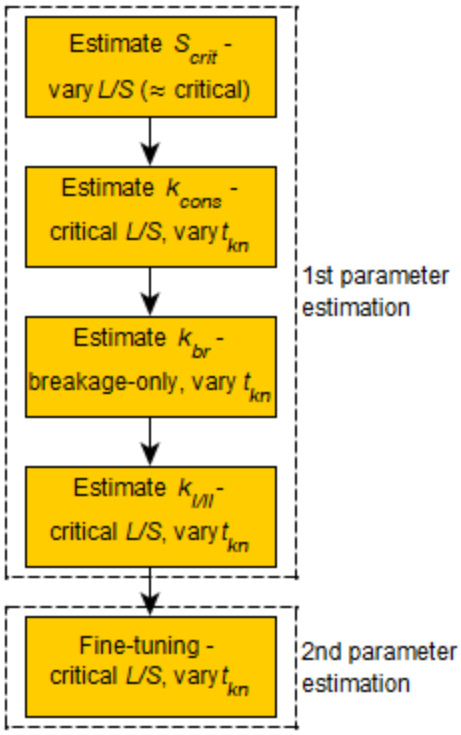

Figure 7.2: Workflow for parameter estimation

To estimate parameters, experiments are selected that isolate the effect of individual parameters by promoting the relevant rate process. In a 1st estimation, the best fit is determined for the four parameters individually, and the residual three parameters are kept constant. At this stage, the parameters are estimated in the following order to minimise the effect of parameters which are still unknown: S_{crit}; k_{cons}; k_{br}; $k_{I/II}$. The parameter values determined are used as inputs for subsequent estimations. For this estimation, parameters are varied manually as well as using the gPROMS optimisation algorithm to find the best fit. k_{cons} is estimated using porosity data of selected experiments, and the discrete PSD profile is used for the remaining parameters (see Chapter 6). Experiments with varying kneading time t_{kn} are selected to estimate kinetic modelling

parameters for better results (see Section 6.2).

To estimate S_{crit}, experiments that show the transition between nucleation-only (below critical L/S) and induction growth regime (critical L/S) are selected (Exp 12 and 16: $V = 10\,\mathrm{L}$; $L/S = 0.15 - 0.17$), and it has to be ensured that the estimate for S_{crit} is between the pore saturation S of the two experiments chosen. k_{cons} is estimated using porosity data in the induction growth regime with varying time (Exp 16, 30, 31, 32, 34 and 36: $V = 10\,\mathrm{L}$; $L/S = 0.17$; $t = 6\,\mathrm{min} - 11\,\mathrm{min}$). k_{br} is estimated using breakage-only experiments, in which breakage is more dominant than growth (Exp 1, 8, 9, 10 and 11: $V = 2\,\mathrm{L}$; $L/S = 0.15$; $t = 1\,\mathrm{min} - 6\,\mathrm{min}$). $k_{I/II}$ is estimated using PSD data in the induction growth regime, in which coalescence is dominant (Exp 16, 30, 31, 32, 34 and 36: $V = 10\,\mathrm{L}$; $L/S = 0.17$; $t = 6\,\mathrm{min} - 11\,\mathrm{min}$). Experimental data in the rapid growth regime is not considered for parameter estimation because it is considered outside the conventional operating space. Finally, all parameters are estimated simultaneously for fine-tuning (2^{nd} estimation) using experiments in the induction growth regime because all rate processes occur simultaneously (Exp 16, 30, 31, 32, 34, 36 and 37: $V = 10\,\mathrm{L}$; $L/S = 0.17$; $t = 6\,\mathrm{min} - 11\,\mathrm{min}$). The experimental dataset chosen to estimate these parameters is very promising because the experiments selected isolate the mechanisms and focus on the critical operating regimes. Furthermore, all experiments are conducted at lab scale (2 L and 10 L) which is ideal for scale-up purposes.

The parameter estimates are assessed based on the experimental data used previously. For the model validation, the model is assessed based on predictions of new experimental data. This more rigorous assessment includes experimental data at various scales (2 L, 10 L, 25 L and 70 L), which is necessary to assess the performance of a predictive model for scale-up. The performance at 25 L and 70 L is particularly important because experiments at these scales are not used for parameter estimation.

The model performance is also assessed based on the relative sum of squared errors $RSSE_O$ for the four CQAs:

$$RSSE_O = \frac{1}{n}\sum_{i=1}^{n}\left(\frac{O_{exp} - O_{sim}}{\max\left(O_{exp}, O_{sim}\right)}\right)^2 \tag{7.5}$$

with

$$O = \left[D_{50}, W\left(< 90\,\mu\mathrm{m}\right), W\left(> 1\,\mathrm{mm}\right), \varepsilon\right] \tag{7.6}$$

where O_{exp} and O_{sim} are the experimental and simulation CQA results respectively, and n is

the total number of experiments. Additionally, predictions of the critical liquid-to-solid ratio L/S are assessed using experimental findings (see Section 6.3.6). The critical L/S is here identified as the highest L/S at which $D_{50} < 500\,\mu m$ and $W\,(> 1\,mm) < 0.1\,\frac{kg}{kg}$.

7.3 *Results and discussion*

7.3.1 Parameter sensitivity analysis

All Sobol' indices $\zeta_{i,j}$ above 0.01 are displayed in Figure 7.3. The results show that 6 out of 20 parameters (K_d, k_{cons}, S_{crit}, k_{br}, $k_{I,II}$ and h_a) have a significant impact ($\zeta_{i,j} > 0.01$). All other 14 parameters have a negligible impact on the four CQAs ($\zeta_{i,j} < 0.01$). Full results are shown in Appendix D.3. Overall, the consolidation coefficient k_{cons} has the most decisive impact, especially on fines mass fraction and porosity. Interactions are identified for all CQAs related to particle size (volume moment mean diameter, fines mass fraction, coarse mass fraction). This is expected as all these parameters have direct or indirect impact on mechanisms that influence granule size. For porosity, the interaction is determined to be negligible as only one parameter k_{cons} has a significant impact. The material property nuclei-to-drop diameter ratio K_d is measured using a characterisation method. The modelling parameters consolidation coefficient k_{cons}, critical pore saturation S_{crit}, collision coefficient $k_{I,II}$ and breakage coefficient k_{br} cannot be measured and are estimated. Additionally, the height of asperities h_a is identified to have a small impact on the CQAs ($\zeta_{i,j} \approx 0.01$). However, a strong interaction between h_a and S_{crit} is determined based on an analytical assessment (see Section 5.2.6). Therefore, a reasonable value for h_a is assumed. Consequently, those parameter values are determined based on literature data and reasonable assumptions. Figure 7.4 shows that reasonable parameter values are obtained from different sources, and only a relatively small proportion of parameters need to be estimated, which is crucial for predictive modelling. Table 7.1 lists all modelling parameters that are not estimated using the PBM approach.

7.3.2 Parameter estimation

The parameter estimates are displayed in Table 7.2. The relatively narrow confidence intervals show that promising estimates are obtained. Furthermore, the 2nd estimates of both modelling approaches are very similar to the 1st estimates, confirming that the parameters are only fine-tuned in the 2nd estimation. Having said this, one parameter k_{cons} is estimated with a wide confidence interval,

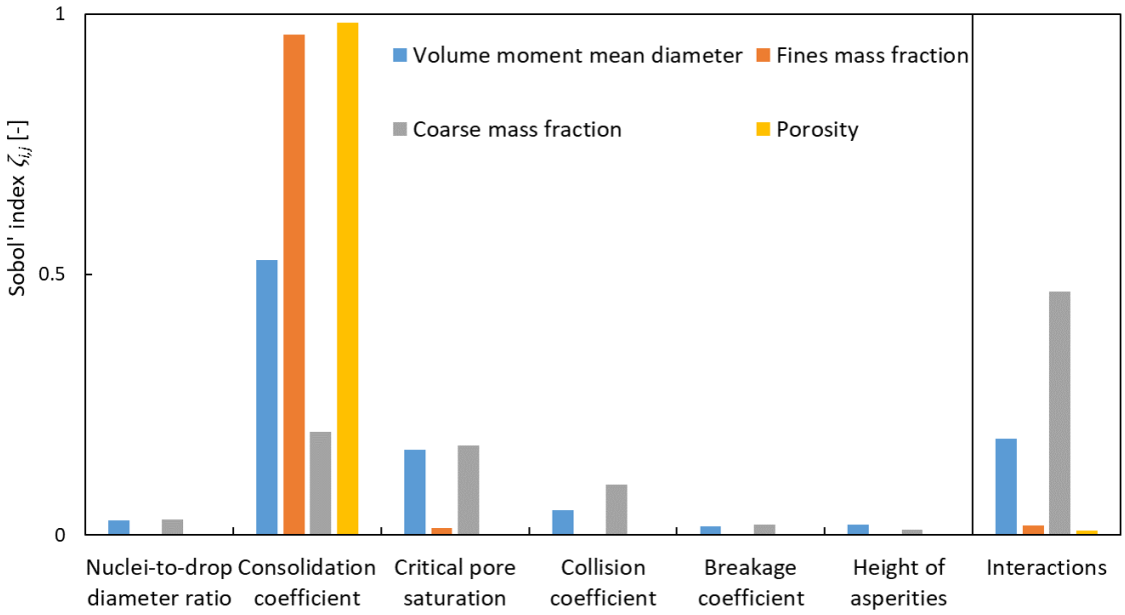

Figure 7.3: Relevant first-order Sobol' indices results ($\zeta_{i,j} > 0.01$) and total parameter interactions

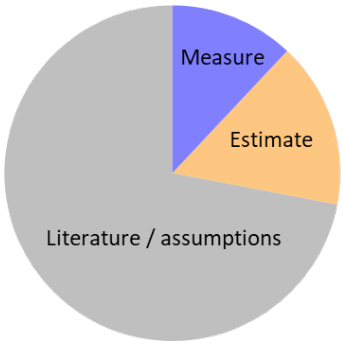

Figure 7.4: Usage of parameter determination methods

and the 2nd estimate deviates significantly from the 1st estimate. Both observations indicate that the parameter's effect is not significant in this range. A sensitivity analysis shows that k_{cons} has a significant impact on the results when $k_{cons} < 1$. For $k_{cons} > 1$, the impact of k_{cons} is marginal because the endpoint porosity is reached nearly instantly. This indicates that consolidation is rapid for $k_{cons} > 1$ (see Appendix D.4).

Compared to the 1-comp PBM results, the 2-comp PBM gives slightly deviated values for the kinetic parameters (k_{cons}, k_{br} and $k_{I/II}$) because of shorter exposure times to their respective rate processes. In 2-comp PBM, each rate process is assumed to occur only in one specific compartment (see Section 5.2.8).

Table 7.2: Parameter estimation results (95 % confidence interval)

Parameter	1-comp PBM		2-comp PBM	
	1st estimation	2nd estimation	1st estimation	2nd estimation
S_{crit} [−]	0.15	0.149 ± 0.002	0.15	0.149 ± 0.002
k_{cons} [−]	1	3 ± 2	1	4 ± 2
k_{br} [−]	0.0027 ± 0.0002	0.0034 ± 0.0003	0.029 ± 0.002	0.033 ± 0.003
$k_{I/II}$ $\left[\log_{10} \mu m^{1.5}\right]$	13.51 ± 0.04	13.56 ± 0.08	13.41 ± 0.04	13.38 ± 0.02

The parameter correlations (2nd estimation using 1-comp PBM) are shown in Table 7.3. Any parameter pair with a correlation greater than 0.7 is considered strongly correlated, a correlation less than 0.5 is considered to be low, and a negligible correlation is depicted by a correlation less than 0.25 [Munro, 2005]. S_{crit} shows strong correlations of around 0.7 with k_{cons} and $k_{I/II}$. These results support that the impact of S_{crit} and k_{cons} on the time needed to form a liquid layer are both significant. S_{crit} and $k_{I/II}$ are correlated because coalescence strongly depends on both parameters (see Section 5.2). k_{cons} has a low correlation of around 0.3 with two parameters $k_{I/II}$ and k_{br}. Consolidation does not directly interact with coalescence and breakage. Nevertheless, all three rate processes have an effect on the PSD. That is why a low correlation between the main parameters for these three rate processes is reasonable. k_{br} does not show a significant correlation (< 0.15) with the two remaining parameters S_{crit} and $k_{I/II}$ because breakage does not depend on pore saturation or directly interact with coalescence.

Table 7.3: Parameter correlation for the 1-comp PBM

Parameter	S_{crit}	k_{cons}	k_{br}	$k_{I/II}$
S_{crit}	1			
k_{cons}	0.73	1		
k_{br}	0.13	0.31	1	
$k_{I/II}$	0.70	0.33	0.10	1

Simulation results are compared to experimental data used previously for parameter estimation (Figures 7.5, 7.6 and 7.7). The comparison includes PSD profiles of selected experiments, porosity ε and three PSD parameters (mass-median diameter D_{50}, fines mass fraction W ($< 90\,\mu m$) and coarse mass fraction W ($> 1\,mm$)). Both modelling approaches (1-comp PBM and 2-comp PBM) give nearly identical results because both approaches are based on very similar assumptions (see Section 5.2). The PSD profiles at both experimental conditions agree well with the experimental results, as the peak is well captured (Figure 7.5). The trajectories of the porosity represent the measurements well (Figure 7.6), and also the D_{50} and W ($< 90\,\mu m$) are in very good agreement (Figure 7.7a). While the trend of W ($> 1\,mm$) is captured well, a small quantitative mismatch occurs at kneading times above 3 min (Figure 7.7c). This mismatch is slightly higher for the 1-comp PBM approach. This small mismatch becomes more apparent by examining the PSD profiles more closely (Figure 7.5). The experiments show a mono-modal PSD at low kneading times, and a broad, bi-modal PSD at high kneading times. While the mono-modal PSD is represented very well, PSD at higher kneading times disagrees slightly because it remains mono-modal. Considering all this, both models are capable of representing this experimental data, as they capture the trend for porosity and important PSD parameters at these critical conditions.

Figure 7.8 compares the PSD profile of the simulations with experimental duplicates. Both models give very similar results, and the experimental PSD is represented well. The peaks of the model PSD are between the peaks of the experimental duplicates, which indicates that the model error is smaller than the experimental error for these conditions. Having said that, the aforementioned mismatch at larger particle size is also observed in this case. The experimental data shows a broad, bi-modal PSD with particles well above 2 mm, and the models result in mono-modal PSD with a

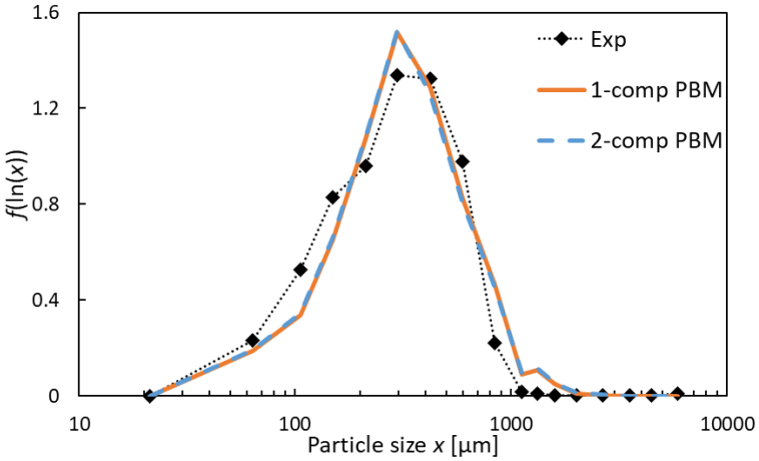

(a) Exp 32: $t_{kn} = 1$ min

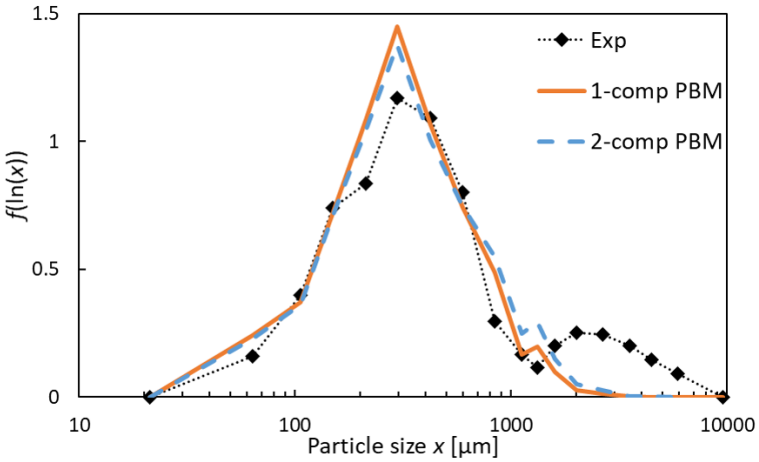

(b) Exp 34: $t_{kn} = 3$ min

Figure 7.5: Comparison of experimental PSD data and fit (Exp 32 and 34: $V = 10\,\mathrm{L}$; $L/S = 0.17$; $Fr = 23$)

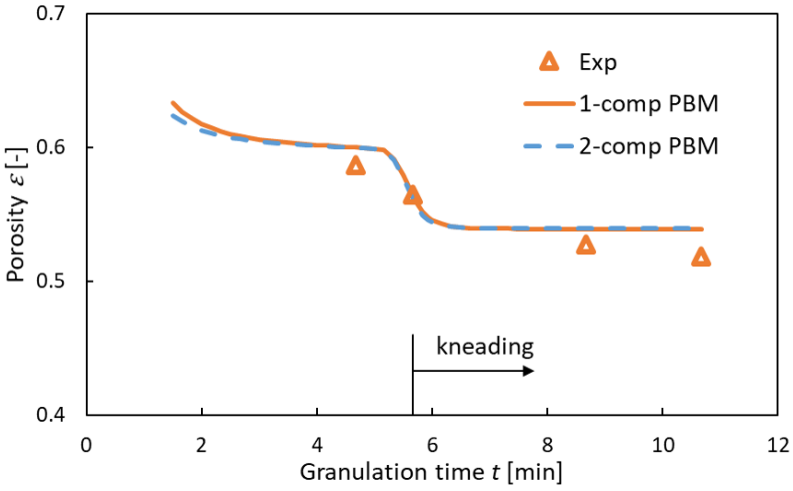

Figure 7.6: Comparison of experimental porosity data and fit (Exp 16 and 30-36: $V = 10\,\mathrm{L}$; $t_{sp} = 5.7\,\mathrm{min}$; $L/S = 0.17$; $Fr = 23$; $\Psi_a = 0.3$)

negligible amount above 2 mm. All things considered, both models are promising approaches and are further assessed because experimental data is well represented. For further model assessment, new experimental data is predicted at a wider range of conditions and different equipment scales.

7.3.3 Model validation

Liquid-to-solid ratio

Figures 7.9, 7.10 and 7.11 show a comparison of PSD predictions and experimental data with varying L/S at three different scales: 10 L, 25 L and 70 L. The 1-comp PBM predictions are in good qualitative and quantitative agreement at these scales. The strong effect of L/S on the PSD, which is observed experimentally, is predicted well. Additionally, the predictions are in very good quantitative agreement at low L/S ($S < S_{crit}$). The critical L/S, at which the PSD starts to increase significantly, is slightly underpredicted by around 0.01 at 25 L and 70 L (Figures 7.10 and 7.11). This small mismatch results in a marginal offset (in D_{50} and W (> 1 mm)) and quantitative mismatch at the critical L/S. The predicted optimum operating range is slightly smaller than in practice due to this offset. Consequently, the model prediction for the operating range is too conservative which is only minor concern in process design and scale-up. This mismatch is not observed at 10 L because experimental data at critical L/S is used to estimate parameters (see Section 7.2). The models predict

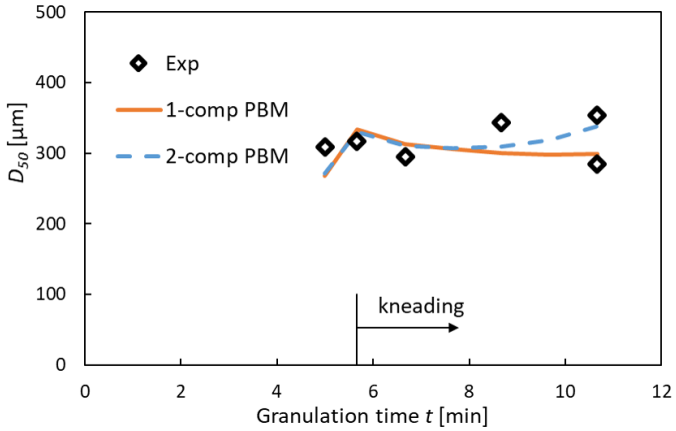

(a) Mass-median diameter D_{50}

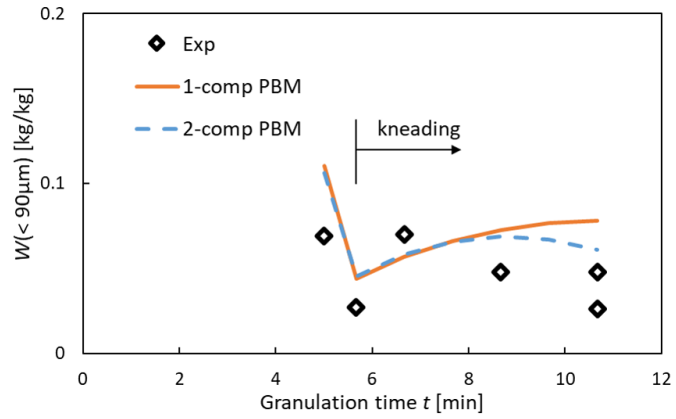

(b) Fines mass fraction W (< 90 µm)

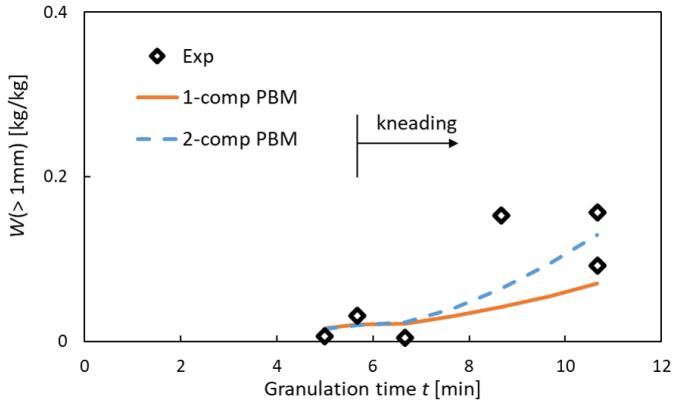

(c) Coarse mass fraction W (> 1 mm)

Figure 7.7: Comparison of experimental particle size data and fit (Exp 16 and 30-36: $V = 10$ L; $t_{sp} = 5.7$ min; $L/S = 0.17$; $Fr = 23$; $\Psi_a = 0.3$)

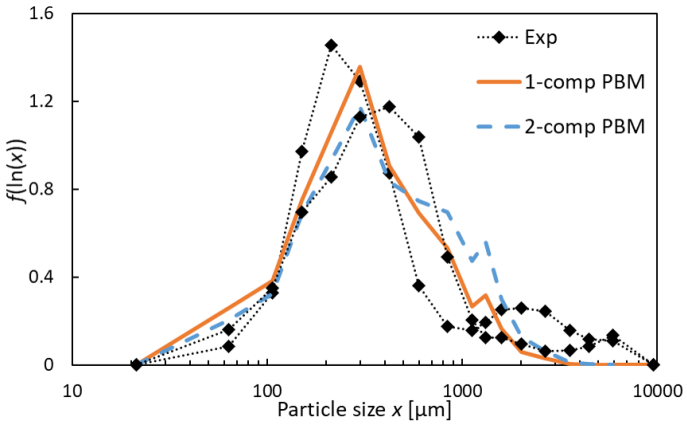

Figure 7.8: Assessment of fit based on PSD (Exp 16 and 36: $V = 10\,\mathrm{L}$; $L/S = 0.17$; $Fr = 23$; $t = 11\,\mathrm{min}$)

the PSD to increase further above the critical L/S. However, the predictions do not show the drastic increase which is observed experimentally ($S \gg S_{crit}$). Consequently, experimental data at very high L/S is not predicted accurately. Overall, the predictions of the critical L/S and PSD in the optimum operating range is in good agreement with experimental data across three different scales. Therefore, it is concluded that the predictive modelling approach is applicable for scale-up purposes.

Figure 7.12 compares PSD predictions and experimental data with varying liquid-to-solid ratio L/S at 2 L scale. At low L/S, the predictions for D_{50} and W (> 1 mm) are in good agreement with the experimental data. Both modelling approaches predict a significant size increase at $L/S = 0.17-0.21$ and an almost constant particle size above $L/S = 0.19$. The experimental data shows a slight size increase upto $L/S = 0.25$ and a significant increase for $L/S > 0.25$. This shows that the model qualitatively disagrees with experimental data for $L/S > 0.17$ at 2 L scale. It is concluded that the mismatch is a result of the dissimilar process behaviour at 2 L, which is described in Section 6.3.6.

Kneading time

Predictions for porosity and PSD are compared to experimental data with varying time at 70 L in Figure 7.13. Only the trajectory of the porosity is a model prediction because the porosity at the endpoint is used to estimate empirical parameters (see Section 6.3.5). Even though the endpoint porosity is considerably overpredicted, the porosity at the beginning of the kneading phase is in reasonable agreement (Figure 7.13a). The experiments show a decrease in porosity at the beginning

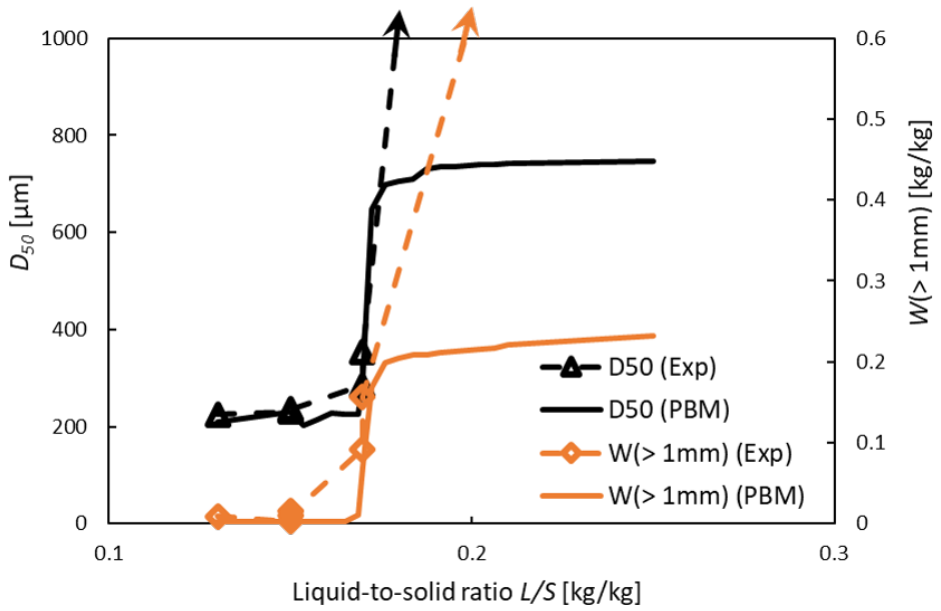

Figure 7.9: 1-comp PBM predictions and experimental data with varying L/S at 10 L (Exp 12, 15-17, 22, 23, 36 and 37: $Fr = 23$)

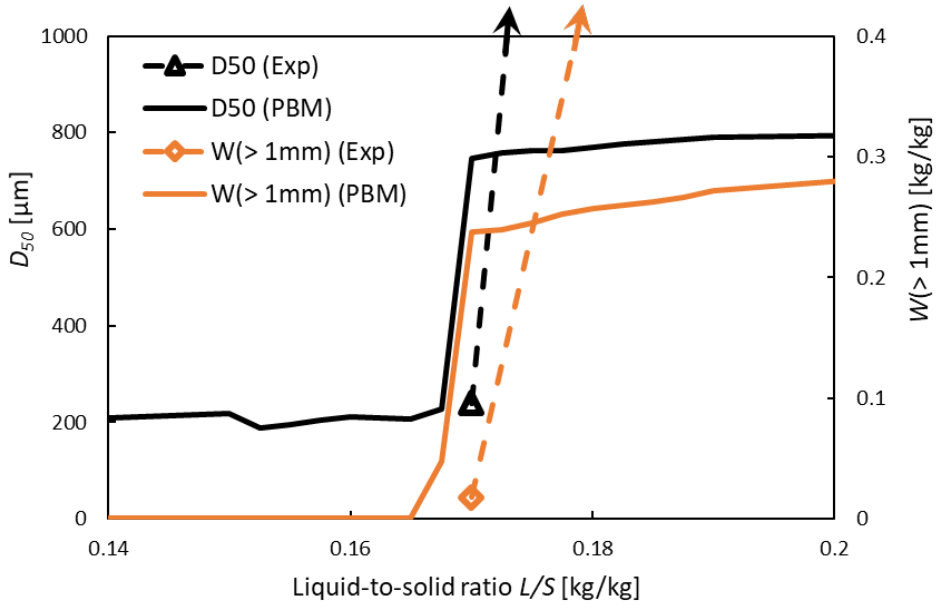

Figure 7.10: 1-comp PBM predictions and experimental data with varying L/S at 25 L (Exp 38-40: $Fr = 22$)

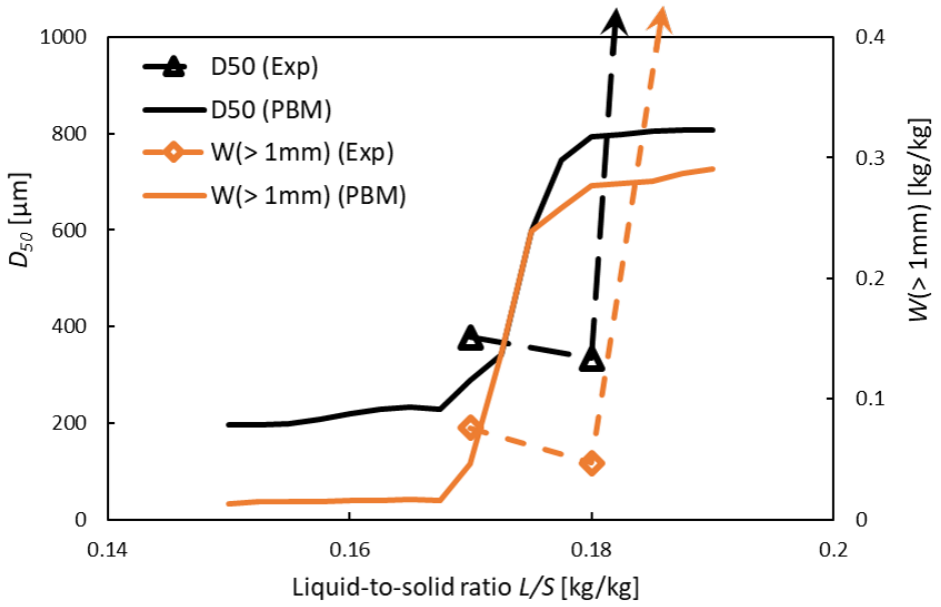

Figure 7.11: 1-comp PBM predictions and experimental data with varying L/S at 70 L (Exp 44-46: $Fr = 12$)

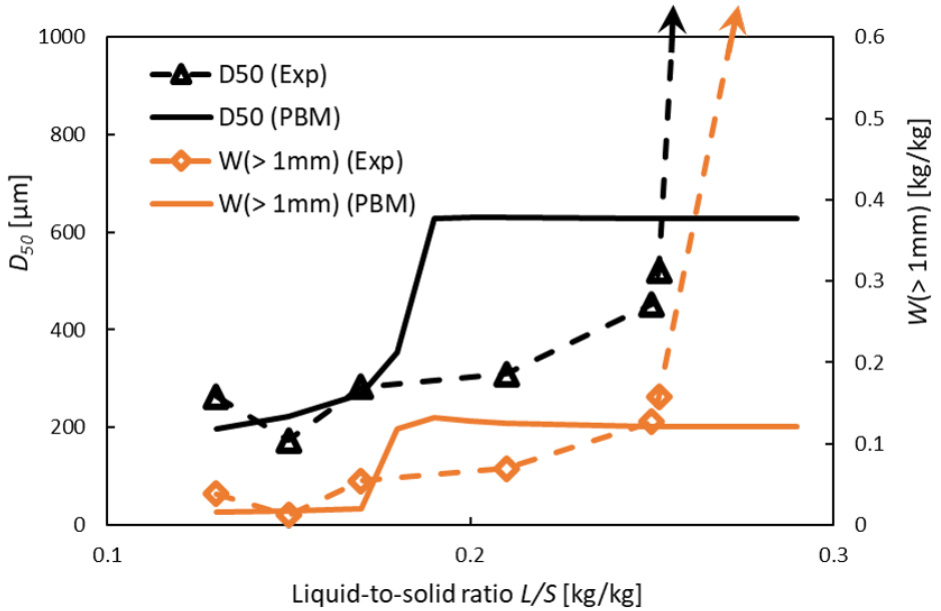

Figure 7.12: 1-comp PBM predictions and experimental data with varying L/S at 2 L (Exp 1, 4-7, 27 and 28: $Fr = 23$)

of the kneading phase, while the models predict a very similar decrease slightly before that. The PSD prediction is very accurate at the beginning of the kneading phase (Figure 7.13b). As porosity decreases over time (see Figure 7.13a), pore saturation S is increasing. For this reason, the effect of granulation time is similar to the effect of increasing L/S. With increasing time, a slight offset at the start of the significant size increase is observed at $t \approx 13$ min ($S \approx S_{crit}$), and the PSD at the granulation endpoint is drastically underpredicted ($S \gg S_{crit}$). On the one hand, the mismatch in the endpoint porosity is likely to lead to a slight underprediction of growth, but on the other hand, growth is predicted to slow down, as D_{50} and W (> 1 mm) are levelling off. This indicates that the models are not capable to predict a significantly larger particle size.

Overall performance

1-comp PBM predictions of the critical L/S are compared to experimental data in Figure 7.14. The predictions are in very good agreement with the experimental data at the scales 10 L, 25 L and 70 L. For scale-up, accurate predictions of the critical L/S are important, especially for these larger scales. As the 1-comp PBM is capable of predicting the critical L/S, it is a useful tool to predict the desired operating range. The critical L/S is considerably underpredicted at 2 L but this mismatch is not severe for scale-up purposes as this scale is smaller than the initial scale of 10 L.

All model CQA results are compared to experimental data in Figures 7.15 and 7.16. Experiments with a kneading time greater than 2 min are predicted to reach the endpoint porosity ε (Figures 7.6 and 7.13a), and experiments with very low L/S (< 0.15) are predicted to reach maximum endpoint porosity of 0.6 (see Section 5.2.4). High porosity measurements are represented well as the predictions only slightly deviate from the experimental data. A more significant mismatch is observed for low porosity measurements which are observed under at high W (> 1 mm) above 0.3 $\frac{\text{kg}}{\text{kg}}$ (indicated by the solid fill ■ in Figure 7.15a). This mismatch is a direct consequence of the mismatch of the empirical correlation for the endpoint porosity which is observed at the same experimental conditions (see Section 6.3.5).

As shown in Figure 7.15b, the D_{50} predictions are in acceptable agreement with the experimental data. The models are capable of predicting the experimental D_{50} results below 1000 µm. In this range, the models tend to overpredict the experimental data confirming that the predictions are slightly too conservative. Having said this, high experimental D_{50} results are noticeably underpredicted confirming the quantitative mismatch in the rapid growth regime. A quantitative mismatch in the

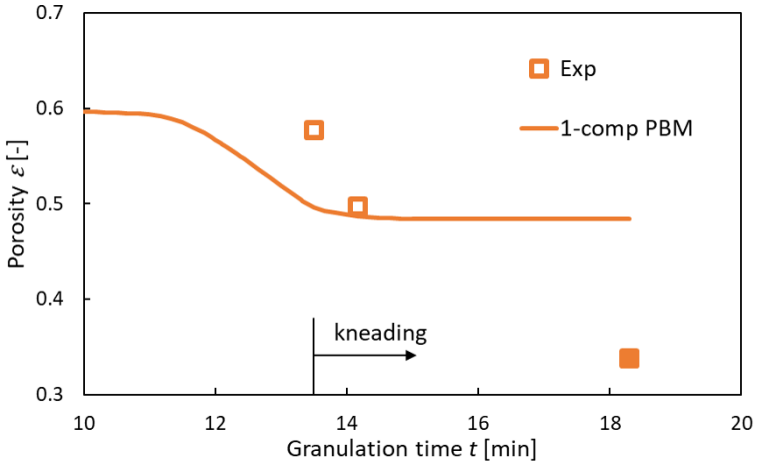

(a) Porosity ε

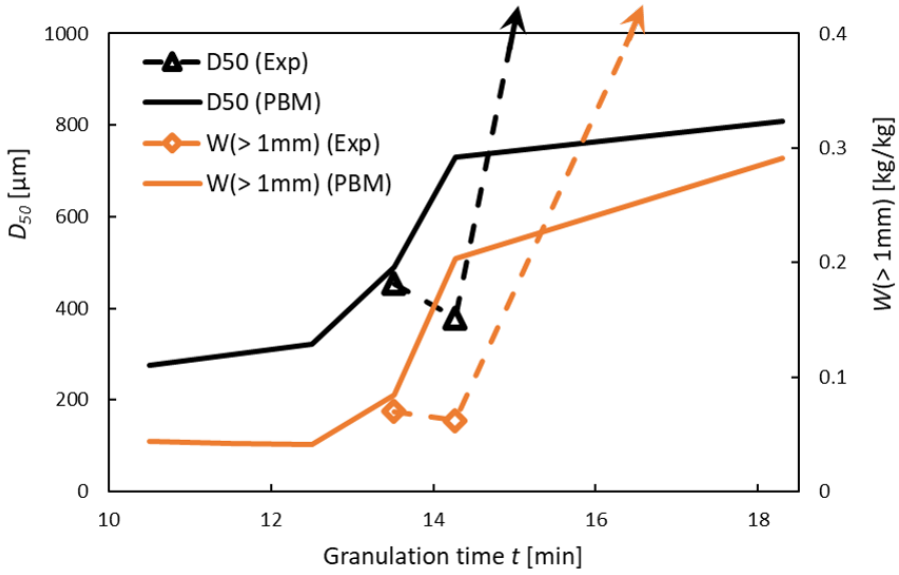

(b) Mass-median diameter D_{50} and coarse mass fraction W ($>$ 1 mm)

Figure 7.13: 1-comp PBM predictions and experimental data with varying granulation time t at 70 L (Exp 42, 43 and 45: $L/S = 0.19$; $Fr = 12$)

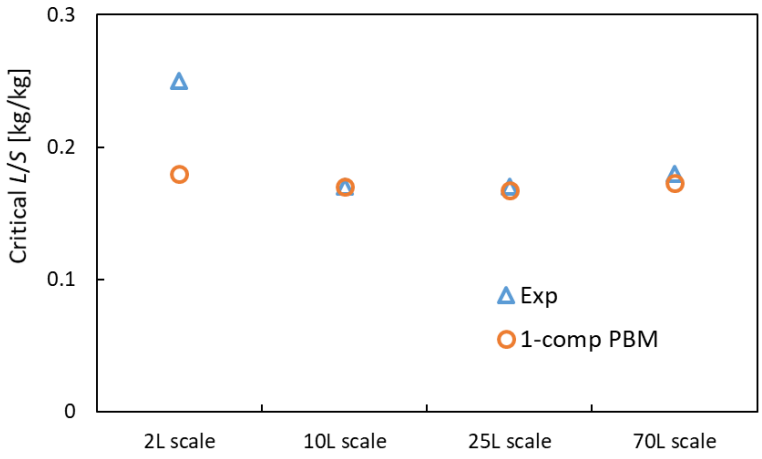

Figure 7.14: Critical L/S predictions across scales

rapid growth regime is not a concern for this application because an operation in this regime is not desired.

Figure 7.16a shows that W ($< 90\,\mu m$) is predicted well by the 1-comp PBM. Most experimental results are predicted accurately, and no trend is identified for the small mismatches. The comparison of the W ($> 1\,mm$) results follows the trend identified for the D_{50} results. Most experiments are predicted accurately but conservative overpredictions are observed for $W\,(> 1\,mm) < 0.2\,\frac{kg}{kg}$ and underpredictions for $W\,(> 1\,mm) \gg 0.2\,\frac{kg}{kg}$.

To sum up, the PBM approach is capable of predicting the critical L/S across scales. This is necessary for scale-up because the optimum operating range depends heavily on this critical L/S. Predicting the optimum operating range has been a challenge in scale-up of high-shear wet granulation because conventional scale-up approaches, which are based on dimensionless groups and heuristics, often fail to provide accurate predictions. Additionally, experimental PSD data below S_{crit} is predicted very accurately with both modelling approaches. For $S \approx S_{crit}$, results are slightly overpredicted but still in good agreement. Outside the optimum operating range ($S \gg S_{crit}$), a drastic size increase is predicted but the final PSD is underpredicted significantly.

7.3.4 Compartmentalisation

Figure 7.17 compares the D_{50} predictions of the 2-comp PBM approach to the experimental data at 10 L, 25 L and 70 L. The model predictions are similar to the predictions of the 1-comp PBM

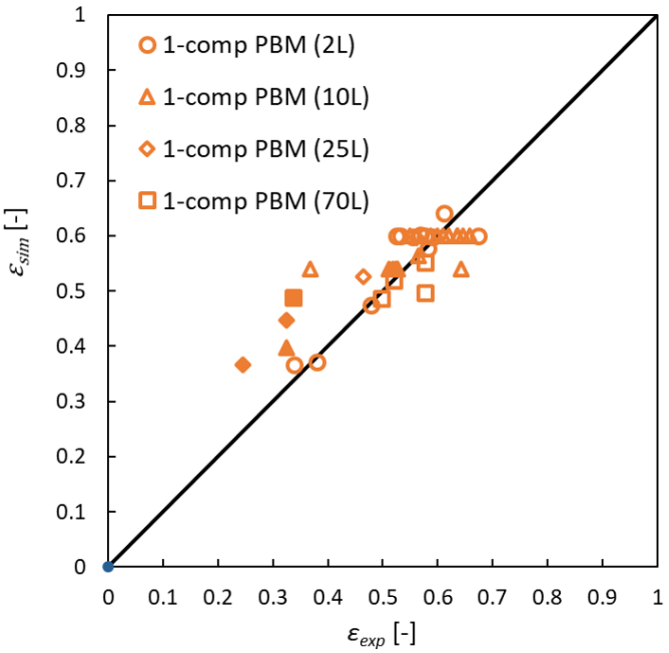

(a) Porosity ε

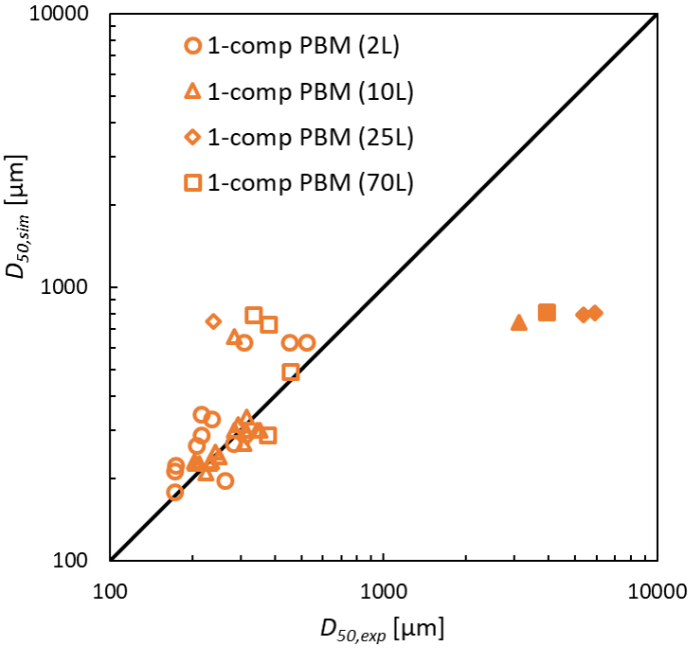

(b) Mass-median diameter D_{50}

Figure 7.15: Comparison of simulation and experimental porosity and D_{50} results across scales

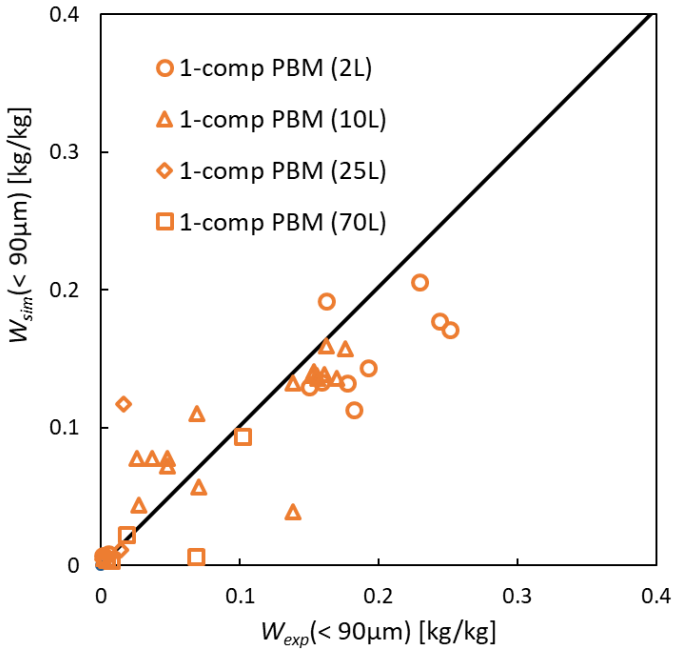

(a) Fines mass fraction W (< 90 µm)

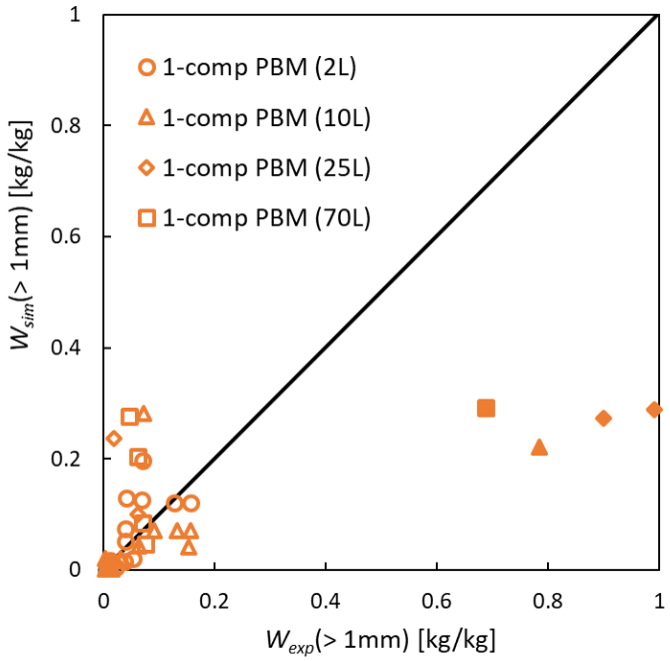

(b) Coarse mass fraction W (> 1 mm)

Figure 7.16: Comparison of simulation and experimental mass fraction results across scales

approach (see Figures 7.9, 7.10 and 7.11). The critical L/S is predicted well at these scales, and the D_{50} predictions are in good agreement below the critical L/S. Above the critical L/S, a quantitative mismatch between the predictions and experimental data is observed.

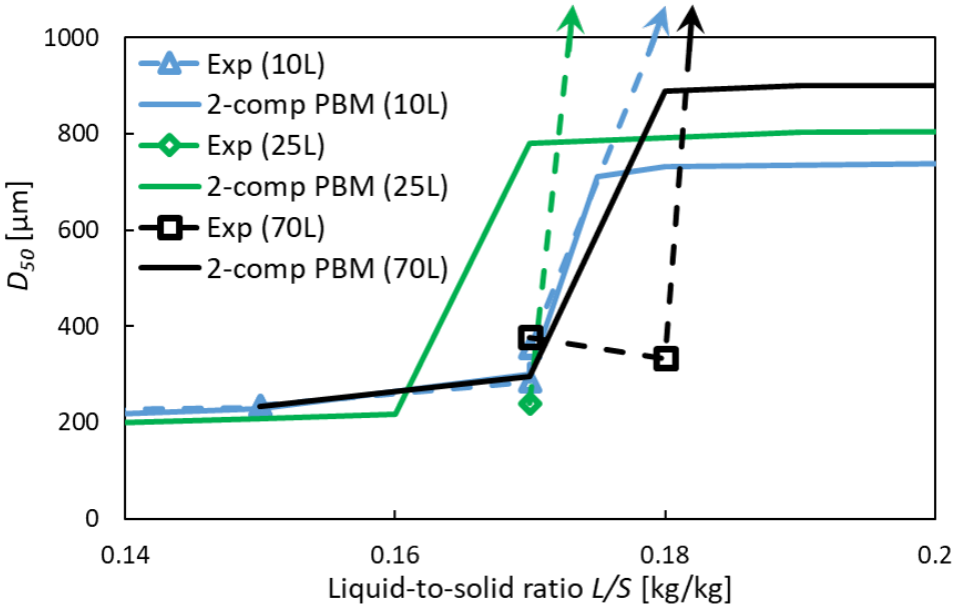

Figure 7.17: 2-comp PBM predictions and experimental data with varying L/S at 10 L-70 L

Figure 7.18 compares PSD predictions of the 1-comp and 2-comp PBM approaches with varying liquid-to-solid ratio L/S at 2 L scale. While the predictions of the 1-comp and 2-comp PBM approaches are very similar at 10 L and larger, the predictions differ considerably at 2 L. The 2-comp PBM approach predicts a considerably larger D_{50} and higher W (> 1 mm) are predicted by the 2-comp PBM approach. Both modelling approaches fail to predict critical L/S, at which the size significantly increases and the PSD at $L/S > 0.19$. As the 1-comp PBM with the well-mixed assumption (see Section 5.2) results in a better agreement overall (Figure 7.12), it is concluded that this assumption is more applicable at the small 2 L scale.

Figure 7.19 shows a prediction at low Froude number Fr of 2 at 25 L. The model parameters are estimated using experimental data in the roping flow regime ($Fr > 20$). With $Fr \ll 20$, the model is used to predict behaviour in the bumping flow regime (see Section 2.2). Both models include assumptions that are considered to be inappropriate in the bumping flow regime at large scale: well mixed (1-comp) and roping powder flow pattern (2-comp). Having said this, both PSD

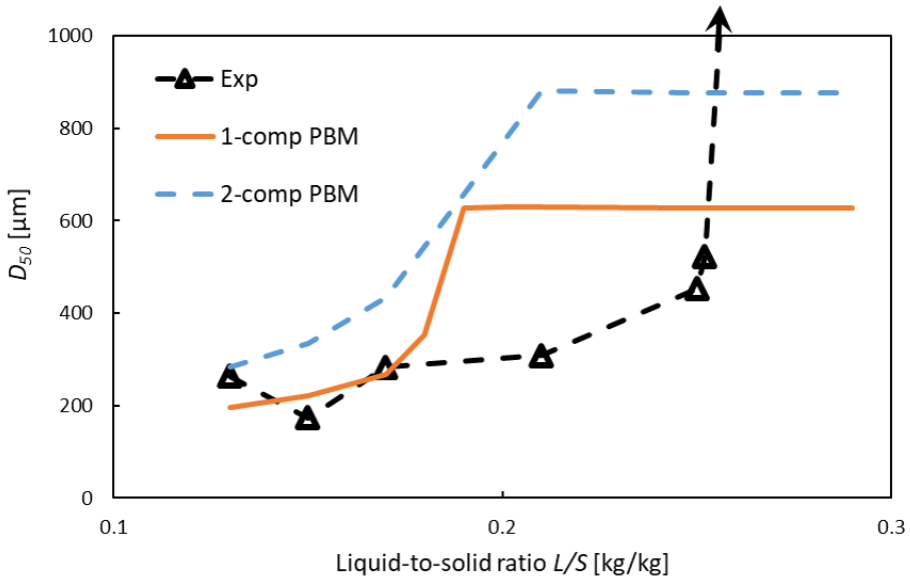

(a) Mass-median diameter D_{50}

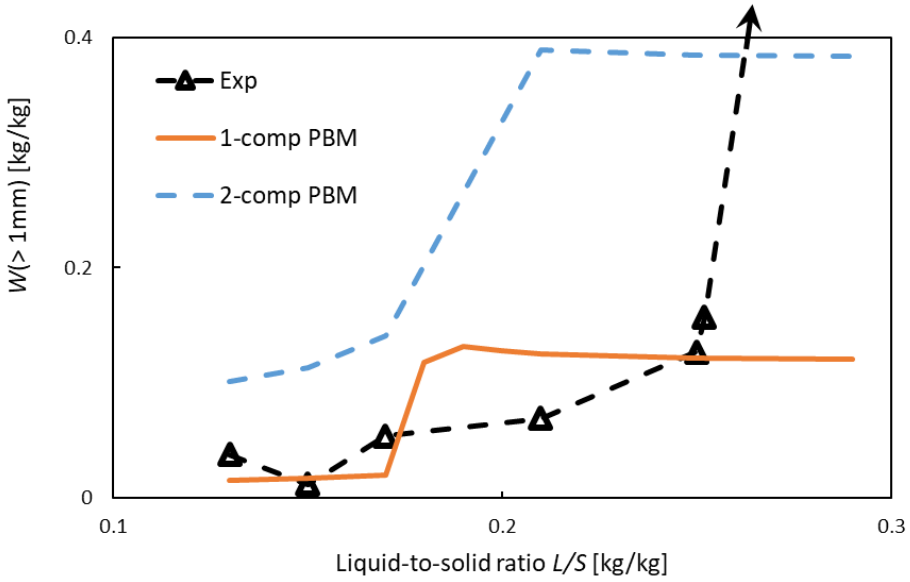

(b) Coarse mass fraction W (> 1 mm)

Figure 7.18: Predictions and experimental data with varying L/S at 2 L (Exp 1, 4-7 and 27: $Fr = 23$)

model predictions are in acceptable agreement with the experimental data. A small mismatch is identified at smaller particle size. While the models predict the presence of fine particles below 90 µm, the experimental data only shows a negligible amount in this size range. Overall, the accuracy of this prediction is close to the accuracy in the roping flow regime. This finding indicates that both modelling approaches can predict results outside the roping flow regime.

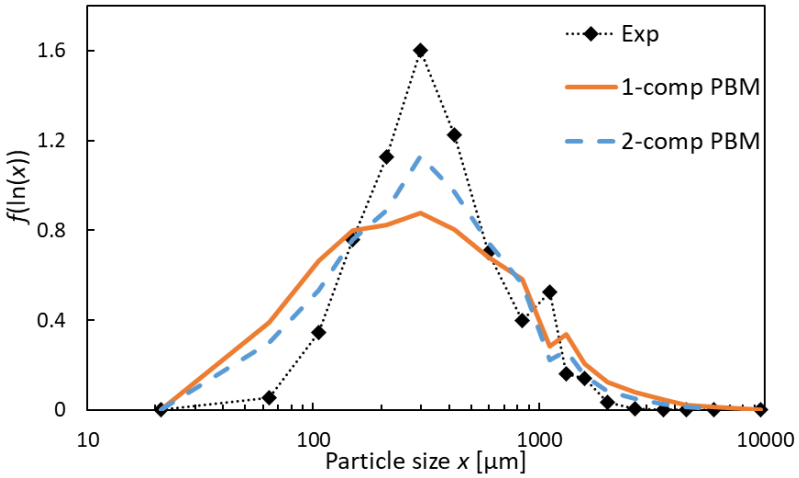

Figure 7.19: PSD prediction in the bumping flow regime (Exp 41: $V = 25\,\mathrm{L}$; $L/S = 0.19$; $Fr = 2$)

The relative sum of squared error $RSSE_O$ is shown for the CQA predictions in Figure 7.20 to compare both modelling approaches (1-comp PBM and 2-comp PBM). The average relative error is very similar for both modelling approaches but 1-comp PBM predictions result in a slightly smaller $RSSE_O$ of all CQAs results. The poor predictions of the 2-comp PBM approach at the 2 L scale are identified as the cause for this. The errors for the porosity results are similar because both approaches apply the same correlations to model porosity (Section 5.2.4). It is emphasised that $RSSE_O$ of different CQA results is not comparable because the error is divided by the absolute result to determine the $RSSE_O$. Especially W ($< 90\,\mu\mathrm{m}$) and W ($> 1\,\mathrm{mm}$) tend to have results close to 0 which produces very large relative errors for minor deviations.

Both modelling approaches (1-comp and 2-comp PBM) only disagree at the 2 L scale due to a high coarse mass fraction predicted by the 2-comp PBM approach. This overprediction is likely to be a consequence of inappropriate assumptions made about the mixing regime in compartmental modelling (CM). At the small 2 L scale, the experimental mixing conditions are likely to be better compared to the larger scales, which lead to a reduced circulation time and more breakage. As roping

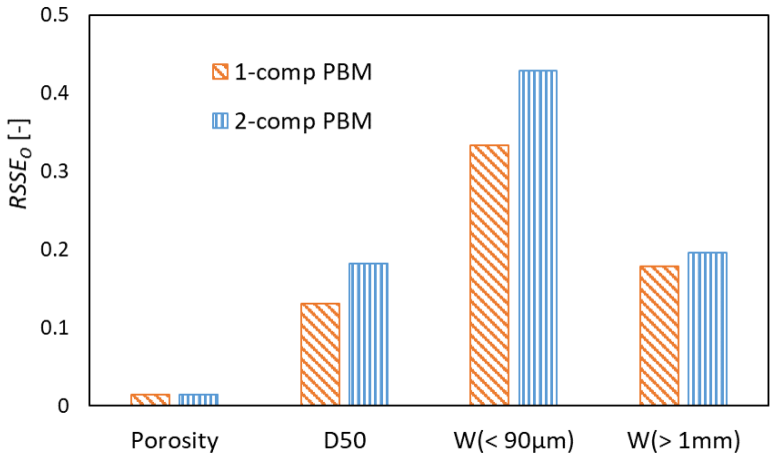

Figure 7.20: Relative sum of squared errors $RSSE_O$

flow is assumed at all scales to derive the powder flow in the 2-comp PBM approach, breakage is likely to be underpredicted. In the 1-comp PBM approach, the granulator is assumed to be well-mixed which appears to be the more appropriate assumption at 2 L due to the better agreement with experimental data. Overall, the 1-comp PBM approach is to be preferred for this 1-D PBM approach (see Section 5.2) because of slightly higher accuracy and 65 % lower computational time (see Section 5.2.8). The application of CM is limited in 1-D PBM because it is only beneficial to represent the breakage zone. The results indicate that the effect of circulation time on breakage is sufficiently captured with appropriate assumptions in the 1-comp PBM approach (see Section 5.2.7). The usage of CM for multi-D PBM needs to be assessed independently. In a multi-D PBM framework (see Section 2.3.1), CM can be used to improve the representation of the spray zone to predict liquid distribution and the effect on wet granulation mechanisms. Additional model predictions are compared to experimental data in Appendix D.1.

7.3.5 Model limitations

While the model is proved to be a powerful tool, there are three areas in which its limitations are apparent: (1) Growth after induction time at $S \approx S_{crit}$, (2) Rapid growth at $S \gg S_{crit}$ and (3) Nuclei breakage in mechanical dispersion regime.

In the induction growth regime ($S \approx S_{crit}$), experimental data shows the formation of a bi-modal PSD, while the original peak remains below 500 µm (Figure 7.21a). Even though the models predict

a size increase with increasing S, the results contradict the experimental finding (Figure 7.21b). The PSD remains mono-modal but the peak shifts to larger particle sizes. This mismatch becomes more apparent at high S (here: $t = 11$ min). Since a 1-D PBM framework is employed, the liquid content is assumed to be equal for all granules of the same size (see Section 5.2.1). Especially under poor mixing conditions, this assumption is not applicable, as granules are likely to have a broad distribution of liquid content. As a result, some very wet granules are likely to coalesce and form large granules, while the liquid content of most granules is not sufficient for further growth (bi-modal PSD). Furthermore, the liquid content of large (coalesced) granules is likely to be higher than average because they have been formed from very wet smaller granules (illustrated in Figure 7.22). This phenomenon potentially further increases growth for large granules. In contrast to that, all granules of the same size start coalescing simultaneously under the assumption of equal liquid content. The result is a more continuous shift of the peak, which qualitatively disagrees with experimental observations at $S \geq S_{crit}$. For this reason, 1-D PBM is not suitable to capture coalescence well because of the effect of broad liquid content distribution.

In the rapid growth regime ($S \gg S_{crit}$), very large particles (> 5 mm) are formed in experiments (Figure 7.23). The model predicts that particles do not exceed a diameter of 3 mm, and for this reason, the model fails to predict the outcome at very high S. This mismatch is likely caused by the aforementioned representation of granule liquid content in 1-D PBM. The experimental data used for parameter estimation is obtained at $S \approx S_{crit}$. At these conditions, only a fraction of granules contains sufficient liquid for coalescence. To account for this, the collision coefficient $k_{I/II}$ is underestimated. At $S \gg S_{crit}$, a majority of granules fulfil the coalescence criterion. Using the value estimated for $k_{I/II}$, the predicted coalescence rate is several times lower than observed experimentally (illustrated in Figure 7.22). Consequently, a 1-D approach is unable to predict experimental data accurately over a wide range of pore saturation conditions. Furthermore, (granule) tensile strength is assumed to be a function of capillary number only (see Section 5.2.4). Having said that, experimental observations have shown that tensile strength can also increase with increasing pore saturation and decreasing porosity [Pohlman and Litster, 2015]. In the rapid growth regime, pore saturation is very high, and porosity is typically quite low compared to the induction growth regime. For this reason, the model is likely to underestimate tensile strength and hence overpredict breakage. However, the representation of tensile strength is believed to have a minor impact of the PSD due to the typically stronger impact of coalescence.

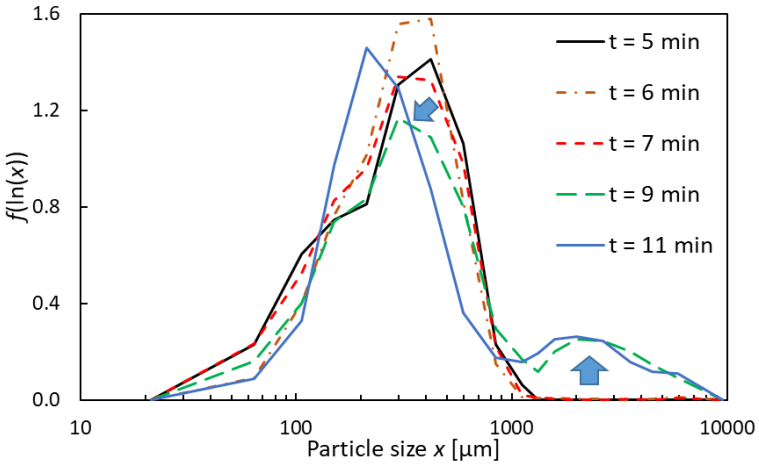

(a) Exp 16, 30, 31, 32 and 34

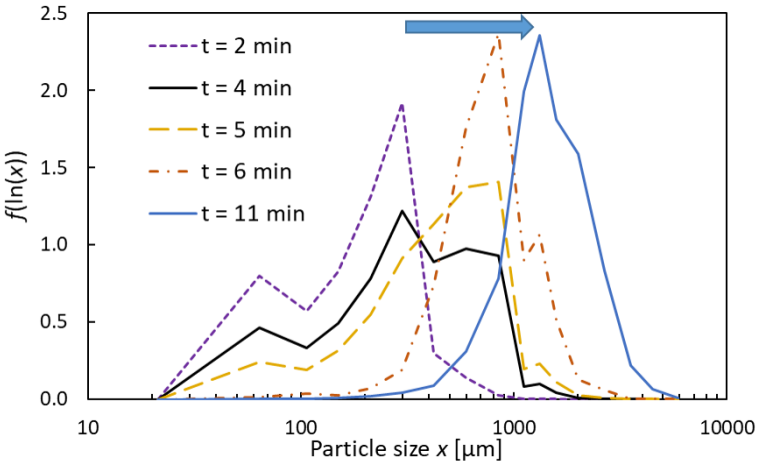

(b) 1-comp PBM

Figure 7.21: Evolution of particle size distribution (arrows indicate change with time t)

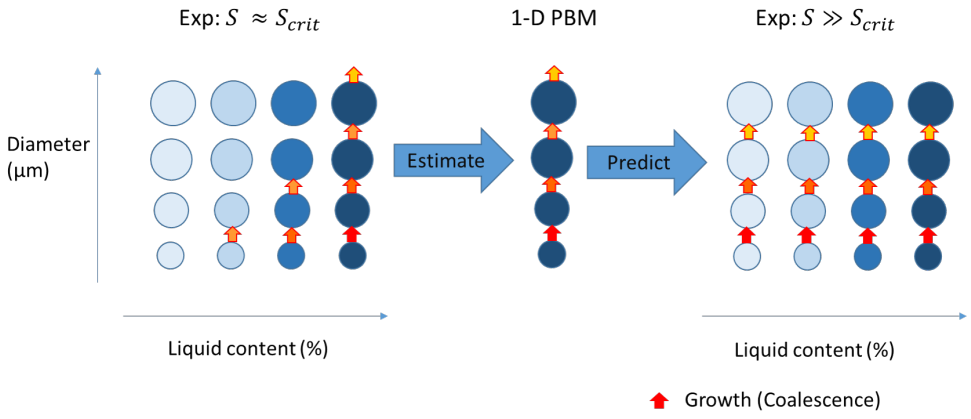

Figure 7.22: Effect of liquid distribution on coalescence (depending on pore saturation S) and consequences for 1-D PBM

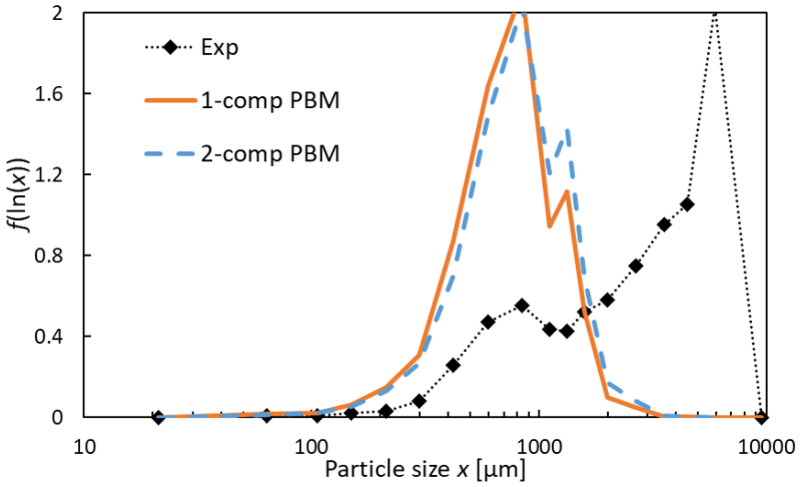

Figure 7.23: PSD prediction of rapid growth experiment (Exp 17: $V = 10\,\mathrm{L}$; $L/S = 0.21$; $Fr = 23$)

The effect of breakage is more decisive when coalescence does not occur. This can be observed at very low pore saturation. To illustrate this, predictions of experiments with large nuclei (> 1 mm) are assessed. This is achieved experimentally by a high dimensionless spray flux Ψ_a and/or large drop diameter d_d (mechanical dispersion regime; see Section 2.1.1). Nuclei are very porous granules with low pore saturation. For these reasons, tensile strength is underestimated, and especially breakage of large nuclei is underpredicted. As a consequence, the PSDs of these experiments are overpredicted by both PBM approaches (Figure 7.24).

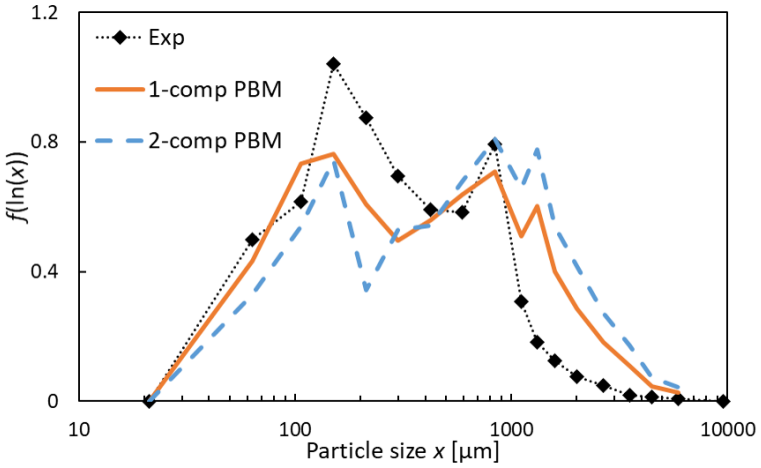

(a) Exp 8: $V = 2\,\mathrm{L}$; $\Psi_a = 0.9$; $d_d = 100\,\mu\mathrm{m}$; $t_{kn} = 0\,\mathrm{min}$; $L/S = 0.15$; $Fr = 23$

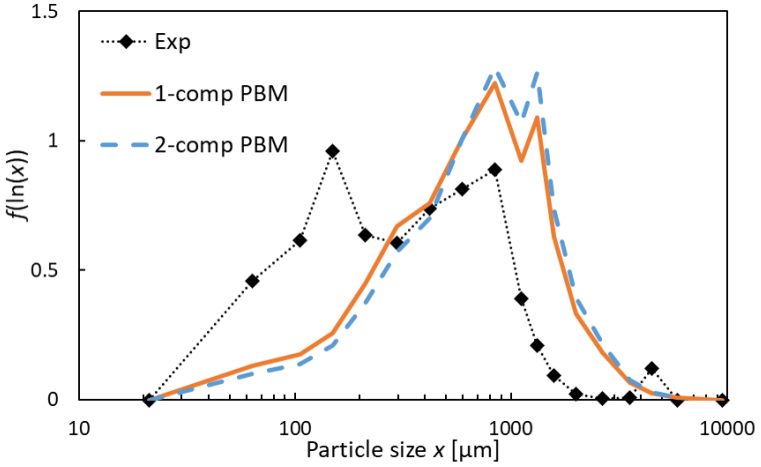

(b) Exp 16-1: $V = 10\,\mathrm{L}$; $\Psi_a = 0.7$; $d_d = 230\,\mu\mathrm{m}$; $t_{kn} = 5\,\mathrm{min}$; $L/S = 0.17$; $Fr = 23$

Figure 7.24: PSD prediction of experiments in the mechanical dispersion regime

7.4 *Conclusions*

A PBM approach is applied to model high-shear wet granulation, and the model's predictive power is critically assessed based on a case study. Through sensitivity analysis, the most important modelling parameters are identified and subsequently estimated using data from 7 small-scale experiments. Both models are assessed and validated based on experimental predictions at four scales (2 L-70 L) with a wide range of operating conditions. Model predictions are in good agreement with experimental results for the optimum operating range (critical L/S) and the CQAs within this optimum operating range at scales above 10 L. The modelling approach is hence considered to be predictive across scales. Therefore, it is useful for model-driven design (MDD) including scale-up purposes. Conventional scale-up approaches often fail to provide reliable predictions.

By comparing two versions of this model (1-comp and 2-comp PBM), compartmental modelling (CM) assumptions are assessed. Even though both modelling approaches are suitable for further usage (e.g. model-driven design), the 1-comp PBM approach is recommended due to its simplicity and slightly better performance. Extreme conditions, which result in rapid growth or mechanical binder dispersion, are predicted qualitatively but results for porosity and particle size distribution (PSD) can differ substantially, possibly due to the fundamental modelling approaches chosen.

Chapter 8

MODEL-DRIVEN DESIGN: A NOVEL SCALE-UP FRAMEWORK FOR PARTICULATE PROCESSES

8.1 *Introduction*

As the experimental effort strongly increases with scale, reducing the number of large-scale experiments by maximising the informative value of experimental data is of great interest in scale-up. In model-driven design (MDD), this is achieved by utilising small-scale experimental data effectively to predict behaviour at lab, intermediate and large scale. This approach is very beneficial for experimental design because the behaviour is studied rigorously using simulation data to derive the critical and optimum operating. The incentives of MDD for scale-up are discussed further in Section 2.2.

In this chapter, a MDD approach for scaling up particulate processes is proposed. The framework is applied and evaluated in a case study based on wet granulation in a high-shear mixer.

8.2 *Method development*

Wang et al. [2019] presented an MDD approach for particulate processes. An extension of this approach for scale-up purposes is presented in Figure 8.1.

First, critical quality attributes (CQAs) are identified based on process and product understanding. The CQAs capture the most relevant product properties, and reliable measurement techniques have to be available to determine them. The product could be an intermediate product if the focus lays on a specific process unit.

The modelling approach needs to be conceptualised by defining the problem and characterising the system. At this stage, the effect of scale needs to be addressed by understanding all influences that change with scale. On this basis, suitable modelling approaches are identified that fulfil the requirements formulated previously. A model or submodels only need to be developed if no appropriate approach is available. The model is verified by studying the underlying theory of the

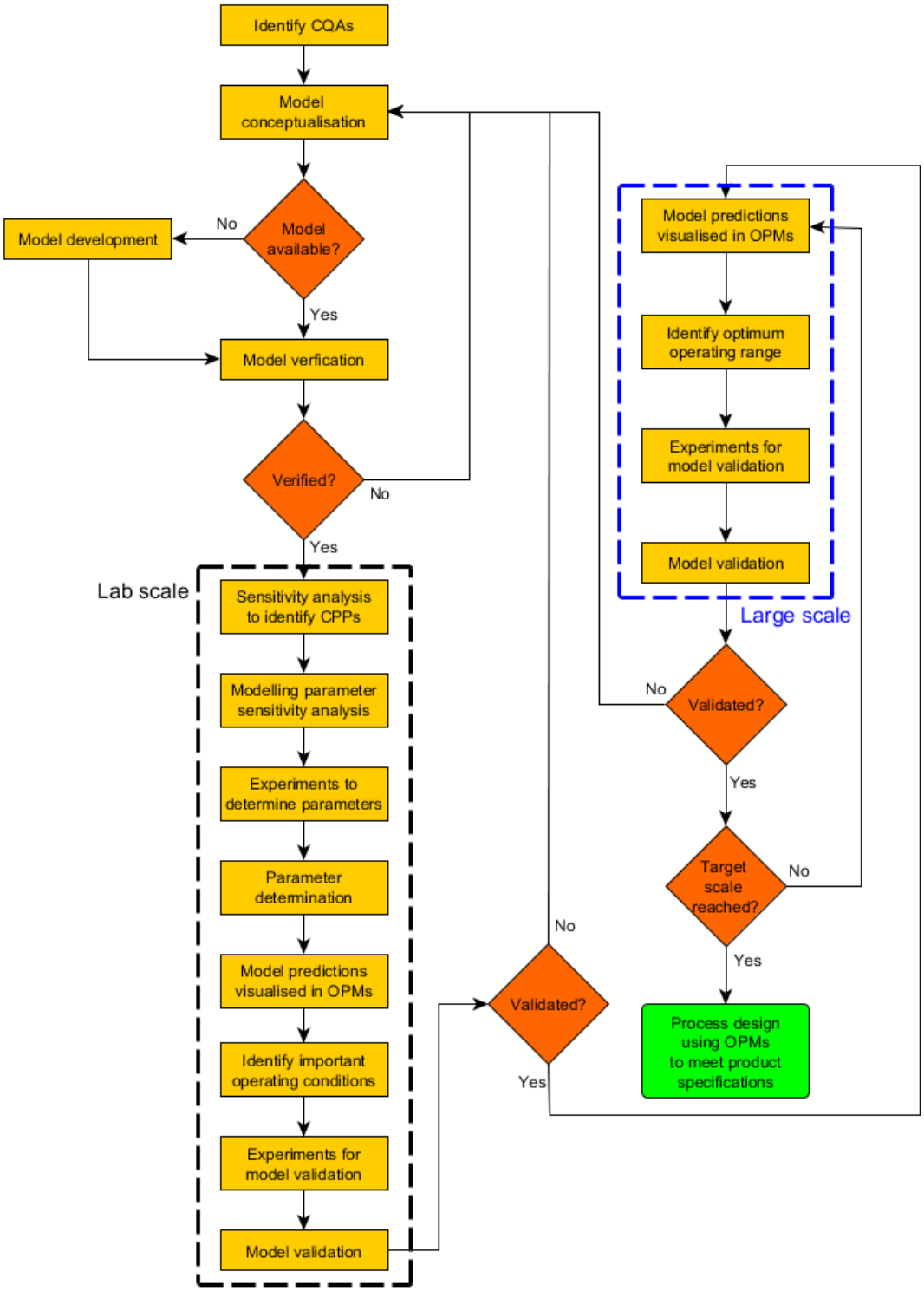

Figure 8.1: Model-driven design workflow for scale-up

model, critically evaluating the main assumptions and analysing the model behaviour based on simulation results. Thereby, it has to be ensured that the model includes sufficient mechanistic understanding and captures the effect of scale.

A verified model is first applied at lab scale. The critical process parameters (CPPs) are identified based on a sensitivity analysis including all operating parameters. In the sensitivity analysis, the parameter ranges have to be selected carefully to cover the full space, and parameters need to be varied simultaneously to assess the combined effect. A second sensitivity analysis is required to identify the essential modelling parameters. Only essential modelling parameters have to be measured or estimated to keep the experimental effort at a minimum. The remaining parameters are obtained by making reasonable assumptions and based on literature data (see Section 7.2).

Experiments are designed for parameter estimation and material characterisation. The identified CPPs and their critical ranges should be considered in the experimental design. The uncertainty of the experimental results needs to be determined to evaluate the accuracy of model results. The uncertainty should be determined based on replicates of the most relevant or critical conditions.

Physical properties are derived from the characterisation tests. The remaining essential parameters are estimated from lab-scale experiments. A reliable parameter estimation technique is described in Section 7.2.

The model is validated based on model predictions. For this purpose, model predictions are visualised in operating performance maps (OPMs). Important operating conditions are identified using OPMs to design additional experiments for model validation. Important operating conditions include the optimum and critical conditions as well as conditions that show model limitations. The model is validated at lab scale by assessing the accuracy of the model predictions at the important operating conditions.

After a successful model validation at lab scale, the model is used to predict the process behaviour at large scale. The optimum operating range is identified using OPMs, and experiments are designed to validate model predictions. After successful model validation, these tasks need to be completed for every process scale included until the target scale is reached. At target scale, the process is designed using OPMs that visualise product specifications.

8.3 *Case study*: *high-shear wet granulation*

A case study is conducted to assess the MDD approach developed. High-shear wet granulation is chosen for this scale-up case study. This process is known to be challenging to scale up. The key decisions and outcomes are summarised in Table 8.1.

Table 8.1: Overview of MDD tasks

Task	Outcome	Explanation
Identify CQAs (see Section 6.2)	PSD (D_{50}, $W(<90\,\mu m)$, $W(>1\,mm)$) and porosity	Decisive for many other material characteristics and very relevant for downstream processes
Model conceptualisation (see Chapter 2)	PBM approach including (semi-)mechanistic kernels	Predictive process model over wide operating range and across scales
Model verification (see Section 5.4)	Critical assumptions verified and model behaviour analysed	Based on simulations and experiments
Identify CPPs (see Appendix D.2 and Section 6.3)	L/S, impeller tip speed v_t and kneading time t_{kn}	Based on their impact on CQAs determined by sensitivity analysis and confirmed experimentally
Modelling parameter sensitivity analysis (see Section 7.3.1)	Impactful parameters identified: S_{crit}, k_{cons}, $k_{I/II}$, k_{br}	Based on their impact on CQAs identified by Sobol' indices
Experiments to determine parameters (see Chapter 6)	Vary CPPs with strong focus on critical conditions	Improve parameter estimates and model predictions
Parameter determination (see Section 7.3.2)	Universal values for modelling parameters	Based on characteristic tests/literature data and limited number of parameters to estimate
Model predictions	OPMs and individual predictions	Screen wide operating range and investigate important behaviour in detail

Continued on next page

Table 8.1 – continued from previous page

Task	Outcome	Explanation
Identify important operating conditions	Optimum operating range and extreme conditions	Assess model predictions rigorously and identify model limitations (lab scale only)
Model validation (see Section 7.3.3)	Predictive model for process design and scale-up	Assessment of model predictions and identification of model limitations
Process design to meet product specifications	Optimum operating conditions at target scale	Identify operating conditions using OPMs

In this chapter, the validated model is used to study and compare the process behaviour across scales. Therefore, the process behaviour is predicted at three different scales following the constant Froude number (CFN) scale-up approach. CFN is chosen to ensure an operation in the roping flow regime (see Section 2.2). Additionally, a wide range of operating conditions is evaluated by visualising the key results on operating performance maps (OPMs), and the desired operating range is identified based on the predicted outcome. As key results, the mass-based median diameter D_{50} and granule porosity ε at the granulation endpoint are visualised. To determine D_{50}, 700 simulations (1-comp PBM approach) are carried out at each scale, and the porosity profile is determined by evaluating Eq 5.29. Furthermore, product specifications are formulated for the CQAs to identify desired operating range (Table 8.2). To validate the predictions, the results are compared to large-scale experimental data which covers the critical range of conditions.

Table 8.2: Product specifications

Critical quality attribute	Minimum	Maximum
Fines mass fraction W ($< 90\,\mu m$) $\left[\frac{kg}{kg}\right]$	0	0.1
Coarse mass fraction W ($> 1\,mm$) $\left[\frac{kg}{kg}\right]$	0	0.15

8.3.1 *Investigating process behaviour upon scale-up*

The performance at different scales is predicted in Figure 8.2. For this comparison, the constant

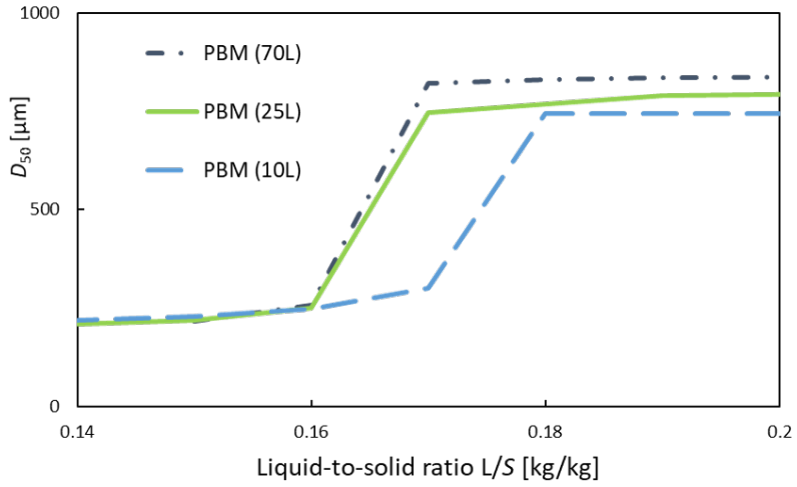

(a) Mass-median diameter D_{50}

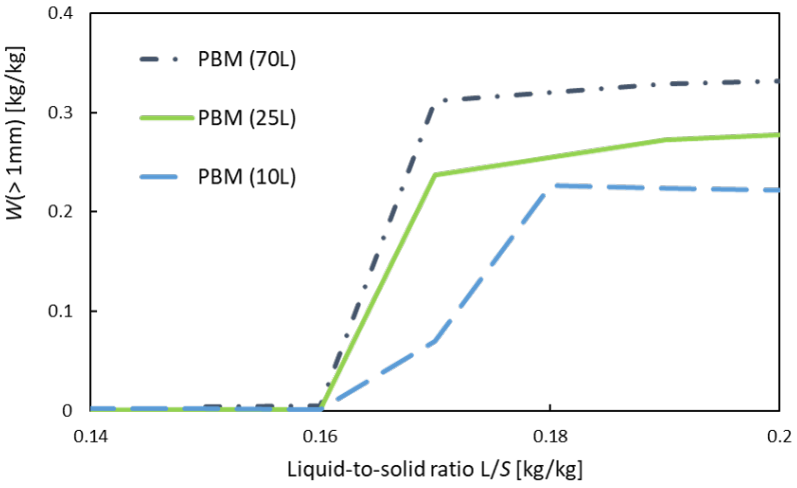

(b) Coarse mass fraction W (> 1 mm)

Figure 8.2: CFN scale-up prediction from 10 L to 70 L (Fr = 23)

Froude number (CFN) scale-up approach is applied. At all scales, the D_{50} and W (> 1 mm) are almost constant up to a critical L/S and increase significantly above this critical L/S. The critical L/S ranges from 0.16 to 0.17 depending on the scale. The predictions show that the D_{50} and W (> 1 mm) level off at very high L/S, however, it is concluded that these results are distinctly

underpredicted (see Section 7.3.5). While the results at low L/S are very similar at all scales, the behaviour differs considerably at larger L/S. With increasing scale, the critical L/S is predicted to decrease continuously. Additionally, the size increase around the critical L/S is stronger at larger scales. Consequently, L/S needs to be reduced with increasing scale to produce a similar D_{50} and W (> 1 mm), and a narrower operating range is available to achieve these critical conditions, which are desired in many applications. This demonstrates that a CFN approach cannot be used to predict the operating range at larger scales because L/S is commonly kept constant across scales.

With increasing scale, L/S needs to decrease to achieve similar product properties because of an increasing tip speed in the CFN approach. To maintain a constant Froude number, a higher tip speed is required at large scale which results in a decrease in porosity. Additionally, poor mixing conditions at large scale can lead to a decrease in granule breakage and poor liquid distribution. The trends identified in this analysis agree with experimental observations (see Section 6.3). The requirement to adjust the operating conditions continuously with increasing scale has been identified previously [Iveson and Litster, 1998b]. Even though this requirement is widely known, an approach that gives further guidance on the specific adjustment needed is currently not available.

8.4 *Operating performance maps*

Operating performance maps (OPMs) are diagrams that visualise the most important results over a wide range of operating conditions. By analysing OPMs, the process behaviour can be explored, and critical and optimum operating ranges can be identified. This approach has the potential to support important design and scale-up decisions.

The porosity profile after a kneading time of 5 min is visualised in Figure 8.3. The predicted range of endpoint porosity ranges from 0.45 to 0.6. This shows that v_t and L/S have a significant impact on porosity, in addition to granulation time. This OPM shows that the experimental conditions need to be well chosen if granule porosity is critical for further processing. In addition to the effect on the granulation process, porosity is known to have a decisive impact on important quality attributes such as compressibility and flowability [Kawashima et al., 1994; Abdullah and Geldart, 1999]. As it has been concluded that only v_t and L/S have a decisive impact on the endpoint porosity, this OPM is applicable at all scales.

The predicted mass-median diameter D_{50} after a kneading time of 5 min is shown in Figure 8.4. The results of the three scales investigated are in very good qualitative agreement. At all scales, the

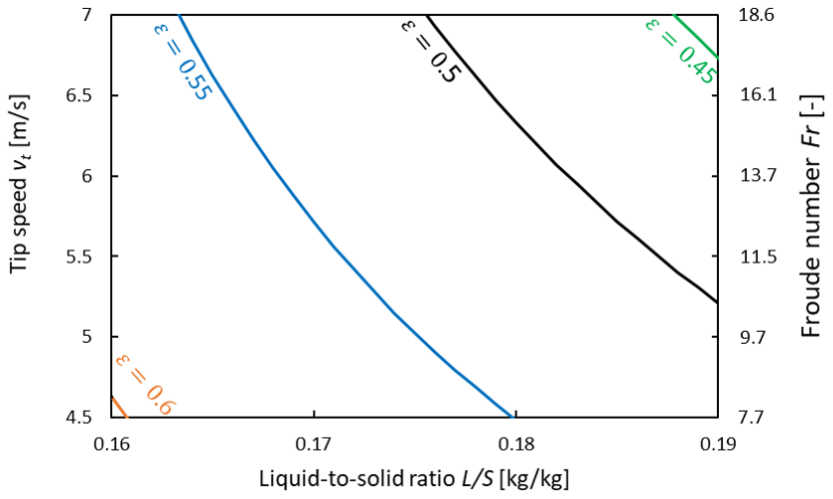

Figure 8.3: Predicted porosity profile after 5 min kneading (Fr for 70 L scale)

D_{50} ranges from 200 µm to above 600 µm. For this case study, it is considered that a D_{50} above 600 µm is not suitable for further processing. At low L/S of up to almost 0.17, the D_{50} is rather small and does not exceed 250 µm. Under these conditions, the L/S is not sufficient for high consolidation or layering rates, and the pore saturation S does consequently not suffice for coalescence. A larger D_{50} is achieved when a critical L/S is exceeded. At this point, the critical pore saturation S_{crit} is reached, and granule size increases significantly due to coalescence. This significant size increase is depicted by narrow D_{50} ranges. The critical L/S strongly depends on v_t due to the impact of v_t on the porosity. Finally, $S \gg S_{crit}$ leads to a very large D_{50} above 600 µm due to rapid growth.

With increasing scale, a more significant size increase is observed for $S > S_{crit}$. A combination of influencing factors are responsible for this trend. Firstly, an equivalent v_t implies a lower impeller speed n_{imp} and lower Froude number Fr at large scale. As n_{imp} directly affects the circulation time, particles reach the breakage zone less often which consequently results in a lower breakage rate. A low Fr indicates poor mixing conditions and poor liquid distribution. Poor liquid distribution promotes the formation of large, dense lumps and rapid growth. Secondly, the processing time increases because the dimensionless spray flux Ψ_a is kept in the same range across scales. A constant Ψ_a approach requires longer spray times at large scale if the spray area does not increase proportionally to the equipment scale, and a longer processing time results in more growth as coalescence is dominant under these conditions. This shows that constant v_t and Ψ_a lead to lower

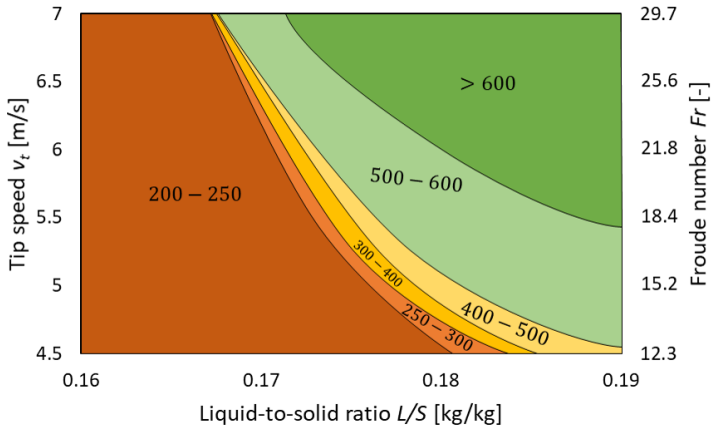

(a) 10 L

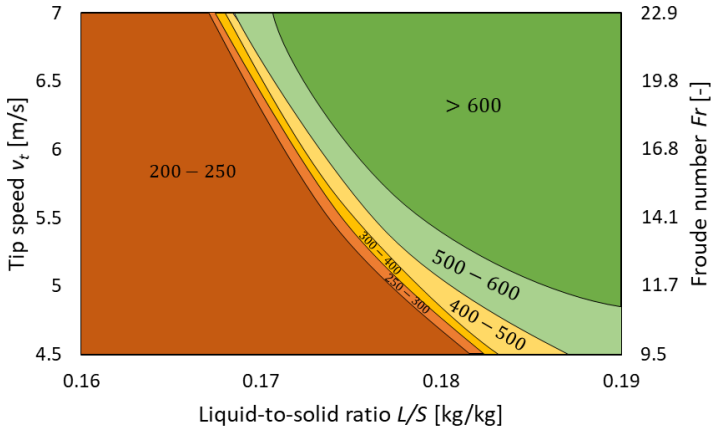

(b) 25 L

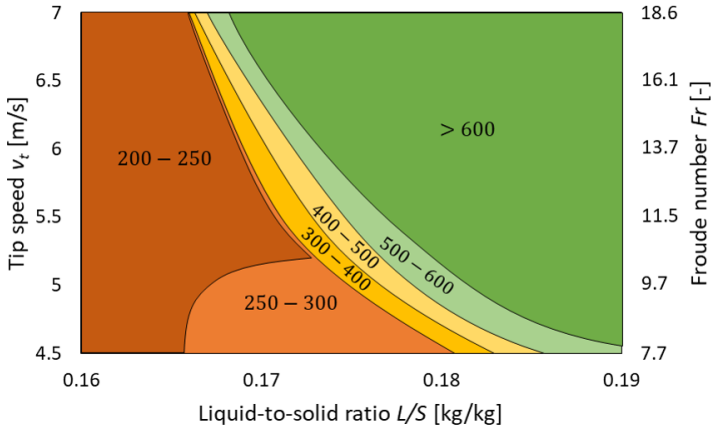

(c) 70 L

Figure 8.4: Predicted D_{50} [µm] after 5 min kneading with $\Psi_a = 0.2 - 0.4$ (10 L: $t_{sp} = 5\,\text{min} - 6\,\text{min}$; 25 L: $t_{sp} = 10\,\text{min} - 12\,\text{min}$; 70 L: $t_{sp} = 11\,\text{min} - 13\,\text{min}$)

breakage rates, poor liquid distribution and longer processing times and hence, a larger D_{50}.

Due to equipment limitations, a relatively long spray time is required at 25 L, and spray conditions differ substantially at 70 L. This explains the very narrow D_{50} ranges at 25 L. The nuclei size distributions are predicted based on the dimensionless spray flux Ψ_a and Sauter mean drop diameter d_d (Figure 8.5). The nuclei size distribution at 10 L and 25 L are rather narrow with very little large nuclei, while the nuclei size distribution at 70 L is significantly broader with a peak that is shifted to the right. All in all, the amount of large nuclei is considerably higher at 70 L. Overall, it is concluded that spray conditions at 10 L and 25 L are comparable because of the similar nuclei size distribution. The spray conditions at 70 L, however, differ substantially due to the significant increase in nuclei size distribution.

Moreover, these results show that the nuclei size distribution does not just depend on the Ψ_a but also on d_d. In this case, the effect of d_d even dominates because a larger and broader nuclei size distribution is observed with decreasing Ψ_a. This can just be explained by the significant increase in d_d.

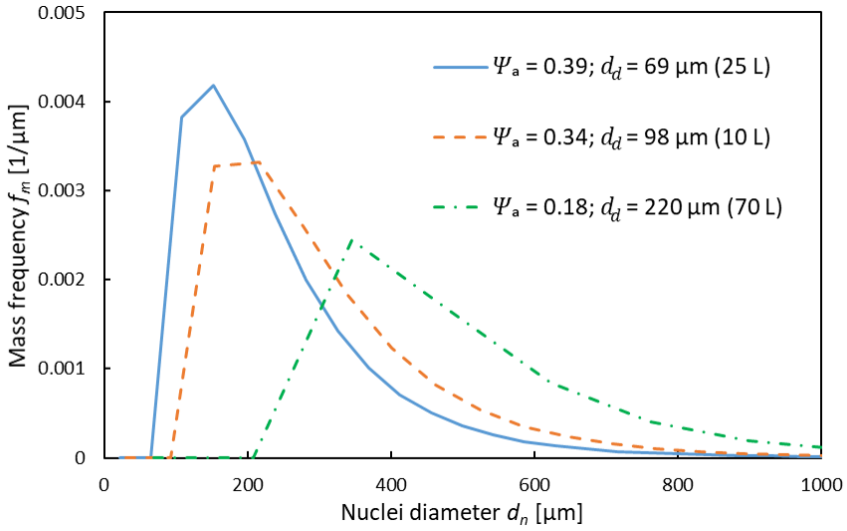

Figure 8.5: Nuclei size distribution and spray conditions (Ψ_a dimensionless spray flux; d_d Sauter mean drop diameter)

Figure 8.6 shows the experimental conditions required to fulfil the product specifications listed in Table 8.2. At very low tip speed v_t and liquid-to-solid ratio L/S, the product specifications are not met because the fines mass fraction W (< 90 µm) exceeds the upper limit of 0.1. By increasing

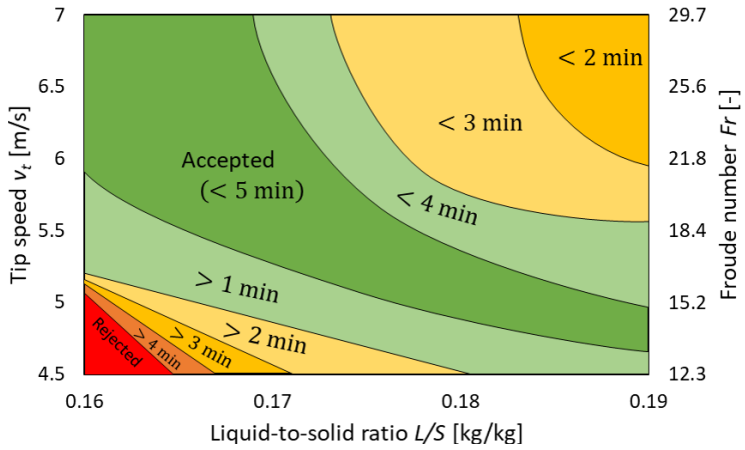

(a) 10 L scale

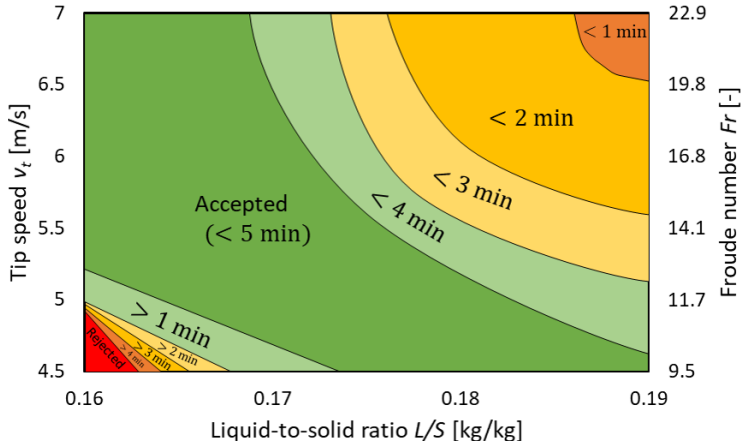

(b) 25 L scale

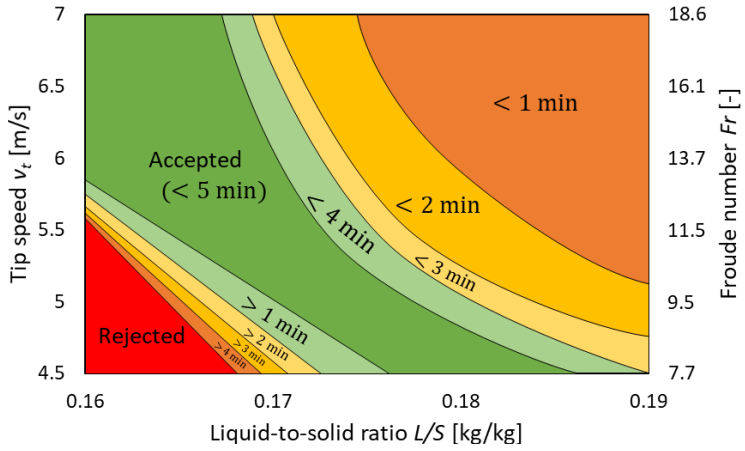

(c) 70 L scale

Figure 8.6: Predicted kneading time t_{kn} to fulfil product specifications (0 min $< t_{kn} <$ 5 min)

either v_t or L/S, growth is promoted, and W ($< 90\,\mu m$) decreases. At first, a high kneading time t_{kn} of at least 4 min is required to meet the product specifications. By increasing v_t or L/S further, the minimum t_{kn} decreases continuously until it reaches 0. In this operating range, any t_{kn} is suitable to meet the product specification (tested: $0\,min < t_{kn} < 5\,min$). At very high v_t and L/S, the product specifications are not met at high t_{kn} because the coarse mass fraction W ($> 1\,mm$) exceeds the upper limit of 0.15. $W\,(> 1\,mm) > 0.15$ indicates an operation in the rapid growth regime. In this range, the maximum t_{kn} decreases continuously with v_t and L/S.

Even though the results are qualitatively similar across scales, quantitative differences are observed. At low v_t and L/S, minor differences are identified, as a slightly longer t_{kn} is required at 10 L due to the rather short spray time. Significant differences are identified at high v_t and L/S, as the regimes (here: maximum t_{kn}) are considerably narrower at larger scales. As a result, the optimum operating range decreases continuously with increasing scale. This consequently makes the operation at large scale more challenging. As the effect of scale is much more pronounced at high v_t and L/S than at low v_t and L/S, it is concluded that the longer spray time does not have a great effect. Since results are compared at equivalent v_t and L/S (similar to constant tip speed (CTS) approach), the breakage rate and liquid distribution decrease significantly with increasing scale, as explained previously. These reasons are responsible for the shift of the rapid growth and the decrease in the optimum operating range. This shows that a CTS approach is insufficient to predict the operating regimes (especially rapid growth) at larger scales reliably because L/S should be decreased with increasing scale to ensure a similar operation. Decreasing v_t is not recommended for scale-up because this would result in a drastically lower Froude number Fr at large scale. A low Fr is likely to lead to poor mixing because of a different mixing regime [Tran, 2015]. However, the mixing regime is not represented appropriately to study this effect, as a 1-comp PBM approach is used to predict these results. For this reason, decreasing v_t might have an unfavourable impact on the CQAs which is not predicted well by this modelling approach.

8.5 *MDD for scale-up and comparison to conventional approach*

An experimental design for parameter estimation at lab scale is shown in Table 8.3. Lab scale is the smallest scale that shows comparable process behaviour. In this case study, the 10 L is identified to be the appropriate lab scale. The particle size distribution (PSD) and porosity of every experiment need to be determined. In Exp $1-6$, the impeller tip speed v_t and liquid-to-solid ratio L/S are

varied. Based on the porosity data, the endpoint porosity parameters $e_{1..3}$ (Eq 5.30) are estimated. The critical L/S at high v_t is derived from Exp $1-4$ by identifying the minimum L/S at which a bi-modal PSD is observed (see Section 6.3.6). Triplicates are performed at critical conditions in Exp $7-8$ to assess the reproducibility. The process behaviour during the kneading phase is investigated by reducing the kneading time t_{kn} at critical conditions in Exp $9-11$. It is recommended to evaluate the power input to identify the critical kneading time range [Levin, 2007]. Exp $7-11$ (critical L/S) are recommended for the parameter estimation of the four rate parameters: S_{crit}, k_{cons}, k_{br} and $k_{I/II}$. The sequential parameter estimation method described in Section 7.2 is recommended. The remaining experiments (Exp $1-6$) can be used to validate the estimates for the rate parameters at lab scale. Additional experiments with extreme conditions to identify model limitations are not essential because limitations of this model are already identified (see Section 7.3.5).

Table 8.3: Recommended experimental design at lab scale (specific for the case study and generic guidelines)

Exp	v_t $\left[\frac{\text{m}}{\text{s}}\right]$	L/S $\left[\frac{\text{kg}}{\text{kg}}\right]$	t_{kn} [min]	Explanation
$1-4$	6.5 (high)	0.13, 0.15, 0.17, 0.19	5 (high)	Vary L/S to determine critical L/S
$5-6$	5.5 (low)	0.15, 0.19	5 (high)	and estimate $e_{1..3}$
$7-8$	6.5 (high)	0.17 (critical)	5 (high)	Triplicates to assess reproducibility
$9-11$	6.5 (high)	0.17 (critical)	0, 1, 3	Reduce t_{kn} to determine critical t_{kn}

Consolidation can potentially be primarily investigated at smaller scale ($< 10\,\text{L}$ because the consolidation kinetics is identified to be very comparable over a wider range of scales (see Section 6.3.5). Consequently, material consumption can be reduced by carrying out Exp $5-6$ at smaller scale. When rapid consolidation kinetics are observed, it is recommended to set $k_{cons} = 2-3$. Formulations with rapid drop penetration are likely to show rapid consolidation kinetics.

At intermediate and target scale, the optimum operating range is identified using OPMs, and experiments are designed within this optimum operating range to validate the model predictions. For the experimental design, choosing the most critical conditions is essential. Most critical are the corner points of the desired operating range (Figure 8.7a). If the desired operating range is a regular rectangle, the most critical extremes can be chosen alternatively (Figure 8.7b). Additionally, the

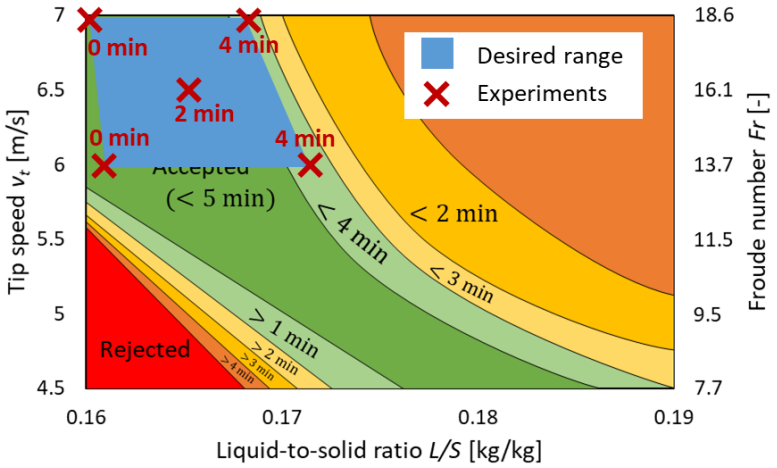

(a) Recommended experimental design

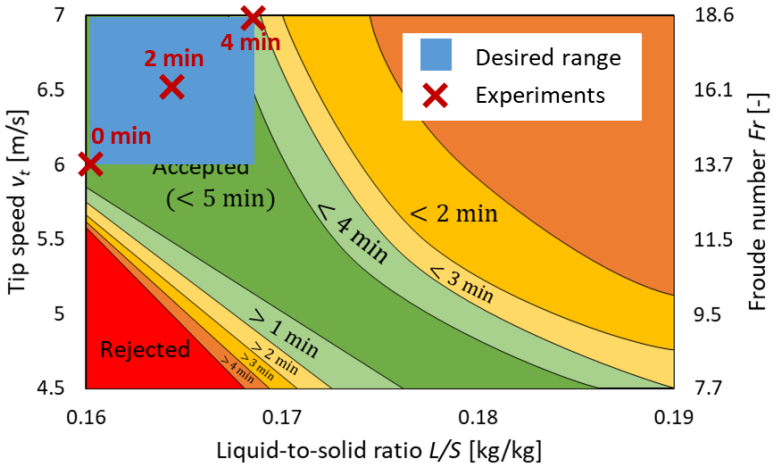

(b) Reduced experimental design

Figure 8.7: Experimental design at intermediate and target scale including kneading time t_{kn} (here at 70 L scale)

desired operating point (eg. midpoint) is recommended to consider in the experimental design. If kneading time is considered as an additional degree of freedom, the most critical kneading times are recommended for all corner points and extremes as shown in Figure 8.7. To reduce material consumption, it is possible to skip model validation at intermediate scale. This is only recommended if the experience with a variety of formulations justifies a high level of confidence in the direct scale-up from lab scale to target scale. Theoretically, this modelling approach is suitable for direct scale-up to target scale (see Section 7.3.3).

Conventional scale-up approach are based on a factorial design of experiments (DOE) [Rohrer, 2017]. The experimental effort of a factorial DOE increases with the number of factors or CPPs [Montgomery and Runger, 2014]. To study the effects of the three CPPs of high-shear wet granulation, 11 experiments are required. Additional experiments might be required if the product does not meet the specifications.

Table 8.4 compares the experimental effort of the two scale-up approaches. To estimate the effort, both approaches are assumed to be well established. While both approaches recommend the same number of experiments at lab scale, the MDD approach requires significantly less experiments at intermediate and target scale. Choosing a scale-up approach that requires a limited number of intermediate- and target-scale experiments is beneficial because the experimental effort and material consumption is significantly higher than at lab scale. The keys to the MDD approach are predictive modelling and OPMs. In OPMs, promising predictions of the optimum operating range are obtained, which are very beneficial for the experimental design at intermediate and target scale. Consequently, the experimental effort of the MDD scale-up approach is significantly lower compared to conventional approaches and the estimated reduction in material consumption is between 33 % – 63 %.

Table 8.4: Experimental effort required for MDD and conventional scale-up approaches and material consumption for this case study

Scale	MDD	Conventional
Lab	11 exp.	11 exp.
Intermediate	0 – 5 exp.	11 exp.
Target	3 – 5 exp.	11 exp.
Material consumption	37 % – 67 %	100 %

8.6 *Conclusions*

In this chapter, a MDD approach is proposed for scale-up of particulate processes. Guidance on all tasks required for this approach is given, and an appropriate experimental design method is described based on a case study. Applying MDD effectively is beneficial for scale-up because the process behaviour can be investigated more rigorously. Additionally, it substantially reduces the demand for experimental effort compared to conventional scale-up approaches. The approach is assessed based on a high-shear wet granulation case study. The results demonstrate that the CQAs and operating space can be predicted well across scales using the predictive modelling approach.

The operating space is explored, and the results show that the optimum operating range decreases significantly with increasing scale. To achieve an equivalent granulation endpoint, the operating conditions (e.g. liquid-to-solid ratio L/S) consequently need to be adjusted across scales. This is necessary to avoid rapid growth behaviour, which is known to become an increasing operational risk at larger scales. Conventional scale-up approaches like constant Froude number (CFN) and constant tip speed (CTS) fail to predict the optimum operating range due to inherent principles. Additionally, the product can be designed using the operating performance maps (OPMs) as the CQAs are predicted over a wide range of operating conditions. OPMs are a practical tool to identify the optimum operating range if the product is subject to specifications.

Chapter 9

CONCLUSIONS AND RECOMMENDATIONS

9.1 *Conclusions*

The key scientific contributions of this study are:

1. A new predictive nuclei size distribution model is developed and validated based on a log-normal distribution (LND) for formulations with rapid drop penetration.
2. A novel model verification, sensitivity analysis, parameter estimation and validation workflow is developed and applied using a novel predictive high-shear wet granulation model.
3. A model-driven design (MDD) workflow is customised for scale-up of particulate processes with the objective to minimise the experimental effort required.
4. Operating performance maps (OPMs) are developed as a visualisation tool for key results and product specifications to investigate the process behaviour over a wide operating range and identify the optimum conditions.

In this section, the main conclusions of the thesis, organised by chapters, are summarised:

In Chapter 4:

1. The log-normal distribution (LND) model is capable of predicting the nuclei size distribution for a wide range of spray conditions. The empirical parameters of the LND model are estimated using data from Monte Carlo simulations (MCS).
2. Predictions of both alternatives (modified Poisson distribution (MPD) model and Hapgood's PD model) diverge from experimental and MCS results at a high dimensionless nucleation numbers ($\Psi_n > 0.5$). Neither model contains a nuclei coalescence criterion that is applicable under these circumstances.

In Chapter 5:

3. For the development of a predictive model, the effects of the operating parameters and equipment design/scale need to be explicitly addressed. Consequently, a single set of modelling parameter values is applicable for the relevant operating range and across scales.

In Chapter 6:

4. Each wet granulation mechanism is isolated to improve the quality of experimental results and reduce the experimental effort.
5. Experimental design needs to consider experiments that are useful to verify critical modelling assumptions, estimate modelling parameters and assess model predictions over a wide range of operating conditions.

In Chapter 7:

6. The new Gaussian Process approach to sensitivity analysis is successful in reducing the number of fitting parameters by focussing on impactful parameters.
7. For scale-up purposes, the modelling parameters should be estimated primarily based on lab-scale granulation experiments, and characterisation test results should be used to derive parameters that depend on physical properties.
8. A predictive scale-up model successfully predicted the performance at different scales and over a wide range of operating conditions.
9. Appropriate assumptions about the powder flow pattern results in a better model performance than the application of compartmental modelling (CM).
10. A quantitative mismatch between model predictions and experimental results is observed at rapid growth conditions. This is the result of poor liquid distribution which is not appropriately captured in the 1-D PBM approach.

In Chapter 8:

11. Scale-up of particulate processes can be performed by model-driven design (MDD).
12. The operating performance maps (OPMs) are a useful visualisation and decision-making tool, in which a wide operating range is explored for experimental design and process scale-up.

9.2 *Recommendations for future work*

In future work, it is recommended to apply the MDD approach in design and scale-up studies for other particulate processes that are applied heavily in industry. This approach is particularly beneficial

for processes that are difficult to scale up using conventional methods: wet and dry granulation, crystallisation, spherical agglomeration, spray drying, among other processes.

To further establish the MDD approach for high-shear wet granulation, it should be applied with different equipment, materials and formulations. Especially, formulation that are difficult to process e.g. due to a high contact angle between powder and liquid should be investigated. These formulations might require substantial modifications or new (sub)models because current modelling approaches typically assume low contact angles.

To further improve the high-shear wet granulation model, the Young's modulus (Eq 5.46) should be represented as a function of the Capillary number similarly to dimensionless strength (Eq 5.32) to include more mechanistic understanding of physical properties. Additionally, the representation for granule properties (e.g. porosity, dynamic yield strength or Young's modulus) can be improved by capturing additional influences.

The liquid content or liquid distribution is known to have an effect, and this influence typically also varies across scales. For these reasons, model predictions for the granule properties can be improved by capturing the effect of liquid distribution appropriately. A 1-D PBM is not suitable to capture this effect because the liquid distribution is not tracked. A multi-D PBM approach is required to utilise such improved representations. Especially, poor liquid distribution can be captured using a multi-D PBM approach. Therefore, an appropriate representation of the spray zone is beneficial which adds liquid only to solid material that is exposed to the spray. This can be achieved using appropriate assumptions or by compartmental modelling (CM).

The empirical porosity correlation (Eq 5.30) can be improved by including key dimensionless groups as inputs instead of operating conditions. The Stokes deformation number relates the effect of the impeller tip speed to granule strength. Compared to the impeller tip speed, the Stokes deformation number has a more decisive impact on porosity and should be evaluated to determine the minimum porosity. For this purpose, it is recommended to measure the dynamic granule strength at minimum porosity and representative size for the chosen formulation. A more mechanistic porosity correlations, which includes the relevant granule properties, is beneficial because the consolidation behaviour of different formulations can be directly compared to each other. Additionally, a drastic drop in porosity is observed when the critical pore saturation is reached. For this reason, pore saturation is recommended as an input instead of the liquid-to-solid ratio. However, the inclusion of pore saturation would result in an implicit porosity correlation because pore saturation depends on

porosity. Consequently, estimating the empirical parameters would be more challenging.

Parameter estimation should be based on lab-scale granulation experiments, and the usage of characterisation tests to derive first estimates should be investigated additionally. To estimate the empirical porosity parameters, the impeller tip speed/Stokes deformation number should be varied at low and high pore saturation in lab-scale experiments. Additionally, first estimates for modelling parameters (e.g. critical pore saturation) could be derived from characterisation tests like drop nucleation experiments to reduce material consumption.

9.3 *Recommendations for industrial implementation*

This work shows that MDD principles improve the workflow for industrial scale-up of particulate processes. The benefits of applying MDD are more accurate predictions of the process behaviour at larger scales which reduces experimental effort and material consumption.

Especially the lower experimental effort at intermediate and target scales is a key benefit of applying MDD. This is achieved by employing a model that is predictive across scales. A rigorous model calibration and assessment is consequently recommended at lab scale. At intermediate and target scales, critical model predictions only need to be validated experimentally.

NOMENCLATURE

List of Indices

$'$	Auxiliary
$'$	Dimensionless
$*$	Critical
$*$	Dimensionless
0	Constant
0	Initial
1	Single-drop nuclei
32	Sauter mean
43	Volume moment mean
50	Mass-median
$\bar{}$	Average
ϵ	Porosity
$\tilde{}$	Reduced
a	Asperities
bed	Bed

br	Breakage
$bulk$	Bulk
c	Circulation
ch	Chopper
$coal$	Coalescence
$coll$	Collision
$cons$	Consolidation
cp	Critical packing
$crit$	Critical
d	Diameter
d	Drawing area
d	Drop
d	Dynamic
E	Elasticity
eff	Effective
env	Envelope
exp	Experiment
ext	External
f	Fill

f	Frequency
g	Granule
$gran$	Granule-specific
I	Type I
i	Index
i	Parent particle
i	Size class
II	Type II
imp	Impeller
int	Internal
j	Daughter particle
j	Index
k	Index
kin	Kinetic
kn	Kneading
l	Liquid
lay	Layering
lv	Liquid-vapour
m	Mass-specific

max	Maximum
min	Minimum
n	Nozzle
n	Nuclei
n	Number
nuc	Nucleation
O	Measured quantity (CQA)
p	Drop penetration
p	Pore
p	Primary particle
s	Solid
sim	Simulation
sp	Spray
t	Impeller tip
tap	Tap
tot	Total
un	Unpenetrated
v	Void
w	Wet

wet	Wetting	
X	Measured quantity	
x	Coordinate	

List of Symbols

$\dot{A}$	Flux of the powder bed surface area through the spray zone	$\left[\frac{\mathrm{m}^2}{\mathrm{s}}\right]$
A	Area	$\left[\mathrm{m}^2\right]$
A	Empirical parameter	$[-]$
a	Area	$\left[\mathrm{m}^2\right]$
AR	Aspect ratio of primary particles	$\left[\frac{\mathrm{m}}{\mathrm{m}}\right]$
$\dot{b}$	Volume-specific birth rates	$\left[\frac{\mathrm{s}}{\mathrm{m}^3}\right]$
B	Cumulative fragment size distribution function	$[-]$
B	Empirical parameter	$[-]$
B	Subregion area	$\left[\mathrm{m}^2\right]$
b	Discrete fragment size distribution function	$[-]$
b	Empirical parameter	$[-]$
C	Rate	$\left[\frac{1}{\mathrm{s}}\right]$
c	Constant	$[-]$
c	Empirical parameter	$[-]$
c	Moisture content	$\left[\frac{\mathrm{kg}}{\mathrm{kg}}\right]$

Ca	Capillary number	$[-]$
$\dot{d}$	Volume-specific death rates	$\left[\frac{\mathrm{s}}{\mathrm{m}^3}\right]$
D	Diameter	[m]
d	Diameter	[m]
D_{eff}	Binary effective diffusivity	$\left[\frac{\mathrm{m}^2}{\mathrm{s}}\right]$
E	Young's modulus	$\left[\frac{\mathrm{N}}{\mathrm{m}^2}\right]$
e	Empirical porosity parameter	$[-]$
E_m	Energy	[J]
F	Force	[N]
f	Frequency	$[-]$
f_{Mat}	Material strength parameter	$\left[\frac{\mathrm{kg\,m}}{\mathrm{J}}\right]$
Fr	Froude number	$[-]$
$\dot{G}$	Rate of change	$\left[\frac{\mathrm{m}^3}{\mathrm{s}}\right]$
G	Shear rate	$\left[\frac{1}{\mathrm{s}}\right]$
g	Gravitational acceleration	$\left[\frac{\mathrm{m}}{\mathrm{s}^2}\right]$
H	Height	[m]
h	Height	[m]
K	Nucleation size ratio	$[-]$
K	Rate	$[-]$

k	Rate constant	$[-]$
k	Ratio of agglomerate area to drop area	$\left[\frac{\mathrm{m}^2}{\mathrm{m}^2}\right]$
L	Length	$[\mathrm{m}]$
L/S	Liquid-to-solid ratio	$\left[\frac{\mathrm{kg}}{\mathrm{kg}}\right]$
M	Mass	$[\mathrm{kg}]$
m	Empirical nucleation parameter	$[-]$
m	Mass	$[\mathrm{kg}]$
ν	Poisson's ratio	$[-]$
N	Distribution function	$[-]$
n	Exponent	$[-]$
n	Frequency	$\left[\frac{1}{\mathrm{s}}\right]$
n	Number	$[-]$
n	Volume-specific number density	$\left[\frac{1}{\mathrm{m}^3}\right]$
N_A	Avogadro constant	$[-]$
P	Probability	$[-]$
P	Spray pressure	$[\mathrm{bar}]$
p	Empirical parameter	$[-]$
p	Precision	$[-]$
p	Set of operating parameters	$[-]$

$\dot{Q}$	Particle flow	$\left[\frac{1}{s}\right]$
q	Empirical parameter	$[-]$
R	Ideal gas constant	$\left[\frac{J K}{mol}\right]$
R	Pore radius	$[m]$
r	Empirical parameter	$[-]$
r	Radius	$[m]$
$RSSE$	Relative sum of squared errors	$[-]$
S	Pore saturation	$\left[\frac{m^3}{m^3}\right]$
s	Empirical nucleation parameter	$[-]$
St_v	Viscous Stokes number	$[-]$
St_{def}	Stokes deformation number	$[-]$
Str^*	Dimensionless strength	$[-]$
T	Auxiliary variable	$[-]$
T	Temperature	$[K]$
t	Time	$[s]$
$\dot{V}$	Volumetric flowrate	$\left[\frac{m^3}{s}\right]$
V	Volume	$\left[m^3\right]$
v	Velocity	$\left[\frac{m}{s}\right]$
v	Volume	$\left[m^3\right]$

W	Cumulative mass fraction	$\left[\frac{\text{kg}}{\text{kg}}\right]$
w	Mass fraction	$\left[\frac{\text{kg}}{\text{kg}}\right]$
w	Width of the spray zone	[m]
Δx	Inter-particle gap	[m]
$\vec{x}$	Set of granule properties	[−]
x	Coordinate	[m]
x	Particle diameter	[m]
x	Set of parameters	[−]
Y	Yield strength	$\left[\frac{\text{N}}{\text{m}^2}\right]$
y	Coordinate (direction of powder flow)	[m]
z	Dimensionless location	[−]
α	Spray cone angle	[°]
β	Coalescence rate	$\left[\frac{1}{\text{s}}\right]$
γ	Capillary force per unit length	$\left[\frac{\text{N}}{\text{s}}\right]$
γ	Surface tension	$\left[\frac{\text{N}}{\text{m}}\right]$
δ	Thickness	[m]
δ''	Permanent deformation	[m]
ϵ	Strain	[−]
ε	Porosity	[−]

ζ	Sobol' index	[−]
θ	Dynamic contact angle	[rad]
ϑ	Age of the granule	[s]
λ	Intensity function	[−]
μ	(Logarithmic) mean	[−]
μ	Binder viscosity	[Pa s]
ξ	Decision variable	[−]
O	Key product properties	[−]
π	Mathematical constant	[−]
ρ	Density	$\left[\frac{\mathrm{kg}}{\mathrm{m}^3}\right]$
σ	(Logarithmic) standard deviation	[−]
σ	Stress	[Pa]
τ	Residence time	[s]
τ	Shear stress	[Pa]
τ_p	Dimensionless drop penetration time	[−]
ϕ	Volumetric ratio	[−]
φ	Shape factor	[−]
Ψ_a	Dimensionless spray flux	[−]
Ψ_n	Dimensionless nucleation number	[−]

ω	Angular velocity	$\left[\frac{\text{rad}}{\text{s}}\right]$

BIBLIOGRAPHY

Abberger, T., Seo, A., and Schæfer, T. (2002). The effect of droplet size and powder particle size on the mechanisms of nucleation and growth in fluid bed melt agglomeration. *International Journal of Pharmaceutics*, 249(1-2):185–197.

Abdullah, E. C. and Geldart, D. (1999). The use of bulk density measurements as flowability indicators. *Powder Technology*, 102(2):151–165.

Abrahamsson, P. J., Kvist, P., Reynolds, G., Yu, X., Niklasson Björn, I., Hounslow, M. J., and Rasmuson, A. (2018). Analysis of mesoscale effects in high-shear granulation through a computational fluid dynamics–population balance coupled compartment model. *Particuology*, 36:1–12.

Adetayo, A. A. and Ennis, B. J. (1997). Unifying approach to modeling granule coalescence mechanisms. *AIChE Journal*, 43(4):927–934.

Adetayo, A. A., Litster, J. D., Pratsinis, S. E., and Ennis, B. J. (1995). Population balance modelling of drum granulation of materials with wide size distribution. *Powder Technology*, 82(1):37–49.

Agrawal, R. and Naveen, Y. (2011). Pharmaceutical processing–a review on wet granulation technology. *International Journal of Pharmaceutical Frontier Research*, 1(1):65–83.

Aikawa, S., Fujita, N., Myojo, H., Hayashi, T., and Tanino, T. (2008). Scale-up studies on high shear wet granulation process from mini-scale to commercial scale. *Chemical and Pharmaceutical Bulletin*, 56(10):1431–1435.

Allen, T. (1968). *Particle size measurement*. Chapman and Hall Ltd, London.

Ameye, D., Keleb, E., Vervaet, C., Remon, J. P., Adams, E., and Massart, D. L. (2002). Scaling-up of a lactose wet granulation process in Mi-Pro high shear mixers. *European Journal of Pharmaceutical Sciences*, 17(4-5):247–251.

Andrews, G. E. and Berndt, B. C. (2005). *Ramanujan's Lost Notebook*, volume 1. Springer, New York.

Austin, L., Shoji, K., Bhatia, V., Jindal, V., Savage, K., and Klimpel, R. (1976). Some results on the description of size reduction as a rate process in various mills. *Industrial & Engineering Chemistry Process Design and Development*, 15(1):187–196.

Austin, L. G., Bagga, P., and Celik, M. (1981). Breakage properties of some materials in a laboratory ball mill. *Powder Technology*, 28(2):235–243.

Ax, K., Feise, H., Sochon, R., Hounslow, M., and Salman, A. (2008). Influence of liquid binder dispersion on agglomeration in an intensive mixer. *Powder Technology*, 179(3):190–194.

Barrasso, D. (2015). *Multi-scale modeling of wet granulation processes*. PhD thesis, Rutgers University-Graduate School-New Brunswick.

Barrasso, D., El Hagrasy, A., Litster, J. D., and Ramachandran, R. (2015a). Multi-dimensional population balance model development and validation for a twin screw granulation process. *Powder Technology*, 270:612–621.

Barrasso, D., Eppinger, T., Pereira, F. E., Aglave, R., Debus, K., Bermingham, S. K., and Ramachandran, R. (2015b). A multi-scale, mechanistic model of a wet granulation process using a novel bi-directional PBM–DEM coupling algorithm. *Chemical Engineering Science*, 123:500–513.

Barrasso, D. and Ramachandran, R. (2012). A comparison of model order reduction techniques for a four-dimensional population balance model describing multi-component wet granulation processes. *Chemical Engineering Science*, 80:380–392.

Barrasso, D. and Ramachandran, R. (2015). Multi-scale modeling of granulation processes: bi-directional coupling of PBM with DEM via collision frequencies. *Chemical Engineering Research and Design*, 93:304–317.

Barrasso, D. and Ramachandran, R. (2016). Qualitative assessment of a multi-scale, compartmental PBM–DEM model of a continuous twin-screw wet granulation process. *Journal of Pharmaceutical Innovation*, 11(3):231–249.

Barrasso, D., Tamrakar, A., and Ramachandran, R. (2014). A reduced order PBM–ANN model of a multi-scale PBM–DEM description of a wet granulation process. *Chemical Engineering Science*, 119:319–329.

Barrasso, D., Tamrakar, A., and Ramachandran, R. (2015c). Model order reduction of a multi-scale PBM–DEM description of a wet granulation process via ANN. *Procedia Engineering*, 102:1295–1304.

Barrasso, D., Walia, S., and Ramachandran, R. (2013). Multi-component population balance modeling of continuous granulation processes: a parametric study and comparison with experimental trends. *Powder Technology*, 241:85–97.

Berthiaux, H., Varinot, C., and Dodds, J. (1996). Approximate calculation of breakage parameters from batch grinding tests. *Chemical Engineering Science*, 51(19):4509–4516.

Biggs, C. A., Sanders, C., Scott, A. C., Willemse, A. W., Hoffman, A. C., Instone, T., Salman, A. D., and Hounslow, M. J. (2003). Coupling granule properties and granulation rates in high-shear granulation. *Powder Technology*, 130(1):162–168.

Börner, M., Peglow, M., and Tsotsas, E. (2013). Derivation of parameters for a two compartment population balance model of wurster fluidised bed granulation. *Powder Technology*, 238:122–131.

Bouffard, J., Bertrand, F., and Chaouki, J. (2012). A multiscale model for the simulation of granulation in rotor-based equipment. *Chemical Engineering Science*, 81:106–117.

Boukouvala, F., Dubey, A., Vanarase, A., Ramachandran, R., Muzzio, F. J., and Ierapetritou, M. (2012). Computational approaches for studying the granular dynamics of continuous blending processes, 2–population balance and data-based methods. *Macromolecular Materials and Engineering*, 297(1):9–19.

Boukouvala, F., Gao, Y., Muzzio, F., and Ierapetritou, M. G. (2013). Reduced-order discrete element method modeling. *Chemical Engineering Science*, 95:12–26.

Boukouvala, F., Muzzio, F. J., and Ierapetritou, M. G. (2010). Predictive modeling of pharmaceutical processes with missing and noisy data. *AIChE Journal*, 56(11):2860–2872.

Braumann, A., Goodson, M. J., Kraft, M., and Mort, P. R. (2007). Modelling and validation of granulation with heterogeneous binder dispersion and chemical reaction. *Chemical Engineering Science*, 62(17):4717–4728.

Braumann, A., Kraft, M., and Mort, P. R. (2010a). Parameter estimation in a multidimensional granulation model. *Powder Technology*, 197(3):196–210.

Braumann, A., Kraft, M., and Wagner, W. (2010b). Numerical study of a stochastic particle algorithm solving a multidimensional population balance model for high shear granulation. *Journal of Computational Physics*, 229(20):7672–7691.

Braumann, A., Man, P. L. W., and Kraft, M. (2011). The inverse problem in granulation modeling–two different statistical approaches. *AIChE Journal*, 57(11):3105–3121.

Brilliantov, N. V., Spahn, F., Hertzsch, J., and Pöschel, T. (1996). Model for collisions in granular gases. *Physical review E*, 53(5):5382.

Broadbent, S. R. and Callcott, T. G. (1956). A matrix analysis of processes involving particle assemblies. *Philosophical Transactions of the Royal Society of London. Series A, Mathematical and Physical Sciences*, 249(960):99–123.

Broyden, C. G. (1970). The convergence of a class of double-rank minimization algorithms: 2. the new algorithm. *IMA Journal of Applied Mathematics*, 6(3):222–231.

Brunier, B., Sheibat-Othman, N., Othman, S., Chevalier, Y., and Bourgeat-Lami, E. (2017). Modelling particle growth under saturated and starved conditions in emulsion polymerization. *The Canadian Journal of Chemical Engineering*, 95(2):208–221.

Cameron, I. T., Wang, F. Y., Immanuel, C. D., and Stepanek, F. (2005). Process systems modelling and applications in granulation: A review. *Chemical Engineering Science*, 60(14):3723–3750.

Campbell, G. A., Clancy, D. J., Zhang, J. X., Gupta, M. K., and Oh, C. K. (2011). Closing the gap in series scale up of high shear wet granulation process using impeller power and blade design. *Powder Technology*, 205(1-3):184–192.

Capece, M., Bilgili, E., and Dave, R. (2011). Identification of the breakage rate and distribution parameters in a non-linear population balance model for batch milling. *Powder Technology*, 208(1):195–204.

Capece, M., Bilgili, E., and Dave, R. (2014a). Insight into first-order breakage kinetics using a particle-scale breakage rate constant. *Chemical Engineering Science*, 117:318–330.

Capece, M., Bilgili, E., and Davé, R. N. (2014b). Formulation of a physically motivated specific breakage rate parameter for ball milling via the discrete element method. *AIChE Journal*, 60(7):2404–2415.

Chan, E. L., Washino, K., Ahmadian, H., Bayly, A., Alam, Z., Hounslow, M. J., and Salman, A. D. (2015). Dem investigation of horizontal high shear mixer flow behaviour and implications for scale-up. *Powder Technology*, 270:561–568.

Chaturbedi, A., Bandi, C. K., Reddy, D., Pandey, P., Narang, A., Bindra, D., Tao, L., Zhao, J., Li, J., Hussain, M., et al. (2017). Compartment based population balance model development of a high shear wet granulation process via dry and wet binder addition. *Chemical Engineering Research and Design*, 123:187–200.

Chaturbedi, A., Pandey, P., Bindra, D., Reddy, J. P., Lang, B., Buckley, D., and Ramachandran, R. (2018). Predictive population balance model development and validation of the effect of high shear wet granulation process parameters on granule properties. *Powder Technology*, 338:391–401.

Chaudhury, A., Armenante, M. E., and Ramachandran, R. (2015). Compartment based population balance modeling of a high shear wet granulation process using data analytics. *Chemical Engineering Research and Design*, 95:211–228.

Chaudhury, A., Barrasso, D., Pandey, P., Wu, H., and Ramachandran, R. (2014a). Population balance model development, validation, and prediction of CQAs of a high-shear wet granulation process: towards QbD in drug product pharmaceutical manufacturing. *Journal of Pharmaceutical Innovation*, 9(1):53–64.

Chaudhury, A., Barrasso, D., Pohlman, D. A., Litster, J. D., and Ramachandran, R. (2017). Mechanistic modeling of high-shear and twin screw mixer granulation processes. In Pandey, P. and Bharadwaj, R., editors, *Predictive Modeling of Pharmaceutical Unit Operations*, pages 99–135. Woodhead Publishing.

Chaudhury, A., Kapadia, A., Prakash, A. V., Barrasso, D., and Ramachandran, R. (2013). An extended cell-average technique for a multi-dimensional population balance of granulation describing aggregation and breakage. *Advanced Powder Technology*, 24(6):962–971.

Chaudhury, A., Sen, M., Barrasso, D., and Ramachandran, R. (2016). Population balance models for pharmaceutical processes. In Ierapetritou, M. G. and Ramachandran, R., editors, *Process Simulation and Data Modeling in Solid Oral Drug Development and Manufacture*, pages 43–83. Springer, New York.

Chaudhury, A., Wu, H., Khan, M., and Ramachandran, R. (2014b). A mechanistic population balance model for granulation processes: Effect of process and formulation parameters. *Chemical Engineering Science*, 107:76–92.

CIA (2015). UK chemical and pharmaceutical industry facts and figures. Technical report, Chemical Indusries Association.

Clancy, D. (2017). Continuous secondary process selection and the modeling of batch and continuous wet granulation. In *Predictive Modeling of Pharmaceutical Unit Operations*, pages 343–381. Elsevier.

Cleary, P. W., Morrisson, R., and Morrell, S. (2003). Comparison of DEM and experiment for a scale model SAG mill. *International Journal of Mineral Processing*, 68(1-4):129–165.

Cleary, P. W. and Sawley, M. L. (2002). DEM modelling of industrial granular flows: 3D case studies and the effect of particle shape on hopper discharge. *Applied Mathematical Modelling*, 26(2):89–111.

Costa, C. B. B., Maciel, M. R. W., and Maciel Filho, R. (2007). Considerations on the crystallization modeling: Population balance solution. *Computers & Chemical Engineering*, 31(3):206–218.

Cryer, S. A. (1999). Modeling agglomeration processes in fluid-bed granulation. *AIChE Journal*, 45(10):2069–2078.

Cundall, P. A. and Strack, O. D. L. (1979). A discrete numerical model for granular assemblies. *Géotechnique*, 29(1):47–65.

Darelius, A., Brage, H., Rasmuson, A., Niklasson Björn, I., and Folestad, S. (2006). A volume-based multi-dimensional population balance approach for modelling high shear granulation. *Chemical Engineering Science*, 61(8):2482–2493.

Davis, N. J. (2016). *Mechanical dispersion of semi-solid binders in high-shear granulation*. PhD thesis, Purdue University.

de Koster, S. A. L. (2018). *Experimental investigation and modelling of consolidation and layering mechanisms in high-shear granulation*. PhD thesis, The University of Sheffield.

de Koster, S. A. L., Pitt, K., Litster, J. D., and Smith, R. M. (2019). High-shear granulation: An investigation into the granule consolidation and layering mechanism. *Powder Technology*, 355:514–525.

Denesuk, M., Smith, G. L., Zelinski, B. J. J., Kreidl, N. J., and Uhlmann, D. R. (1993). Capillary penetration of liquid droplets into porous materials. *Journal of Colloid and Interface Science*, 158(1):114–120.

Dhanarajan, A. P. and Bandyopadhyay, R. (2007). An energy-based population-balance approach to model granule growth and breakage in high-shear wet granulation processes. *AAPS PharmSciTech*, 8(3):E118–E125.

Dullien, F. A. L. (1979). *Porous media: fluid transport and pore structure*. Academic press.

Ennis, B. J. and Litster, J. D. (2008). Particle size enlargement. In Perry, R. H. and Green, D. W., editors, *Perry's Chemical Engineers' Handbook, 8th Edition*, pages 21–73–21–82. McGraw-Hill, New York.

Ennis, B. J., Tardos, G., and Pfeffer, R. (1991). A microlevel-based characterization of granulation phenomena. *Powder Technology*, 65(1-3):257–272.

Faure, A., Grimsey, I. M., Rowe, R. C., York, P., and Cliff, M. J. (1999). Process control in a high shear mixer-granulator using wet mass consistency: The effect of formulation variables. *Journal of Pharmaceutical Sciences*, 88(2):191–195.

Faure, A., York, P., and Rowe, R. C. (2001). Process control and scale-up of pharmaceutical wet granulation processes: a review. *European Journal of Pharmaceutics and Biopharmaceutics*, 52(3):269–277.

Filbet, F. and Laurençot, P. (2004). Numerical simulation of the smoluchowski coagulation equation. *SIAM Journal on Scientific Computing*, 25(6):2004–2028.

Forrest, S., Bridgwater, J., Mort, P. R., Litster, J., and Parker, D. J. (2003). Flow patterns in granulating systems. *Powder Technology*, 130(1):91–96.

Freireich, B., Ketterhagen, W. R., and Wassgren, C. (2011a). Intra-tablet coating variability for several pharmaceutical tablet shapes. *Chemical Engineering Science*, 66(12):2535–2544.

Freireich, B., Kumar, R., Ketterhagen, W., Su, K., Wassgren, C., and Zeitler, J. A. (2015). Comparisons of intra-tablet coating variability using DEM simulations, asymptotic limit models, and experiments. *Chemical Engineering Science*, 131:197–212.

Freireich, B., Li, J., Litster, J., and Wassgren, C. (2011b). Incorporating particle flow information from discrete element simulations in population balance models of mixer-coaters. *Chemical Engineering Science*, 66(16):3592–3604.

Freireich, B., Litster, J., and Wassgren, C. (2009). Using the discrete element method to predict collision-scale behavior: a sensitivity analysis. *Chemical Engineering Science*, 64(15):3407–3416.

Fries, L., Antonyuk, S., Heinrich, S., and Palzer, S. (2011). DEM–CFD modeling of a fluidized bed spray granulator. *Chemical Engineering Science*, 66(11):2340–2355.

Gantt, J. A., Cameron, I. T., Litster, J. D., and Gatzke, E. P. (2006). Determination of coalescence kernels for high-shear granulation using DEM simulations. *Powder Technology*, 170(2):53–63.

Gao, Y., Ierapetritou, M., and Muzzio, F. (2012a). Periodic section modeling of convective continuous powder mixing processes. *AIChE Journal*, 58(1):69–78.

Gao, Y., Muzzio, F. J., and Ierapetritou, M. G. (2012b). Optimizing continuous powder mixing processes using periodic section modeling. *Chemical Engineering Science*, 80:70–80.

Gavi, E. (2019). Application of a mechanistic model of batch fluidized bed drying at laboratory and pilot scale. *Drying Technology*, pages 1–17.

Goldfarb, D. (1970). A family of variable-metric methods derived by variational means. *Mathematics of Computation*, 24(109):23–26.

Gunawan, R., Fusman, I., and Braatz, R. D. (2004). High resolution algorithms for multidimensional population balance equations. *AIChE Journal*, 50(11):2738–2749.

Haff, P. K. and Werner, B. T. (1986). Computer simulation of the mechanical sorting of grains. *Powder Technology*, 48(3):239–245.

Haibo, Z., Chuguang, Z., and Minghou, X. (2005). Multi-Monte Carlo approach for general dynamic equation considering simultaneous particle coagulation and breakage. *Powder Technology*, 154(2):164–178.

Hapgood, K. P., Amelia, R., Zaman, M. B., Merrett, B. K., and Leslie, P. (2010). Improving liquid distribution by reducing dimensionless spray flux in wet granulation–a pharmaceutical manufacturing case study. *Chemical Engineering Journal*, 164(2-3):340–349.

Hapgood, K. P., Litster, J. D., Biggs, S. R., and Howes, T. (2002). Drop penetration into porous powder beds. *Journal of Colloid and Interface Science*, 253(2):353–366.

Hapgood, K. P., Litster, J. D., and Smith, R. (2003). Nucleation regime map for liquid bound granules. *AIChE Journal*, 49(2):350–361.

Hapgood, K. P., Litster, J. D., White, E. T., Mort, P. R., and Jones, D. G. (2004). Dimensionless spray flux in wet granulation: Monte-Carlo simulations and experimental validation. *Powder Technology*, 141(1):20–30.

Hapgood, K. P., Tan, M. X. L., and Chow, D. W. Y. (2009). A method to predict nuclei size distributions for use in models of wet granulation. *Advanced Powder Technology*, 20(4):293–297.

Hassanpour, A., Kwan, C. C., Ng, B. H., Rahmanian, N., Ding, Y. L., Antony, S. J., Jia, X. D., and Ghadiri, M. (2009). Effect of granulation scale-up on the strength of granules. *Powder Technology*, 189(2):304–312.

Hassanpour, A., Pasha, M., Susana, L., Rahmanian, N., Santomaso, A. C., and Ghadiri, M. (2013). Analysis of seeded granulation in high shear granulators by discrete element method. *Powder Technology*, 238:50–55.

Hassanpour, A., Tan, H., Bayly, A., Gopalkrishnan, P., Ng, B., and Ghadiri, M. (2011). Analysis of particle motion in a paddle mixer using discrete element method (DEM). *Powder Technology*, 206(1):189–194.

He, X., Lunday, K. A., Li, L.-C., and Sacchetti, M. J. (2008). Formulation development and process scale up of a high shear wet granulation formulation containing a poorly wettable drug. *Journal of Pharmaceutical Sciences*, 97(12):5274–5289.

Hertz, H. (1881). Über die Berührung fester elastischer Körper. *Journal für die reine und angewandte Mathematik*, 92:156–171.

HM Treasury (2010). Energy market assessment. Technical report, HM Treasury.

Hoffmann, A. C. and Finkers, H. J. (1995). A relation for the void fraction of randomly packed particle beds. *Powder Technology*, 82(2):197–203.

Holm, P. (1987). Effect of impeller and chopper design on granulation in a high speed mixer. *Drug Development and Industrial Pharmacy*, 13(9-11):1675–1701.

Holm, P., Schaefer, T., and Larsen, C. (2001). End-point detection in a wet granulation process. *Pharmaceutical Development and Technology*, 6(2):181–192.

Horsthuis, G. J. B., van Laarhoven, J. A. H., van Rooij, R. C. B. M., and Vromans, H. (1993). Studies on upscaling parameters of the gral high shear granulation process. *International Journal of Pharmaceutics*, 92(1-3):143–150.

Hounslow, M. J. (1998). The population balance as a tool for understanding particle rate processes. *KONA Powder and Particle Journal*, 16(0):179–193.

Hounslow, M. J., Oullion, M., and Reynolds, G. K. (2009). Kinetic models for granule nucleation by the immersion mechanism. *Powder Technology*, 189(2):177–189.

Hounslow, M. J., Pearson, J. M. K., and Instone, T. (2001). Tracer studies of high-shear granulation: II. population balance modeling. *AIChE Journal*, 47(9):1984–1999.

Hounslow, M. J., Ryall, R. L., and Marshall, V. R. (1988). A discretized population balance for nucleation, growth, and aggregation. *AIChE Journal*, 34(11):1821–1832.

Hulburt, H. M. and Katz, S. (1964). Some problems in particle technology: A statistical mechanical formulation. *Chemical Engineering Science*, 19(8):555–574.

Immanuel, C. D. and Doyle III, F. J. (2005). Solution technique for a multi-dimensional population balance model describing granulation processes. *Powder Technology*, 156(2):213–225.

Ingram, G. D. and Cameron, I. T. (2004). Challenges in multiscale modelling and its application to granulation systems. *Developments in Chemical Engineering and Mineral Processing*, 12(3-4):293–308.

Ingram, G. D. and Cameron, I. T. (2005). Formulation and comparison of alternative multiscale models for drum granulation. *Computer Aided Chemical Engineering*, 20(C):481–486.

Iooss, B. and Lemaître, P. (2015). A review on global sensitivity analysis methods. In *Uncertainty management in simulation-optimization of complex systems*, pages 101–122. Springer.

Iveson, S. M. (2002). Limitations of one-dimensional population balance models of wet granulation processes. *Powder Technology*, 124(3):219–229.

Iveson, S. M., Beathe, J. A., and Page, N. W. (2002). The dynamic strength of partially saturated powder compacts: the effect of liquid properties. *Powder Technology*, 127(2):149–161.

Iveson, S. M. and Litster, J. D. (1998a). Fundamental studies of granule consolidation Part 2: Quantifying the effects of particle and binder properties. *Powder Technology*, 99(3):243–250.

Iveson, S. M. and Litster, J. D. (1998b). Growth regime map for liquid-bound granules. *AIChE Journal*, 44(7):1510.

Iveson, S. M., Litster, J. D., and Ennis, B. J. (1996). Fundamental studies of granule consolidation Part 1: Effects of binder content and binder viscosity. *Powder Technology*, 88(1):15–20.

Iveson, S. M., Litster, J. D., Hapgood, K., and Ennis, B. J. (2001a). Nucleation, growth and breakage phenomena in agitated wet granulation processes: a review. *Powder Technology*, 117(1):3–39.

Iveson, S. M. and Page, N. W. (2005). Dynamic strength of liquid-bound granular materials: The effect of particle size and shape. *Powder Technology*, 152(1-3):79–89.

Iveson, S. M., Page, N. W., and Litster, J. D. (2003). The importance of wet-powder dynamic mechanical properties in understanding granulation. *Powder Technology*, 130(1-3):97–101.

Iveson, S. M., Wauters, P. A. L., Forrest, S., Litster, J. D., Meesters, G. M. H., and Scarlett, B. (2001b). Growth regime map for liquid-bound granules: further development and experimental validation. *Powder Technology*, 117(1):83–97.

Jain, N., Ottino, J. M., and Lueptow, R. M. (2002). An experimental study of the flowing granular layer in a rotating tumbler. *Physics of Fluids*, 14(2):572–582.

Jia, Z., Davis, E., Muzzio, F. J., and Ierapetritou, M. G. (2009). Predictive modeling for pharmaceutical processes using kriging and response surface. *Journal of Pharmaceutical Innovation*, 4(4):174–186.

John, V., Mitkova, T., Roland, M., Sundmacher, K., Tobiska, L., and Voigt, A. (2009). Simulations of population balance systems with one internal coordinate using finite element methods. *Chemical Engineering Science*, 64(4):733–741.

Johnson, K. L. (1985). *Contact mechanics*. Cambridge University Press.

Kapur, P. C. (1972a). Kinetics of granulation by non-random coalescence mechanism. *Chemical Engineering Science*, 27(10):1863–1869.

Kapur, P. C. (1972b). Self-preserving size spectra of comminuted particles. *Chemical Engineering Science*, 27(2):425–431.

Kapur, P. C. and Fuerstenau, D. W. (1969). Coalescence model for granulation. *Industrial & Engineering Chemistry Process Design and Development*, 8(1):56–62.

Kastner, C. A., Brownbridge, G. P. E., Mosbach, S., and Kraft, M. (2013). Impact of powder characteristics on a particle granulation model. *Chemical Engineering Science*, 97:282–295.

Kawashima, Y., Cui, F., Takeuchi, H., Niwa, T., Hino, T., and Kiuchi, K. (1994). Improvements in flowability and compressibility of pharmaceutical crystals for direct tabletting by spherical crystallization with a two-solvent system. *Powder Technology*, 78(2):151–157.

Kayrak-Talay, D., Dale, S., Wassgren, C., and Litster, J. (2013). Quality by design for wet granulation in pharmaceutical processing: assessing models for a priori design and scaling. *Powder Technology*, 240:7–18.

Kayrak-Talay, D. and Litster, J. D. (2011). A priori performance prediction in pharmaceutical wet granulation: Testing the applicability of the nucleation regime map to a formulation with a broad size distribution and dry binder addition. *International Journal of Pharmaceutics*, 418(2):254–264.

Keningley, S. T., Knight, P. C., and Marson, A. D. (1997). An investigation into the effects of binder viscosity on agglomeration behaviour. *Powder Technology*, 91(2):95–103.

Ketterhagen, W. R., am Ende, M. T., and Hancock, B. C. (2009). Process modeling in the pharmaceutical industry using the discrete element method. *Journal of Pharmaceutical Sciences*, 98(2):442–470.

Klimpel, R. R. and Austin, L. G. (1984). The back-calculation of specific rates of breakage from continuous mill data. *Powder Technology*, 38(1):77–91.

Korson, L., Drost-Hansen, W., and Millero, F. J. (1969). Viscosity of water at various temperatures. *The Journal of Physical Chemistry*, 73(1):34–39.

Kostoglou, M. (2007). Extended cell average technique for the solution of coagulation equation. *Journal of colloid and interface science*, 306(1):72–81.

Kostoglou, M., Dovas, S., and Karabelas, A. J. (1997). On the steady-state size distribution of dispersions in breakage processes. *Chemical Engineering Science*, 52(8):1285–1299.

Kostoglou, M. and Karabelas, A. J. (1998). Theoretical analysis of the steady state particle size distribution in limited breakage processes. *Journal of Physics A: Mathematical and General*, 31(44):8905.

Kristensen, H. G., Holm, P., and Schaefer, T. (1985a). Mechanical properties of moist agglomerates in relation to granulation mechanisms Part I. deformability of moist, densified agglomerates. *Powder Technology*, 44(3):227–237.

Kristensen, H. G., Holm, P., and Schaefer, T. (1985b). Mechanical properties of moist agglomerates in relation to granulation mechanisms Part II. effects of particle size distribution. *Powder Technology*, 44(3):239–247.

Kristensen, H. G. and Schaefer, T. (1987). Granulation: A review on pharmaceutical wet-granulation. *Drug development and industrial pharmacy*, 13(4-5):803–872.

Kulju, T., Paavola, M., Spittka, H., Keiski, R. L., Juuso, E., Leiviskä, K., and Muurinen, E. (2016). Modeling continuous high-shear wet granulation with DEM–PB. *Chemical Engineering Science*, 142:190–200.

Kumar, A., Gernaey, K. V., De Beer, T., and Nopens, I. (2013). Model-based analysis of high shear wet granulation from batch to continuous processes in pharmaceutical production–a critical review. *European Journal of Pharmaceutics and Biopharmaceutics*, 85(3):814–832.

Kumar, A., Vercruysse, J., Mortier, S. T. F. C., Vervaet, C., Remon, J. P., Gernaey, K. V., De Beer, T., and Nopens, I. (2016). Model-based analysis of a twin-screw wet granulation system for continuous solid dosage manufacturing. *Computers & Chemical Engineering*, 89:62–70.

Kumar, J. (2006). *Numerical approximations of population balance equations in particulate systems*. PhD thesis, Otto-von-Guericke-Universität Magdeburg.

Kumar, J., Peglow, M., Warnecke, G., and Heinrich, S. (2008a). The cell average technique for solving multi-dimensional aggregation population balance equations. *Computers & Chemical Engineering*, 32(8):1810–1830.

Kumar, J., Peglow, M., Warnecke, G., and Heinrich, S. (2008b). An efficient numerical technique for solving population balance equation involving aggregation, breakage, growth and nucleation. *Powder Technology*, 182(1):81–104.

Kumar, J., Peglow, M., Warnecke, G., Heinrich, S., and Mörl, L. (2006). Improved accuracy and convergence of discretized population balance for aggregation: The cell average technique. *Chemical Engineering Science*, 61(10):3327–3342.

Kumar, J., Warnecke, G., Peglow, M., and Heinrich, S. (2009). Comparison of numerical methods for solving population balance equations incorporating aggregation and breakage. *Powder Technology*, 189(2):218–229.

Kumar, R., Freireich, B., and Wassgren, C. (2015). DEM–compartment–population balance model for particle coating in a horizontal rotating drum. *Chemical Engineering Science*, 125:144–157.

Kumar, S. and Ramkrishna, D. (1996a). On the solution of population balance equations by discretization-I. a fixed pivot technique. *Chemical Engineering Science*, 51(8):1311–1332.

Kumar, S. and Ramkrishna, D. (1996b). On the solution of population balance equations by discretization-II. a moving pivot technique. *Chemical Engineering Science*, 51(8):1333–1342.

Kumar Akkisetty, P., Lee, U., Reklaitis, G. V., and Venkatasubramanian, V. (2010). Population balance model-based hybrid neural network for a pharmaceutical milling process. *Journal of Pharmaceutical Innovation*, 5(4):161–168.

Kuo, H. P., Knight, P. C., Parker, D. J., Adams, M. J., and Seville, J. P. K. (2004). Discrete element simulations of a high-shear mixer. *Advanced Powder Technology*, 15(3):297–309.

Kuwabara, G. and Kono, K. (1987). Restitution coefficient in a collision between two spheres. *Japanese Journal of Applied Physics*, 26(8R):1230.

Landin, M. (2017). Artificial intelligence tools for scaling up of high shear wet granulation process. *Journal of Pharmaceutical Sciences*.

Landin, M. and Rowe, R. C. (2013). Artificial neural networks technology to model, understand and optimize drug formulations. In *Formulation Tools for Pharmaceutical Development*, pages 7–37. Woodhead Publishing Ltd, Oxford.

Landin, M., York, P., Cliff, M. J., and Rowe, R. C. (1999). Scaleup of a pharmaceutical granulation in planetary mixers. *Pharmaceutical Development and Technology*, 4(2):145–150.

Lasinski, M. E., Curtis, J. S., and Pekny, J. F. (2004). Effect of system size on particle-phase stress and microstructure formation. *Physics of Fluids*, 16(2):265–273.

Le, P. K., Avontuur, P., Hounslow, M. J., and Salman, A. D. (2009). The kinetics of the granulation process: right from the early stages. *Powder Technology*, 189(2):149–157.

Lee, J. (1994). Density waves in the flows of granular media. *Physical Review E*, 49(1):281.

Lee, K., Kim, T., Rajniak, P., and Matsoukas, T. (2008). Compositional distributions in multicomponent aggregation. *Chemical Engineering Science*, 63(5):1293–1303.

Lee, K. F., Dosta, M., McGuire, A. D., Mosbach, S., Wagner, W., Heinrich, S., and Kraft, M. (2017). Development of a multi-compartment population balance model for high-shear wet granulation with discrete element method. *Computers & Chemical Engineering*, 99:171–184.

Levenberg, K. (1944). A method for the solution of certain non-linear problems in least squares. *Quarterly of Applied Mathematics*, 2(2):164–168.

Levenspiel, O. (1980). The monod equation: a revisit and a generalization to product inhibition situations. *Biotechnology and bioengineering*, 22(8):1671–1687.

Levin, M. G. (2007). Wet granulation : End-point determination and scale-up. In Swarbrick, J., editor, *Encyclopedia of Pharmaceutical Technology*, pages 4078–4098. CRC Press.

Li, J., Freireich, B. J., Wassgren, C. R., and Litster, J. D. (2013a). Experimental validation of a 2-D population balance model for spray coating processes. *Chemical Engineering Science*, 95:360–365.

Li, J., Wassgren, C., and Litster, J. D. (2013b). Multi-scale modeling of a spray coating process in a paddle mixer/coater: the effect of particle size distribution on particle segregation and coating uniformity. *Chemical Engineering Science*, 95:203–210.

Liffman, K. (1992). A direct simulation Monte-Carlo method for cluster coagulation. *Journal of Computational Physics*, 100(1):116–127.

Lin, Y., Lee, K., and Matsoukas, T. (2002). Solution of the population balance equation using constant-number Monte Carlo. *Chemical Engineering Science*, 57(12):2241–2252.

Liss, E. D. and Glasser, B. J. (2001). The influence of clusters on the stress in a sheared granular material. *Powder Technology*, 116(2):116–132.

Litster, J. (2016). *Design and Processing of Particulate Products*. Cambridge University Press.

Litster, J. and Ennis, B. (2004). *The science and engineering of granulation processes*, volume 15. Springer Science & Business Media.

Litster, J. D. (2003). Scaleup of wet granulation processes: science not art. *Powder Technology*, 130(1-3):35–40.

Litster, J. D., Hapgood, K. P., Michaels, J. N., Sims, A., Roberts, M., and Kameneni, S. K. (2002). Scale-up of mixer granulators for effective liquid distribution. *Powder Technology*, 124(3):272–280.

Litster, J. D., Hapgood, K. P., Michaels, J. N., Sims, A., Roberts, M., Kameneni, S. K., and Hsu, T. (2001). Liquid distribution in wet granulation: dimensionless spray flux. *Powder Technology*, 114(1):32–39.

Litster, J. D., Smit, D. J., and Hounslow, M. J. (1995). Adjustable discretized population balance for growth and aggregation. *AIChE Journal*, 41(3):591–603.

Liu, L. X. and Litster, J. D. (2002). Population balance modelling of granulation with a physically based coalescence kernel. *Chemical Engineering Science*, 57(12):2183–2191.

Liu, L. X., Litster, J. D., Iveson, S. M., and Ennis, B. J. (2000). Coalescence of deformable granules in wet granulation processes. *AIChE Journal*, 46(3):529–539.

Liu, L. X., Robinson, D. J., and Addai-Mensah, J. (2012). Population balance based modelling of nickel laterite agglomeration behaviour. *Powder Technology*, 223:92–97.

Liu, L. X., Smith, R., and Litster, J. D. (2009). Wet granule breakage in a breakage only high-hear mixer: Effect of formulation properties on breakage behaviour. *Powder Technology*, 189(2):158–164.

Liu, L. X., Zhou, L., Robinson, D. J., and Addai-Mensah, J. (2013a). A nuclei size distribution model including nuclei breakage. *Chemical Engineering Science*, 86:19–24.

Liu, P. Y., Yang, R. Y., and Yu, A. B. (2013b). DEM study of the transverse mixing of wet particles in rotating drums. *Chemical Engineering Science*, 86:99–107.

Luo, G., Xu, B., Zhang, Y., Cui, X., Li, J., Shi, X., and Qiao, Y. (2017). Scale-up of a high shear wet granulation process using a nucleation regime map approach. *Particuology*, 31:87–94.

Mackaplow, M. B., Rosen, L. A., and Michaels, J. N. (2000). Effect of primary particle size on granule growth and endpoint determination in high-shear wet granulation. *Powder Technology*, 108(1):32–45.

Madec, L., Falk, L., and Plasari, E. (2003). Modelling of the agglomeration in suspension process with multidimensional kernels. *Powder Technology*, 130(1):147–153.

Mahoney, A. W. and Ramkrishna, D. (2002). Efficient solution of population balance equations with discontinuities by finite elements. *Chemical Engineering Science*, 57(7):1107–1119.

Mantzaris, N. V., Daoutidis, P., and Srienc, F. (2001a). Numerical solution of multi-variable cell population balance models: I. finite difference methods. *Computers & Chemical Engineering*, 25(11):1411–1440.

Mantzaris, N. V., Daoutidis, P., and Srienc, F. (2001b). Numerical solution of multi-variable cell population balance models. II. spectral methods. *Computers & Chemical Engineering*, 25(11):1441–1462.

Mantzaris, N. V., Daoutidis, P., and Srienc, F. (2001c). Numerical solution of multi-variable cell population balance models. III. finite element methods. *Computers & Chemical Engineering*, 25(11):1463–1481.

Marchisio, D. L. and Fox, R. O. (2005). Solution of population balance equations using the direct quadrature method of moments. *Journal of Aerosol Science*, 36(1):43–73.

Marchisio, D. L., Pikturna, J. T., Fox, R. O., Vigil, R. D., and Barresi, A. A. (2003). Quadrature method of moments for population-balance equations. *AIChE Journal*, 49(5):1266–1276.

Marigo, M., Davies, M., Leadbeater, T., Cairns, D. L., Ingram, A., and Stitt, E. H. (2013). Application of positron emission particle tracking (PEPT) to validate a discrete element method (DEM) model of granular flow and mixing in the turbula mixer. *International Journal of Pharmaceutics*, 446(1):46–58.

Maronga, S. J. and Wnukowski, P. (1997). Modelling of the three-domain fluidized-bed particulate coating process. *Chemical Engineering Science*, 52(17):2915–2925.

Marrel, A., Iooss, B., Laurent, B., and Roustant, O. (2009). Calculations of Sobol indices for the Gaussian process metamodel. *Reliability Engineering & System Safety*, 94(3):742–751.

Marshall, C. L., Rajniak, P., and Matsoukas, T. (2011). Numerical simulations of two-component granulation: Comparison of three methods. *Chemical Engineering Research and Design*, 89(5):545–552.

Matsoukas, T., Kim, T., and Lee, K. (2009). Bicomponent aggregation with composition-dependent rates and the approach to well-mixed state. *Chemical Engineering Science*, 64(4):787–799.

Matsumoto, M. and Nishimura, T. (1998). Mersenne twister: a 623-dimensionally equidistributed uniform pseudo-random number generator. *ACM Trans. Model. Comput. Simul.*, 8(1):3–30.

Maxim, R., Fu, J. S., Pickles, M., Salman, A., and Hounslow, M. (2004). Modelling effects of processing parameters on granule porosity in high-shear granulation. *Granular Matter*, 6(2-3):131–135.

McGuire, A. D., Mosbach, S., Lee, K. F., Reynolds, G., and Kraft, M. (2018a). A high-dimensional, stochastic model for twin-screw granulation–Part 1: Model description. *Chemical Engineering Science*, 188:221–237.

McGuire, A. D., Mosbach, S., Lee, K. F., Reynolds, G., and Kraft, M. (2018b). A high-dimensional, stochastic model for twin-screw granulation Part 2: Numerical methodology. *Chemical Engineering Science*, 188:18–33.

Meier, M., John, E., Wieckhusen, D., Wirth, W., and Peukert, W. (2008). Characterization of the grinding behaviour in a single particle impact device: studies on pharmaceutical powders. *European Journal of Pharmaceutical Sciences*, 34(1):45–55.

Meyer, K., Bück, A., and Tsotsas, E. (2015). Dynamic multi-zone population balance model of particle formulation in fluidized beds. *Procedia engineering*, 102:1456–1465.

Michaels, J. N. (2003). Toward rational design of powder processes. *Powder Technology*, 138(1):1–6.

Michaels, J. N., Farber, L., Wong, G. S., Hapgood, K., Heidel, S. J., Farabaugh, J., Chou, J.-H., and Tardos, G. I. (2009). Steady states in granulation of pharmaceutical powders with application to scale-up. *Powder Technology*, 189(2):295–303.

Milton, R. A. and Brown, S. F. (2020). Minimum reduced order modelling. In preparation.

Miyamoto, Y., Ogawa, S., Miyajima, M., Matsui, M., Sato, H., Takayama, K., and Nagai, T. (1997). An application of the computer optimization technique to wet granulation process involving explosive growth of particles. *International Journal of Pharmaceutics*, 149(1):25–36.

Montgomery, D. C. and Runger, G. C. (2014). *Applied statistics and probability for engineers*. John Wiley and Sons.

Mort, P. R. (2005). Scale-up of binder agglomeration processes. *Powder Technology*, 150(2):86–103.

Muguruma, Y., Tanaka, T., and Tsuji, Y. (2000). Numerical simulation of particulate flow with liquid bridge between particles (simulation of centrifugal tumbling granulator). *Powder Technology*, 109(1):49–57.

Munro, B. H. (2005). *Statistical methods for health care research*, volume 5. Lippincott Williams & Wilkins.

Nakamura, H., Fujii, H., and Watano, S. (2013). Scale-up of high shear mixer-granulator based on discrete element analysis. *Powder Technology*, 236:149–156.

National Research Council (2003). *Beyond the molecular frontier: Challenges for chemistry and chemical engineering*. The National Academies Press, Washington, DC.

Nelder, J. A. and Mead, R. (1965). A simplex method for function minimization. *The Computer Journal*, 7(4):308–313.

Nicmanis, M. and Hounslow, M. J. (1996). A finite element analysis of the steady state population balance equation for particulate systems: Aggregation and growth. *Computers & Chemical Engineering*, 20:S261–S266.

Niklasson Björn, I., Jansson, A., Karlsson, M., Folestad, S., and Rasmuson, A. (2005). Empirical to mechanistic modelling in high shear granulation. *Chemical Engineering Science*, 60(14):3795–3803.

Ouchiyama, N. and Tanaka, T. (1980). Stochastic model for compaction of pellets in granulation. *Industrial & Engineering Chemistry Process Design and Development*, 19(4):555–560.

Oulahna, D., Cordier, F., Galet, L., and Dodds, J. A. (2003). Wet granulation: the effect of shear on granule properties. *Powder Technology*, 130(1-3):238–246.

Oullion, M., Reynolds, G. K., and Hounslow, M. J. (2009). Simulating the early stage of high-shear granulation using a two-dimensional Monte-Carlo approach. *Chemical Engineering Science*, 64(4):673–685.

Pallas, N. R. and Harrison, Y. (1990). An automated drop shape apparatus and the surface tension of pure water. *Colloids and Surfaces*, 43(2):169–194.

Pandey, P. and Badawy, S. (2016). A quality by design approach to scale-up of high-shear wet granulation process. *Drug development and industrial pharmacy*, 42(2):175–189.

Pandey, P., Song, Y., Kayihan, F., and Turton, R. (2006). Simulation of particle movement in a pan coating device using discrete element modeling and its comparison with video-imaging experiments. *Powder Technology*, 161(2):79–88.

Pandya, J. D. and Spielman, L. A. (1983). Floc breakage in agitated suspensions: effect of agitation rate. *Chemical Engineering Science*, 38(12).

Passalacqua, A., Laurent, F., Madadi-Kandjani, E., Heylmun, J. C., and Fox, R. O. (2018). An open-source quadrature-based population balance solver for openfoam. *Chemical Engineering Science*, 176:306–318.

Pigou, M., Morchain, J., Fede, P., Penet, M.-I., and Laronze, G. (2018). New developments of the extended quadrature method of moments to solve population balance equations. *Journal of Computational Physics*, 365:243–268.

Pitt, K., Smith, R. M., de Koster, S. A. L., Litster, J. D., and Hounslow, M. J. (2018). Kinetics of immersion nucleation driven by surface tension. *Powder Technology*, 335:62–69.

Pohlman, D. A. (2015). *Multi-scale modeling of high-shear granulation*. PhD thesis, Purdue University.

Pohlman, D. A. and Litster, J. D. (2015). Coalescence model for induction growth behavior in high shear granulation. *Powder Technology*, 270:435–444.

Poon, J. M.-H., Immanuel, C. D., Doyle III, F. J., and Litster, J. D. (2008). A three-dimensional population balance model of granulation with a mechanistic representation of the nucleation and aggregation phenomena. *Chemical Engineering Science*, 63(5):1315–1329.

Portillo, P. M., Muzzio, F. J., and Ierapetritou, M. G. (2007). Hybrid DEM–compartment modeling approach for granular mixing. *AIChE Journal*, 53(1):119–128.

Rahmanian, N., Ghadiri, M., and Ding, Y. (2008a). Effect of scale of operation on granule strength in high shear granulators. *Chemical Engineering Science*, 63(4):915–923.

Rahmanian, N., Ng, B., Hassanpour, A., Ding, Y., Antony, J., Jia, X., Ghadiri, M., van der Wel, P., Krug-Polman, A., York, D., Bayly, A., and Tan, S. H. (2008b). Scale-up of high-shear mixer granulators. *KONA Powder and Particle Journal*, 26:190–204.

Rajniak, P., Stepanek, F., Dhanasekharan, K., Fan, R., Mancinelli, C., and Chern, R. T. (2009). A combined experimental and computational study of wet granulation in a wurster fluid bed granulator. *Powder Technology*, 189(2):190–201.

Ramachandran, R. and Barton, P. I. (2010). Effective parameter estimation within a multi-dimensional population balance model framework. *Chemical Engineering Science*, 65(16):4884–4893.

Ramachandran, R. and Chaudhury, A. (2012). Model-based design and control of a continuous drum granulation process. *Chemical Engineering Research and Design*, 90(8):1063–1073.

Ramachandran, R., Immanuel, C. D., Stepanek, F., Litster, J. D., and Doyle III, F. J. (2009). A mechanistic model for breakage in population balances of granulation: Theoretical kernel development and experimental validation. *Chemical Engineering Research and Design*, 87(4):598–614.

Ramkrishna, D. (1985). The status of population balances. *Reviews in Chemical Engineering*, 3(1):49–95.

Ramkrishna, D. and Mahoney, A. W. (2002). Population balance modeling. Promise for the future. *Chemical Engineering Science*, 57(4):595–606.

Rao, S. S. (2009). *Engineering optimization: Theory and practice*. John Wiley & Sons.

Reynolds, G. K., Fu, J. S., Cheong, Y. S., Hounslow, M. J., and Salman, A. D. (2005). Breakage in granulation: a review. *Chemical Engineering Science*, 60(14):3969–3992.

Ristow, G. H. and Herrmann, H. J. (1994). Density patterns in two-dimensional hoppers. *Physical Review E*, 50(1):R5.

Rohrer, P. A. (2017). Experimental study on scale up of high shear wet granulation. Master's thesis, School of Life Sciences FHNW.

Rumpf, H. (1973). Physical aspects of comminution and new formulation of a law of comminution. *Powder Technology*, 7(3):145–159.

Sanders, C. F. W., Willemse, A. W., Salman, A. D., and Hounslow, M. J. (2003). Development of a predictive high-shear granulation model. *Powder Technology*, 138(1):18–24.

Sastry, K. V. S. (1975). Similarity size distribution of agglomerates during their growth by coalescence in granulation or green pelletization. *International Journal of Mineral Processing*, 2(2):187–203.

Sato, Y., Okamoto, T., and Watano, S. (2005). Scale-up of high shear granulation based on agitation power. *Chemical and Pharmaceutical Bulletin*, 53(12):1547–1550.

Sayin, R. (2016). *Mechanistic studies of twin screw granulation*. PhD thesis, Purdue University.

Schæfer, T., Taagegaard, B., Thomsen, L. J., and Kristensen, H. G. (1993). Melt pelletization in a high shear mixer. V. effects of apparatus variables. *European Journal of Pharmaceutical Sciences*, 1(3):133–141.

Scott, A. C., Hounslow, M. J., and Instone, T. (2000). Direct evidence of heterogeneity during high-shear granulation. *Powder Technology*, 113(1):205–213.

Sehmbi, H. (2019). Investigation of nucleation in high shear wet granulation. Master's thesis, The University of Sheffield.

Selma, B., Bannari, R., and Proulx, P. (2010). Simulation of bubbly flows: Comparison between direct quadrature method of moments (dqmom) and method of classes (cm). *Chemical Engineering Science*, 65(6):1925–1941.

Sen, M., Barrasso, D., Singh, R., and Ramachandran, R. (2014). A multi-scale hybrid CFD–DEM–PBM description of a fluid-bed granulation process. *Processes*, 2(1):89–111.

Sen, M., Chaudhury, A., Singh, R., John, J., and Ramachandran, R. (2013a). Multi-scale flowsheet simulation of an integrated continuous purification–downstream pharmaceutical manufacturing process. *International Fournal of Pharmaceutics*, 445(1-2):29–38.

Sen, M., Dubey, A., Singh, R., and Ramachandran, R. (2013b). Mathematical development and comparison of a hybrid PBM–DEM description of a continuous powder mixing process. *Journal of Powder Technology*, 2013.

Sen, M., Singh, R., Vanarase, A., John, J., and Ramachandran, R. (2012). Multi-dimensional population balance modeling and experimental validation of continuous powder mixing processes. *Chemical Engineering Science*, 80:349–360.

Shanmugam, S. (2015). Granulation techniques and technologies: recent progresses. *BioImpacts: BI*, 5(1):55.

Shanno, D. F. (1970). Conditioning of quasi-newton methods for function minimization. *Mathematics of Computation*, 24(111):647–656.

Sheshadri, K. and Fritzson, P. (2011). MathPDE: A package to solve PDEs by finite differences. *Mathematica Journal*, 13.

Shi, L., Feng, Y., and Sun, C. C. (2010). Roles of granule size in over-granulation during high shear wet granulation. *Journal of Pharmaceutical Sciences*, 99(8):3322–3325.

Shi, L., Feng, Y., and Sun, C. C. (2011). Massing in high shear wet granulation can simultaneously improve powder flow and deteriorate powder compaction: A double-edged sword. *European Journal of Pharmaceutical Sciences*, 43(1-2):50–56.

Shirazian, S., Darwish, S., Kuhs, M., Croker, D. M., and Walker, G. M. (2018). Regime-separated approach for population balance modelling of continuous wet granulation of pharmaceutical formulations. *Powder Technology*, 325:420–428.

Shirazian, S., Ismail, H. Y., Singh, M., Shaikh, R., Croker, D. M., and Walker, G. M. (2019). Multi-dimensional population balance modelling of pharmaceutical formulations for continuous twin-screw wet granulation: Determination of liquid distribution. *International Journal of Pharmaceutics*.

Sirois, P. J. and Craig, G. D. (2000). Scaleup of a high-shear granulation process using a normalized impeller work parameter. *Pharmaceutical Development and Technology*, 5(3):365–374.

Smith, M. and Matsoukas, T. (1998). Constant-number Monte Carlo simulation of population balances. *Chemical Engineering Science*, 53(9):1777–1786.

Smith, R. M. (2007). *Wet Granule Breakage in High Shear Mixer Graunlators*. PhD thesis, The University of Queensland.

Smrčka, D., Dohnal, J., and Štěpánek, F. (2015). Effect of process scale-up on the dissolution of granules with a high content of active pharmaceutical ingredient. *Powder Technology*, 285:88–95.

Sobol', I. M. (2001). Global sensitivity indices for nonlinear mathematical models and their Monte Carlo estimates. *Mathematics and Computers in Simulation*, 55(1-3):271–280.

Sood, A., Awasthi, A., and Bharti, R. (2016). A population balance model for butyl acrylate emulsion polymerization. *Indian Chemical Engineer*, 58(1):40–60.

Soos, M., Sefcik, J., and Morbidelli, M. (2006). Investigation of aggregation, breakage and restructuring kinetics of colloidal dispersions in turbulent flows by population balance modeling and static light scattering. *Chemical Engineering Science*, 61(8):2349–2363.

Štěpánek, F., Rajniak, P., Mancinelli, C., Chern, R. T., and Ramachandran, R. (2009). Distribution and accessibility of binder in wet granules. *Powder Technology*, 189(2):376–384.

Stewart, R. L., Bridgwater, J., Zhou, Y. C., and Yu, A. B. (2001). Simulated and measured flow of granules in a bladed mixer – a detailed comparison. *Chemical Engineering Science*, 56(19):5457–5471.

Su, J., Gu, Z., Li, Y., Feng, S., and Xu, X. Y. (2007). Solution of population balance equation using quadrature method of moments with an adjustable factor. *Chemical Engineering Science*, 62(21):5897–5911.

Sulttan, S. and Rohani, S. (2019). Coupling of CFD and population balance modelling for a continuously seeded helical tubular crystallizer. *Journal of Crystal Growth*, 505:19–25.

Taguchi, Y. (1992). Powder turbulence: direct onset of turbulent flow. *Journal de Physique II*, 2(12):2103–2114.

Tan, H. S., Goldschmidt, M. J. V., Boerefijn, R., Hounslow, M. J., Salman, A. D., and Kuipers, J. A. M. (2004a). Building population balance model for fluidized bed melt granulation: lessons from kinetic theory of granular flow. *Powder Technology*, 142(2):103–109.

Tan, H. S., Salman, A. D., and Hounslow, M. J. (2004b). Kinetics of fluidised bed melt granulation: IV. selecting the breakage model. *Powder Technology*, 143:65–83.

Tan, H. S., Salman, A. D., and Hounslow, M. J. (2005a). Kinetics of fluidised bed melt granulation III: tracer studies. *Chemical Engineering Science*, 60(14):3835–3845.

Tan, H. S., Salman, A. D., and Hounslow, M. J. (2005b). Kinetics of fluidised bed melt granulation V: simultaneous modelling of aggregation and breakage. *Chemical Engineering Science*, 60(14):3847–3866.

Tao, J., Pandey, P., Bindra, D. S., Gao, J. Z., and Narang, A. S. (2015). Evaluating scale-up rules of a high-shear wet granulation process. *Journal of Pharmaceutical Sciences*, 104(7):2323–2333.

Tardos, G. I., Hapgood, K. P., Ipadeola, O. O., and Michaels, J. N. (2004). Stress measurements in high-shear granulators using calibrated ”test” particles: application to scale-up. *Powder Technology*, 140(3):217–227.

Tardos, G. I., Khan, M. I., and Mort, P. R. (1997). Critical parameters and limiting conditions in binder granulation of fine powders. *Powder Technology*, 94(3):245–258.

Tilton, L. W. and Taylor, J. K. (1922). Accurate representation of the refractivity and density of distilled water as a function of temperature. *Phys. Rev*, 2(20):249.

Tran, A. L. H. (2015). *Powder flow in bertical high shear mixer granulators*. PhD thesis, The University of Queensland.

Vale, H. M. and McKenna, T. F. (2005). Solution of the population balance equation for two-component aggregation by an extended fixed pivot technique. *Industrial & Engineering Chemistry Research*, 44(20):7885–7891.

Verkoeijen, D., Pouw, G. A., Meesters, G. M. H., and Scarlett, B. (2002). Population balances for particulate processes-a volume approach. *Chemical Engineering Science*, 57(12):2287–2303.

Vogel, L. and Peukert, W. (2003). Breakage behaviour of different materials – construction of a mastercurve for the breakage probability. *Powder Technology*, 129(1):101–110.

Vogel, L. and Peukert, W. (2004). Determination of material properties relevant to grinding by practicable labscale milling tests. *International Journal of Mineral Processing*, 74:S329–S338.

Vogel, L. and Peukert, W. (2005). From single particle impact behaviour to modelling of impact mills. *Chemical Engineering Science*, 60(18):5164–5176.

Walton, O. R. and Braun, R. L. (1986). Viscosity, granular-temperature, and stress calculations for shearing assemblies of inelastic, frictional disks. *Journal of Rheology*, 30(5):949–980.

Wang, F. Y., Ge, X. Y., Balliu, N., and Cameron, I. T. (2006). Optimal control and operation of drum granulation processes. *Chemical Engineering Science*, 61(1):257–267.

Wang, L. G., Morrissey, J. P., Sousani, M., Barrasso, D., Slade, D., Hanley, K., Ooi, J. Y., and Litster, J. D. (2019). Model driven design in particulate products manufacturing. In 9^{th} *International Granulation Workshop*, Lausanne, Switzerland.

Wauters, P. A. L., Jakobsen, R. B., Litster, J. D., Meesters, G. M. H., and Scarlett, B. (2002). Liquid distribution as a means to describing the granule growth mechanism. *Powder Technology*, 123(2):166–177.

Wauters, P. A. L., Scarlett, B., Liu, L. X., Litster, J. D., and Meesters, G. M. H. (2003). A population balance model for high shear granulation. *Chemical Engineering Communications*, 190(10):1309–1334.

Wehrlé, P., Nobelis, P., Cuiné, A., and Stamm, A. (1993). Scaling-up of wet granulation a statistical methodology. *Drug Development and Industrial Pharmacy*, 19(16):1983–1997.

Wildeboer, W. J., Litster, J. D., and Cameron, I. T. (2005). Modelling nucleation in wet granulation. *Chemical Engineering Science*, 60(14):3751–3761.

Wynn, E. J. W. (1996). Improved accuracy and convergence of discretized population balance of Lister et al. *AIChE Journal*, 42(7):2084–2086.

Yamane, K., Nakagawa, M., Altobelli, S. A., Tanaka, T., and Tsuji, Y. (1998). Steady particulate flows in a horizontal rotating cylinder. *Physics of Fluids*, 10(6):1419–1427.

Yang, R. Y., Zou, R. P., and Yu, A. B. (2003). Microdynamic analysis of particle flow in a horizontal rotating drum. *Powder Technology*, 130(1):138–146.

Yu, X., Hounslow, M. J., and Reynolds, G. K. (2016). Representing spray zone with cross flow as a well-mixed compartment in a high shear granulator. *Powder Technology*, 297:429–437.

Yu, X., Hounslow, M. J., Reynolds, G. K., Rasmuson, A., Niklasson Björn, I., and Abrahamsson, P. J. (2017). A compartmental CFD–PBM model of high shear wet granulation. *AIChE Journal*, 63(2):438–458.

Yuan, C., Laurent, F., and Fox, R. (2012). An extended quadrature method of moments for population balance equations. *Journal of Aerosol Science*, 51:1–23.

Zhang, J., Hu, Z., Ge, W., Zhang, Y., Li, T., and Li, J. (2004). Application of the discrete approach to the simulation of size segregation in granular chute flow. *Industrial & Engineering Chemistry Research*, 43(18):5521–5528.

Zhao, H., Maisels, A., Matsoukas, T., and Zheng, C. (2007). Analysis of four Monte Carlo methods for the solution of population balances in dispersed systems. *Powder Technology*, 173(1):38–50.

Žižek, K., Hraste, M., and Gomzi, Z. (2013). High shear granulation of dolomite–I: Effect of shear regime on process kinetics. *Chemical Engineering Research and Design*, 91(1):70–86.

Žižek, K., Hraste, M., and Gomzi, Z. (2014). High shear granulation of dolomite–II: Effect of amount of binder liquid on process kinetics. *Chemical Engineering Research and Design*, 92(6):1091–1106.

Appendix A

ANALYSIS CALCULATIONS

A.1 *Particle size distribution*

The particle mass and maximum particle diameter of size range i are Δm_i and x_i respectively. All particles are assumed to be between 45 µm and 7 mm.

Cumulative mass fraction $W\,(< x_i)$:

$$W\,(< x_i) = \frac{\sum_{j=1}^{i} \Delta m_j}{\sum_{j=1}^{n} \Delta m_j} \tag{A.1}$$

Cumulative residue mass fraction $W\,(> x_i)$:

$$W\,(> x_i) = 1 - W\,(< x_i) \tag{A.2}$$

Results from two measurements are used to cover the particle size range using both sieve towers (for fine and coarse product; one representative sample for each analysis). The fine product sieve analysis results Δm_i are not adjusted, and to determine the particle size distribution (PSD) above 1 mm, the coarse product sieve analysis results $\Delta m_i'$ are normalised by using mass fraction $W\,(> 1\,\text{mm})$ from the fine product sieve analysis:

$$\Delta m_i = \frac{\Delta m_i'}{\sum_{j=1}^{n} \Delta m_j'} \frac{W\,(> 1\,\text{mm})}{W'\,(> 1\,\text{mm})} \tag{A.3}$$

where $'$ indicates the coarse product measurements.

Sieve analysis results (Table A.1) are used to determine the PSD. Eqs A.1, A.2 and A.3 are applied:

$$W\,(> 1\,\text{mm}) = \frac{\Delta m\,(> 1\,\text{mm})}{\sum_{j} \Delta m_j} = \frac{15.7\,\text{g}}{100\,\text{g}} = 0.157 \tag{A.4}$$

Table A.1: Sieve analysis results (Exp 16)

Fine product	i	x_i [µm]	Δm_i [g]
	0	45	
< 90 µm	1	90	2.6
90 µm-125 µm	2	125	4.7
125 µm-180 µm	3	180	15.4
180 µm-250 µm	4	250	20.8
250 µm-355 µm	5	355	19.7
355 µm-500 µm	6	500	13.0
500 µm-710 µm	7	710	5.5
710 µm-1000 µm	8	1000	2.6
> 1000 µm			15.7

Coarse product	i	x_i' [µm]	$\Delta m_i'$ [g]
< 1000 µm		1000	83.6
1000 µm-1250 µm	9	1250	1.6
1250 µm-1400 µm	10	1400	1.0
1400 µm-1800 µm	11	1800	2.9
1800 µm-2240 µm	12	2240	2.6
2240 µm-3150 µm	13	3150	3.8
3150 µm-4000 µm	14	4000	1.7
4000 µm-5000 µm	15	5000	1.2
> 5000 µm	16	7000	1.7

$$W'(>1\,\text{mm}) = \frac{\sum_{j=1}^{9} \Delta m'_j - \Delta m'(>1\,\text{mm})}{\sum_j \Delta m'_j} = \frac{100.1\,\text{g} - 83.6\,\text{g}}{100.1\,\text{g}} = 0.165 \tag{A.5}$$

$$\Delta m_9 = \frac{\Delta m'_i}{\sum_j \Delta m'_j} \frac{W(>1\,\text{mm})}{W'(>1\,\text{mm})} = \frac{1.6\,\text{g}}{100.1\,\text{g}} \frac{0.157}{0.165} = 0.015\,\text{g} \tag{A.6}$$

$\Delta m_{10..16}$ are calculated using the same approach.

The calculation of the mass frequency $f_{m,1}$ and log mass frequency $f_1(\ln x)$ are demonstrated as examples:

$$f_{m,1} = \frac{\Delta m_1}{\sum_{j=1}^{16} \Delta m_j} \frac{1}{x_1 - x_0} = \frac{2.6\,\text{g}}{100.1\,\text{g}} \frac{1}{90\,\mu\text{m} - 45\,\mu\text{m}} = 0.000\,58\,\frac{1}{\mu\text{m}} = 0.58\,\frac{1}{\text{mm}} \tag{A.7}$$

$$f_1(\ln x) = \frac{\Delta m_1}{\sum_{j=1}^{16} \Delta m_j} \frac{1}{\log_{10}(x_1/x_0)} = \frac{2.6\,\text{g}}{100.1\,\text{g}} \frac{1}{\log_{10}(90\,\mu\text{m}/45\,\mu\text{m})} = 0.086 \tag{A.8}$$

The geometric mean diameter $\bar{x}_1$ is determined:

$$\bar{x}_1 = \sqrt{x_0 x_1} = \sqrt{45\,\mu\text{m}\,90\,\mu\text{m}} = 64\,\mu\text{m} \tag{A.9}$$

The PSD results of Exp 16 are displayed in Table A.2.

A.2 Porosity

Average envelope density ρ_{env} measured (GeoPyc; Exp 36):

$$\rho_{env} = 0.657\,\frac{\text{kg}}{\text{m}^3} \tag{A.10}$$

Porosity ε (GeoPyc; Exp 36) using skeletal density ρ_s result (see Section 3.1:

$$\varepsilon = 1 - \frac{\rho_{env}}{\rho_s} = 1 - \frac{0.657\,\frac{\text{kg}}{\text{m}^3}}{1.412\,\frac{\text{kg}}{\text{L}}} = 0.53 \tag{A.11}$$

Tap density ρ_{tap} measured (Exp 36):

$$\rho_{tap} = 0.422\,\frac{\text{kg}}{\text{m}^3} \tag{A.12}$$

Table A.2: PSD results (Exp 16)

i	x_i [µm]	$\bar{x}_i$ [µm]	Δm_i [g]	$f_{m,i}$ $\left[\frac{1}{\text{mm}}\right]$	$f_i(\ln x)$ [−]
−1	10				
0	45	21	0	0	0
1	90	64	2.6	0.58	0.09
2	125	106	4.7	1.34	0.33
3	180	150	15.4	2.80	0.97
4	250	212	20.8	2.97	1.46
5	355	298	19.7	1.88	1.29
6	500	421	13	0.90	0.87
7	710	596	5.5	0.26	0.36
8	1000	843	2.6	0.09	0.17
9	1250	1118	1.5	0.06	0.16
10	1400	1323	1.0	0.06	0.19
11	1800	1588	2.8	0.07	0.25
12	2240	2008	2.5	0.06	0.26
13	3150	2656	3.6	0.04	0.24
14	4000	3550	1.6	0.02	0.16
15	5000	4472	1.1	0.01	0.12
16	7000	5916	1.6	0.01	0.11
17	13000	9539	0	0	0

Estimated envelope density ρ_{env} (Tap density; Exp 36) assuming a bed porosity ε_{bed} of 0.38:

$$\rho_{env} = \frac{\rho_{tap}}{1 - \varepsilon_{bed}} = \frac{0.422 \frac{\text{kg}}{\text{m}^3}}{1 - 0.38} = 0.680 \frac{\text{kg}}{\text{m}^3} \tag{A.13}$$

Porosity ε (Tap density; Exp 36):

$$\varepsilon = 1 - \frac{\rho_{env}}{\rho_s} = 1 - \frac{0.680 \frac{\text{kg}}{\text{m}^3}}{1.412 \frac{\text{kg}}{\text{L}}} = 0.52 \tag{A.14}$$

Appendix B

EXPERIMENTAL DATA

B.1 *Spray characteristics*

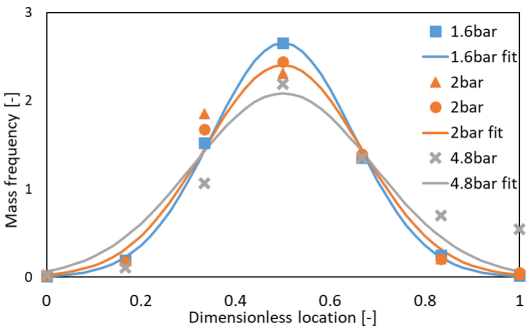

(a) 0.4 mm nozzle; 30° spray cone angle; x direction

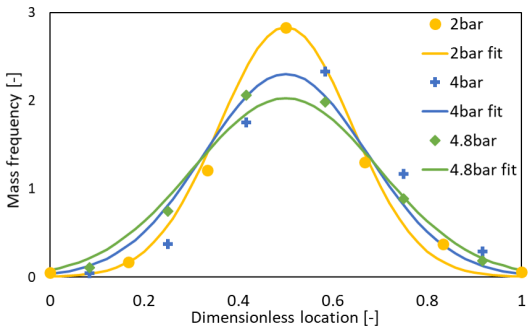

(b) 0.8 mm nozzle; 30° spray cone angle; x direction

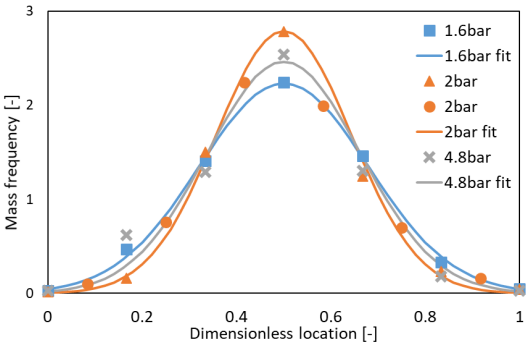

(c) 0.4 mm nozzle; 30° spray cone angle; y direction

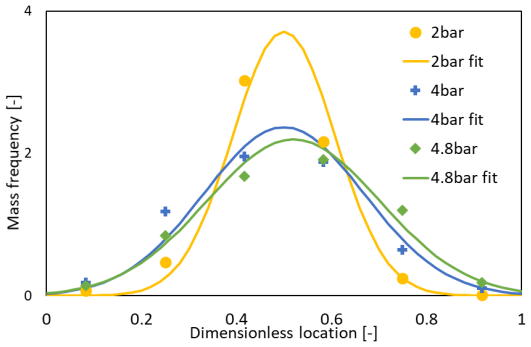

(d) 0.8 mm nozzle; 30° spray cone angle; y direction

Figure B.1: Spatial drop distribution results

Table B.1: Standard deviation of spatial drop distribution (normalised with width of spray cone)

Nozzle	Pressure [bar]	σ_x [−]	σ_y [−]
0.4 mm; 30°	1.6	0.150	0.179
0.4 mm; 30°	2.0	0.166	0.143
0.4 mm; 30°	4.8	0.191	0.162
0.8 mm; 30°	2.0	0.141	0.107
0.8 mm; 30°	4.0	0.173	0.168
0.8 mm; 30°	4.8	0.197	0.182

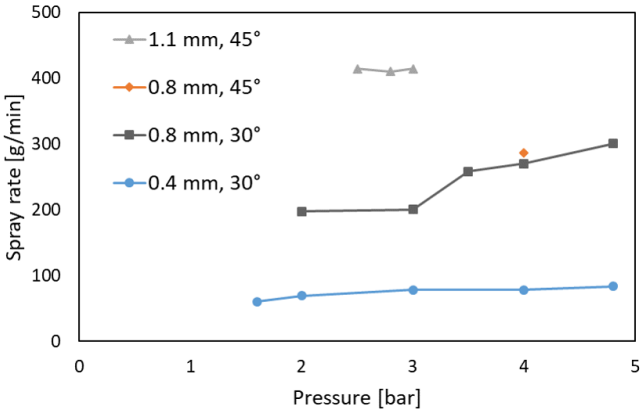

Figure B.2: Spray rate as a function of pressure

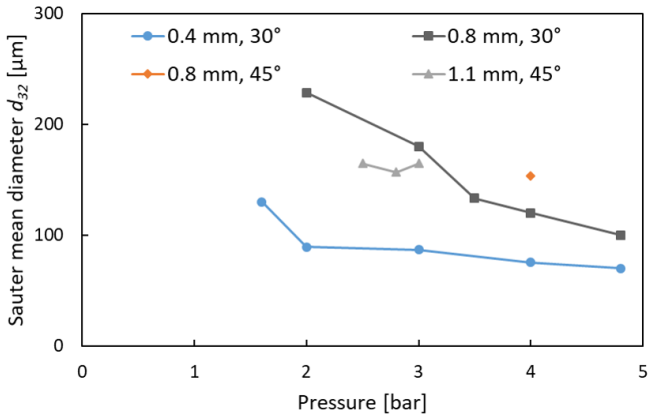

Figure B.3: Sauter mean drop diameter as a function of pressure

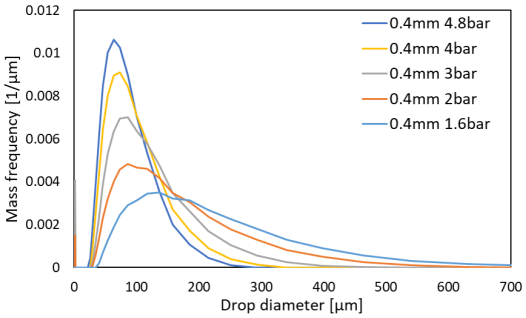

(a) 0.4 mm nozzle; 30° spray cone angle; centre

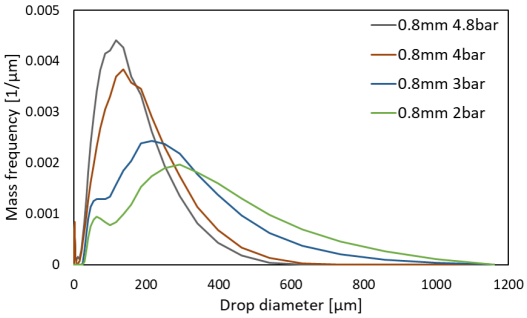

(b) 0.8 mm nozzle; 30° spray cone angle; centre

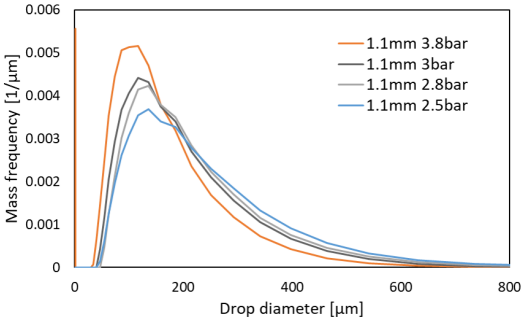

(c) 1.1 mm nozzle; 45° spray cone angle; centre

Figure B.4: Drop size distribution results

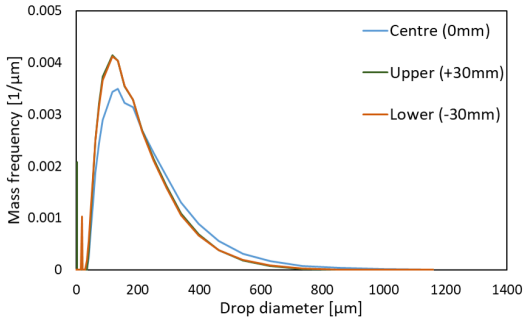

(a) 0.4 mm nozzle; 30° spray cone angle; 1.6 bar spray pressure

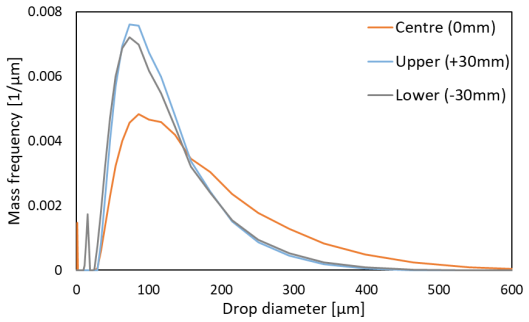

(b) 0.4 mm nozzle; 30° spray cone angle; 2.0 bar spray pressure

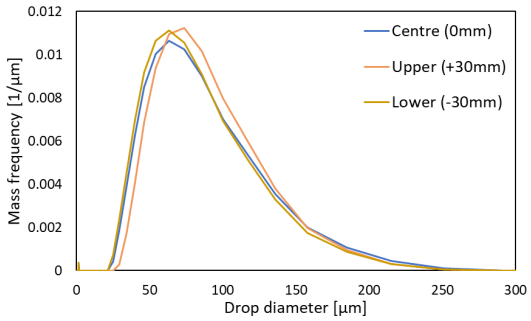

(c) 0.4 mm nozzle; 30° spray cone angle; 4.8 bar spray pressure

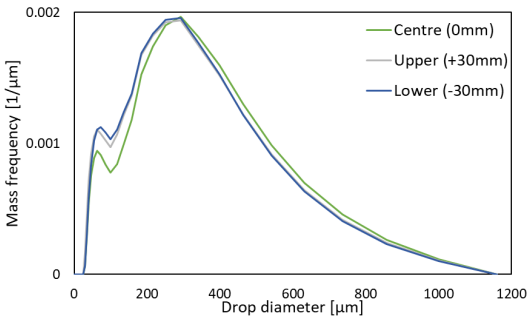

(d) 0.8 mm nozzle; 30° spray cone angle; 2.0 bar spray pressure

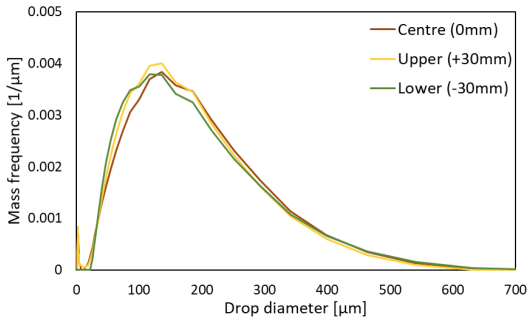

(e) 0.4 mm nozzle; 30° spray cone angle; 4.0 bar spray pressure

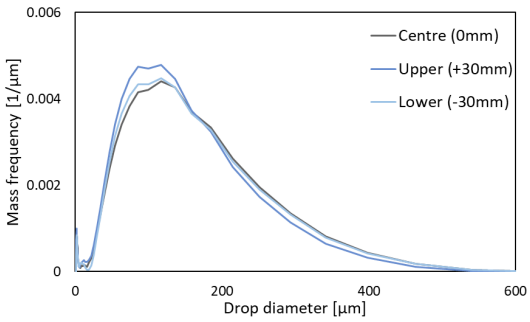

(f) 0.4 mm nozzle; 30° spray cone angle; 4.8 bar spray pressure

Figure B.5: Drop size distribution results

B.2 Drop penetration time

The drop penetration time t_p is estimated (see Section 2.1.1):

$$t_p = 1.35 \frac{V_d^{2/3}}{\varepsilon_{eff}^2 R_{eff}} \frac{\mu}{\gamma^{lv} \cos\theta} \tag{B.1}$$

with

$$\varepsilon_{eff} = \varepsilon_{tap}(1 - \varepsilon_{bulk} + \varepsilon_{tap}) \tag{B.2}$$

$$R_{eff} = \frac{\varphi d_{32} \varepsilon_{eff}}{3(1 - \varepsilon_{eff})} \tag{B.3}$$

where V_d is the drop volume, ε_{eff} is the effective bed porosity, R_{eff} is the effective pore radius, μ is the binder viscosity, γ^{lv} is the liquid-vapour surface tension, θ is the dynamic contact angle, ε_{bulk} is the bulk porosity, ε_{tap} is the tapped porosity, φ is a shape factor, and d_{32} is the Sauter mean diameter of the powder bed particles. The bed velocity is assumed to be 15 % of the impeller tip speed to estimate the circulation time t_c:

$$t_c = \frac{0.15}{n_{imp}} \tag{B.4}$$

where n_{imp} is the impeller rate. The dimensionless drop penetration τ_p is defined as:

$$\tau_p = \frac{t_p}{t_c} \tag{B.5}$$

The penetration time of water into the powder bed is estimated for Exp 1 ($V = 2\,\mathrm{L}$; $v_t = 4.4\,\frac{\mathrm{m}}{\mathrm{s}}$) using Eq. B.1 to B.5. The viscosity and surface tension of water is 1 mPa s and 72.9 $\frac{\mathrm{mN}}{\mathrm{m}}$ respectively [Korson et al., 1969; Pallas and Harrison, 1990]. The dynamic contact angle of 0° is assumed. A Sauter mean diameter is determined for the dry powder d_p and spray drops d_d: 102 µm and 98 µm respectively. The drop penetration time t_p and dimensionless drop penetration time τ_p are determined:

$$t_p = 3.1 \times 10^{-5}\,\mathrm{s} \tag{B.6}$$

$$\tau_p = 0.002 \tag{B.7}$$

The drop penetration time is negligibly small. Hence, nucleation can be assumed to be rapid. The dimensionless drop penetration time is smaller than 0.1 which confirms the applicability of the LND model to determine the nuclei size distribution.

B.3 *Nucleation-only experiments*

Additional results from nucleation-only experiments can be found in Figure B.6, and the experimental conditions are listed in Table B.2. However, the spray conditions of Exp 25 lead to a rather small Sauter mean drop diameter of 69 µm, and only nuclei above 180 µm is only identified. As a result, it is that a significant amount of small nuclei is not determined. This could explain the mismatch between the predictions and experimental data at small nuclei diameters. The spray characteristics of Exp 26 showed that a pressure of 2.0 bar is not sufficient to form a fully developed spray pattern (0.8 mm nozzle): significantly narrower spatial drop distribution and a wide drop size distribution with drops above 1 mm (see Appendix B.1)

Table B.2: Plan of nucleation-only experiments including conditions and relevant dimensionless groups (V granulator volume, n_{imp} impeller rate, $\dot{V}$ spray rate, t_{sp} spray time, L/S mass-based liquid to solid ratio, Fr Froude number, St_{def} Stokes deformation number, Ψ_a dimensionless spray flux, n_{ch} chopper rate, t_{kn} kneading time, σ_x standard deviation of spatial drop distribution)

Exp	V [L]	n_{imp} $\left[\frac{1}{\text{min}}\right]$	$\dot{V}$ $\left[\frac{\text{mL}}{\text{min}}\right]$	t_{sp} [s]	v_t $\left[\frac{\text{m}}{\text{s}}\right]$	Fr [−]	St_{def} [−]	Ψ_a [−]	n_{ch} $\left[\frac{1}{\text{min}}\right]$	t_{kn} [min]	σ_x [−]
24	10	350	60	20	6.2	23	4.7×10^{-3}	0.3	0	0	0.17
25	10	350	80	20	6.2	23	4.7×10^{-3}	0.7	0	0	0.17
26	10	350	200	20	6.2	23	4.7×10^{-3}	0.5	0	0	0.15

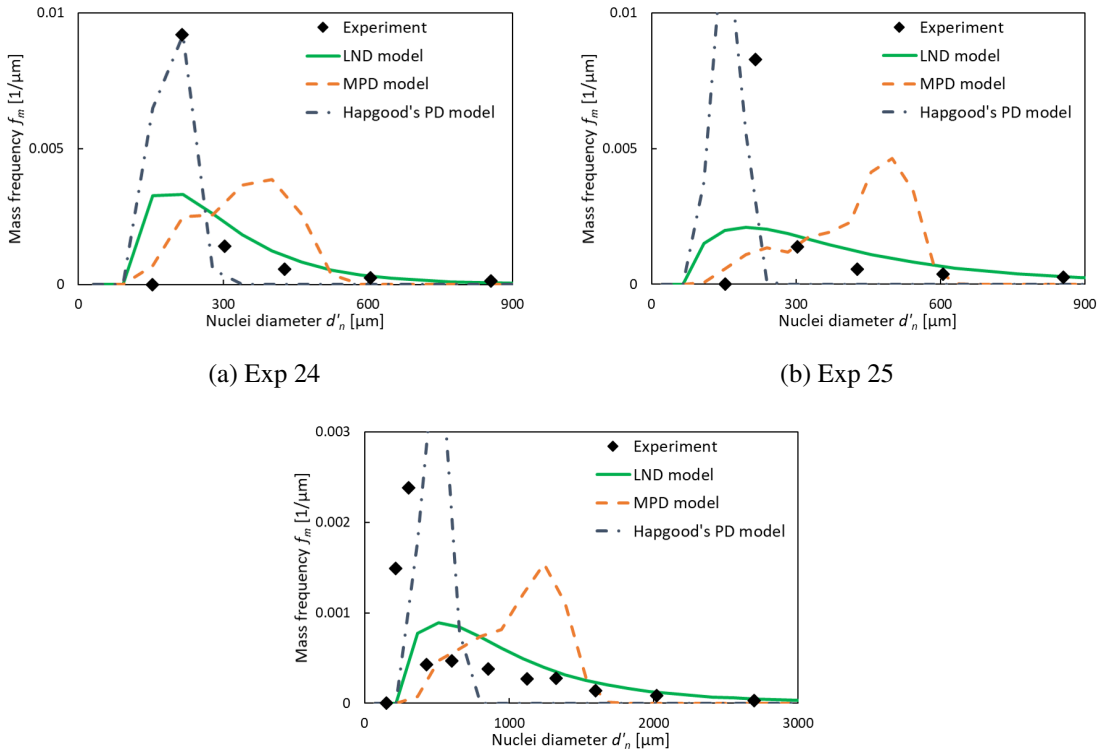

(a) Exp 24

(b) Exp 25

(c) Exp 26

Figure B.6: Nuclei size distribution results from nucleation-only experiments

B.4 Granulation experiments

GeoPyc and tap density porosity results are plotted including the coarse mass fraction W (> 1 mm) according to Figure B.7.

(a) GeoPyc (b) Tap density

Figure B.7: Symbols of porosity results depending on the coarse mass fraction W (> 1 mm)

Experimental data from granulation experiments is shown in Figures B.8, B.9, B.10 and B.11.

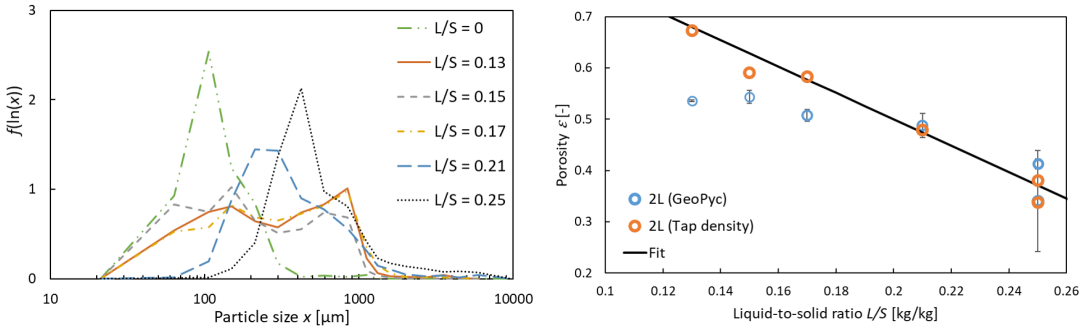

(a) Exp 1, 4-7 and 27: $V = 2\,\mathrm{L}$; $Fr = 23$; $v_t = 4.4\,\frac{\mathrm{m}}{\mathrm{s}}$; $\Psi_a = 0.9$

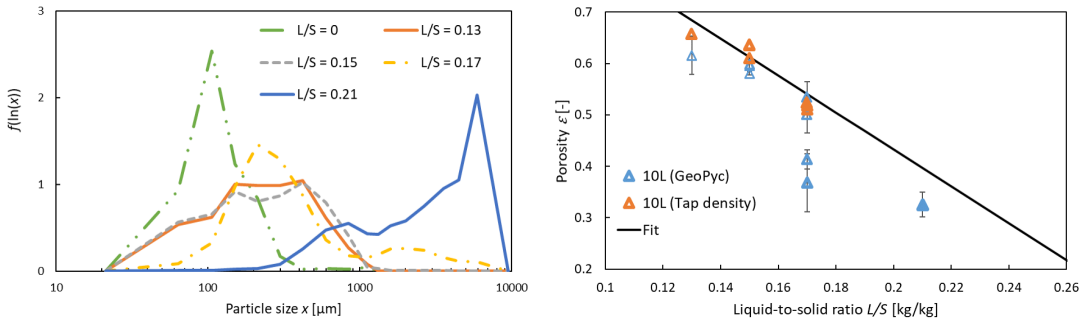

(b) Exp 12, 15-17, 22, 23, 36 and 37: $V = 10\,\mathrm{L}$; $Fr = 23$; $v_t = 6.2\,\frac{\mathrm{m}}{\mathrm{s}}$; $\Psi_a = 0.3$

Figure B.8: Effect of liquid-to-solid ratio on porosity and PSD at 2 L

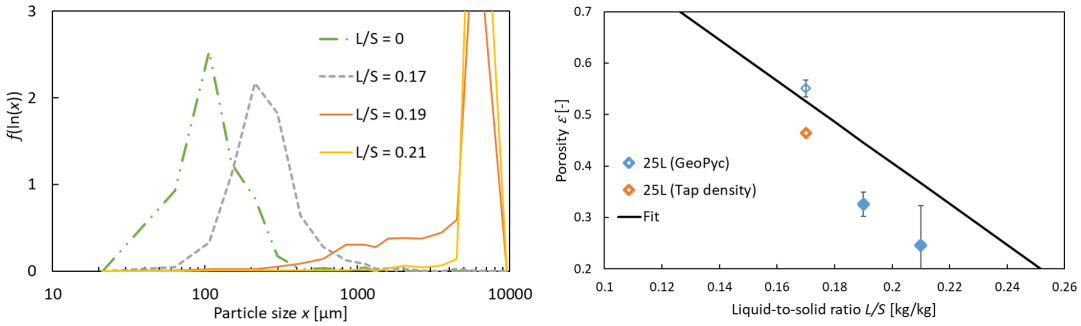

(a) Exp 38-40: $V = 25\,\mathrm{L}$; $Fr = 22$; $v_t = 6.9\,\frac{\mathrm{m}}{\mathrm{s}}$; $\Psi_a = 0.4$

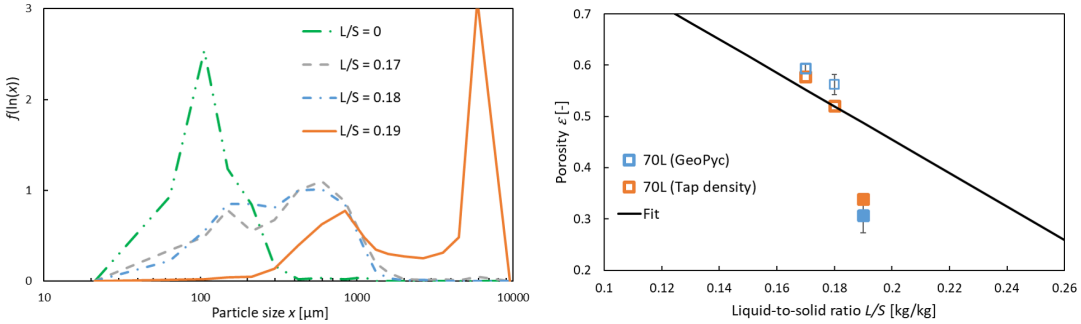

(b) Exp 44-46: $V = 70\,\mathrm{L}$; $Fr = 12$; $v_t = 5.6\,\frac{\mathrm{m}}{\mathrm{s}}$; $\Psi_a = 0.3$

Figure B.9: Effect of liquid-to-solid ratio on porosity and PSD at different scales

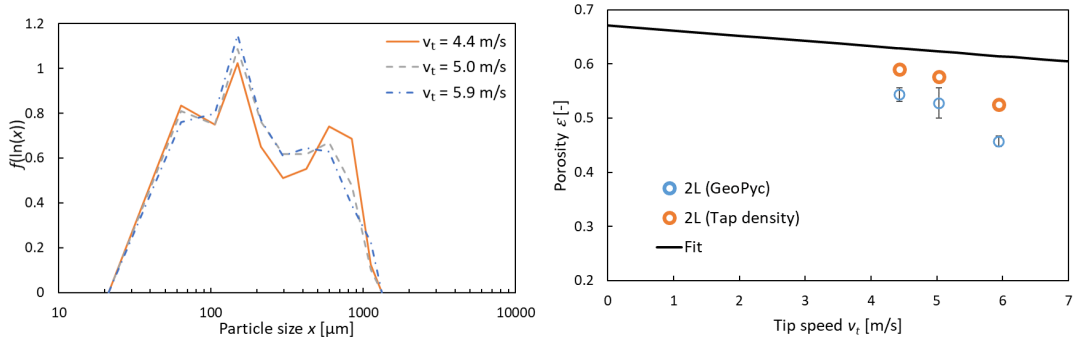

(a) Exp 1-3: $V = 2\,\mathrm{L}$; $t_{kn} = 5\,\mathrm{min}$; $L/S = 0.15$

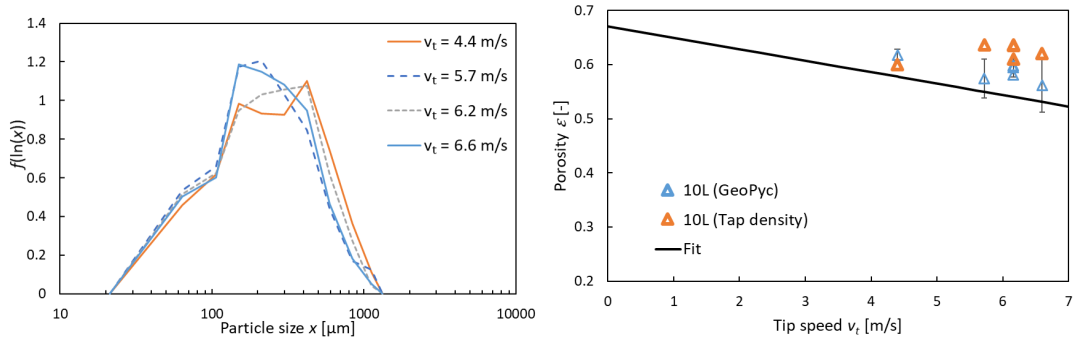

(b) Exp 12-14 and 19: $V = 10\,\mathrm{L}$; $t_{kn} = 5\,\mathrm{min}$; $L/S = 0.15$

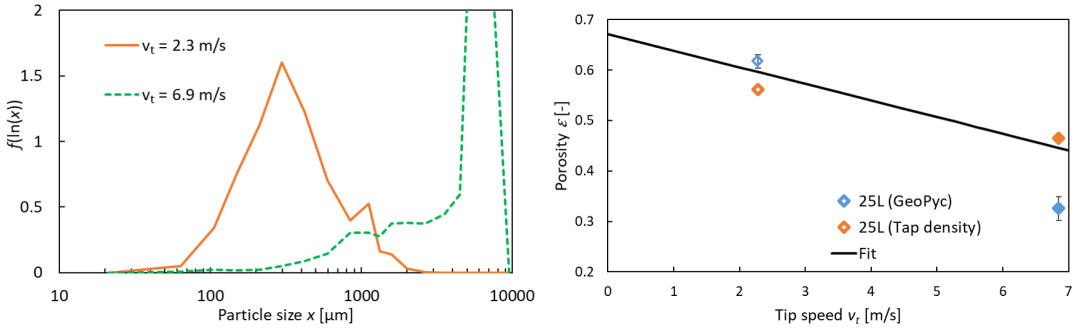

(c) Exp 38 and 41: $V = 25\,\mathrm{L}$; $t_{kn} = 5\,\mathrm{min}$; $L/S = 0.19$

Figure B.10: Effect of impeller tip speed on porosity and PSD at different liquid-to-solid ratios and scales

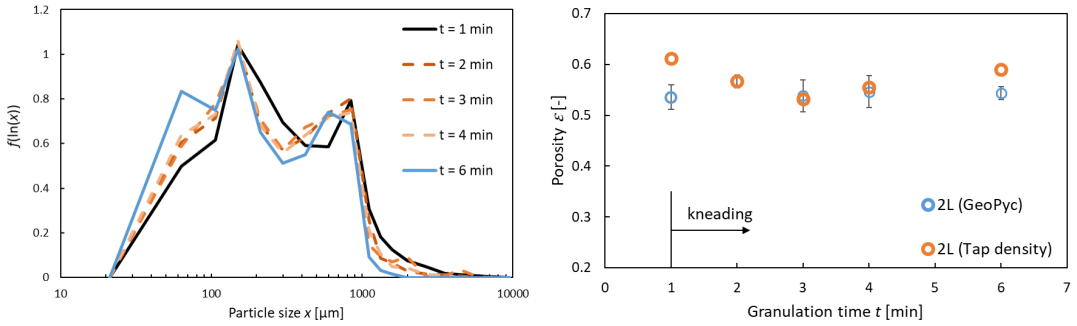

(a) Exp 1 and 8-11: $V = 2\,\mathrm{L}$; $t_{sp} = 1\,\mathrm{min}$; $L/S = 0.15$; $Fr = 23$; $\Psi_a = 0.9$

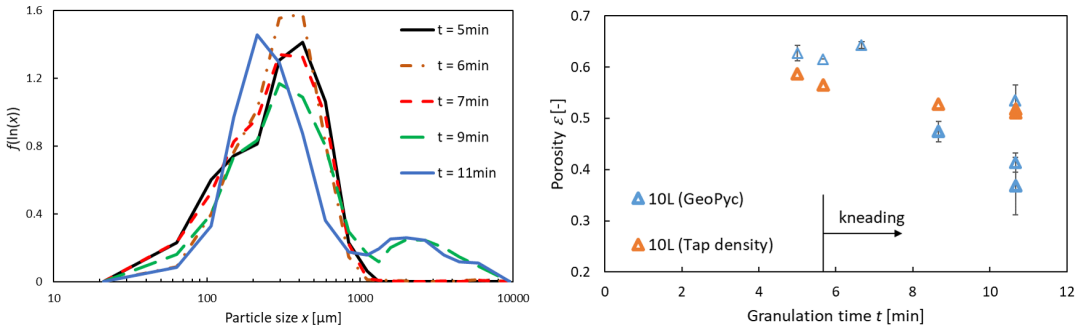

(b) Exp 16 and 30-36: $V = 10\,\mathrm{L}$; $t_{sp} = 5.7\,\mathrm{min}$; $L/S = 0.17$; $Fr = 23$; $\Psi_a = 0.3$

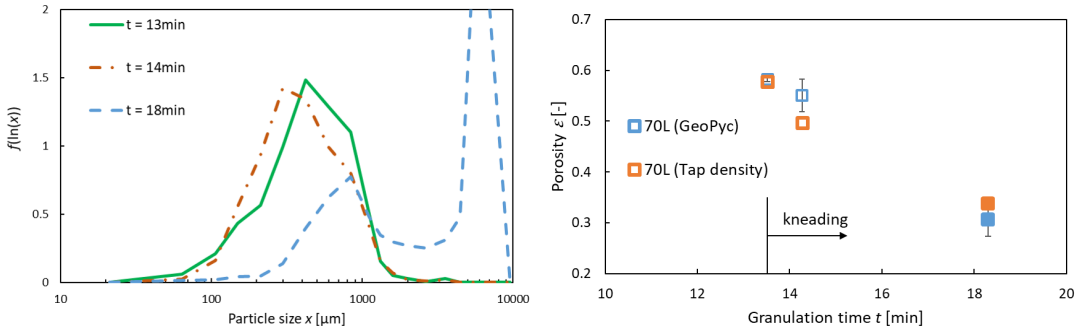

(c) Exp 42, 43 and 45: $V = 70\,\mathrm{L}$; $t_{sp} = 13\,\mathrm{min}$; $L/S = 0.19$; $Fr = 12$; $\Psi_a = 0.3$

Figure B.11: Effect of kneading time on porosity and PSD at different liquid-to-solid ratios and scales

B.5 Drying techniques

Figures B.12 and B.13 compare the PSD of tray dried and fluid bed dried samples.

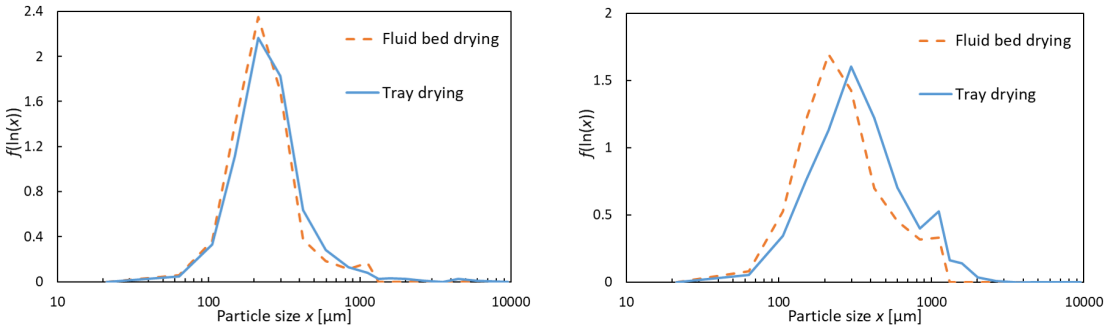

(a) Exp 39: $v_t = 6.9\,\frac{\mathrm{m}}{\mathrm{s}}$

(b) Exp 41: $v_t = 2.3\,\frac{\mathrm{m}}{\mathrm{s}}$

Figure B.12: PSD results of fluid bed dried and tray dried samples ($V = 25\,\mathrm{L}$; $t_{sp} = 12.2\,\mathrm{min}$; $L/S = 0.19$; $t_{kn} = 5\,\mathrm{min}$)

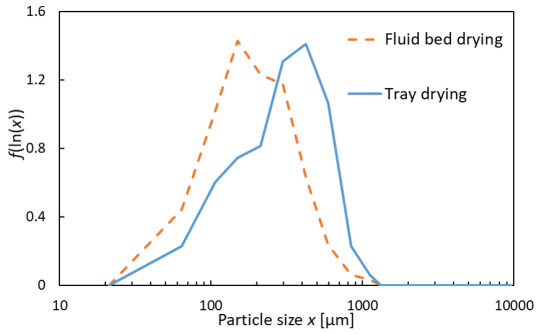

(a) Exp 30: $L/S = 0.15$; $t_{kn} = 0\,\text{min}$

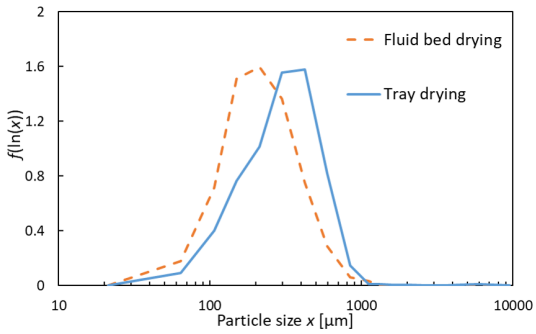

(b) Exp 31: $t_{kn} = 0\,\text{min}$

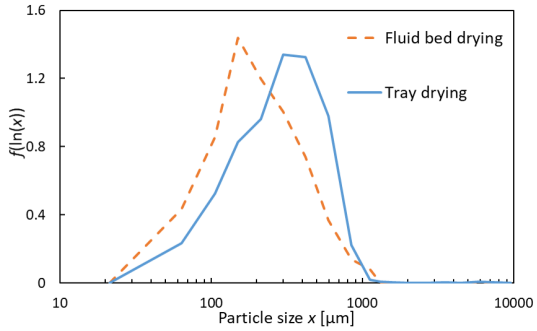

(c) Exp 32: $t_{kn} = 1\,\text{min}$

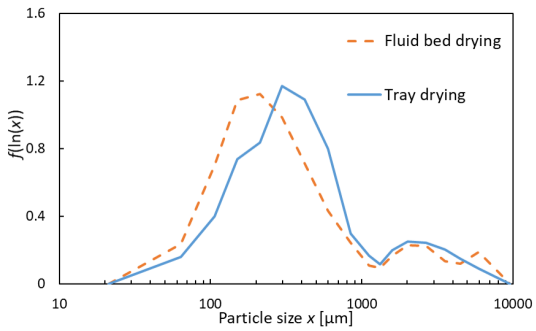

(d) Exp 34: $t_{kn} = 3\,\text{min}$

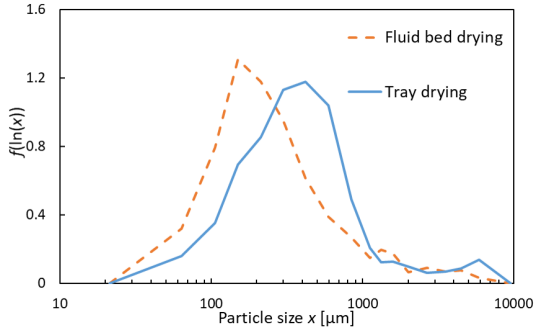

(e) Exp 36: $t_{kn} = 5\,\text{min}$

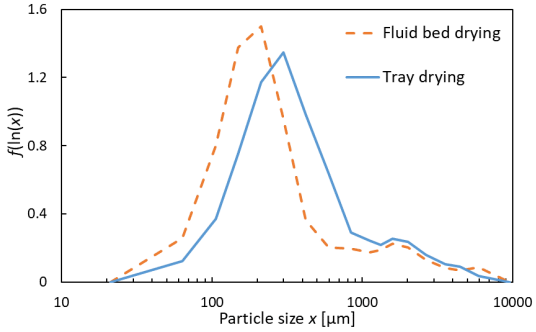

(f) Exp 37: $t_{kn} = 5\,\text{min}$

Figure B.13: PSD results of fluid bed dried and tray dried samples ($V = 10\,\text{L}$; $t_{sp} = 5.7\,\text{min}$; $L/S = 0.17$; $v_t = 6.2\,\frac{\text{m}}{\text{s}}$)

After 70 L experiments, only a 300 g sample is taken, and the residual wet material (> 14 kg) is dried in a 90 L DIOSNA fluid bed processor CAP70 (Dierks & Söhne GmbH). The product was milled before and after drying with a 10 mm and 2 mm conical sieve mill respectively. Any size reduction might be a result of milling or the fluid bed conditions (Figure B.14).

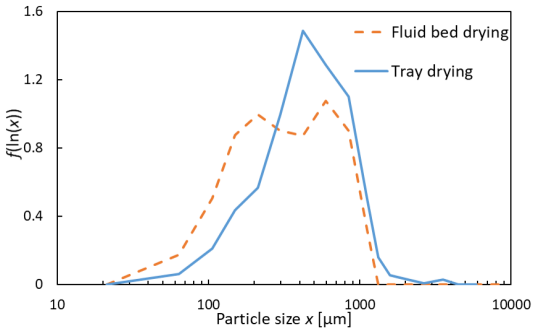

(a) Exp 42

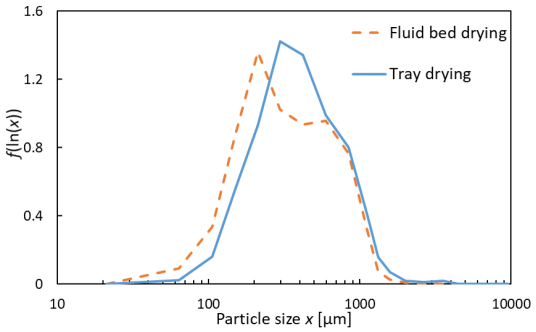

(b) Exp 43

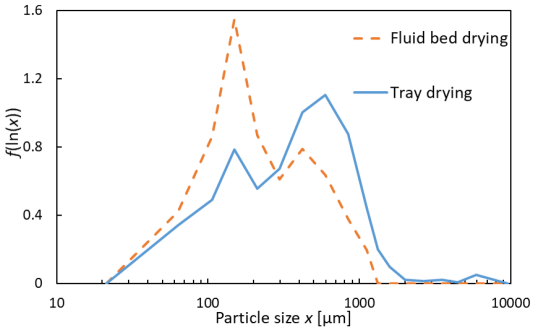

(c) Exp 44

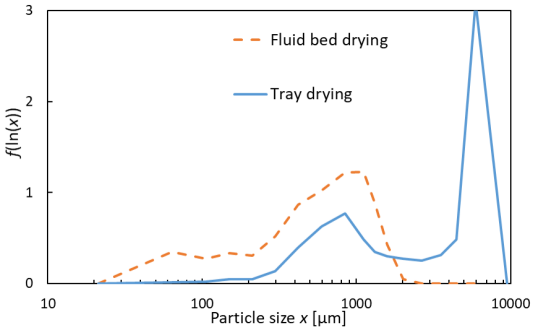

(d) Exp 45

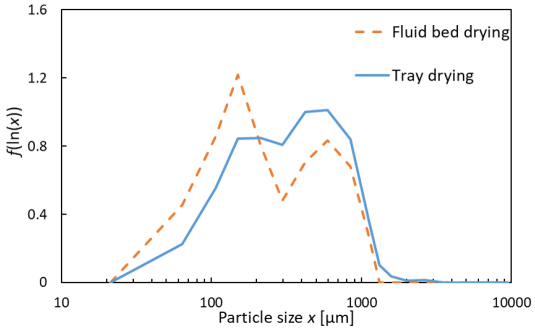

(e) Exp 46

Figure B.14: PSD results of fluid bed dried and tray dried samples of 70 L experiments

Appendix C

MODELLING

*C.*1 *Flowsheets*

Flowsheets for the 1-comp and 2-comp PBM approach are displayed in Figure C.1. The sieve analysis model determines the PSD by taking the granule and powder size distribution and their respective mass fraction into account. Therefore, the grid of sieve trays for the experimental characterisation (see Section 3.3.3) is applied as discretisation method.

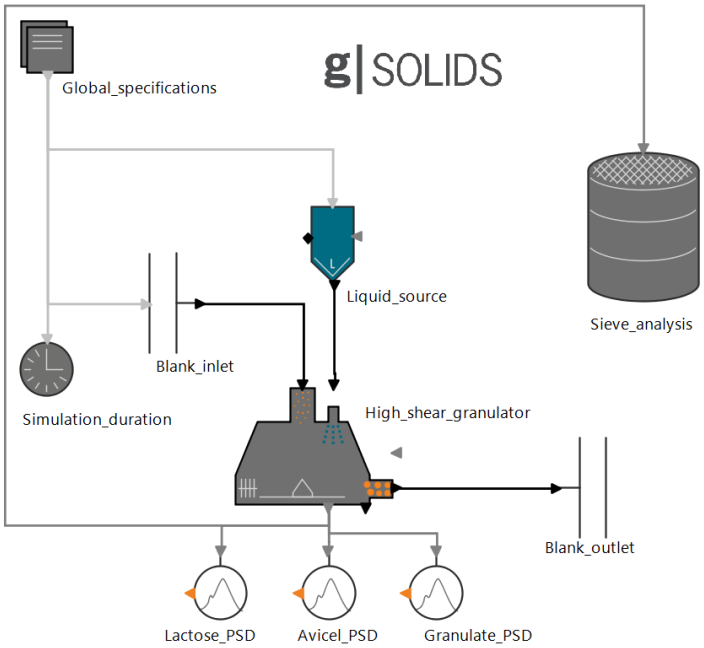

(a) 1-comp PBM approach

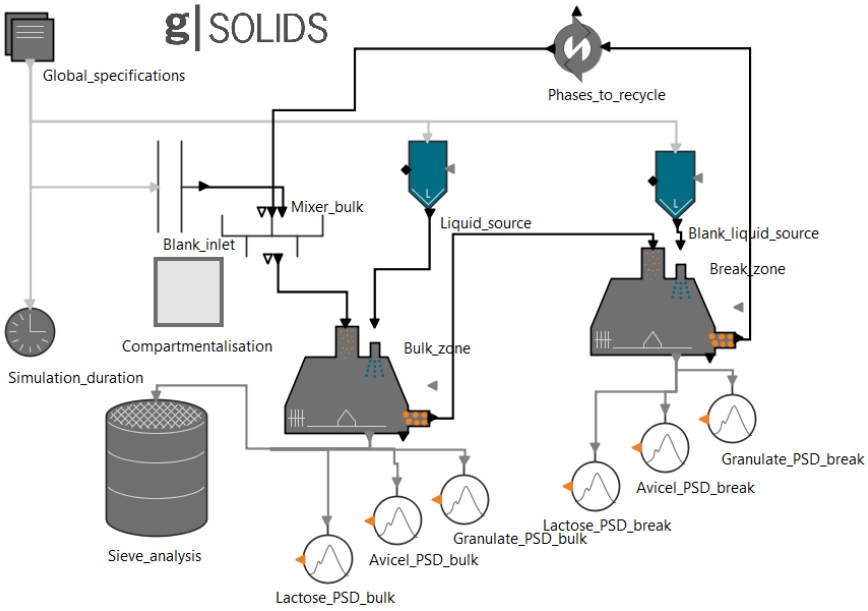

(b) 2-comp PBM approach

Figure C.1: gPROMS flowsheets

C.2 Input parameters for model verification

The input parameters for the model verification simulation are listed in Table C.1.

Table C.1: Overview of parameters

Parameter	Value
$\rho_s \left[\frac{\mathrm{kg}}{\mathrm{m}^3}\right]$	1412
d_p [µm] (Eq. 5.32)	102
K_d [−] (Eq. 5.19)	1.26
d_d [µm] (Eq. 5.19)	98
w [m] (Eq. 5.20)	0.06
σ_x [−] (Eq. 5.21)	0.17
$L/S \left[\frac{\mathrm{kg}}{\mathrm{kg}}\right]$	0.18
$v_t \left[\frac{\mathrm{m}}{\mathrm{s}}\right]$ (Eq. 5.33)	6.2
S_{crit} [−]	0.149
k_{cons} [−]	3
k_{br} [−]	0.0034
$k_{I,II} \left[\log_{10} \mathrm{m}^{1.5}\right]$	13.56
$\rho_l \left[\frac{\mathrm{kg}}{\mathrm{m}^3}\right]$	1000
$\rho_{bulk} \left[\frac{\mathrm{kg}}{\mathrm{m}^3}\right]$ (Eq. 5.13)	416.7
μ [mPa s] (Eq. 5.35)	1
$\gamma^{lv} \left[\frac{\mathrm{mN}}{\mathrm{m}}\right]$ (Eq. 5.32)	72.9
θ [°] (Eq. 5.32)	0
h_a [µm] (Eq. 5.47)	1
$f_{Mat} \left[\frac{\mathrm{kg\,m}}{\mathrm{J}}\right]$ (Eq. 5.58)	1
$E_{m,kin} \left[\frac{\mathrm{J}}{\mathrm{kg}}\right]$ (Eq. 5.58)	1000
q [−] (Eq. 5.61)	1
$d_{j,min}$ [µm] (Eq. 5.61)	10
ν [−] (Eq. 5.43)	0.03
k_E [−] (Eq. 5.46)	24.2

Continued on next page

Table C.1 – continued from previous page

Parameter	Value
p_E [−] (Eq. 5.46)	0.17
q_E [−] (Eq. 5.46)	−6.9
r_E [−] (Eq. 5.46)	−1.5
A [−] (Eq. 5.35)	7
B [−] (Eq. 5.35)	221
n [−] (Eq. 5.35)	0.58
m_1 [−] (Eq. 5.22)	−3.0
m_2 [−] (Eq. 5.22)	1.9
m_3 [−] (Eq. 5.22)	−0.05
s_1 [−] (Eq. 5.22)	−3.4
s_2 [−] (Eq. 5.22)	1.0
s_3 [−] (Eq. 5.22)	0.32
e_1 [−] (Eq. 5.30)	0.58
e_2 [−] (Eq. 5.30)	0.13
e_3 [−] (Eq. 5.30)	0.67

C.3 Model implementation

Modelling code for the custom kinetics models implemented within the gPROMS Formulated-Products high-shear granulation library model is provided:

Pore saturation (Calculate_porosity_gFP):

```
EQUATION
   FOR phase IN active_phases DO
      FOR z:=1 TO no_grid_pts(phase) DO
         porosity(phase,z) * (total_volume_per_size_protected(phase,z) *
            ↪ (1 + high_threshold)
            - liquid_volume_on_surface_per_size_protected(phase,z) +
```

```
            ↪ effective_zero)
        = pore_volume_per_size_protected(phase,z) ;
    void_fraction(phase,z) = intra_particle_void_volume(phase,z)
        / (total_volume_per_size_protected(phase,z) -
            ↪ liquid_volume_on_surface_per_size_protected(phase,z) +
            ↪ volume_threshold) ;
    2*pore_saturation_protected(phase,z)*10^6 =
        (1.0e-5 + pore_saturation(phase,z)*10^6) + SQRT((1.0e-5 -
            ↪ pore_saturation(phase,z)*10^6)^2 + (1.0e-5)^2);
    2*porosity_protected(phase,z)*10^6 =
        (1.0e-5 + porosity(phase,z)*10^6) + SQRT((1.0e-5 - porosity(
            ↪ phase,z)*10^6)^2 + (1.0e-5)^2);
    2*liquid_volume_total_per_size_protected(phase,z)*10^6 =
        (1.0e-5 + liquid_volume_total_per_size(phase,z)*10^6) + SQRT
            ↪ ((1.0e-5 - liquid_volume_total_per_size(phase,z)*10^6)
            ↪ ^2 + (1.0e-5)^2);
    2*void_fraction_protected(phase,z)*10^6 =
        (1.0e-5 + void_fraction(phase,z)*10^6) + SQRT((1.0e-5 -
            ↪ void_fraction(phase,z)*10^6)^2 + (1.0e-5)^2);
    2*pore_volume_per_size_protected(phase,z)*10^6 =
        (1.0e-5 + pore_volume_per_size(phase,z)*10^6) + SQRT((1.0e-5
            ↪ - pore_volume_per_size(phase,z)*10^6)^2 + (1.0e-5)^2);
    2*liquid_layer_thickness_protected(phase,z)*10^6 =
        (1.0e-5 + liquid_layer_thickness(phase,z)*10^6) + SQRT((1.0e
            ↪ -5 - liquid_layer_thickness(phase,z)*10^6)^2 + (1.0e-5)
            ↪ ^2);
    2*liquid_volume_on_surface_per_size_protected(phase,z)*10^6 =
        (1.0e-5 + liquid_volume_on_surface_per_size(phase,z)*10^6) +
            ↪ SQRT((1.0e-5 - liquid_volume_on_surface_per_size(phase,
            ↪ z)*10^6)^2 + (1.0e-5)^2);
END # FOR z:=2 TO no_FVBs(phase) DO
```

```
# Calculate pore volume per size class, including liquid.
FOR i:=1 TO has_liquid(phase) DO
    FOR z:=1 TO no_grid_pts(phase) DO
        liquid_volume_total_per_size(phase,z) =
            SIGMA(mass_components_distributed(phase,liquid_components*
                ↪ components_in_phase(phase),z))
                / SIGMA(liquid_density(,active_phases_liquid)) ;
        pore_volume_per_size(phase,z) =
            liquid_volume_in_pores_per_size(phase,z)
            + intra_particle_void_volume(phase,z)
            * Status_signal_distributed_void(phase,z) ;
        liquid_volume_on_surface_per_size(phase,z) =
            pore_volume_per_size_protected(phase,z)
            * (pore_saturation_protected(phase,z) -
                ↪ pore_saturation_critical(phase,z)) ;
        liquid_volume_total_per_size_protected(phase,z) =
            liquid_volume_in_pores_per_size(phase,z) +
                ↪ liquid_volume_on_surface_per_size_protected(phase,z
                ↪ ) ;
    END # FOR z:=1 TO no_grid_pts(phase) DO
END # FOR i:=1 TO has_liquid(phase) DO

# Calculate pore volume per size class for phases without liquid.
FOR i:=1 TO 1 - has_liquid(phase) DO
    FOR z:=1 TO no_grid_pts(phase) DO
        pore_volume_per_size(phase,z) =
            SIGMA((mass_components_distributed(phase,liquid_components
                ↪ *components_in_phase(phase),z)))
                / SIGMA(liquid_density(,active_phases_liquid))
            + (intra_particle_void_volume(phase,z)) *
```

```
                ↪ Status_signal_distributed_void(phase,z) ;
        END # FOR z:=1 TO no_grid_pts(phase) DO
    END # FOR i:=1 TO 1 - has_liquid(phase) DO

CASE operating_status OF
    WHEN unit_on:
        CASE porosity_status OF
            WHEN porosity_high:
              FOR z:=1 TO no_grid_pts(phase) DO
                  liquid_volume_total_per_size_protected(phase,z) *
                      ↪ high_threshold
                      = (pore_saturation(phase,z) *
                          ↪ pore_volume_per_size_protected(phase,z))
                          * high_threshold ;
              END #For z
              SWITCH TO porosity_low IF MAX(ABS($pore_saturation(,) /
                  ↪ porosity(,))) > 1E5
                                  AND MAX(pore_saturation(,)) > 1E2
                                  AND MIN(porosity(,)) < 2E-2 ;
            WHEN porosity_low:
              FOR z:=1 TO no_grid_pts(phase) DO
                  $pore_saturation(phase,z) * high_threshold = (
                      ↪ liquid_volume_total_per_size_protected(phase,z)
                          / (pore_volume_per_size_protected(phase,z)
                          + standard_threshold *
                              ↪ liquid_volume_total_per_size_protected(
                              ↪ phase,z))
                      - pore_saturation(phase,z)) * high_threshold ; END
                          ↪ #For z
              SWITCH TO porosity_high IF MAX(ABS($pore_saturation(,) /
                  ↪ porosity(,))) < 1E-3
```

```
                                OR MAX(pore_saturation(,)) < 1E1
                                OR MIN(porosity(,)) > 5E-2 ;
    END # CASE porosity_status OF

  FOR z:=1 TO no_grid_pts(phase) DO
      density_envelope(phase,z) =
          MIN(SIGMA(composite_skeletal_density(,phase)),
          MAX(SIGMA(composite_skeletal_density(,phase)) * 0.1,
          total_mass_per_size_protected(phase,z) /
              ↪ total_volume_per_size_protected(phase,z))) ;
      $liquid_layer_thickness(phase,z) = 1 * (sdd(phase).L(z) *
          ↪ porosity_protected(phase,z)
          / shape_fac_area(phase)
          * shape_fac_vol(phase)
          * (pore_saturation_protected(phase,z) -
              ↪ pore_saturation_critical(phase,z))
          - liquid_layer_thickness(phase,z)) ;
  END #For z

SWITCH TO unit_off IF operating_status < 0.5
      OR SIGMA(mass_components_distributed(active_phases,,)) /
         SIGMA(mass_components_distributed(,,)) < mass_threshold ;

WHEN unit_off:
  FOR z:=1 TO no_grid_pts(phase) DO
      $density_envelope(phase,z) = (total_mass_per_size_protected(
          ↪ phase,z)
          / (total_volume_per_size_protected(phase,z) +
              ↪ volume_threshold) - density_envelope(phase,z)) ;
      $pore_saturation(phase,z) = ( MIN(
          ↪ liquid_volume_total_per_size_protected(phase,z)
```

```
                / pore_volume_per_size_protected(phase,z) ,
                    ↪ pore_saturation_critical(phase,z) )
            - pore_saturation(phase,z) ) ;
        #Calculate liquid layer thickness
        $liquid_layer_thickness(phase,z) = (sdd(phase).L(z) *
            ↪ porosity_protected(phase,z)
            * (pore_saturation_protected(phase,z) -
                ↪ pore_saturation_critical(phase,z))
            - liquid_layer_thickness(phase,z)) ;
    END #For z
  SWITCH TO unit_on IF operating_status > 0.5
        AND SIGMA(mass_components_distributed(active_phases,,)) /
            SIGMA(mass_components_distributed(,,)) > 1E-2 ;
END # CASE operating_status OF

 # Calculate total volume per size class.
 FOR z:=1 TO no_grid_pts(phase) DO
    2*total_mass_per_size_protected(phase,z)*10^6 =
        (1.0e-5 + total_mass_per_size(phase,z)*10^6) + SQRT((1.0e-5 -
            ↪  total_mass_per_size(phase,z)*10^6)^2 + (1.0e-5)^2);
    2*total_volume_per_size_protected(phase,z)*10^6 =
        (1.0e-5 + total_volume_per_size(phase,z)*10^6) + SQRT((1.0e-5
            ↪  - total_volume_per_size(phase,z)*10^6)^2 + (1.0e-5)^2)
            ↪ ;
    total_mass_per_size(phase,z) = SIGMA(mass_components_distributed(
        ↪ phase,,z)) ;
    total_volume_per_size(phase,z) =
        SIGMA(mass_components_distributed(phase,,z)
            / solid_skeletal_density(,active_phases_solid)))
        + liquid_volume_total_per_size_protected(phase,z)
        + intra_particle_void_volume(phase,z) ;
```

```
      END # FOR z:=1 TO no_grid_pts(phase) DO
   END # FOR phase IN active_phases DO

   FOR phase IN active_phases DO
      # Calculate per-particle volumes and masses.
      FOR z:=1 TO no_grid_pts(phase) DO
         V(phase,z) = shape_fac_vol(phase) * sdd(phase).L(z)^3
            * conv_mu_to_m^3 * volume_conversion_factor ;
         M(phase,z) = density_envelope(phase,z) * V(phase,z) ;
      END # FOR z:=1 TO no_grid_pts(phase) DO
   END # FOR phase IN active_phases DO

INITIAL
   liquid_layer_thickness(,) = 0 ;
   density_envelope(,) = 1000 ;
   pore_saturation(,) = pore_saturation_initial ;
```

Nuclei size distribution (Nucleation_empirical_gFP):

```
SET
   m_1 := -3.019 ;
   m_2 := 1.875 ;
   m_3 := -0.045650818 ;
   s_1 := -3.432 ;
   s_2 := 0.9784 ;
   s_3 := 0.3243647 ;

EQUATION
   bed_velocity = Calculate_bed_velocity.bed_velocity ;

   mu_log_normal = LOG(L0/SQRT(1+sd^2/L0^2));
   sigma_log_normal_unprotected = SQRT(LOG(1+sd^2/L0^2));
```

```
    2*sigma_log_normal*10^6 =
        (1.0e-5 + sigma_log_normal_unprotected*10^6) + SQRT((1.0e-5 -
            ↪ sigma_log_normal_unprotected*10^6)^2 + (1.0e-5)^2);

    mu_log_normal = LOG(d32_drops_spray) + ((m_1 *
        ↪ spatial_standard_dev_spray + m_2) *
        ↪ nucleation_number_dimensionless + m_3) ;
    sigma_log_normal = (s_1 * spatial_standard_dev_spray + s_2) *
        ↪ nucleation_number_dimensionless + s_3 ;

    2*total_volume_flowrate*10^6 =
        (1.0e-5 + Volume_flowrate_calculation.total_volume_flowrate*10^6) +
            ↪ SQRT((1.0e-5 - Volume_flowrate_calculation.
            ↪ total_volume_flowrate*10^6)^2 + (1.0e-5)^2);

    area_flux_powder_spray_zone = width_spray_zone * bed_velocity ;
    spray_flux_dimensionless * area_flux_powder_spray_zone * d32_drops_spray
        ↪  / conversions.length_conversion("micron") = 3 *
        ↪ total_volume_flowrate / 2 ;
    nucleation_number_dimensionless = spray_flux_dimensionless *
        ↪ nucleation_diameter_ratio^2 ;
```

Consolidation (Custom_consolidation_kinetics_gFP):

```
UNIT
    Calculate_porosity AS Calculate_porosity_gFP
    Calculate_bed_velocity AS Calculate_bed_velocity_gFP

SET
            Kinetic_parameter_names := ["Rate coefficient", "Minimum porosity
                ↪ ", "Maximum porosity", "e1 parameter", "e2 parameter", "e3
```

```
            ↪  parameter"] ;

        mega_conversion_factor := 1E6 ;
        milli_conversion_factor := 1E-3 ;
        very_large_number := 1E9 ;
        large_number := 1E3 ;

EQUATION
      FOR phase IN consolidating_phase DO
        FOR i:=1 TO Number_of_grid_points-1 DO
          density_envelope(i+1) = Calculate_porosity.density_envelope(
              ↪ phase,i)
              * Calculate_porosity.mass_conversion_factor /
                  ↪ Calculate_porosity.volume_conversion_factor ;
          porosity_FVB(i+1) = Calculate_porosity.porosity_protected(
              ↪ phase,i) ;
        END # FOR i:=1 TO Number_of_grid_points-1 DO

        density_envelope(1) = Calculate_porosity.density_envelope(phase
            ↪ ,1)
            * Calculate_porosity.mass_conversion_factor /
                ↪ Calculate_porosity.volume_conversion_factor ;
        porosity_FVB(1) = Calculate_porosity.porosity_protected(phase,1)
            ↪ ;
      END # FOR phase IN consolidating_phase DO

        Rate_coefficient = Kinetic_parameters("Rate coefficient") ;
        porosity_min = Kinetic_parameters("Minimum porosity") ;
        porosity_max = Kinetic_parameters("Maximum porosity") ;
        e_1_porosity = Kinetic_parameters("e1 parameter") ;
        e_2_porosity = Kinetic_parameters("e2 parameter") ;
```

```
    e_3_porosity = Kinetic_parameters("e3 parameter") ;

    porosity_endpoint = MIN(porosity_max, MAX(porosity_min,
        ↪ e_1_porosity * Calculate_bed_velocity.tip_speed * (
        ↪ e_2_porosity - liquid_to_solid_ratio) + e_3_porosity)) ;

    impact_frequency = Calculate_bed_velocity.impeller_frequency
        / Calculate_bed_velocity.minute ;
    impact_velocity = Calculate_bed_velocity.bed_velocity ;

2*mass_solids_protected*10^6 =
    (1.0e-5 + mass_solids*10^6) + SQRT((1.0e-5 - mass_solids*10^6)^2
        ↪ + (1.0e-5)^2);

FOR i:=1 TO Number_of_grid_points DO
    Consolidation_rate_unprotected(i) = Rate_coefficient * (
        ↪ porosity_FVB(i) - porosity_endpoint) * impact_frequency
        * (1 - EXP(-Stokes_deformation_number(i))) ;
    2*Consolidation_rate(i)*10^6 =
        (1.0e-5 + Consolidation_rate_unprotected(i)*10^6) + SQRT((1.0
            ↪ e-5 - Consolidation_rate_unprotected(i)*10^6)^2 + (1.0e
            ↪ -5)^2);

    capillary_number(i) * surface_tension * milli_conversion_factor *
        ↪  COS(contact_angle) * Length(i)
        = liquid_viscosity * impact_velocity * primary_particle_size
            ↪ ;
    strength_dimensionless(i) = A_str + B_str * MAX(0,
        ↪ capillary_number(i))^n_str ;
    strength_dimensionless(i) * surface_tension *
        ↪ milli_conversion_factor * COS(contact_angle)
```

```
            = yield_stress_dynamic(i) * primary_particle_size ;
        Stokes_deformation_number(i) * yield_stress_dynamic(i) *
            ↪ mega_conversion_factor
            = density_envelope(i) * Calculate_porosity.
                ↪ mass_conversion_factor
            / Calculate_porosity.volume_conversion_factor *
                ↪ impact_velocity^2 / 2 ;
    END
```

Layering (Custom_layering_kinetics_gFP):

```
UNIT
   Calculate_porosity AS Calculate_porosity_gFP

SET
        Kinetic_parameter_names := ["Rate coefficient"] ;

        fines_fraction_threshold := 0.1 ;
        large_number := 1e2 ;

EQUATION
        Rate_coefficient = Kinetic_parameters("Rate coefficient") ;
        pore_saturation_initial = Calculate_porosity.
            ↪ pore_saturation_initial ;

        FOR phase IN active_phase DO
            FOR i:=1 TO Number_of_grid_points-1 DO
                liquid_layer_thickness(i) = Calculate_porosity.
                    ↪ liquid_layer_thickness(phase,i) ;
                pore_saturation(i) = Calculate_porosity.
                    ↪ pore_saturation_protected(phase,i) ;
            END # FOR i:=1 TO Number_of_grid_points-1 DO
```

```
    pore_saturation(Number_of_grid_points) = Calculate_porosity.
        ↪ pore_saturation_protected(phase,no_grid_pts(phase)) ;
    liquid_layer_thickness(Number_of_grid_points) =
        ↪ Calculate_porosity.liquid_layer_thickness(phase,
        ↪ no_grid_pts(phase)) ;
END # FOR phase IN consolidating_phase DO

FOR phase IN active_phase DO
    FOR i:=1 TO Number_of_grid_points-1 DO
        pore_saturation_critical(i) = Calculate_porosity.
            ↪ pore_saturation_critical(phase,i) ;
    END # FOR i:=1 TO Number_of_grid_points-1 DO

    pore_saturation_critical(Number_of_grid_points) =
        ↪ Calculate_porosity.pore_saturation_critical(phase,
        ↪ no_grid_pts(phase)) ;
END # FOR phase IN consolidating_phase DO

total_mass_holdup_solids = SIGMA(mass_components_distributed(,,))
    ↪ ;

FOR z:=1 TO Number_of_grid_points DO
    2*layering_occurs_protected(z)*10^6 =
        (1.0e-5 + layering_occurs(z)*10^6) + SQRT((1.0e-5 -
            ↪ layering_occurs(z)*10^6)^2 + (1.0e-5)^2);

    layering_occurs(z) * 2 - 1 =
        TANH((liquid_layer_thickness(z) - very_high_threshold) *
            ↪ 10) ;
    donor_present(z) * 2 - 1 = TANH((fines_fraction -
```

```
            ↪ very_high_threshold) * 10) ;
        fine_fraction_low(z) * 2 - 1 = TANH((fines_fraction_threshold
            ↪  - fines_fraction) * large_number) ;

        2*Layering_growth_rate(z)*10^6 =
            (1.0e-5 + Layering_growth_rate_unprotected(z)*10^6) + SQRT
                ↪ ((1.0e-5 - Layering_growth_rate_unprotected(z)
                ↪ *10^6)^2 + (1.0e-5)^2);

        Layering_growth_rate_unprotected(z) = Rate_coefficient *
            ↪ layering_occurs_protected(z)
            * liquid_layer_thickness(z) * donor_present(z)
            / inter_particle_volumetric_void_fraction /
                ↪ pore_saturation_initial
            * ( (1 - fine_fraction_low(z))
            + fines_fraction / fines_fraction_threshold *
                ↪ fine_fraction_low(z) ) ;
    END
```

Coalescence (Custom_agglomeration_rate_gFP):

```
UNIT
   Calculate_collision_scenario_Liu AS Calculate_collision_scenario_Liu_gFP

SET
    Kernel_parameter_names := ["Rate Type I II"] ;
    Number_of_particles := 2 ;

EQUATION
   beta_1 = Kernel_parameters("Rate Type I II") ;
   beta_2 = Kernel_parameters("Rate Type I II") ;
```

```
    FOR i:=1 TO Number_of_grid_points_1 DO
        FOR j:=1 TO Number_of_grid_points_2 DO
            Agglomeration_rate_kernel(i,j) =
                ↪ Agglomeration_rate_kernel_unprotected(i,j) ;

            Agglomeration_rate_kernel_unprotected(i,j) =
                Calculate_collision_scenario_Liu.Calculate_bed_velocity.
                    ↪ bed_velocity
                * ( Length_1(i) + Length_2(j) )^2 * SQRT( 1 / (Length_1(i)
                    ↪ )^3 + 1 / (Length_2(j))^3 )
                * ( 10^(-beta_1) * Calculate_collision_scenario_Liu.
                    ↪ coalescence_I_occurs(i,j)
                + 10^(-beta_2) * Calculate_collision_scenario_Liu.
                    ↪ deformation_occurs_protected(i,j)
                    * Calculate_collision_scenario_Liu.
                        ↪ coalescence_II_occurs(i,j) )
                * ( 1 - Calculate_collision_scenario_Liu.
                    ↪ surface_dry_occurs_protected(i,j) ) ;
        END #For j
    END #For i
```

Collision scenario (Calculate_collision_scenario_Liu_gFP):

```
UNIT
    Calculate_porosity AS ARRAY(Number_of_particles) OF
        ↪ Calculate_porosity_gFP
    Calculate_bed_velocity AS Calculate_bed_velocity_gFP

SET
    mega_conversion_factor := 1E6 ;
    milli_conversion_factor := 1E-3 ;
    large_number := 1E1 ;
```

```
EQUATION
   FOR part:=1 TO Number_of_particles DO
      FOR i:=1 TO no_grid_pts(part) DO
         liquid_layer_thickness(part,i) = Calculate_porosity(part).
            ↪ liquid_layer_thickness_protected(active_phases(part),i) ;
         porosity(part,i) = Calculate_porosity(part).porosity_protected(
            ↪ active_phases(part),i) ;
         pore_saturation(part,i) = Calculate_porosity(part).
            ↪ pore_saturation_protected(active_phases(part),i) ;
         mass_granule(part,i) = Calculate_porosity(part).M(active_phases(
            ↪ part),i) ;
      END # FOR i:=1 TO Number_of_grid_points_1 DO
   END # FOR p:=1 TO Number_of_particles DO

   impact_velocity = Calculate_bed_velocity.bed_velocity ;

   FOR part:=1 TO Number_of_particles DO
      FOR i:=1 TO no_grid_pts(part) DO
         capillary_number(part,i) * surface_tension *
            ↪ milli_conversion_factor * COS(contact_angle) * Length(part
            ↪ ,i)
            = liquid_viscosity * impact_velocity * primary_particle_size
               ↪ ;
         strength_dimensionless(part,i) = A_str + B_str *
            ↪ capillary_number_protected(part,i)^n_str ;
         strength_dimensionless(part,i) * surface_tension *
            ↪ milli_conversion_factor * COS(contact_angle) =
            yield_stress_dynamic(part,i) * mega_conversion_factor
            * primary_particle_size / conversions.length_conversion("
               ↪ micron") ;
```

```
        Youngs_modulus_dimensionless(part,i) * surface_tension *
            ↪ milli_conversion_factor * COS(contact_angle)
            = Youngs_modulus(part,i) * mega_conversion_factor
                * primary_particle_size / conversions.length_conversion("
                    ↪ micron") ;
        2*capillary_number_protected(part,i)*10^6 =
            (1.0e-5 + capillary_number(part,i)*10^6) + SQRT((1.0e-5 -
                ↪ capillary_number(part,i)*10^6)^2 + (1.0e-5)^2);
    END #For i
END # FOR p:=1 TO Number_of_particles DO

CASE operating_status OF
    WHEN unit_on:
         CASE porosity_status OF
             WHEN porosity_high:
               FOR i:=1 TO no_grid_pts(1) DO
                   FOR j:=1 TO no_grid_pts(2) DO
                       deformation(i,j) = (deformation_occurs_protected(i,
                           ↪ j) *
                           ( ( 8 / 3 * pi )^(1/2) *
                               ↪ diameter_granule_reduced(i,j)
                           * (Stokes_deformation_number_reduced_protected(i
                               ↪ ,j))^(1/2)
                           * ( 1 - 1 /
                               ↪ viscous_Stokes_number_reduced_protected(i
                               ↪ ,j)
                               * LOG( MAX(standard_threshold,
                                   ↪ liquid_layer_thickness_mean_protected(
                                   ↪ i,j) + standard_threshold)
                                   / height_asperities) )
                           * ( 1 - 7.36 *
```

```
                ↪ yield_stress_dynamic_reduced_protected(i,
                ↪ j) / Youngs_modulus_reduced(i,j)
                * (Stokes_deformation_number_reduced
                    ↪ _protected(i,j))^(-1/4)
                * term_A_protected(i,j) ) ) ) ;
    END #For j
END #For i

FOR i:=1 TO no_grid_pts(1) DO
    FOR j:=1 TO no_grid_pts(2) DO
        CASE term_A_status(i,j) OF
            WHEN term_A_low:
            (term_A(i,j)^2 * (1 - 1 /
                ↪ viscous_Stokes_number_reduced_protected(i
                ↪ ,j)
                * LOG( MAX(standard_threshold,
                    ↪ liquid_layer_thickness_mean_protected(
                    ↪ i,j) + standard_threshold) /
                    ↪ height_asperities ) ) )
                = 1 ;

            viscous_Stokes_constant(i,j) =
                ↪ viscous_Stokes_number_reduced_protected(i
                ↪ ,j) ;
            coalescence_I_constant(i,j) =
                ↪ coalescence_I_occurs(i,j) ;
        SWITCH TO term_A_high IF coalescence_I_occurs(i,j)
            ↪ > 0.3 ;

            WHEN term_A_high:
            $(term_A(i,j))
```

```
                    = 1 / SQRT((0.5 * LOG((1 -
                        ↪ coalescence_I_constant(i,j) * 2 + 1)
                        / (1 + coalescence_I_constant(i,j) * 2 -
                            ↪ 1)))
                        / (10 * viscous_Stokes_constant(i,j)))
                            - term_A(i,j) ;
                $viscous_Stokes_constant(i,j) = 0 ;
                $coalescence_I_constant(i,j) = 0 ;
                SWITCH TO term_A_low IF coalescence_I_occurs(i,j
                    ↪ ) < 0.1 ;
            END # CASE term_A_status OF
        END #For j
    END #For i
    SWITCH TO porosity_low IF MAX(pore_saturation(,)) > 1E2
                        AND MIN(porosity(,)) < 2E-2 ;
WHEN porosity_low:
    FOR i:=1 TO no_grid_pts(1) DO
        FOR j:=1 TO no_grid_pts(2) DO
            $deformation(i,j) * standard_threshold = ((
                ↪ deformation_occurs_protected(i,j)) *
                ( ( 8 / 3 * pi )^(1/2) *
                    ↪ diameter_granule_reduced(i,j)
                * (Stokes_deformation_number_reduced_protected(i
                    ↪ ,j))^(1/2)
                * ( 1 - 1 /
                    ↪ viscous_Stokes_number_reduced_protected(i
                    ↪ ,j)
                    * LOG( MAX(standard_threshold,
                        ↪ liquid_layer_thickness_mean_protected(
                        ↪ i,j) + standard_threshold )
                        / height_asperities) )
```

```
                    * ( 1 - 7.36 *
                        ↪ yield_stress_dynamic_reduced_protected(i,
                        ↪ j) / Youngs_modulus_reduced(i,j)
                        * (Stokes_deformation_number_reduced
                            ↪ _protected(i,j))^(-1/4)
                        * (term_A_protected(i,j)) ) ) - deformation(
                            ↪ i,j)) * standard_threshold ;

                    viscous_Stokes_constant(i,j) =
                        ↪ viscous_Stokes_number_reduced_protected(i
                        ↪ ,j) ;
                    coalescence_I_constant(i,j) =
                        ↪ coalescence_I_occurs(i,j) ;

                $((term_A(i,j))) =
                    SQRT(1 / ( 1 - 1 / (
                        ↪ viscous_Stokes_number_reduced_protected(i
                        ↪ ,j))
                        * LOG( MAX(standard_threshold,
                            ↪ liquid_layer_thickness_mean_protected(
                            ↪ i,j)
                            + standard_threshold) / height_asperities
                                ↪  ) ) ) - (term_A(i,j)) ;
            END #For j
        END #For i
        SWITCH TO porosity_high IF MAX(pore_saturation(,)) < 1E1
                            OR MIN(porosity(,)) > 5E-2 ;
  END # CASE porosity_status OF

FOR i:=1 TO no_grid_pts(1) DO
   FOR j:=1 TO no_grid_pts(2) DO
```

```
            (coalescence_II_occurs(i,j) * 2 - 1) * low_threshold
               = (TANH( ( 0.172 /
                  ↪ viscous_Stokes_number_reduced_protected(i,j)
               * ( diameter_granule_reduced(i,j) /
                  liquid_layer_thickness_mean_protected(i,j) )^2
               * ( term_A_protected(i,j)^(-2) )^(5/4)
               * ( ( (liquid_layer_thickness_mean_protected(i,j) /
                  ↪ height_asperities)^2 - 1 )
                  + 2 * liquid_layer_thickness_mean_protected(i,j) /
                     ↪ (deformation_protected(i,j))
                  * ( liquid_layer_thickness_mean_protected(i,j) /
                     ↪ height_asperities - 1 )
                  + 2 * liquid_layer_thickness_mean_protected(i,j)^2
                     ↪ / (deformation_protected(i,j))^2
                  * LOG( MAX(standard_threshold,
                     ↪ liquid_layer_thickness_mean_protected(i,j) +
                     ↪  standard_threshold)
                     / height_asperities) )
               * ( 1 - 7.36 * yield_stress_dynamic_reduced_protected(
                  ↪ i,j) / Youngs_modulus_reduced(i,j)
                  * (Stokes_deformation_number_reduced_protected(i,j)
                     ↪ )^(-1/4)
                  * (term_A_protected(i,j)) )^2
               - (yield_stress_dynamic_reduced_protected(i,j) /
                  ↪ Youngs_modulus_reduced(i,j))^0.5
                  * (Stokes_deformation_number_reduced_protected(i,j)
                     ↪ )^(-9/8) ) ) ) * low_threshold ;
         END #For j
      END #For i

      FOR part:=1 TO Number_of_particles DO
```

```
        FOR i:=1 TO no_grid_pts(part) DO
            Youngs_modulus_dimensionless(part,i) = (k_E *
                ↪ capillary_number_protected(part,i)^p
                * porosity(part,i)^q * pore_saturation(part,i)^r) ;
        END
    END
SWITCH TO unit_off IF operating_status < 0.5
        OR SIGMA(mass_components_distributed(active_phases(1),,))
         + SIGMA(mass_components_distributed(active_phases(2),,)) <
             ↪ mass_threshold
        OR MAX(liquid_layer_thickness_mean_protected(,)) <
            ↪ high_threshold
        OR MAX(deformation_occurs_protected(,)) < 0.1 ;

WHEN unit_off:
    FOR i:=1 TO no_grid_pts(1) DO
        FOR j:=1 TO no_grid_pts(2) DO
            $(term_A(i,j)) =
                SQRT( MAX( standard_threshold, 1 / ( 1 - 1 / (
                    ↪ viscous_Stokes_number_reduced_protected(i,j))
                    * LOG( MAX(standard_threshold,
                        ↪ liquid_layer_thickness_mean_protected(i,j)
                        + standard_threshold) / height_asperities ) ) )
                            ↪ ) - (term_A(i,j)) ;
            coalescence_II_occurs(i,j) = 0 ;

            viscous_Stokes_constant(i,j) =
                ↪ viscous_Stokes_number_reduced_protected(i,j) ;
            coalescence_I_constant(i,j) = coalescence_I_occurs(i,j) ;
            deformation(i,j) = diameter_granule_reduced(i,j)/100 *
                ↪ deformation_occurs_protected(i,j) ;
```

```
            END #For j
        END #For i

        FOR part:=1 TO Number_of_particles DO
            FOR i:=1 TO no_grid_pts(part) DO
                $Youngs_modulus_dimensionless(part,i) = MIN(6000, k_E *
                    ↪ capillary_number_protected(part,i)^p
                    * MAX(0.5, porosity(part,i))^q * pore_saturation(part,
                        ↪ i)^r)
                    - Youngs_modulus_dimensionless(part,i) ;
            END
        END
    SWITCH TO unit_on IF operating_status > 0.5
            AND (SIGMA(mass_components_distributed(active_phases(1),,))
              + SIGMA(mass_components_distributed(active_phases(2),,)))
              / SIGMA(mass_components_distributed(,,)) > 1E-4
            AND MAX(liquid_layer_thickness_mean_protected(,)) >
                ↪ height_asperities
            AND MAX(deformation_occurs(,)) > 0.9 ;
END # CASE operating_status OF

# Express the agglomeration rate kernel for each pair of size classes.
    FOR i:=1 TO no_grid_pts(1) DO
        FOR j:=1 TO no_grid_pts(2) DO
            (- deformation_occurs(i,j) * 2 + 1)
                = (TANH( 10 * (LOG( MAX(standard_threshold,
                    ↪ liquid_layer_thickness_mean_protected(i,j) +
                    ↪ standard_threshold)
                    / height_asperities ) -
                        ↪ viscous_Stokes_number_reduced_protected(i,j)) ) ) ;
```

```
(surface_dry_occurs(i,j) * 2 - 1) * low_threshold
   = (TANH(height_asperities -
      ↪ liquid_layer_thickness_mean_protected(i,j))) *
      ↪ low_threshold ;
coalescence_I_occurs(i,j) = 1 - deformation_occurs_protected(i,j)
   ↪  ;

2*surface_dry_occurs_protected(i,j)*10^6 =
   (1.0e-5 + surface_dry_occurs(i,j)*10^6) + SQRT((1.0e-5 -
      ↪ surface_dry_occurs(i,j)*10^6)^2 + (1.0e-5)^2);
2*term_A_protected(i,j)*10^6 =
   (1.0e-5 + term_A(i,j)*10^6) + SQRT((1.0e-5 - term_A(i,j)
      ↪ *10^6)^2 + (1.0e-5)^2);
2*deformation_protected(i,j)*10^6 =
   (1.0e-5 + deformation(i,j)*10^6) + SQRT((1.0e-5 - deformation
      ↪ (i,j)*10^6)^2 + (1.0e-5)^2);
2*deformation_occurs_protected(i,j)*10^6 =
   (1.0e-5 + deformation_occurs(i,j)*10^6) + SQRT((1.0e-5 -
      ↪ deformation_occurs(i,j)*10^6)^2 + (1.0e-5)^2);
2*mass_reduced_protected(i,j)*10^6 =
   (1.0e-5 + mass_reduced(i,j)*10^6) + SQRT((1.0e-5 -
      ↪ mass_reduced(i,j)*10^6)^2 + (1.0e-5)^2);
2*viscous_Stokes_number_reduced_protected(i,j)*10^6 =
   (1.0e-5 + viscous_Stokes_number_reduced(i,j)*10^6) + SQRT
      ↪ ((1.0e-5 - viscous_Stokes_number_reduced(i,j)*10^6)^2 +
      ↪  (1.0e-5)^2);
2*yield_stress_dynamic_reduced_protected(i,j)*10^6 =
   (1.0e-5 + yield_stress_dynamic_reduced(i,j)*10^6) + SQRT((1.0
      ↪ e-5 - yield_stress_dynamic_reduced(i,j)*10^6)^2 + (1.0e
      ↪ -5)^2);
2*Stokes_deformation_number_reduced_protected(i,j)*10^6 =
```

```
    (1.0e-5 + Stokes_deformation_number_reduced(i,j)*10^6) + SQRT
        ↪ ((1.0e-5 - Stokes_deformation_number_reduced(i,j)*10^6)
        ↪ ^2 + (1.0e-5)^2);


mass_reduced(i,j) = mass_granule(1,i) * mass_granule(2,j) / (
    ↪ mass_granule(1,i) + mass_granule(2,j) ) ;
viscous_Stokes_number_reduced(i,j) * 3 * pi * liquid_viscosity
    * (diameter_granule_reduced(i,j) / conversions.
        ↪ length_conversion("micron"))^2 * standard_threshold
    = (8 * mass_reduced_protected(i,j) / mass_conversion_factor *
        ↪  impact_velocity) * standard_threshold ;
Stokes_deformation_number_reduced(i,j) * 2 * (
    ↪ diameter_granule_reduced(i,j) / conversions.
    ↪ length_conversion("micron"))^3
    * yield_stress_dynamic_reduced_protected(i,j) *
        ↪ mega_conversion_factor
    = (mass_reduced_protected(i,j) / mass_conversion_factor *
        ↪ impact_velocity^2) ;
( ( 1 - Poisson_ratio^2 ) * Youngs_modulus(2,j) + ( 1 -
    ↪ Poisson_ratio^2 ) * Youngs_modulus(1,i) )
    * Youngs_modulus_reduced(i,j) = Youngs_modulus(1,i) *
        ↪ Youngs_modulus(2,j) ;
liquid_layer_thickness_mean(i,j) * 2 = (liquid_layer_thickness(1,
    ↪ i) + liquid_layer_thickness(2,j)) ;
2*liquid_layer_thickness_mean_protected(i,j)*10^6 =
    (1.0e-5 + liquid_layer_thickness_mean(i,j)*10^6) + SQRT((1.0e
        ↪ -5 - liquid_layer_thickness_mean(i,j)*10^6)^2 + (1.0e
        ↪ -5)^2);
yield_stress_dynamic_reduced(i,j) * ( yield_stress_dynamic(1,i) +
    ↪  yield_stress_dynamic(2,j) )
    = yield_stress_dynamic(1,i) * yield_stress_dynamic(2,j) ;
```

```
        END #For j
    END #For i


INITIAL
    term_A(,) = 0 ;
    Youngs_modulus_dimensionless(,) = 100 ;
```

Bed kinetics (Calculate_bed_velocity_gFP):

```
EQUATION
    bed_velocity = 0.15 * tip_speed ;
    tip_speed = pi * impeller_frequency * impeller_diameter / minute ;
```

Compartmental modelling (Compartmentalisation_gFP):

```
UNIT
    Calculate_bed_velocity AS Calculate_bed_velocity_gFP


EQUATION
    volume_total * fill_level = volume_effective ;
    volume_spray = thickness_spray * length_spray * width_spray ;
    volume_breakage = diameter_chopper^2 * length_chopper ;
    volume_effective = volume_breakage + volume_spray + volume_bulk ;

    volume_fraction_spray * volume_effective = volume_spray ;
    volume_fraction_bulk * volume_effective = volume_bulk ;
    volume_fraction_breakage * volume_effective = volume_breakage ;

    residence_time_spray * bed_velocity = length_spray ;
    residence_time_breakage * bed_velocity = diameter_chopper ;

    residence_time_spray * residence_time_breakage * volume_fraction_bulk
        = residence_time_bulk * residence_time_spray *
            ↪ volume_fraction_breakage
```

```
    + residence_time_bulk * residence_time_breakage *
        ↪ volume_fraction_spray ;

split_fraction_to_spray * (diameter_chopper * length_chopper +
    ↪ thickness_spray * width_spray)
    = thickness_spray * width_spray ;

split_fraction_to_breakage * (diameter_chopper * length_chopper +
    ↪ thickness_spray * width_spray)
    = diameter_chopper * length_chopper ;

bed_velocity = Calculate_bed_velocity.bed_velocity ;
```

Appendix D

SIMULATION DATA

*D.*1 *Model results and assessment*

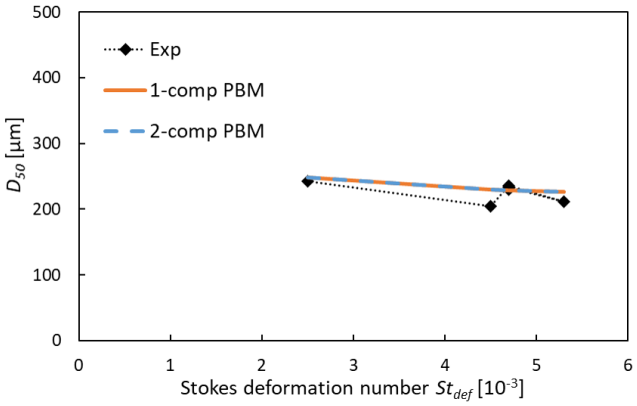

(a) Mass-median diameter D_{50}

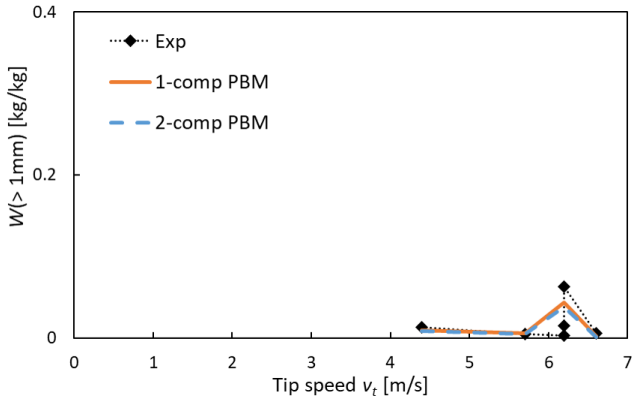

(b) Coarse mass fraction W (> 1 mm)

Figure D.1: Predictions and experimental data with varying tip speed at 10 L (Exp 12-14 and 19: $L/S = 0.15$; $t_{kn} = 5$ min)

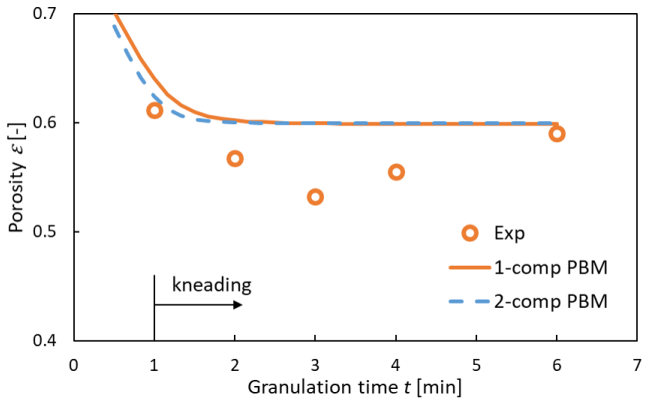

(a) Porosity ε

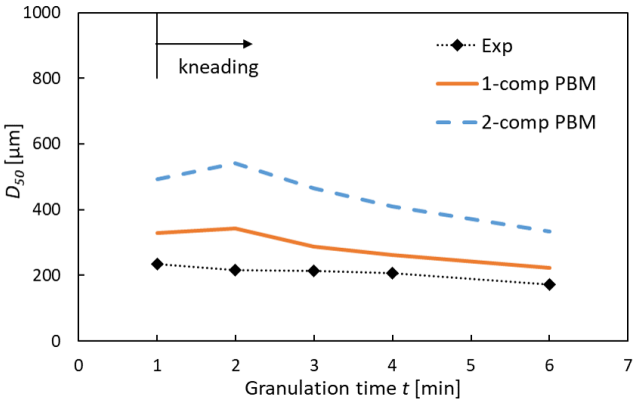

(b) Mass-median diameter D_{50}

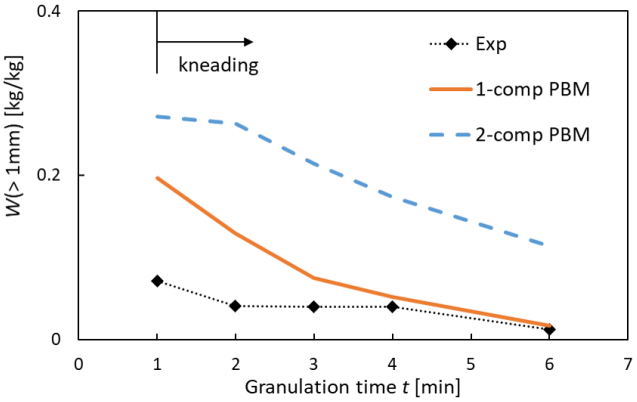

(c) Coarse mass fraction W (> 1 mm)

Figure D.2: Predictions and experimental data with varying time at 2 L (Exp 1 and 8-11: $L/S = 0.15$; $t_{sp} = 1$ min; $Fr = 23$)

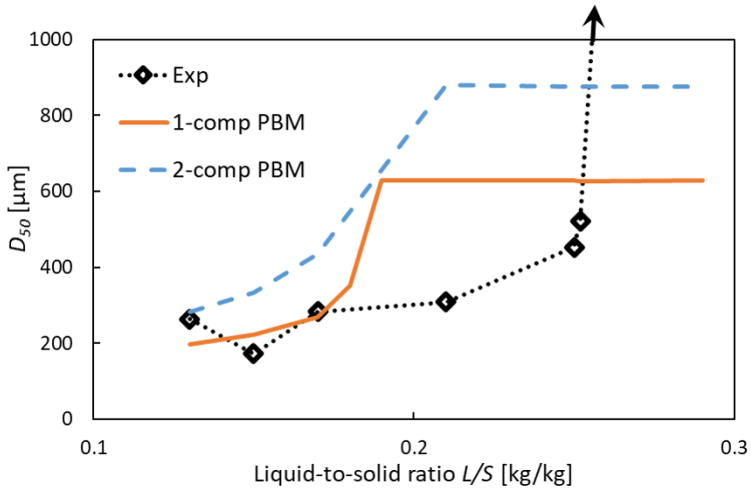

(a) Mass-median diameter D_{50}

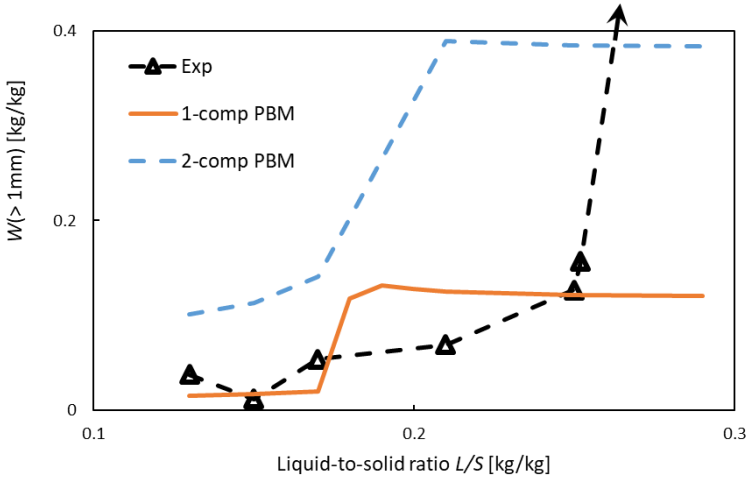

(b) Coarse mass fraction W (> 1 mm)

Figure D.3: Predictions and experimental data with varying L/S at 2 L (Exp 1, 4-7 and 27: $Fr = 23$)

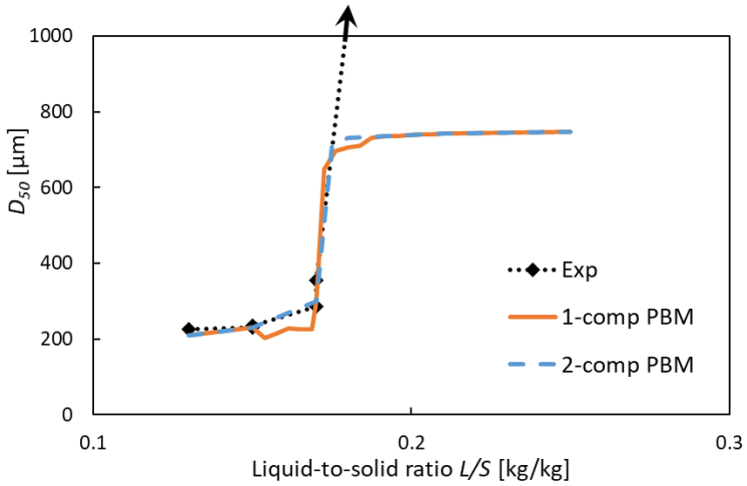

(a) Mass-median diameter D_{50}

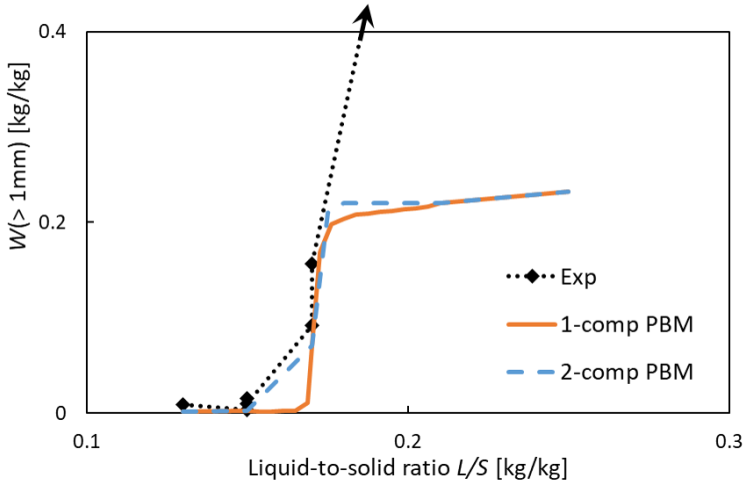

(b) Coarse mass fraction W (> 1 mm)

Figure D.4: Predictions and experimental data with varying L/S at 10 L (Exp 12, 15-17, 22, 23, 36 and 37: $Fr = 23$)

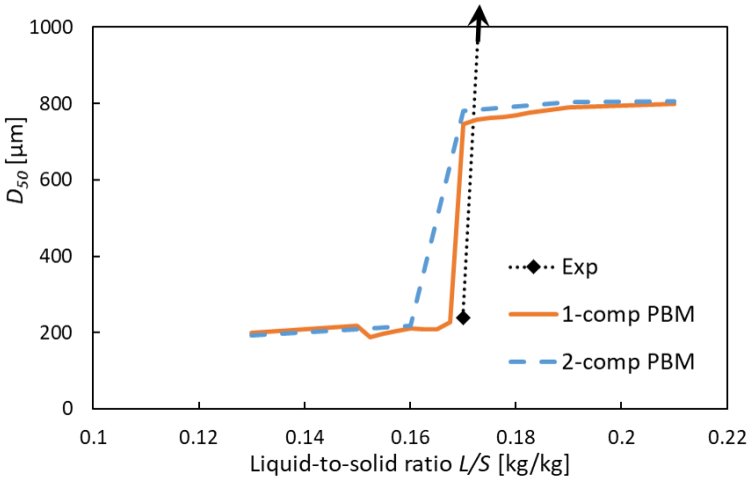

(a) Mass-median diameter D_{50}

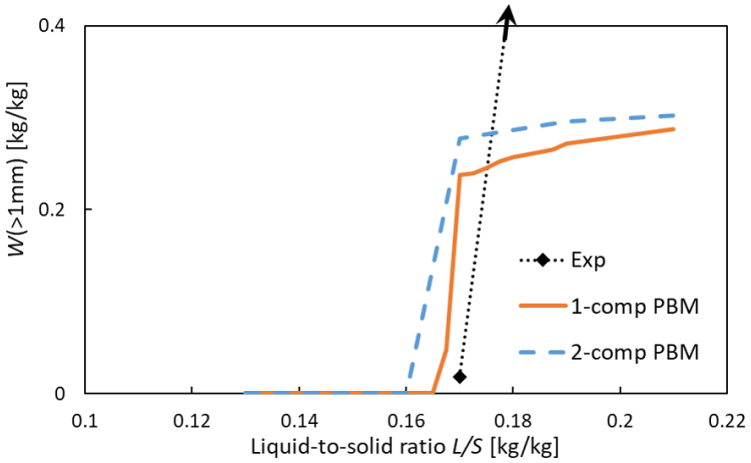

(b) Coarse mass fraction W (> 1 mm)

Figure D.5: Predictions and experimental data with varying L/S at 25 L (Exp 38-40: $Fr = 22$)

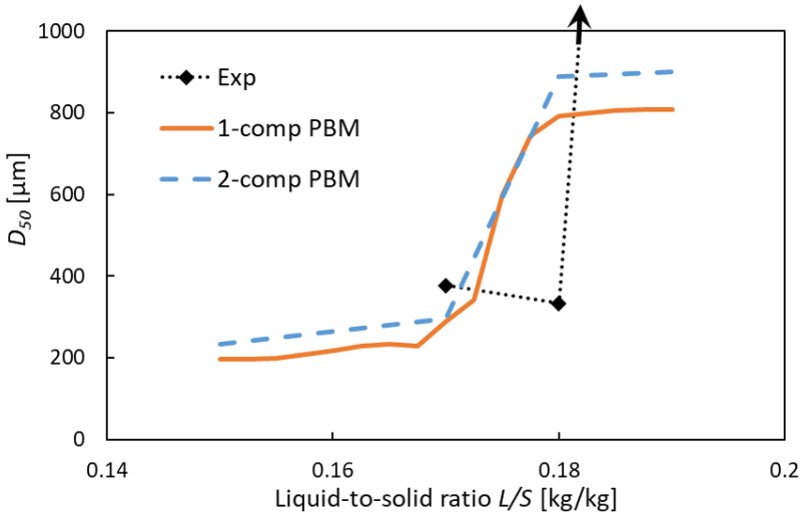

(a) Mass-median diameter D_{50}

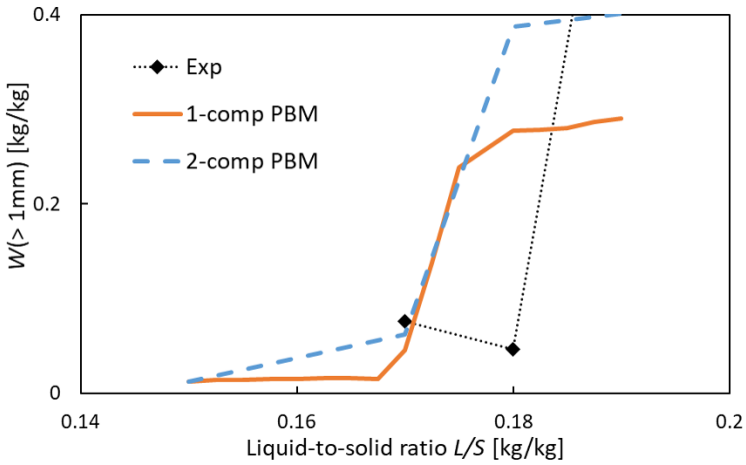

(b) Coarse mass fraction W ($>$ 1 mm)

Figure D.6: Predictions and experimental data with varying L/S at 70 L (Exp 44-46: Fr = 12)

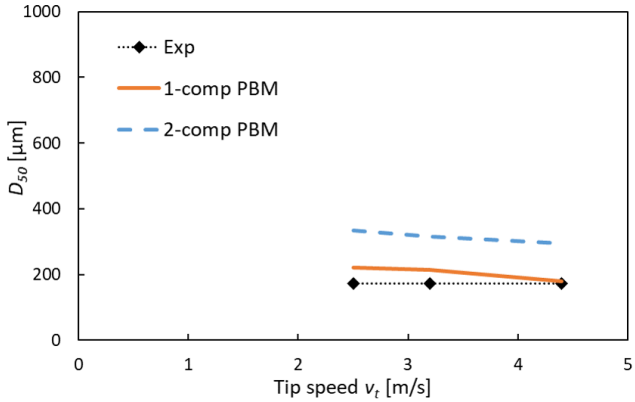

(a) Mass-median diameter D_{50}

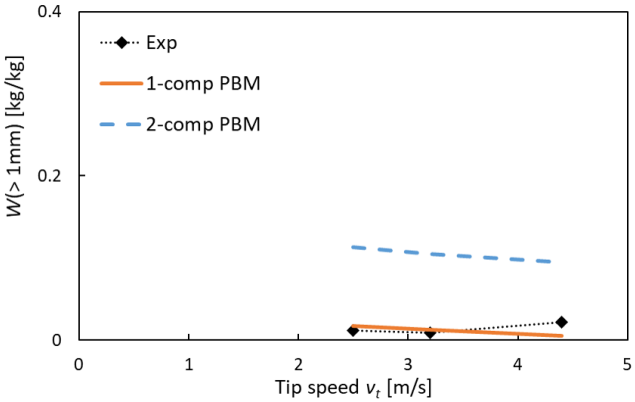

(b) Coarse mass fraction W (> 1 mm)

Figure D.7: Predictions and experimental data with varying impeller tip speed at 2 L (Exp 1-3: $L/S = 0.15$; $t_{kn} = 5$ min)

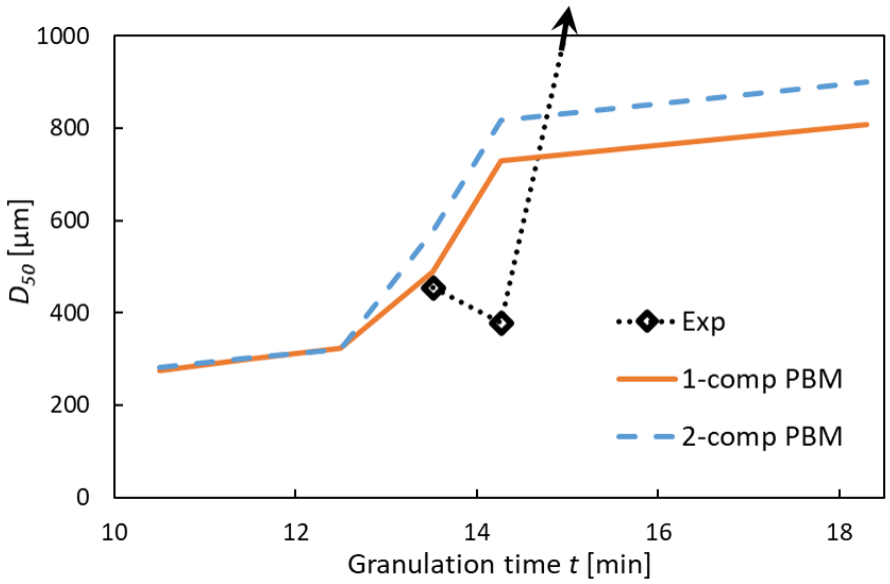

(a) Mass-median diameter D_{50}

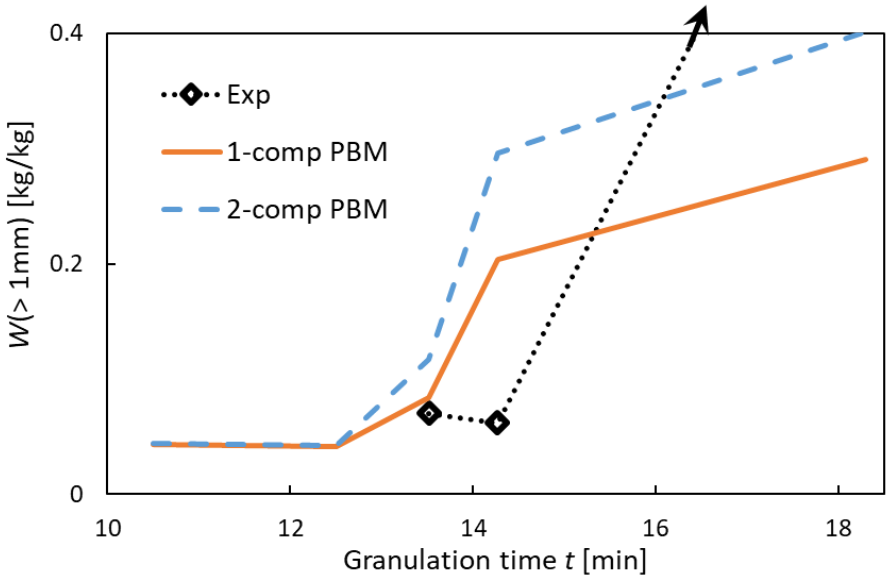

(b) Coarse mass fraction W (> 1 mm)

Figure D.8: Predictions and experimental data with varying granulation time t at 70 L (Exp 42, 43 and 45: $L/S = 0.19$; $Fr = 12$)

Figure D.9 compares model predictions to experimental data. Here, the nuclei diameter is varied by adjusting the dimensionless spray flux Ψ_a. The experiments are carried out a low L/S of 0.15. The model predictions are in very good qualitative and quantitative agreement.

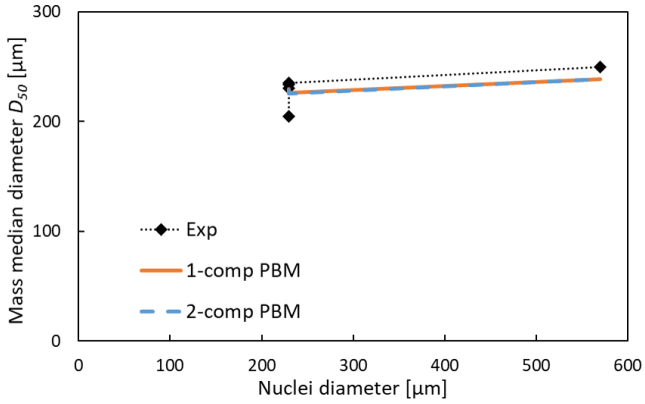

(a) Mass-median diameter D_{50}

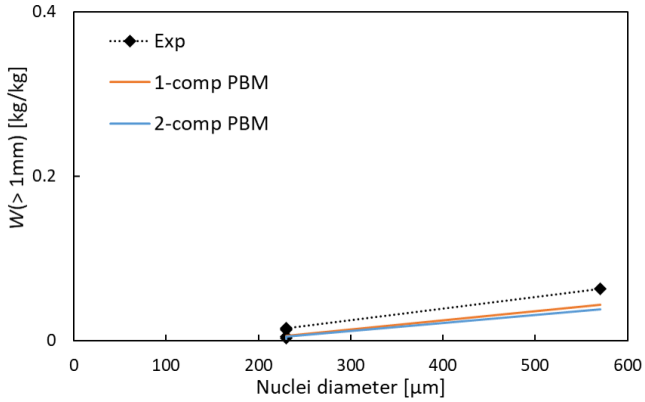

(b) Coarse mass fraction W (> 1 mm)

Figure D.9: Predictions and experimental data with varying nuclei diameter at 10 L (Exp 12 and 20-23: t_{kn} = 5 min; L/S = 0.15)

Comparison of all model and experimental results are displayed in Figures D.10, D.11, D.12, D.13, D.14, D.15 and D.16.

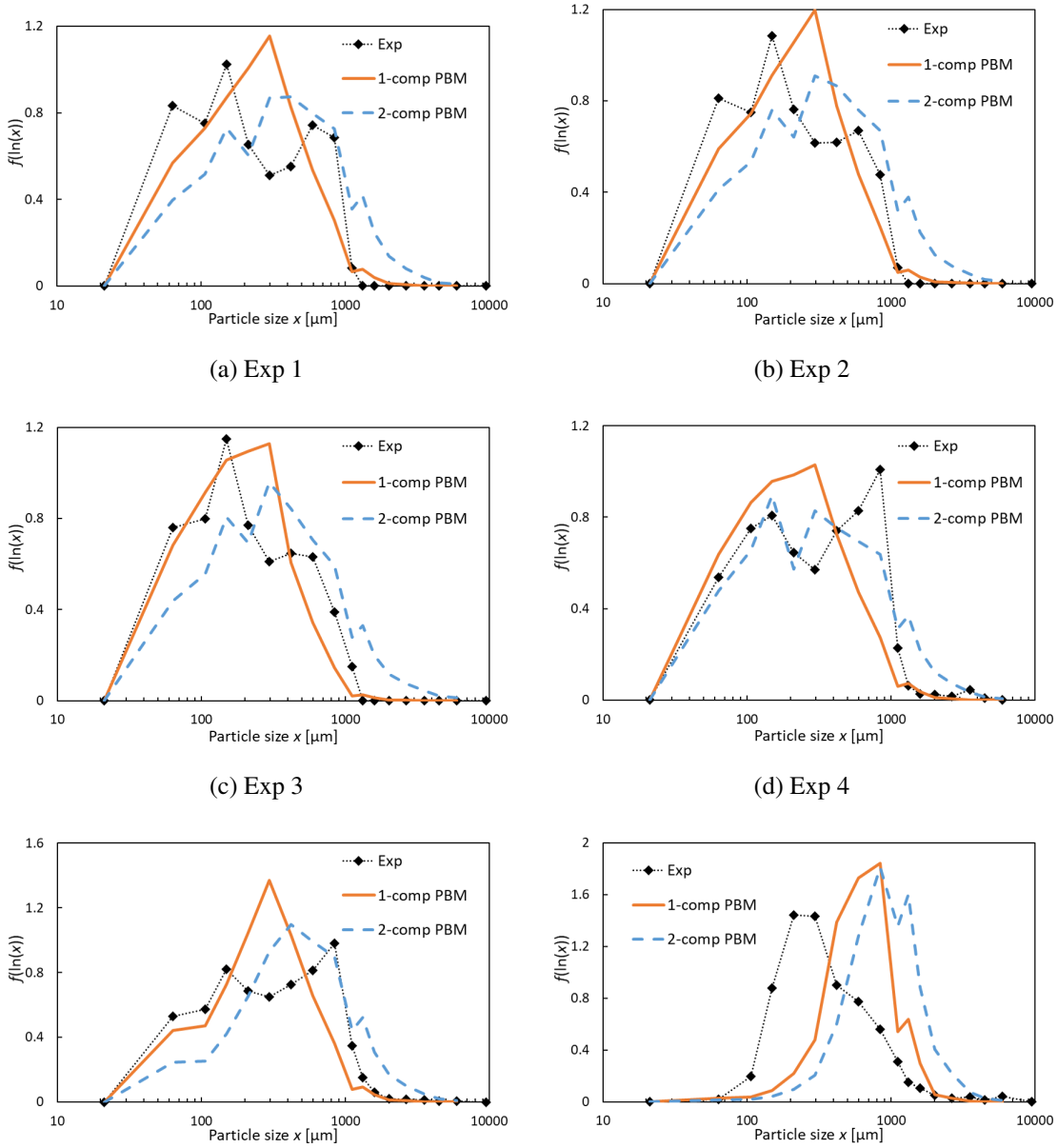

(a) Exp 1

(b) Exp 2

(c) Exp 3

(d) Exp 4

(e) Exp 5

(f) Exp 6

Figure D.10: Model and experimental PSD results (Exp 1-6)

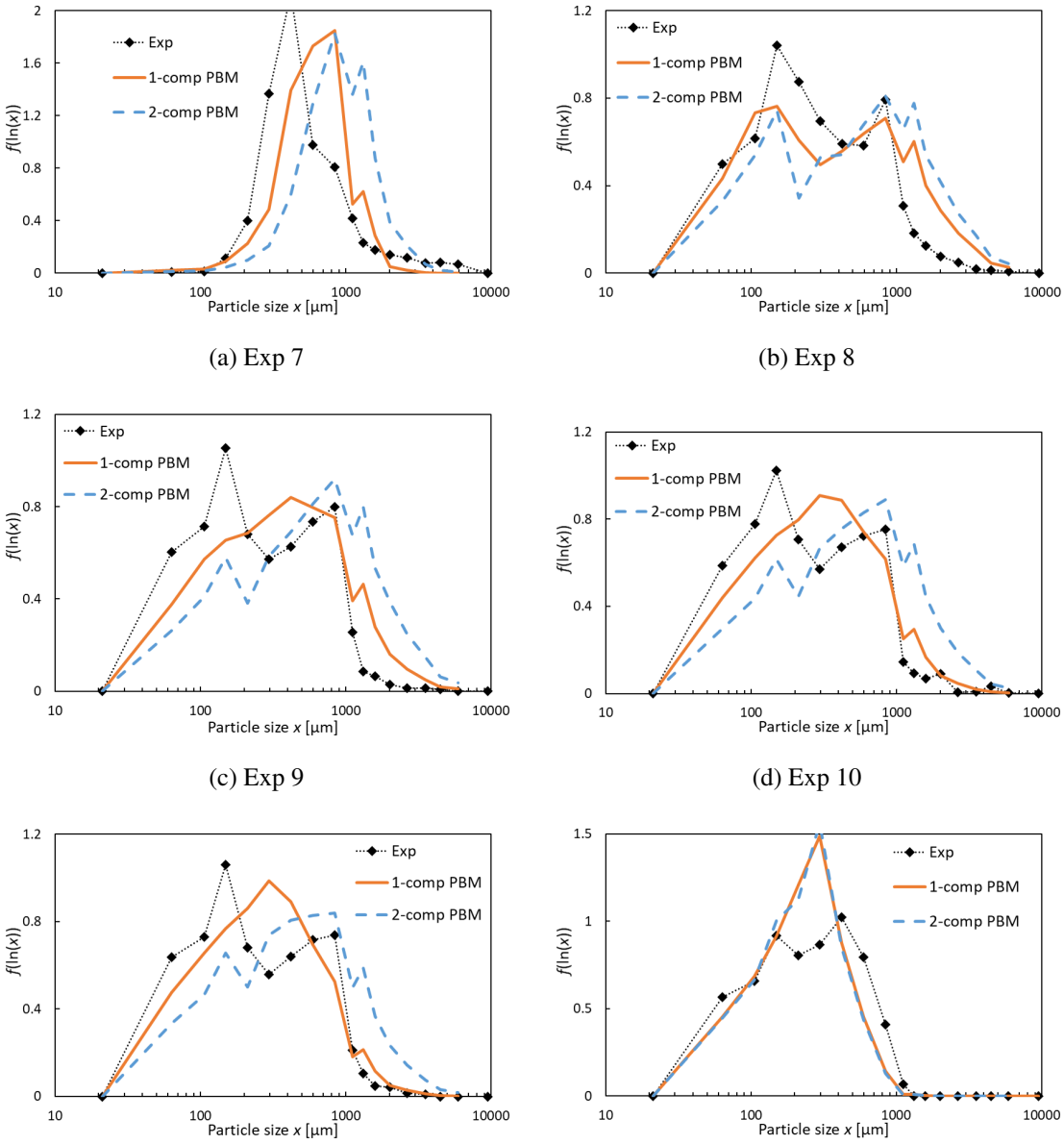

(a) Exp 7

(b) Exp 8

(c) Exp 9

(d) Exp 10

(e) Exp 11

(f) Exp 12

Figure D.11: Model and experimental PSD results (Exp 7-12)

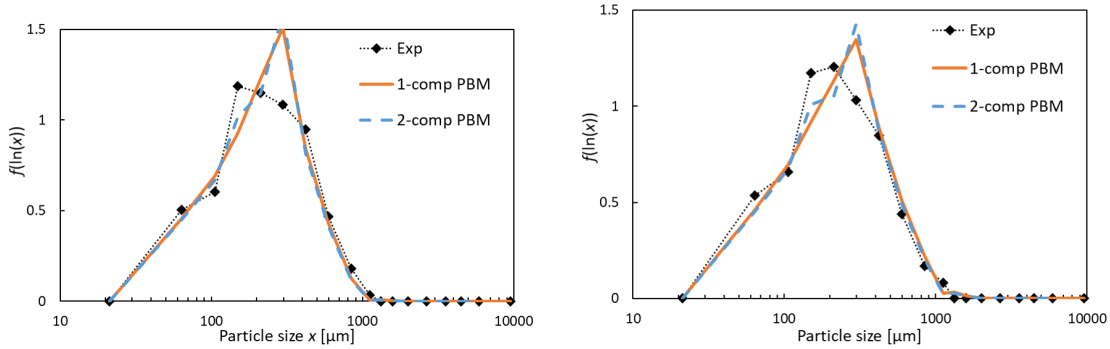

(a) Exp 13

(b) Exp 14

(c) Exp 15

(d) Exp 16

(e) Exp 16-1

(f) Exp 17

Figure D.12: Model and experimental PSD results (Exp 13-17)

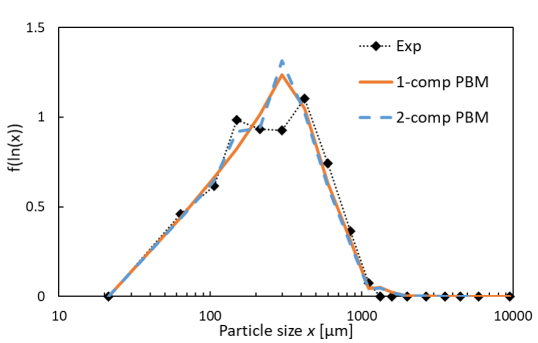

(a) Exp 19

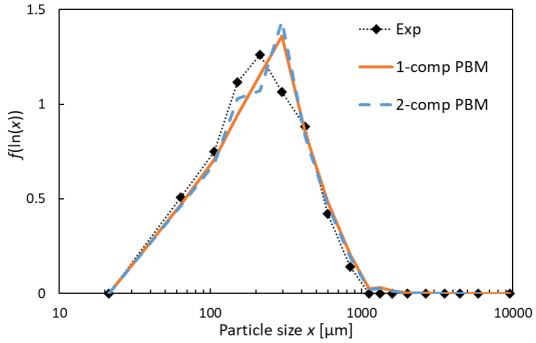

(b) Exp 20

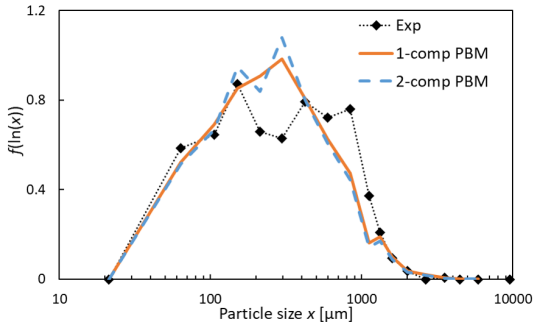

(c) Exp 21

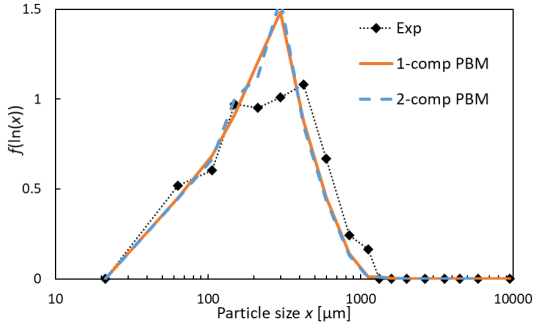

(d) Exp 22

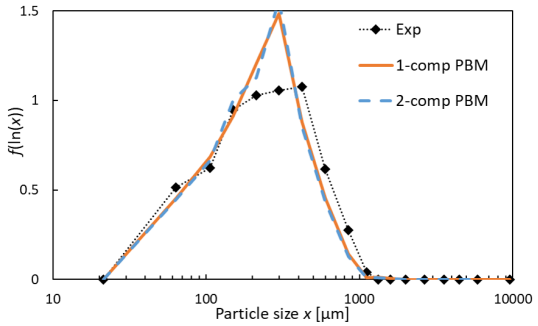

(e) Exp 23

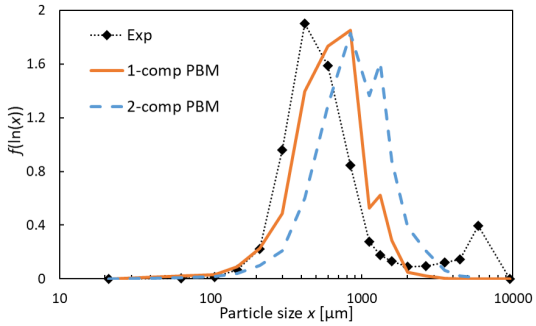

(f) Exp 27

Figure D.13: Model and experimental PSD results (Exp 19-27)

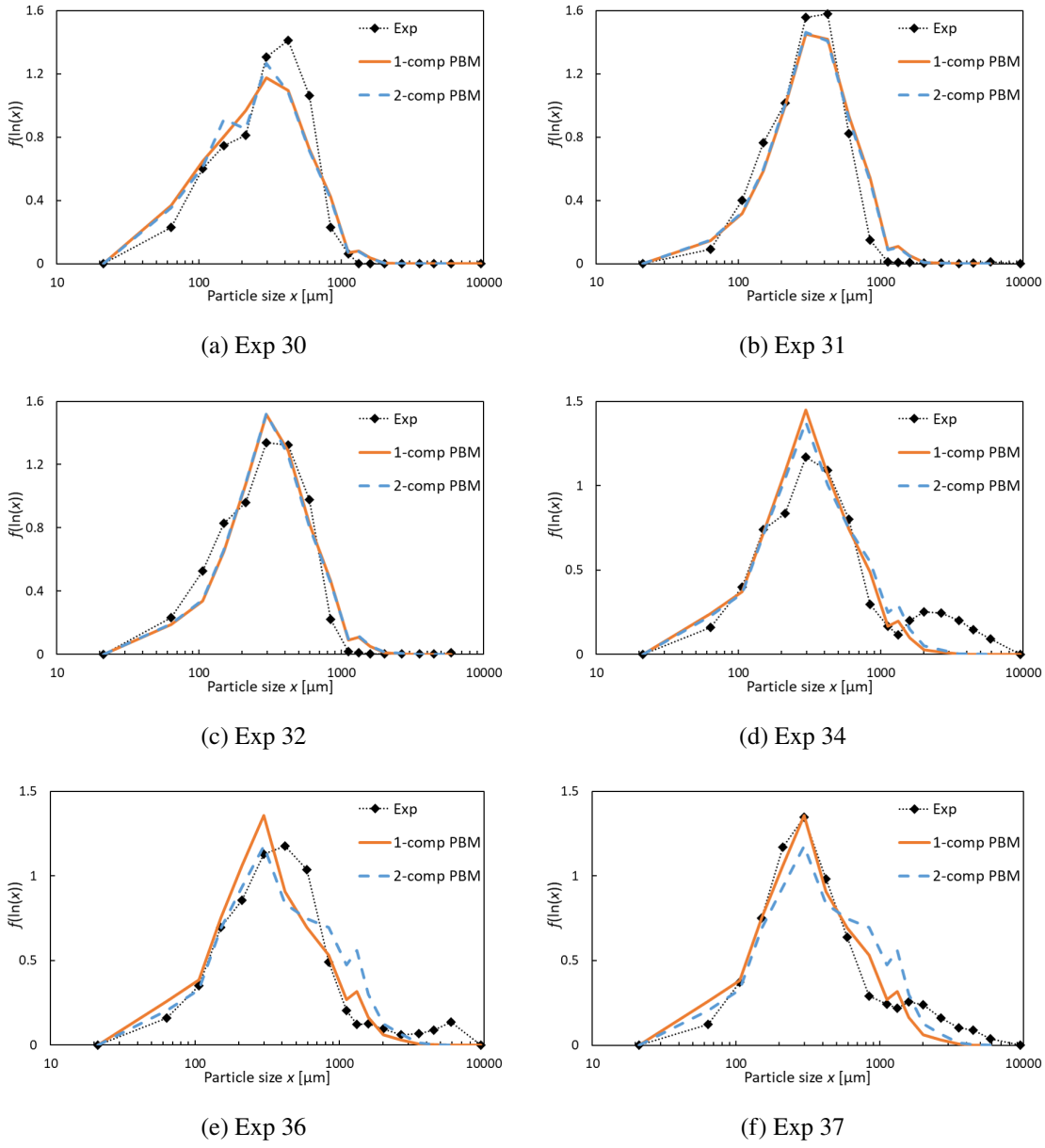

(a) Exp 30

(b) Exp 31

(c) Exp 32

(d) Exp 34

(e) Exp 36

(f) Exp 37

Figure D.14: Model and experimental PSD results (Exp 30-37)

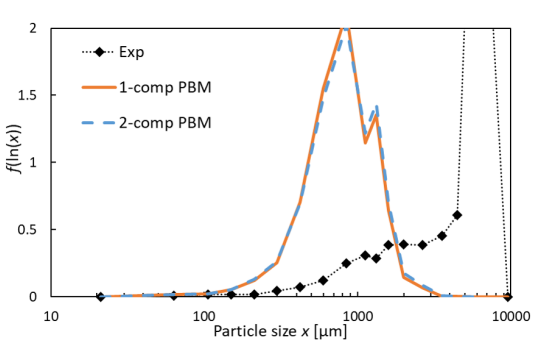

(a) Exp 38

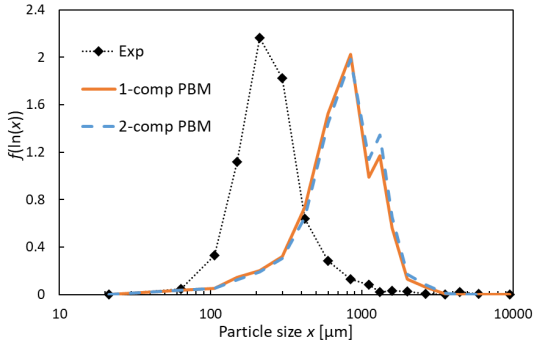

(b) Exp 39

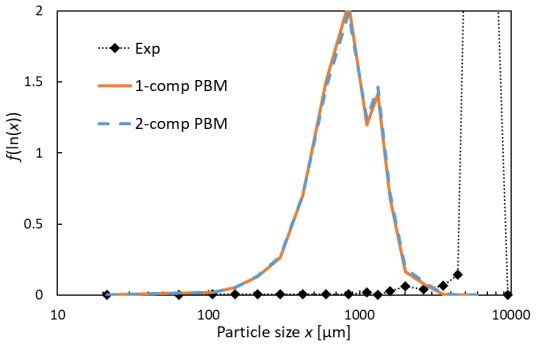

(c) Exp 40

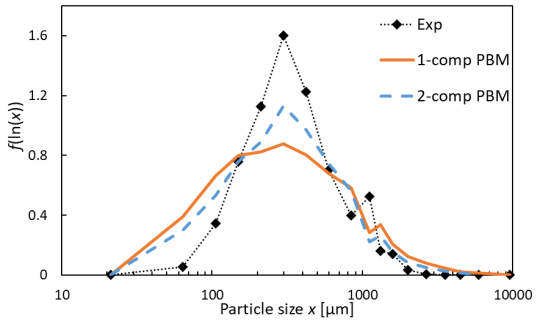

(d) Exp 41

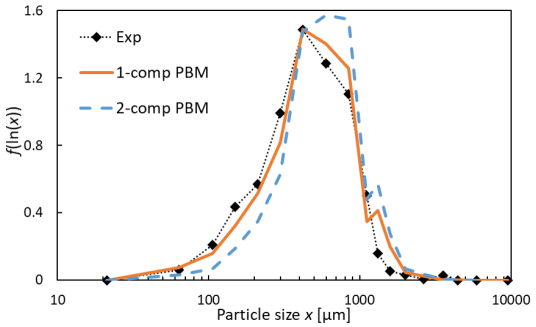

(e) Exp 42

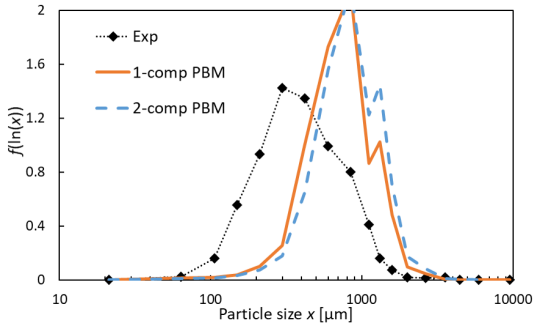

(f) Exp 43

Figure D.15: Model and experimental PSD results (Exp 38-43)

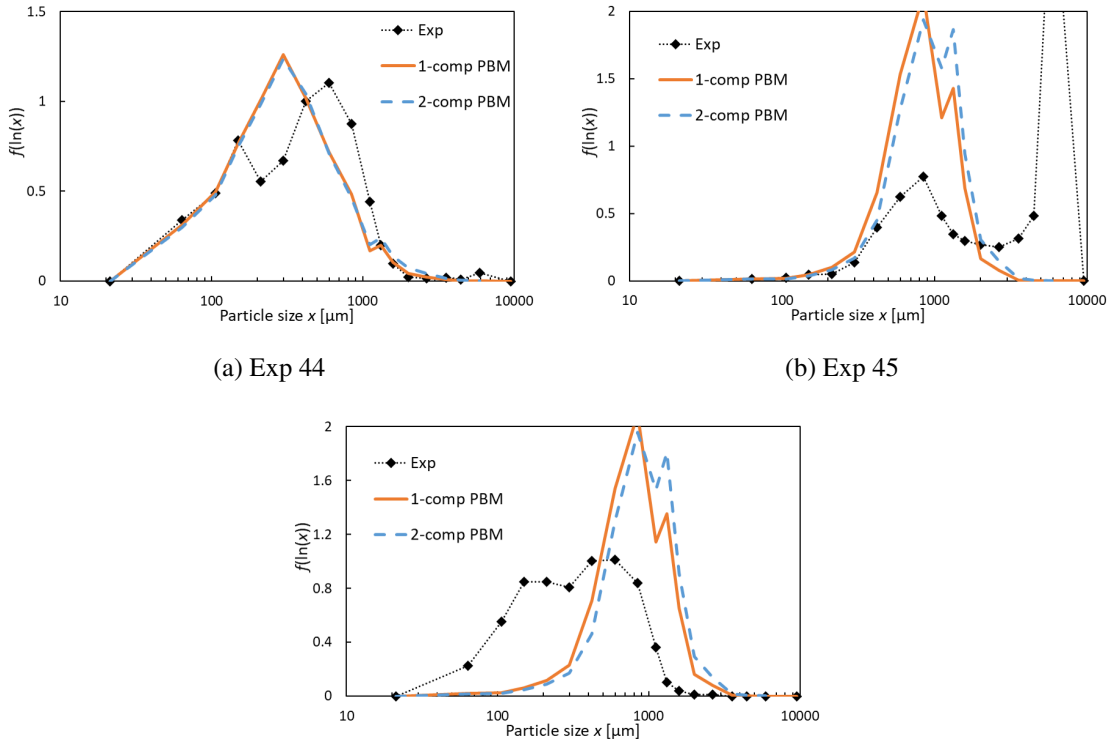

(a) Exp 44

(b) Exp 45

(c) Exp 46

Figure D.16: Model and experimental PSD results (Exp 44-46)

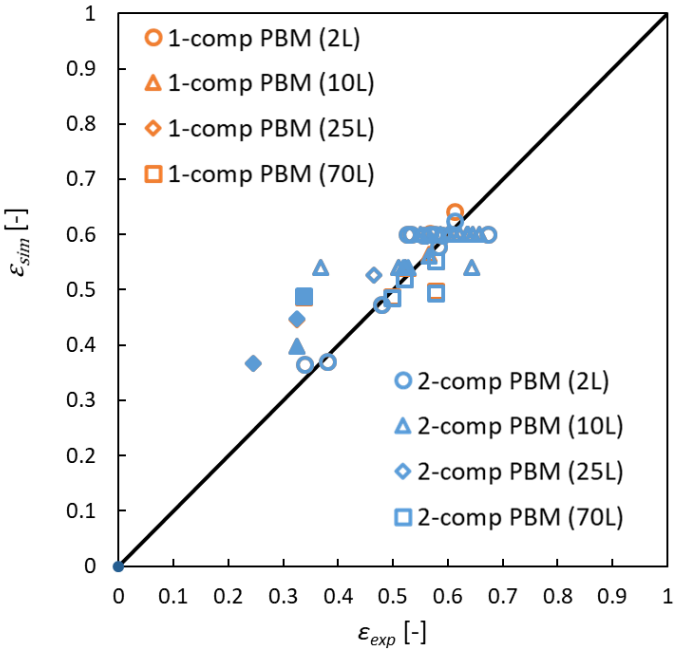

(a) Porosity ε

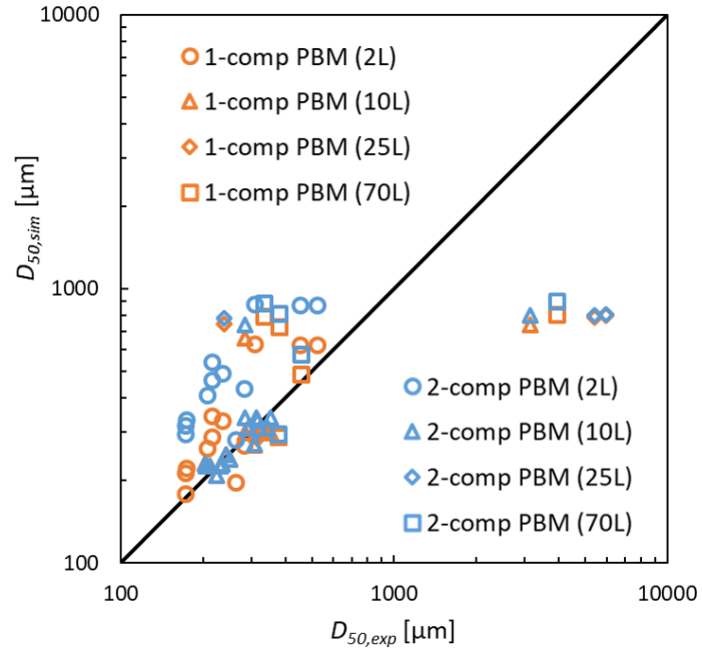

(b) Mass-median diameter D_{50}

Figure D.17: Comparison of simulation and experimental porosity and D_{50} results across scales

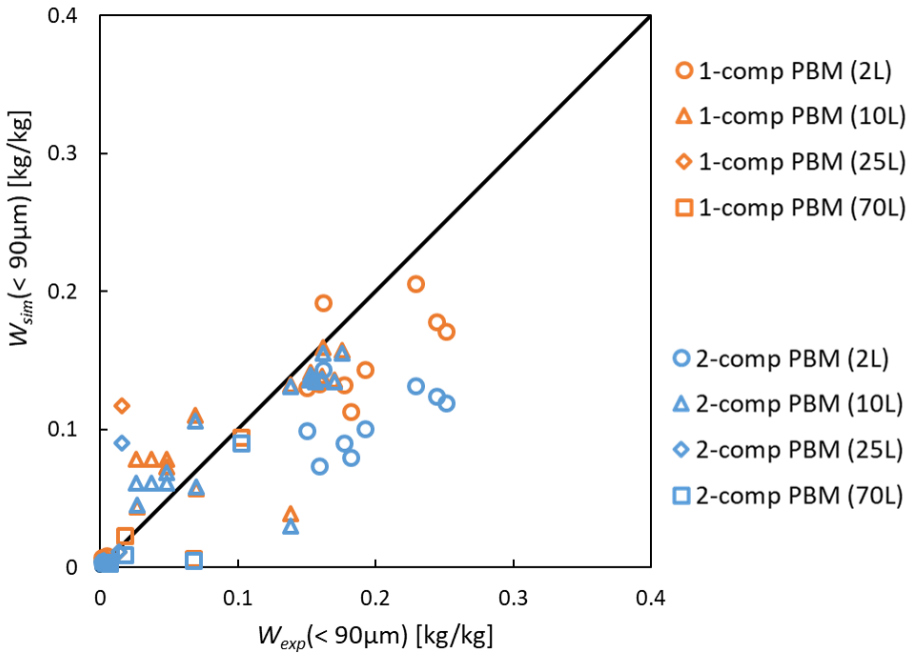

(a) Fines mass fraction W (< 90 µm)

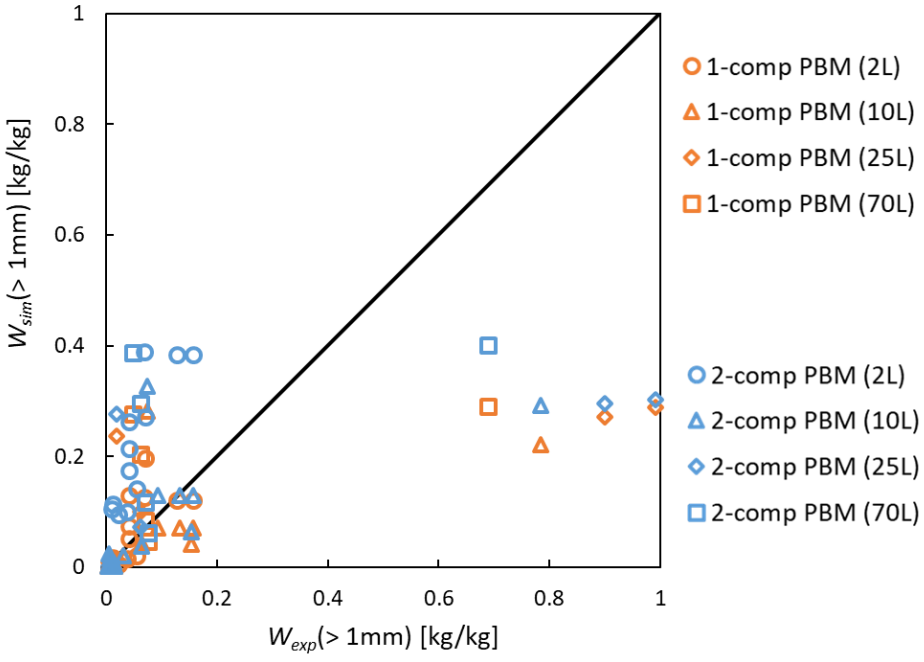

(b) Coarse mass fraction W (> 1 mm)

Figure D.18: Comparison of simulation and experimental mass fraction results across scales

D.2 Operating parameter sensitivity analysis results

First-order Sobol' indices ζ_{ij} determined for all operating parameters are shown in Figure D.19. Liquid-to-solid ratio shows a dominant effect on all CQAs ($\zeta_{ij} > 0.7$). Impeller tip speed and kneading time have a small impact ($0.01 < \zeta_{ij} < 0.1$). Liquid spray rate has a negligible impact ($\zeta_{ij} < 0.01$). Based on these results, the liquid-to-solid ratio, impeller tip speed and kneading time are identified as critical process parameters (CPPs).

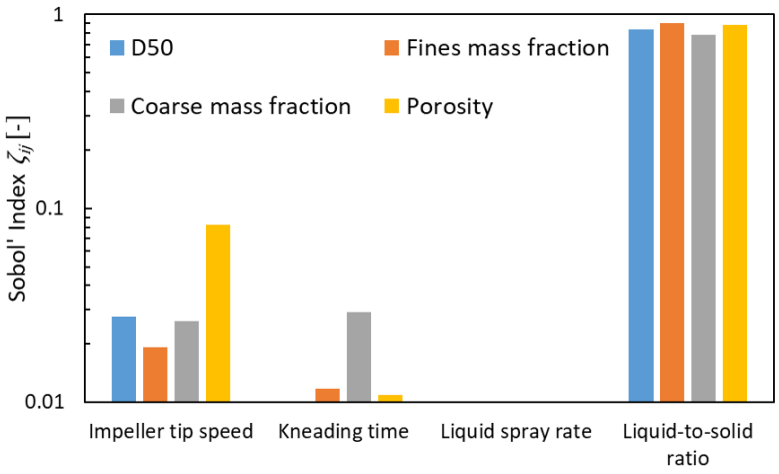

Figure D.19: First-order Sobol' indices results for operating parameters

D.3 Modelling parameter sensitivity analysis results

First-order Sobol' indices ζ_{ij} determined for all modelling parameters are shown in Figure D.20.

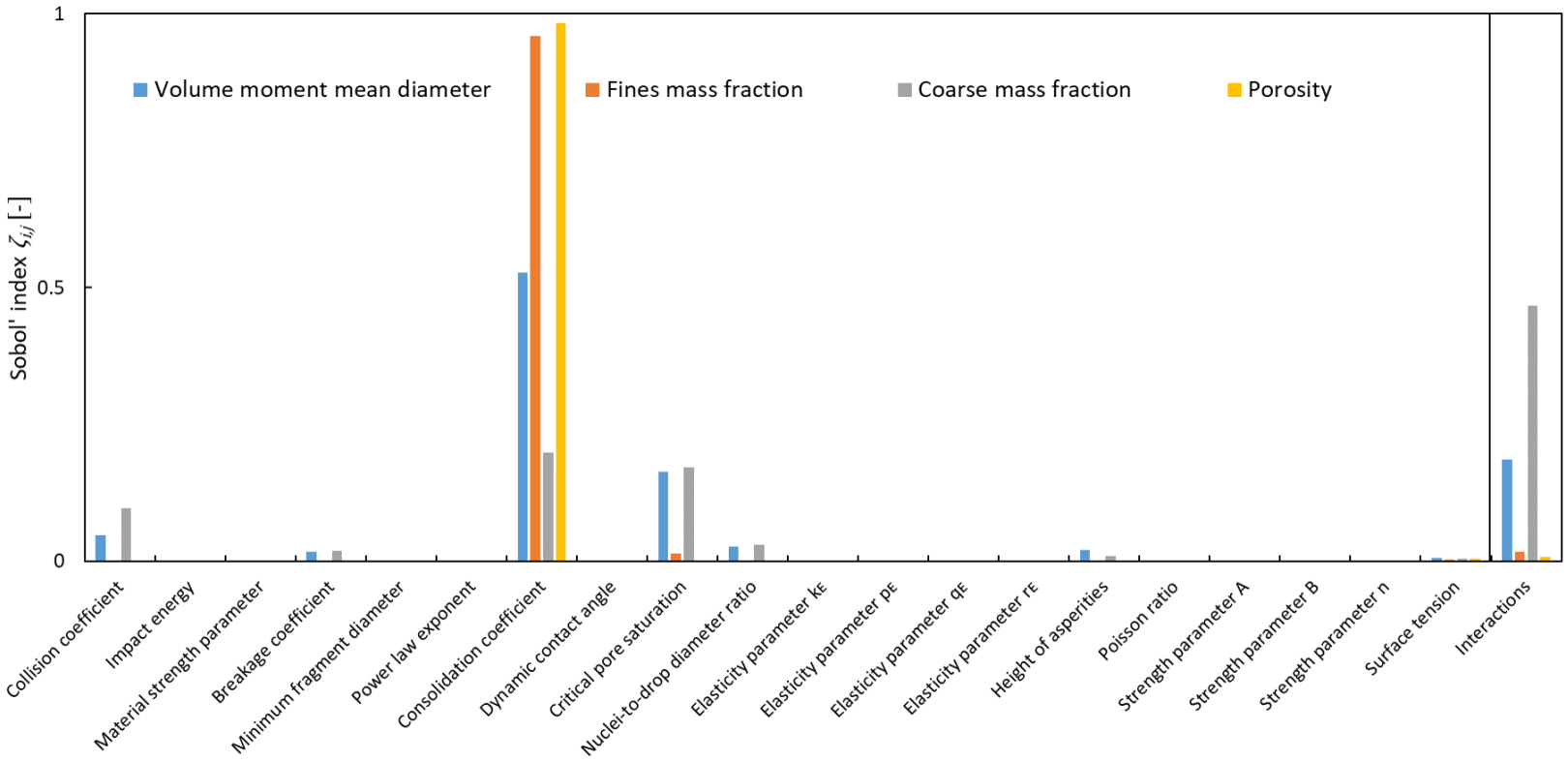

Figure D.20: All first-order Sobol' indices results for modelling parameters

D.4 Consolidation coefficient sensitivity

The parameter estimation resulted in a 95 % confidence interval of the consolidation coefficient $k_{cons} = 1 - 5$ (see Section 7.3.2). Figure D.21 shows that k_{cons} does not have a great effect on the consolidation kinetics within the confidence interval because the porosity profile is almost unchanged. Only $k_{cons} = 1$ results in slightly slower kinetics, and more significant mismatch with the experimental data.

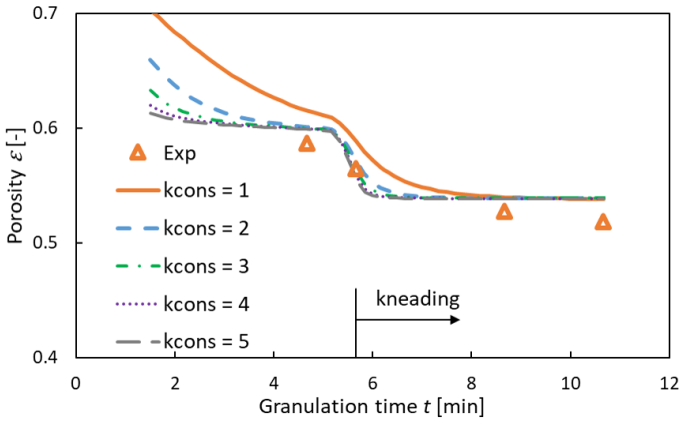

Figure D.21: Sensitivity to k_{cons} (Exp 16, and 30-36: $V = 10\,\mathrm{L}$; $t = 11\,\mathrm{min}$; $L/S = 0.17$; $Fr = 23$; $\Psi_a = 0.3$)

D.5 Approximation

Figure D.22 shows that the approximation successfully avoids zero and negative outputs, while providing very precise values for inputs $> 10^{-10}$.

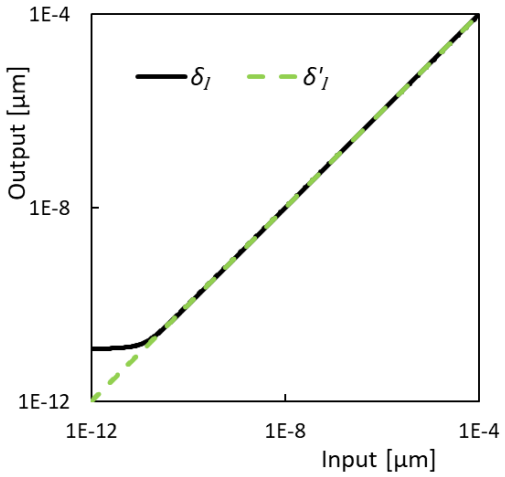

Figure D.22: Approximation for liquid layer thickness δ_l (Eq. 5.69)

Appendix E

ADDITIONAL DOCUMENTS

All experimental and simulation data is available in the documents attached:

`Size distribution.xlsx` - Drop size distributions

`Ubersichtstabelle Naproxen Finish.xlsx` - Experimental data and observations

`Analysis of granulation results.xlsx` - Particle size distributions of granulation experiments

`Results comparison with MCS and exp data - 10exp 10psi - nucleation number.xlsx` - Nuclei size distribution of experiments and all simulations

`Results_spatialdist_015_025.xlsx` - LND model calibration using Monte Carlo simulation results

`Sauter mean powder mixture and nuc-only.xlsx` - Sauter mean calculations

`SBellinghausenKuevetten.xlsx` - Spatial drop distribution results of spray

`Sensitivity analysis own MCS version 2.xlsx` - Sensitivity analysis of MCS

`Calculate Hapgoods PD model.xlsx` - Implementation of Hapgood's PD model

`Calculate Modified PD model.xlsx` - Implementation of MPD model

`Drop nucleation results.xlsx` - Results of drop nucleation experiments

`Density measurements V2.xlsx` - Porosity results from tap density and GeoPyc measurements

`Fitting results - 1comp - 4 parameters.xlsx` - 1-comp PBM results and comparison of experimental and all PBM results

`SSE calculcation.xlsx` - Overview and statistical assessment of PBM results

`Fitting results - 3comp - 4 parameters.xlsx` - 2-comp PBM results

`GSA_for_OPM.rar` - All GSA results for the operating regime maps

PRESENTATIONS AND PUBLICATIONS

Conference presentations

- Bellinghausen, S., Gavi, E., Jerke, L., Ghosh, P. K., Salman, A. D., and Litster, J. D. (2017). Modelling of a high-shear wet granulation process using a population balance framework. In *8th International Granulation Workshop*, Sheffield, UK. (Poster presentation)
- Bellinghausen, S., Gavi, E., Barrasso, D., Jerke, L., Ghosh, P. K., Salman, A. D., and Litster, J. D. (2018). Development and validation of a nucleation kernel for wet granulation. In *8th World Congress on Particle Technology*, Orlando, USA. (Oral presentation)
- Bellinghausen, S., Gavi, E., Jerke, L., Ghosh, P. K., Salman, A. D., and Litster, J. D. (2018). Model-driven scale-up framework for high-shear wet granulation. In *Roche PTDC TIS Forum*, Basel, Switzerland. (Oral presentation)
- Bellinghausen, S., Gavi, E., Barrasso, D., Jerke, L., Ghosh, P. K., Salman, A. D., and Litster, J. D. (2019). Model-driven scale-up approach for high-shear wet granulation. In *PARTEC International Congress on Particle Technology*, Nuremberg, Germany. (Poster presentation)
- Bellinghausen, S., Gavi, E., Jerke, L., Ghosh, P. K., Salman, A. D., and Litster, J. D. (2019). Model-driven scale-up framework for high-shear wet granulation. In *Roche PTDC TIS Forum*, Basel, Switzerland. (Oral presentation)
- Bellinghausen, S., Gavi, E., Barrasso, D., Jerke, L., Ghosh, P. K., Salman, A. D., and Litster, J. D. (2019). Model-driven scale-up approach for high-shear wet granulation. In *9th International Granulation Workshop*, Lausanne, Switzerland. (Poster presentation)

Journal article

- Bellinghausen, S., Gavi, E., Jerke, L., Ghosh, P. K., Salman, A. D., and Litster, J. D. (2019). Nuclei size distribution modelling in wet granulation. *Chemical Engineering Science: X*, 4:100038.